HIGH FIDELITY SIMULATION OF ROTORDYNAMIC MORTON EFFECT BY NONLINEAR TRANSIENT APPROACH

A Dissertation

by

JUNHO SUH

Submitted to the Office of Graduate and Professional Studies of
Texas A&M University
in partial fulfillment of the requirements for the degree of

DOCTOR OF PHILOSOPHY

Chair of Committee,	Alan B. Palazzolo
Committee Members,	Gary Fry
	Robert Handler
	Timothy Jacobs
Head of Department,	Andreas A. Polycarpou

August 2014

Major Subject: Mechanical Engineering

ABSTRACT

The present study is focused on accurate prediction of Morton effect problem including journal asymmetric heating and the corresponding long period amplitude oscillations using a nonlinear time transient rotordynamic simulation. For the analysis of the Morton effect problem, variable viscosity Reynolds equation and three-dimensional energy equation are coupled via temperature and viscosity, and solved simultaneously. Three-dimensional heat transfer equations of bearing and shaft are modeled by a finite element method, and thermally coupled with the fluid film via heat flux boundary condition. Asymmetric heat flux into the synchronously whirling rotor is solved by the orbit time averaged heat flux from fluid film to the spinning journal surface. The journal orbit is calculated by the nonlinear transient dynamic analysis of rotor-bearing system with variable time step numerical integration scheme. For the computation time reduction, modal coordinate transformation is adopted for dynamic and thermal transient analysis. This research explains how the thermal bow induced imbalance force develops in spinning journal with time, and how the vibration level is affected by the thermal bow vector.

This dissertation is also focused on a new modeling method of three-dimensional thermo-elasto-hydro-dynamic cylindrical pivot tilting pad journal bearing (TPJB). For the computational efficiency, modal coordinate transformation is utilized in the flexible pad dynamic model, and pad dynamic behavior is represented only by means of modal coordinate. Fluid film thickness is calculated by a newly developed node based method, where pad arbitrary thermal and elastic deformation, and journal thermal expansion are taken into account simultaneously. This paper presents a new analysis method for a thermo-elasto-hydro-dynamic tilting-pad journal bearing system to reach a static equilibrium condition adopting nonlinear transient dynamic solver. In the nonlinear transient dynamic solver, physical and modal coordinates co-exist for computational efficiency, and transformation between modal and physical coordinate is performed at each numerical integration time step. Nonlinear time transient dynamic analysis and steady thermal analysis are combined to find the static equilibrium condition of the TPJB system, where the singular matrix issue of flexible pad finite element (FE) model is resolved.

DEDICATION

To God who knows all things and my wife Woochung who god gave me

ACKNOWLEDGEMENTS

I would like to thank Dr. Palazzolo for his guidance and support throughout the course of this research in the Vibration Control Electromechanical Laboratory at Texas A&M University. He helped me to be a productive and professional researcher. I also thank my committee members, Dr. Fry, Dr. Handler and Dr. Jacobs for their guidance and support throughout the course of this research.

I also appreciate Dr. Choi, former graduate advisor of my master’s degree in South Korea, for his valuable guidance and support. Special thanks go to Dr. Kang and Dr. Koo for their valuable advices and guidance for my PhD degree.

Thanks also go to my friends and colleagues and the department faculty and staff for making my time at Texas A&M University a great experience. I also want to extend my gratitude to the Turbomachinery Research Consortium who has provided the research funding.

Thanks to my mother, father, sister, mother in law and father in law for their encouragement, patience and love.

Finally thanks to my wife, Woochung, for all her hard work at home with my two daughters, Jiwon and Heewon, while I put in my time at the lab.

NOMENCLATURE

c	Heat Capacity
$\boldsymbol{C_{GYRO}}$	Gyroscopic Matrix
$\boldsymbol{C_{BRG}}$	Bearing Damping Matrix
$\boldsymbol{C_{T}}$	Thermal Damping Matrix Of Heat Conduction F.E. Model
CL_P	Pad Clearance
CL_B	Bearing Clearance
$Cl_{ratio_{therm}}$	Reduced Film Thickness Ratio
d_n	Distance Between *n*th Node And Thermal Shaft Right End
e_n	Thermal Bow Induced Eccentricity at nth Node of F.E. Rotor
e_x	X-Component of Journal Position
e_y	Y-Component of Journal Position
e_G	Distance Between Mass Center And Pivot
E_P	Young's Modulus of Pivot
E_H	Young's Modulus of Pivot Housing
F	Thermal Load
$F_{x_{T.B}}$	Thermal Bow Induced Imbalance Force Acting on X Axis
$F_{y_{T.B}}$	Thermal Bow Induced Imbalance Force Acting on Y Axis
F_o	Fluidic Force Acting on Pad
$\boldsymbol{F_R}$	External Force Acting On Finite Element Rotor
$\boldsymbol{F_{E.P.FL}}$	Fluidic Load on Pad Vector of Elastic Pad F.E. Model

$\boldsymbol{F_{E.P.DRG}}$	Drag Force on Pad Vector of Elastic Pad F.E. Model
$\boldsymbol{F_{E.P.PVT}}$	Pivot Load on Pad Vector of Elastic Pad F.E. Model
$\boldsymbol{F_T}$	Thermal Load in Heat Conduction F.E. Model
$\boldsymbol{F_{E.T}}$	Thermal Load Vector
h_n	*n*th Nodal Film Thickness
$h_{T.E.J}$	Film Clearance Reduction Due to Journal Thermal Expansion
$h_{T.E.P}$	Film Clearance Reduction Due to Pad Thermal Expansion
h	Convective Coefficient
j_n	*n*th Nodal Point on Journal
J_G	Moment of Inertia of Pad
k	Heat Conductivity
k_L	Lubricant Heat Conductivity
k_B	Bearing Heat Conductivity
k_J	Journal Heat Conductivity
$\boldsymbol{K_E}$	Stiffness Matrix of F.E. Structural Model
$\boldsymbol{k_{E.P}}$	Modal Stiffness of Elastic Pad F.E. Model
$\boldsymbol{K_{E.P}}$	Stiffness Matrix of Elastic Pad F.E. Model
$\boldsymbol{K_{STRUC}}$	Finite Element Rotor Stiffness Matrix
$\boldsymbol{K_T}$	Thermal Stiffness Matrix of Heat Conduction F.E. Model
k_p	Pivot Stiffness
$\boldsymbol{K_{BRG}}$	Bearing Stiffness Coefficient Matrix

l_{te}	Axial Position of Shaft Right End
m_G	Pad Mass
$\boldsymbol{m}_{\boldsymbol{E.P}}$	Modal Mass of Elastic Pad F.E. Model
$\boldsymbol{M}_{\boldsymbol{E.P}}$	Mass Matrix of Elastic Pad F.E. Model
M_o	Fluidic Moment Acting on Pivot
$\boldsymbol{M}_{\boldsymbol{R}}$	Mass Matrix of finite element (F.E.) Rotor Model
M_n	Mass At Nth Node of F.E. Rotor
NO_{ROTOR}	Number of Nodes of F.E. Rotor Model
p_{pvt}	Pivot Displacement
p	Fluid Pressure
p_n	*n*th Nodal Point on Pad
$\boldsymbol{P}$	Modal Thermal Load
q	Heat Flux
$\boldsymbol{Q}$	Generalized Modal Temperature
Q_{out}	Fluid Amount of Recirculated Flow
Q_{supply}	Fluid Amount of the Supply Flow
R	Journal Radius
R_H	Circumferential Pivot Housing Radius
R_P	Circumferential Pivot Radius
$R_H{}'$	Transverse Bearing Pivot Radius
t	Time

$T_{avg_{pad}}$	Volume Averaged Temperature of Pad
$T_{ref_{pad}}$	Reference Temperature of Pad
$T_{avg_{shaft}}$	Volume Averaged Shaft Temperature
$T_{ref_{shaft}}$	Reference Temperature of Shaft
t_{pad}	Averaged Pad Thickness
T_0	Reference Fluid Temperature
T^{∞}	Ambient Temperature
T	Temperature
T_{in}	Temperature of Flow Entering into the Leading Edge
T_{out}	Temperature of Recirculated Flow
T_{supply}	Temperature of the Supply Flow
u	Fluid Velocity in The Circumferential Direction
$\boldsymbol{U}$	Shaft Surface Linear Velocity
v_P	Poison's Ratio of Pivot
v_H	Poison's Ratio of Pivot Housing
w	Fluid Velocity in The Axial Direction
$\boldsymbol{X_{E.P}}$	Nodal Displacement Vector of Elastic Pad F.E. Model
$\boldsymbol{X_E}$	Thermal Expansion Vector
$\boldsymbol{X_R}$	Displacement Vector in Physical Coordinate
z	Axial Position
z_{NDE}	Axial Position of Bearing Center

$\boldsymbol{Z}_{\boldsymbol{E.P}}$	Modal Displacement Vector of Elastic Pad F.E. Model
α_{shaft}	Thermal Expansion Coefficient of Shaft
α_{pitch}	Pad Pitch Angle
α_{pad}	Thermal Expansion Coefficient of Pad
β	Viscosity Coefficient
β_{ξ}	Thermal Bow Angle At The End of Thermal Shaft
ρ	Density
ξ	Thermal Bow Axis on X-Y Plane
$\boldsymbol{\xi}_{\boldsymbol{l}}$	Displacement Vector in Modal Coordinate
μ	Fluid Viscosity
δ_{tilt}	Pad Tilting Angle
$\theta_{F.E}$	Thermal Bow Phase Inside Thermal Shaft
θ_{n}	Thermal Bow Phase At Nth Node Of F.E. Rotor
θ_{p}	Pivot Circumferential Position
θ	Circumferential Coordinate
θ_{x}	X-Component of Journal Angular Position
θ_{y}	Y-Component of Journal Angular Position
$\emptyset_{HIGH}$	Phase of High Spot
$\emptyset_{LAG}$	Lagging Phase
$\emptyset_{HOT}$	Phase of Hot Spot
$\boldsymbol{\Phi}_{\boldsymbol{E.P}}$	Eigenvector of Elastic Pad F.E. Model

ω	Journal Spin Speed

TABLE OF CONTENTS

Page

LIST OF FIGURES

LIST OF TABLES

Page

1 INTRODUCTION

1.1 Overview of the Morton Effect

Thermal induced synchronous rotor instability problem, known as the Morton effect is caused by the journal differential heating in fluid film bearing. In the case of synchronous whirl orbit around the equilibrium position, a maximum viscous heating occurs around the minimum film thickness area, and this causes hot spot ($\emptyset_{HOT}$) and cold spot ($\emptyset_{COLD}$) leading to a thermal bending ($\emptyset_{THERM.BOW}$) at the bearing location. Convection of heat in the film is known to displace the hot spot ($\emptyset_{HOT}$) from -20 to 40° ahead of the high spot ($\emptyset_{HIGH}$). The temperature differential across the journal causes a bending moment and resulting bow in the rotating frame that acts like a distributed synchronous excitation in the fixed frame. This thermal bow may cause increased vibration and continued growth of the synchronous orbit into a limit cycle.

The present study is focused on accurate prediction of Morton effect problem including journal asymmetric heating and the corresponding long period amplitude oscillations using a nonlinear time transient rotordynamnic simulation. This paper presents a theoretical model of thermal induced synchronous instability problems in nonlinear rotor-bearing system, and suggests a new computational algorithm for the nonlinear transient analysis of the Morton effect where the dynamic and thermal problems are combined. For the analysis of the Morton effect problem, variable viscosity Reynolds equation and three-dimensional energy equation are coupled via temperature and viscosity, and solved simultaneously. Three-dimensional heat transfer equations of bearing and shaft are modeled by a finite element method, and thermally coupled with the fluid film via heat flux boundary condition. Asymmetric heat flux into the synchronously whirling rotor is solved by the orbit time averaged heat flux from fluid film to the spinning shaft surface. The journal orbit is calculated by the nonlinear transient dynamic analysis of rotor-bearing system with variable time step numerical integration scheme. For the computation time reduction, modal coordinate transformation is adopted in dynamic and thermal transient analysis. Thermal bow effect makes a significant change to dynamic behavior of rotor-bearing system, and thermal hysteresis bode-plot which is one of the characteristics of the Morton effect problem is presented with time varying spin speed.

This paper presents simulation results corresponding with the theoretical Morton effect model explained in the Part I, where the three-dimensional finite element models of bearing, shaft and fluid film are adopted. In addition, it explains how thermal bow induced imbalance force develops in spinning journal with time, and how the vibration level is affected by the thermal bow vector. Shaft asymmetric thermal expansion induced by non-uniform journal heating is simulated, which is one of unique contributions of this research.

1.2 Literature Review

1.2.1 Morton effect simulation

In 1973, Tieu [1] formulated a variational principle based on the local potential and a finite element method (F.E.M.) for the evaluation of the two-dimensional (2D) fluid film thermal gradient in an infinitely wide bearing. In 1986, Khonsari [2] investigated thermo-hydro-dynamic (THD) effects in fluid film journal bearing under static load, and developed a computer algorithm to calculate the 2D temperature distribution in the bearing and fluid film utilizing finite difference method (F.D.M.). Cavitation effect and mixing temperature theory for the evaluation of inlet temperature were studied. Adiabatic boundary condition on the bearing inner surface was imposed for the computation time reduction.

In 1988, Knight and Barrett [3] presented an approximated method for THD tilting-pad journal bearing (TPJB) by use of a simplified heat conduction model. Thermal gradient across the film thickness is assumed to have a second order profile, and pad heat conduction is assumed to be only in the radial direction. The journal surface temperature is calculated by the averaged film temperature in the circumferential direction. In 1990, Earles and Palazzolo [4] calculated nonlinear transient response of spinning shaft supported by thermo-elastic TPJB excited by a large mass imbalance. It is found that the pad flexibility and thermal effect on fluid film increase vibration level and reduce film thickness producing increased maximum temperature.

In 1993, Keogh and Morton [5] presented an asymmetric viscous shearing in the fluid film journal bearing and this phenomenon is referred to as the Morton effect. They developed a new method to solve the dynamic energy balance problem for a pre-defined elliptical orbit in the journal bearing. Short bearing theory and iso-viscosity lubricant were assumed for the simplicity. In the energy equation, axial and circumferential conductions were ignored, and 2D temperature in lubricant, bearing and journal models are considered. The journal surface temperature variations were evaluated by perturbing the orbit. In 1999, Gomiciaga and Keogh [6] presented a new method to evaluate the asymmetric heat flux into the synchronously whirling journal with a prescribed orbit shape based on the orbit time averaged heat flux into the journal and bearing. Steady thermal conditions of the shaft and bearing were evaluated by 3D energy equation adopting finite volume method (F.V.M.) and 3D heat conduction model of the shaft and bearing. In 1999, Larsson [7, 8] examined a relation between journal whirling and journal differential heating in the lubricant and shaft interface. In 2004, Balbahadur and Kirk [9, 10] developed an analytical method for the Morton effect simulation, and studied rotor system supported by plain and tilting-pad journal bearings. The results from the theoretical models were compared with the case studies. It was assumed that the hot spot coincides with the high spot, and a cold spot will be formed on the area with maximum film thickness.

In 2010, Murphy and Lorenz [11] developed an approximate and simplified analytical method to evaluate temperature differential across the journal and its effect on synchronous vibration without the energy equation and shaft heat conduction equation. They conducted the Morton effect simulation adopting linear vector relationship where each vector element has an amplitude and phase. It is assumed that the thermal response is infinitely slow compared with the rotor-dynamic response. In 2012, Childs and Saha [12] presented a computational algorithm for the Morton effect. Shaft thermal gradient induced by the initial elliptic orbit was solved by adding the temperature distributions for the separate forward and backward orbits. Reducing fluid film viscosity and the overhung mass were suggested to mitigate the Morton effect problem.

In 2013, Palazzolo and Lee [13] suggested a finite element (F.E.) model for the varying viscosity fluid film and thermal shaft model. Elastic rotor model was analyzed combined with THD tilting pad bearing, and transient analysis was done adopting staggered integration scheme for the computation time reduction. Insulated thermal boundary condition was imposed at the contact between fluid film and bearing liner, which means pad heat conduction and the resultant pad thermal expansion are not taken into account. 2D energy equation was used for the lubricant temperature evaluation.
To predict the Morton effect problem without a loss of accuracy, a more sophisticated numerical modeling is needed. This research is an extension of Palazzolo and Lee's [13] earlier work. This study adopted more rigorous analysis model such as (1) 3D energy equation, (2) 3D heat conduction model of bearing and shaft, (3) various thermal boundary conditions, (4) asymmetric shaft and pad thermal expansion in the circumferential and axial direction calculated by F.E. model and (5) nonlinear time transient dynamic and thermal analysis with variable time step numerical integration scheme.

Earlier studies evaluated thermal bow angle and phase by analytical method [13]; however, in this research, shaft thermal bending and expansion was evaluated by the 3D thermal gradient in the F.E. shaft model. Earlier studies assumed that the lubricant temperature gradient in the axial direction has uniform profile; however, in the case of Morton effect simulation with bigger orbit size, 3D energy is found to be required for the reliable prediction. The simulation results by 2D and 3D energy equations will be compared by the static equilibrium analysis with zero orbit and nonlinear time transient Morton effect analysis with large size orbit. Modified mixing temperature theory was adopted for more realistic consideration. Modal coordinate transformations in the dynamic and thermal systems are adopted for the computation time reduction without losing accuracy. Thermal time constants of the shaft and bearing structure are much higher than for vibration; therefore, the thermo-dynamic coupled transient analysis model requires a long computation time. So, a staggered integration scheme [13] is adopted to increase the computation efficiency without a loss of accuracy of the dynamic and thermal transient models.

De Jongh and Morton [14] encountered a synchronous vibration problem during the mechanical running test on a centrifugal compressor, for an offshore gas-lift application. The rotor weighs 450 kg and is supported by two tilting-pad journal bearings. Maximum continuous speed of 11,947 rpm could not be achieved due to the excessive synchronous vibration level. It is found that the hot spot lags the high spot by from 15° to 20°, and the vibration problem could be mitigated by reducing the overhung mass.

De Jongh and van der Hoeven [15] investigated the Morton effect problem in two pipeline compressor for a natural gas application, which had passed API 617. The operating speed ranged from 5370rpm to 9400rpm. After the installation at a site, the rotor showed an unstable Morton effect problem. Heat barrier to minimize the thermal bow angle was suggested, and it solved the problem well.

Gomiciaga and Keogh [6] evaluated the journal temperature differential in a plain journal bearing for a prescribed orbit utilizing finite volume method(FVM). They utilized an orbit time averaged heat flux into the journal surface to evaluate the journal temperature differential, and found that the temperature differential increases with rotor spin speed and vibration level. Childs and Saha [16] suggested reducing lubricant viscosity and reducing the overhung mass for the remedy of the Morton effect problem. Palazzolo and Lee [13] developed a Morton effect simulation algorithm based on the two-dimensional (2D) F.E. bearing model. The interface between the lubricant and bearing inner surface is assumed to be thermally insulated, and this causes higher temperature than the pad model with convective boundary condition at the outer surface. Decreasing the lubricant viscosity by increasing its temperature is found to mitigate the Morton effect problem.

The present work utilizes the rotor-bearing system presented by de Jongh and van der Hoeven [15], which is further studied in Balbahadur and Kirk's publication [9]. Some input parameters such as thermal expansion coefficients and pivot shapes were assumed because they were not provided in their research paper. The complete list of parameters explored in the present work is shown in the abstract.

1.2.2 Tilting-pad journal bearing numerical model

Fluidic forces acting on the spinning journal generated by TPJB can be expressed by means of spring and damping forces evaluated by lubrication and elastic theory. In 1964, Lund [17] firstly presented the pad assembly method for the calculation of frequency reduced spring and damping coefficients of TPJB where the harmonic rotor and pad motions are assumed. Finite difference method (FDM) is adopted to solve the fluidic force distribution on the pad where iso-viscous solution is assumed. In 1973, Tieu [1] calculated lubricant temperature distribution for infinitely wide bearing with a prescribed film thickness. FEM is adopted for solving the energy equation. The iso-viscous and the varying viscous cases are solved and compared, where iteration scheme is used. In 1979, Nilson [18] extended Lund's research considering pad bending deformation due to the fluidic pressure distribution. It is shown that the damping coefficient was influenced more in the bigger journal eccentricity than stiffness coefficient due to the pad bending. Film thickness was expressed by means of stationary part and non-stationary part. The two-dimensional (2D) pad deformation is assumed to be constant in the axial direction. For the calculation of pad bending due to the fluidic force, the 2D curved beam finite element (FE) model was clamped at more than two nodal points to avoid a singular matrix problem. In 1987, Lund and Pederson [19] expanded Lund [17] and Nilson's [18] research by considering film thickness perturbation due to the pivot and pad deformations, where FDM is adopted.

Pivot deformation is one of the crucial factors that can make a significant change in the TPJB dynamic behavior. Kirk and Reedy [20] derived pivot stiffness equations of various pivot shapes utilizing the relationship between applied load on pivot and pivot elastic deformation. It can be easily implemented into computer program for the TPJB analysis, and the current research adopted their method in nonlinear transient dynamic analysis for a time varying pivot stiffness.

In 1990, Earles et al. [21] presented an approximate 2D FE TPJB model to simulate the pad bending. The pad deformation was presented by a single degree of freedom, which is the pad radius curvature change. In 1994, Kim et al. [22] presented a 2D TPJB model, where thermal effects are taken into account with generalized Reynolds equation and 2D energy equation. Up-winding scheme is utilized in the energy equation to avoid a numerical instability problem generated by heat convection term.

In 1995, Kim et al. [23] adopted modal coordinate transformation to express the pad elastic deformation by means of modal coordinates and mode shapes. In the same year, Gadangi et al. [24] studied the dynamic response of TPJB considering thermal effects and elastic deformation of pad. Pad deformation had bigger effect on the journal orbit than the thermal effect. Guyan reduction of the 2D pad elastic FE model is conducted for the computation time reduction, where the pad surface degrees of freedom became the master degrees of freedom and others are slave.

In 1995, Desbordes et al. [25] presented a 3D pad deformation model, and calculated the journal orbit under various unbalance eccentricities. For the evaluation of pad elastic deformation under the fluidic pressure distribution, steady pad analysis is adopted where the pad dynamic analysis considering flexibility is not taken into account.

This 3D pad deformation model showed 40 percent lower minimum film thickness than the 2D pad model under a large imbalance motion.

In 2013, Childs and Wilkes [26] assumed the pad surface remains circular under elastic deformation by fluidic force distribution. Iso-viscous Reynolds equation was solved by use of FDM, and the simulation results were compared with experimental results.

Earlier studies have adopted iteration schemes such as Newton-Raphson method to find the journal-pad static equilibrium state. Even when it comes to transient analysis, pad elastic deformation has been assumed to be constant neglecting the FE flexible pad nodal inertia, where additional nodal points besides the pivot nodes are constrained. In this research, the pad elastic deformation is calculated with a full nonlinear time transient numerical integration procedure adopting modal coordinate reduction by selection of modes that govern the pad dynamic behavior.

In 1995, Kim et al. [23] adopted modal coordinate transformation to simulate the 2D TPJB model considering pad flexibility and heat conduction, where four nodal iso-parametric elements are employed to discretize the elastic and thermal problem domains. Newton-Raphson method is adopted to find the journal and pad static equilibrium conditions. To express the pad dynamic behavior, pad tilting angle, pivot translational motion and modal displacement are taken into account separately. However, in this research, pad motion is expressed only by means of modal displacement which includes pivot translational motion and tilting motion.

In 1995, Desbordes et al. [25] simulated 3D pad deformation and investigated its effects on the bearing dynamic behavior adopting F.E. analysis. Dynamic response was simulated at various degrees of initial imbalance forces. Even though it was a dynamic response analysis, pad deformation was simulated on in steady analysis, so the time varying elastic deformation of the pad during a journal orbiting was ignored. In this research, time transient pad dynamic analysis was performed, where pad elastic deformation is changing in a short space of time due to the fluctuating fluidic pressure condition.

In 1995, Gadangi et al. [24] simulated large imbalance motion of spinning journals supported by flexible tilt pad journal bearings, where thermal expansion and pad flexibility were taken into account. As in other earlier studies, pad elastic deformation was assumed to be constant during the time transient analysis even when the fluidic pressure varies during the journal orbiting.

Earlier studies have not considered time varying pad elastic deformation which requires complex numerical procedure and heavy computing. In this research, time transient flexible pad dynamic analysis was performed to find the static equilibrium conditions of spinning journal and pads. Part II provides guidance to bearing designers for developing a reliable prediction method of TPJB dynamic behavior.

2 NUMERICAL MODEL OF FLUID FILM*

Some of the fluid film numerical models discussed in this section came from published researches by Suh and Palazzolo [27, 28].

2.1 Reynolds Equation

The governing equation to obtain a pressure distribution in the thin film is the Reynolds equation, which models the thin fluid film between the two moving planes. The thin film is denoted as the fluid film thickness and is represented by h. The Reynolds equation can be derived from the momentum and the continuity equations [17], yielding pressure and velocity distribution. Integration of the momentum equation provides the velocity distribution in terms of pressure gradients. Substitution of this velocity profile into the flow rate continuity equation will give the Reynolds equation. The generalized Reynolds equation can be expressed as:

$$\boldsymbol{\nabla} \cdot (D_1 \boldsymbol{\nabla} p) + (\boldsymbol{\nabla} D_2) \cdot (\boldsymbol{U_2} - \boldsymbol{U_1}) + (\boldsymbol{\nabla} h) \cdot U_1 + \frac{\partial h}{\partial t} = 0 \tag{1}$$

The above generalized Reynolds equation can be reduced to the following for a fixed bearing and spinning shaft:

$$\boldsymbol{\nabla} \cdot (D_1 \boldsymbol{\nabla} p) + (\boldsymbol{\nabla} D_2) \cdot \boldsymbol{U} + \frac{\partial h}{\partial t} = 0 \tag{2}$$

For a thermo-hydro-dynamic problem, viscosity is a function of the temperature, and the constants D_1 and D_2 can be expressed by:

---

*Reprinted with permission from "Three-Dimensional THD Morton Effect Simulation Part I: Theoretical Model" by Suh, J., and Palazzolo, A, 2014. Journal of Tribology, 136(3), 031707, Copyright 2014 by ASME.

$$D_1 = \int_0^h \int_0^z \frac{\xi}{\mu} d\xi \, dz - \frac{\int_0^h \frac{\xi}{\mu} d\xi}{\int_0^h \frac{1}{\mu} d\xi} \int_0^h \int_0^z \frac{1}{\mu} d\xi \; dz \tag{3}$$

$$D_2 = \frac{\int_0^h \int_0^z \frac{1}{\mu} d\xi \; dz}{\int_0^h \frac{1}{\mu} \, d\xi} \tag{4}$$

The fluid film in the generalized Reynolds equation is assumed to have a laminar flow, invariant pressure in the film thickness direction, a negligible shaft curvature effect, negligible fluid inertia, constant fluid density, and temperature-affected viscosity. Additionally, it is assumed to be an incompressible Newtonian fluid and non-slip at the solid and fluid interface. The relationship between viscosity and temperature of the fluid can be expressed as:

$$\mu = \mu_0 e^{-\beta(T-T_0)} \tag{5}$$

This research considers Reynolds cavitation boundary condition employing a back substitution procedure suggested by Lund and Thomsen [29]. From the Reynolds equation, the velocity profile can be evaluated by the following equation [22]:

$$\boldsymbol{u} = \left(\int_0^z \frac{\xi}{\mu} d\xi - \frac{\int_0^h \frac{\xi}{\mu} d\xi}{\int_0^h \frac{1}{\mu} d\xi} \int_0^z \frac{1}{\mu} d\xi \right) \boldsymbol{\nabla p} + \frac{\int_0^z \frac{1}{\mu} d\xi}{\int_0^h \frac{1}{\mu} d\xi} \cdot \boldsymbol{U} \tag{6}$$

In a conventional two-dimensional analysis, the velocity profile is obtained only at the bearing axial center; however, for the full three-dimensional bearing and fluid film model, the velocity profile should also be obtained in the axial direction. In the case of two-dimensional analysis, $\boldsymbol{\nabla p}$ in the above equation (6) was only in the circumferential direction; however, in the three-dimensional (3D) analysis, $\boldsymbol{\nabla p}$ is evaluated both in the circumferential and axial direction. Thus, the velocity profile, $\boldsymbol{u}$, becomes a 3D vector.

2.2 3D Energy Equation

The temperature distribution in the thin fluid film is governed by the energy equation, which needs thermal boundary conditions, pressure, velocity, and viscosity distribution. The Reynolds equation and the energy equation are coupled via the viscosity profile. The updated viscosity distribution is used in solving the Reynolds equation. For a laminar flow, incompressible, and Newtonian fluid, the energy equation is expressed by [13]:

$$\rho c\left(\frac{\partial T}{\partial t}+u\frac{\partial T}{\partial x}+w\frac{\partial T}{\partial z}\right)=k\left(\frac{\partial^2 T}{\partial x^2}+\frac{\partial^2 T}{\partial y^2}+\frac{\partial^2 T}{\partial z^2}\right)+\mu\left[\left(\frac{\partial u}{\partial y}\right)^2+\left(\frac{\partial w}{\partial y}\right)^2\right] \tag{7}$$

where the conduction is considered in x, y, and z directions, and the convection term is only considered in the x and z directions since the velocity profile created by Reynolds equation has only x and z components. The dissipation term is only considered by $(\partial/\,\partial y)^2$ term since the thin film thickness is only in the film thickness direction. According to Gadangi's research [24], there was no noticeable difference between transient and steady state energy equations in large imbalance transient analysis. So time dependent lubricant temperature $\partial T/\,\partial t$ is not taken into account as seen in (7).

Thin film temperature has a strong influence on the viscosity distribution, and the pressure distribution does not. Viscosity can be assumed to follow an exponential relationship given by (5). On the other hand, density change is small compared to the viscosity change with temperature [30]. Typically the lubricant density changes by around 10% with 100°C change of temperature [31]. The finite element method is used for solving energy equation. Eight nodes isoparametric elements are used for discretizing the film domain. The solution of (7) exhibits spatial temperature oscillation problems as a result of the convection term on the left hand side of the equation (7), so the quadratic up-winding scheme proposed by Zienkiewicz [32] et al. is employed to mitigate the problem. The boundary conditions of the energy equation are as follows:

(a) The one-dimensional mixing temperature theory in the axial direction is used for the inlet fluid temperature.

(b) For the cavitation region, the dissipation term in the energy equation is set to zero.

(c) When cavitation occurs, the lubricant thermal conductivity is replaced with an air thermal conductivity.

2.3 Upwinding Scheme

The convection term in the energy equation causes an oscillation of temperature. To get rid of this problem, the classical Galerkin scheme(8) is modified by adopting the upwinding techniques. The weight function is updated based on the direction and amplitude of the fluid flow velocity. (see (14))

$$W(\xi,\eta,\tau) = N(\xi)N(\eta)N(\tau) \tag{8}$$

$$W(\xi,\eta,\tau) = \big(N(\xi) - \alpha F(\xi)\big)\big(N(\eta) - \beta F(\eta)\big)\big(N(\tau) - \gamma F(\tau)\big) \tag{9}$$

$$W_i(\xi) = N_i(\xi) - \alpha_{ij}\frac{3}{4}(1-\xi)(1+\xi) \tag{10}$$

$$W_i(\eta) = N_i(\eta) - \beta_{ij}\frac{3}{4}(1-\eta)(1+\eta) \tag{11}$$

$$W_i(\xi) = N_i(\tau) - \gamma_{ij}\frac{3}{4}(1-\tau)(1+\tau) \tag{12}$$

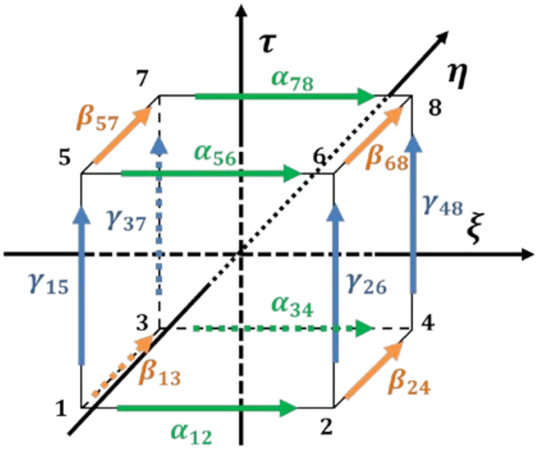

Fig. 1 Three dimensional upwind scheme

The parameters $\alpha, \beta,$ and γ are evaluated depending on the flow direction and local P_e number. The upwinding function, $F(\xi)$, $F(\eta)$, and $F(\tau)$ are polynomials of the zero-th order. In current research, a quadratic upwinding function is employed. For the three dimensional analysis, 3D example is considered here. A natural coordinate system domain of an eight nodes iso-parametric element is shown in Fig. 1. Shape and weight functions are defined based on one dimensional shape and weight functions. According to the node numbers shown in Fig. 1, the one-dimensional shape functions are

$$\begin{array}{lll}
\psi_1(\xi) = \frac{1}{2}(1-\xi) & \psi_1(\eta) = \frac{1}{2}(1-\eta) & \psi_1(\tau) = \frac{1}{2}(1-\tau) \\
\psi_2(\xi) = \frac{1}{2}(1+\xi) & \psi_2(\eta) = \frac{1}{2}(1-\eta) & \psi_2(\tau) = \frac{1}{2}(1-\tau) \\
\psi_3(\xi) = \frac{1}{2}(1-\xi) & \psi_3(\eta) = \frac{1}{2}(1+\eta) & \psi_3(\tau) = \frac{1}{2}(1-\tau) \\
\psi_4(\xi) = \frac{1}{2}(1+\xi) & \psi_4(\eta) = \frac{1}{2}(1+\eta) & \psi_4(\tau) = \frac{1}{2}(1-\tau) \\
\psi_5(\xi) = \frac{1}{2}(1-\xi) & \psi_5(\eta) = \frac{1}{2}(1-\eta) & \psi_5(\tau) = \frac{1}{2}(1+\tau) \\
\psi_6(\xi) = \frac{1}{2}(1+\xi) & \psi_6(\eta) = \frac{1}{2}(1-\eta) & \psi_6(\tau) = \frac{1}{2}(1+\tau) \\
\psi_7(\xi) = \frac{1}{2}(1-\xi) & \psi_7(\eta) = \frac{1}{2}(1+\eta) & \psi_7(\tau) = \frac{1}{2}(1+\tau) \\
\psi_8(\xi) = \frac{1}{2}(1+\xi) & \psi_8(\eta) = \frac{1}{2}(1+\eta) & \psi_8(\tau) = \frac{1}{2}(1+\tau)
\end{array} \tag{13}$$

The general three dimensional weight functions are defined as follows:

$$W = \left(N(\xi) - \alpha F(\xi)\right)\left(N(\eta) - \beta F(\eta)\right)\left(N(\tau) - \gamma F(\tau)\right) \tag{14}$$

The upwinding parameters $\alpha_{ij}, \beta_{ij},$ and γ_{ij} depend on the velocity of element line $i-j$, length of the element line and thermal diffusivity (k). The parameter Pe_{ij} called as a local Peclet number is defined as:

$$Pe_{ij} = \frac{u_{ij} h_{ij}}{k} \tag{15}$$

where h_{ij} is the mesh line size between node number i and j, and k is the thermal diffusivity. The velocity of the element side $i-j$, u_{ij} is defined as follows :

$$u_{ij} = \left\{ \frac{1}{2} \left(\boldsymbol{u_i} + \boldsymbol{u_j} \right) \cdot \boldsymbol{l_{ij}} \right\} \tag{16}$$

where $\boldsymbol{u}_i$denotes the velocity vector at the node i, and $\boldsymbol{l_{ij}}$ is the unit vector of the direction to $i-j$. The optimum parameters of $\alpha_{ij}, \beta_{ij},$ and γ_{ij} can be determined by Pe_{ij}.

$$\begin{aligned} \alpha_{ij} &= coth\left(\frac{Pe_{ij}}{2}\right) - \frac{2}{Pe_{ij}} \\ \beta_{ij} &= coth\left(\frac{Pe_{ij}}{2}\right) - \frac{2}{Pe_{ij}} \\ \gamma_{ij} &= coth\left(\frac{Pe_{ij}}{2}\right) - \frac{2}{Pe_{ij}} \end{aligned} \tag{17}$$

Fig. 2 shows the 3D finite element model of the fluid film in the energy equation, where the film thickness evaluated by the shaft position is a key thing when calculating the temperature distribution of the fluid film.

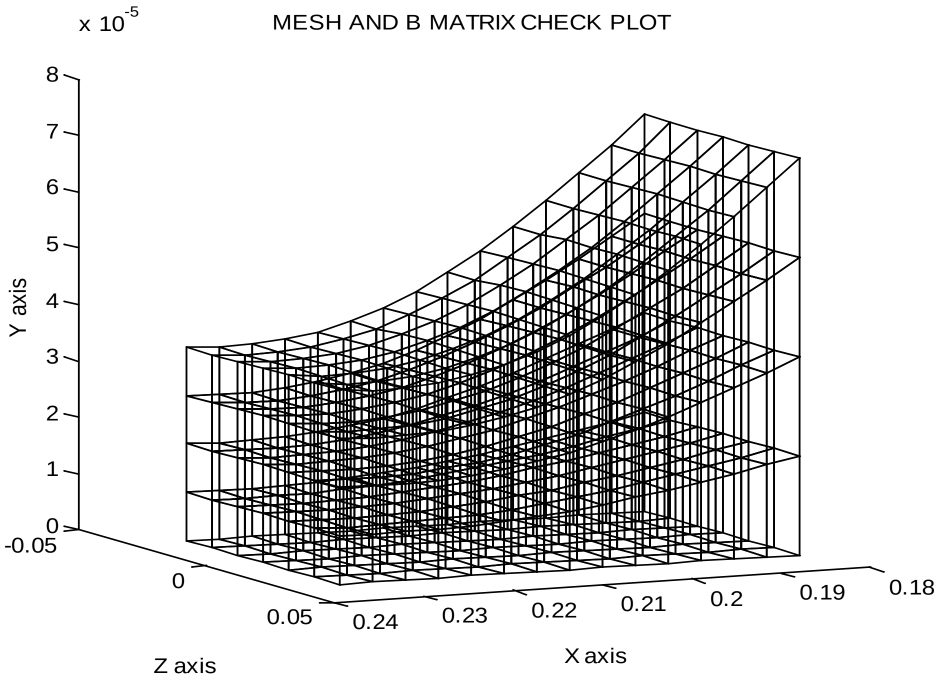

Fig. 2 Three dimensional elements for fluid film

2.4 Mixing Temperature Theory

The fluid temperature distribution flowing into the leading edge of the pad has a significant effect on the bearing dynamic behavior since the fluidic force is influenced by the viscosity, which is a function of the lubricant temperature.

The temperature and the amount of the supply flow are defined as T_{supply} and Q_{supply} respectively, and the temperature and the amount of recirculated flow are T_{out} and Q_{out}. The temperature and amount of flow entering into the leading edge are defined as T_{in} and Q_{in}. The schematic diagram for mixing theory is drawn in Fig. 3.

For the evaluation of the inlet fluid temperature (T_{in}), a modified mixing temperature theory is introduced. The amount of the flow into the pad leading edge (Q_{in}) becomes the sum of the supply (Q_{supply}) and upstream flow (Q_{out}) as seen in (18), and the temperature difference between the upstream flow and supplying flow makes the derivation of the mixing temperature theory.

Firstly, it is assumed that there is no phase change during the mixing and the lubricant specific heat (C_p) is kept constant. The colder supply lubricant (T_{supply}, Q_{supply}) will warm up which means heat energy flows into it. The warmer recirculated flow (T_{out}, Q_{out}) will cool down which means heat energy flows out of it. The whole mixture will wind up at the same temperature flowing into the leading edge (T_{in}, Q_{in}). The energy flowing out of the warmer recirculated lubricant equals the energy flowing into the colder supply flow as seen in (19) and (20), and it can be expressed by (21).

$$Q_{in} = Q_{out} + Q_{supply} \tag{18}$$

$$\Delta E_{gain} = \Delta E_{lost} \tag{19}$$

$$m_{supply} C_p \left(T_{in} - T_{supply}\right) = m_{out} C_p (T_{out} - T_{in}) \tag{20}$$

$$Q_{in} T_{in} = Q_{out} T_{out} + Q_{supply} T_{supply} \tag{21}$$

Substituting (21) into the (18), temperature boundary condition at the leading edge is evaluated by mixing temperature theory as seen by:

$$T_{in} = \frac{Q_{out}^{i-1} \cdot T_{out}^{i-1} + \left(Q_{in}^{i} - Q_{out}^{i-1}\right) \cdot T_{supply}}{Q_{in}^{i}} \tag{22}$$

where *i* denotes the pad number.

In some simulation cases, Q_{out} may exceed Q_{in}, which means $Q_{in} - Q_{out} < 0$, and the conventional mixing temperature theory (22) predicts a physically wrong inlet temperature, so there should be a compensation term to prevent this problem.

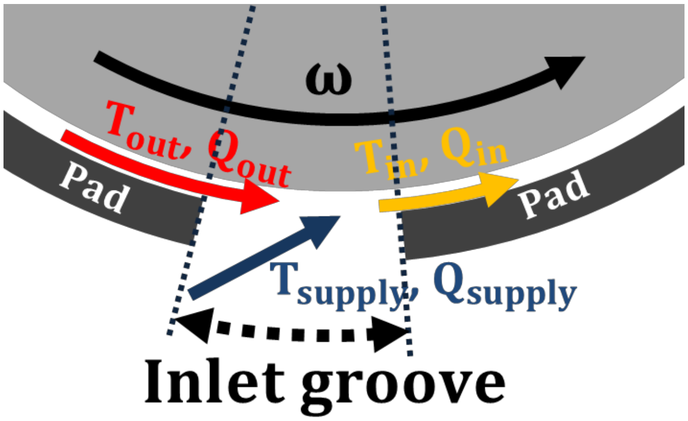

Fig. 3 Oil inlet groove

Another physically impossible case occurs when $Q_{in} - Q_{out} = 0$, which means there is no supply fluid temperature effect in the inlet temperature, which means all recirculated fluid flow into the next pad, and no supply fluid goes into the leading edge of the pad. So, a mixing coefficient(η) is introduced to prevent this problem. The modified mixing temperature theory is presented as seen in (23). If Q_{out} becomes larger than $\eta \cdot Q_{in}^{i}$, the recirculated flow is limited to $\eta \cdot Q_{in}^{i}$. And if $Q_{out}$is smaller than $\eta \cdot Q_{in}^{i}$, the conventional mixing equation(22) is used. In this study, η is fixed at 0.8.

$$T_{in}(z) = \begin{cases} \dfrac{Q_{out}^{i-1}(z) \cdot T_{out}^{i-1}(z) + \left(Q_{in}^{i}(z) - Q_{out}^{i-1}(z)\right) \cdot T_{supply}}{Q_{in}^{i}(z)} & if\ \eta \cdot Q_{in}^{i} > Q_{out}^{i-1} \\ \dfrac{\eta \cdot Q_{in}^{i}(z) \cdot T_{out}^{i-1}(z) + \left(Q_{in}^{i}(z) - \eta \cdot Q_{in}^{i}(z)\right) \cdot T_{supply}}{Q_{in}^{i}(z)} & if\ \eta \cdot Q_{in}^{i} \le Q_{out}^{i-1} \end{cases} \tag{23}$$

If the inlet groove area is assumed to be adiabatic, the energy lost to the surroundings is zero so what is lost by one stream is gathered by the other. The inlet fluid is assumed to be evenly mixed.

$$T_{in}(z) = \begin{cases} \dfrac{Q_{out}^{i-1}(z) \cdot T_{out}^{i-1}(z) + \left(Q_{in}^{i}(z) - Q_{out}^{i-1}(z)\right) \cdot T_{supply}}{Q_{in}^{i}(z)} & if\ \eta \cdot Q_{in}^{i} > Q_{out}^{i-1} \\ \dfrac{\eta \cdot Q_{in}^{i}(z) \cdot T_{out}^{i-1}(z) + \left(Q_{in}^{i}(z) - \eta \cdot Q_{in}^{i}(z)\right) \cdot T_{supply}}{Q_{in}^{i}(z)} & if\ \eta \cdot Q_{in}^{i} \le Q_{out}^{i-1} \end{cases} \tag{24}$$

2.5 Fluidic Pressure Induced Moment

There are two types of fluidic forces acting on the tilting pad, fluidic pressure induced moment and drag torque induced moment. In this section, procedure for the evaluation of fluidic force induced torque will be explained. Fig. 4 shows the schematic diagram for moment caused by fluidic pressure. The nodal fluidic force (F_{DT_n}) acting on the pad surface is divided into two linearly independent forces, $F_{DT_n}\, cos(\theta_{DT\,n})$ and $F_{DT_n} si\, n(\theta_{DT\,n})$ at right angles to each other. Two orthonormal vectors produce the moment acting on the pivot point *p* as seen in (25).

$$\boldsymbol{M_{pf}} = \sum_{n=1}^{N} F_{DT_n} \cdot cos(\theta_{DT\,n}) \cdot \boldsymbol{l_s} - \sum_{n=1}^{N} F_{DT_n} \cdot sin(\theta_{DT\,n}) \cdot \boldsymbol{l_c} \tag{25}$$

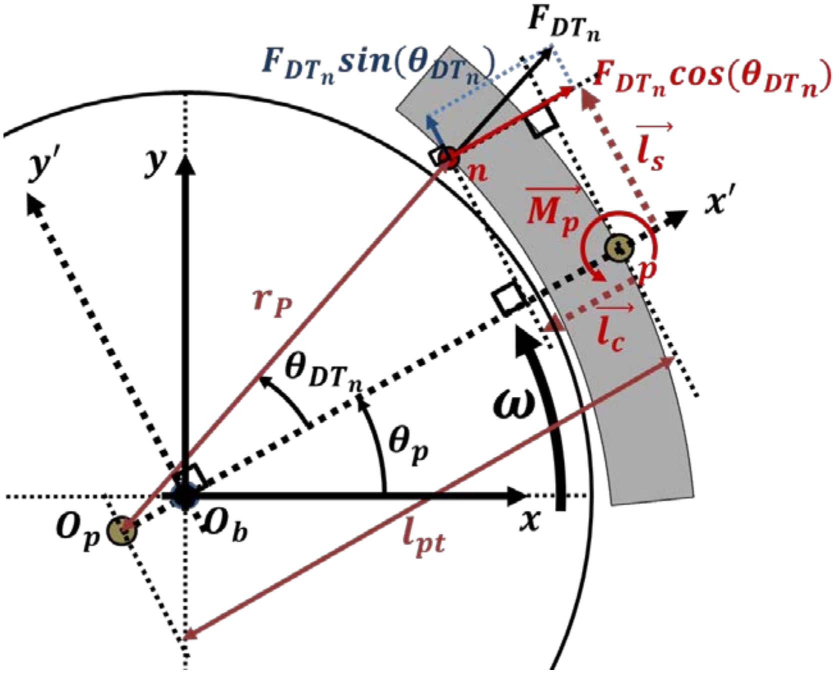

Fig. 4 Fluidic pressure induced moment acting on pivot

2.6 Drag Moment on Pivot

Drag torque effect on the bearing dynamic behavior is investigated in this section. If the journal spins counter clockwise as seen in Fig. 5, lubricant viscous shearing generates drag shear stress τ_{DT_n} acting on the pad surface in the circumferential direction as seen in (26), where u is the fluid velocity in the circumferential direction and r denotes the radial axis. The drag force F_{DT_n} has two force vectors ($F_{DT_n} \cdot sin(\theta_{DT_n})$ and $F_{DT_n} \cdot cos(\theta_{DT_n})$) which are perpendicular to each other. Two orthonormal vectors produce moment acting on the pivot point p as seen in (27).

$$\tau_{DT_n} = \mu \frac{du}{dr} \tag{26}$$

$$M_{pd} = \sum_{n=1}^{N} F_{DT_n} \cdot sin(\theta_{DT_n}) \cdot \boldsymbol{l_s} - \sum_{n=1}^{N} F_{DT_n} \cdot cos(\theta_{DT_n}) \cdot \boldsymbol{l_c} \tag{27}$$

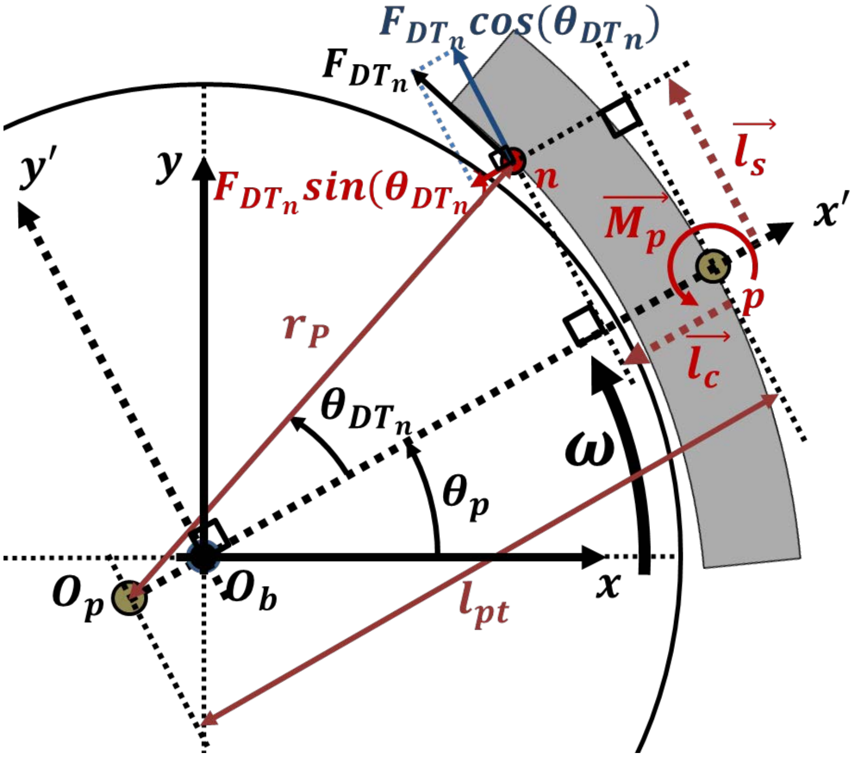

Fig. 5 Drag torque acting on the pivot

2.7 Heat Flux Boundary Condition

Heat flux and temperature boundary condition assigned to the interface between the lubricant and bearing pad can be expressed by (28) and (29). On the other hand, the heat flux boundary condition between the journal and lubricant is not simple due to the moving frame of the spinning shaft and the fixed frame of lubricant. From the shaft's frame spinning counter-clockwise (CCW), the lubricant's fixed frame is moving in a clockwise (CW) direction as seen in Fig. 6. So the flux boundary condition can be expressed by (30) and (31). If the journal is moved into $\theta = \omega t$ in the CCW direction, the lubricant's angular position that meets the shaft's position of $\theta = 0$ is $\theta = \omega t$. At each time step, the heat flux boundary condition between lubricant and spinning shaft is saved in the computer memory. After a single orbiting, the orbit time averaged boundary condition is used for the thermal boundary condition of the spinning shaft. For the heat flux boundary condition of the lubricant in a fixed frame, a modified boundary condition is adopted as seen in (32) and (33).

$$k_L \left.\frac{\partial T_L}{\partial r}\right|_{(r=R+H)} = k_B \left.\frac{\partial T_B}{\partial r}\right|_{(r=R+H)} \tag{28}$$

$$T_L|_{(r=R+H)} = T_B|_{(r=R+H)} \tag{29}$$

$$k_J \left.\frac{\partial T_J}{\partial r}\right|_{(\theta=0,r=R)} = k_L \left.\frac{\partial T_L}{\partial r}\right|_{(\theta=\omega t,r=R)} \tag{30}$$

$$T_J\big|_{(\theta=0,r=R)} = T_L|_{(\theta=\omega t,r=R)} \tag{31}$$

$$k_L \left.\frac{\partial T_L}{\partial r}\right|_{(\theta=0,r=R)} = k_J \left.\frac{\partial T_J}{\partial r}\right|_{(\theta=-\omega t,r=R)} \tag{32}$$

$$T_L|_{(\theta=0,r=R)} = T_J|_{(\theta=-\omega t,r=R)} \tag{33}$$

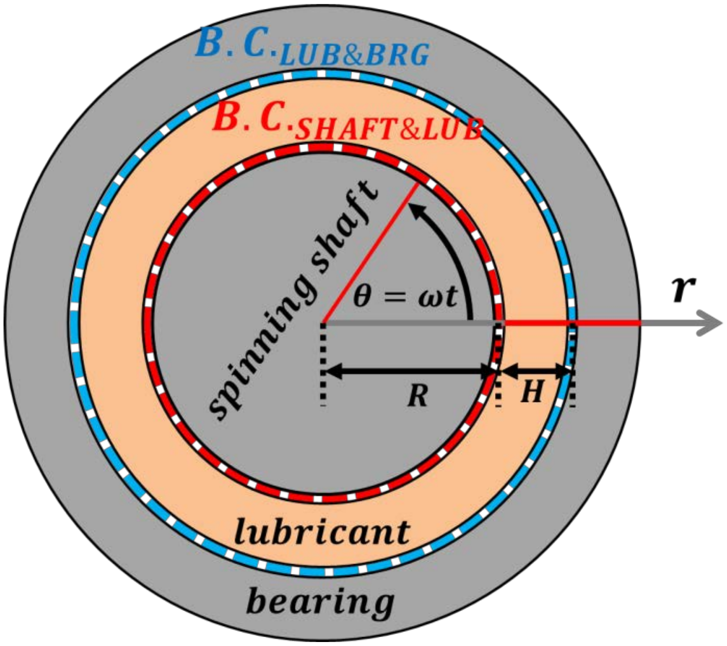

Fig. 6 Temperature and heat flux boundary condition

3 NUMERICAL MODEL OF BEARING-ROTOR SYSTEM*

Some of the bearing-rotor systems modeling methods discussed in this section came from published journals by Suh and Palazzolo [27, 28].

3.1 Rigid Pad Dynamic Model

The pad dynamic model in this research is capable of the pad tilting and pitch motions, and the pivot translation motion. The pitch motion is considered only in the spherical pivot model. The pivot flexibility is known to lower the rotor critical speeds, and increase the vibration amplitude due to the decreased damping coefficients. The equation of pad motion is derived from the Lagrange equation [33], and it is described in (34) and (35), where the pad pitch motion is not explained. In the case of the spherical pivot, one more degree of freedom is considered, and the pad tilting and pitch motions are assumed to be independent of each other. Fig. 7 shows the two degree of freedom pad dynamic model, where both pad tilting and translation motions are considered. The fluidic force ($F_o(t)$) acting on the pad, and the fluidic moment ($M_O(t)$) acting on the pivot are evaluated by the generalized Reynolds equation at each time step. Pad translational motion in the circumferential direction (x) is ignored. The derived pad nonlinear dynamic equation is used for the time transient analysis of the THD rotor-bearing system.

---

* Reprinted with permission from "Three-Dimensional THD Morton Effect Simulation Part I: Theoretical Model" by Suh, J., and Palazzolo, A, 2014. Journal of Tribology, 136(3), 031707, Copyright 2014 by ASME.

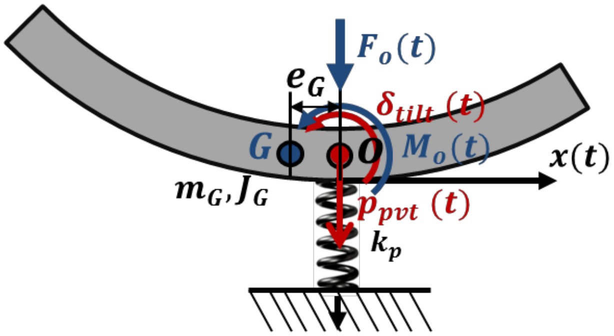

Fig. 7 Pad dynamic model with flexible pivot

$$m_G \ddot{p}_{pvt} - e_G m_G \ddot{\delta}_{tilt} \cos(\delta_{tilt}) + e_G m_G \dot{\delta}_{tilt}^{2} \sin(\delta_{tilt}) + K_p p_{pvt} = F_o(t) \tag{34}$$

$$J_G \ddot{\delta}_{tilt} + e_G m_G cos\delta_{tilt} \ddot{p}_{pvt} + e_G{}^2 m_G cos\delta_{tilt}{}^2 \ddot{\delta}_{tilt} - e_G{}^2 m_G \dot{\delta}_{tilt}{}^2 sin\delta_{tilt} cos\delta_{tilt} = M_O(t) \tag{35}$$

3.2 Flexible Pad Dynamic Model

3.2.1 Pivot constraints

For the pad dynamic analysis, three types of pivot nodal constraint will be discussed: (1) rigid pivot, (2) linear pivot and (3) nonlinear pivot. Fig. 8 shows the flexible pad FE model with two different pivot node groups (A and B). Black-colored node A is located in the axial and circumferential center of the bearing pad outer radial surface. Node groups A and B are located in the same position on the *x*-*y* plane and gray-colored group B is lined up in the z direction as seen in Fig. 8 (c). Firstly, in the rigid pivot model, the center node A is fully clamped. Under this condition, pad can rotate freely in *x, y* and *z* directions. In addition, node group B is constrained in *x* and *y* directions. It is not constrained in *z* direction for the pad elastic deformation in *z* direction under the fluidic force. Secondly, in the linear pivot model, the pivot nodal constraints are identical to the rigid pivot model except for the constraint in *y* direction. All node groups (A and B) are free to move in *y* direction but connected with ground spring in *y* direction with a prescribed pivot stiffness. Lastly, in the nonlinear pivot stiffness model, all node groups (A and B) have the same constraints as the linear pivot model except for ground spring. All nodes are free to move in *y* direction without any constraints. External nonlinear pivot forces act on the pivot nodes in the *y* direction producing pivot translational motion. Table 1 shows the constraints for the three different types of pivot model. At each pivot model and node group, freedom in each direction is described. The nonlinear pivot forces are calculated each time step of nonlinear transient dynamic solver based on Hertzian contact theory [34]. The nonlinear pivot stiffness will be discussed more in detail in next section 3.3.

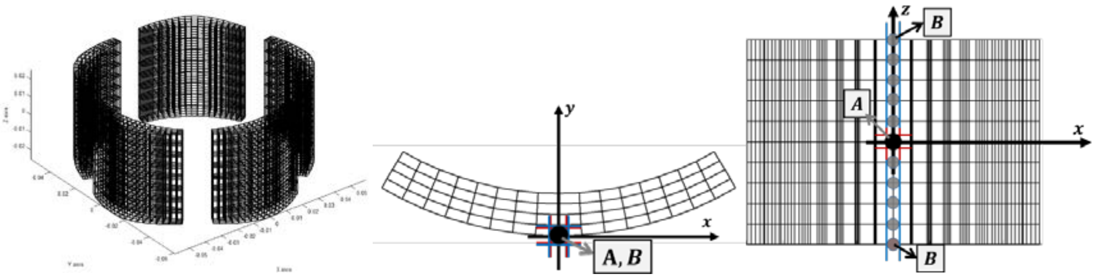

(a) F.E. pad model (b) x-y plane (c) x-z plane

Fig. 8 Nodal constraints of cylindrical pivot tilting-pad dynamic model

Table 1 Nodal constraints for three different pivot models

	Node group A			Node group B		
Direction	x	y	z	x	y	z
Rigid pivot	Fixed	Fixed	Fixed	Fixed	Fixed	Free
Linear pivot	Fixed	Ground spring	Fixed	Fixed	Ground spring	Free
Nonlinear pivot	Fixed	Nonlinear pivot force	Fixed	Fixed	Nonlinear pivot force	Free

3.2.2 Transient pad dynamic analysis

Transient dynamic analysis of flexible pad is one of the unique contributions of this research. Fig. 8 (a) shows the 3D pad FE model. 3D eight-nodes iso-parametric element is adopted to discretize the model domain. The equation of pad dynamic motion is shown in (36), where the pad nodal mass and inertia are taken into account. Internal structural damping is ignored and $\boldsymbol{X}_{\boldsymbol{E.P}}$ represents the pad nodal deformation vector. Each node has three degrees of freedom in *x*, *y* and *z* directions. Three different types of external forces are acting on the pad. $\boldsymbol{F}_{\boldsymbol{E.P.FL}}$ is a fluidic force acting on the pad surface calculated by generalized Reynolds equation. In linear pivot stiffness model, the pivot stiffness is included in pad structural stiffness matrix ($\boldsymbol{K}_{\boldsymbol{E.P}}$), whereas $\boldsymbol{F}_{\boldsymbol{E.P.PVT}}$ is the nonlinear pivot force acting on the pivot nodes in the radial direction in the case of the nonlinear pivot stiffness model.

At given constraints given in Fig. 8 (b and c) and static fluidic load($\boldsymbol{F}_{\boldsymbol{E.P.FL}} + \boldsymbol{F}_{\boldsymbol{E.P.DRG}}$), the steady solution $\mathbf{X}_{\boldsymbol{E.P}} = \boldsymbol{K}_{\boldsymbol{E.P}}^{-1}(\boldsymbol{F}_{\boldsymbol{E.P.FL}} + \boldsymbol{F}_{\boldsymbol{E.P.DRG}})$ will produce a singular matrix problem due to the pad tilting motion, which means there is no specific solution. Earlier studies [22, 23, 25] have applied more constraints except for node groups A and B to avoid this numerical problem without consideration of pad inertia $\boldsymbol{M}_{\boldsymbol{E.P}}$ and time dependent term $\ddot{\boldsymbol{X}}_{\boldsymbol{E.P}}$. The added constraints will produce unrealistic pad deformation under the static fluid force. Desbordes et al. [25] constrained additional line of nodes to control the pad tilting motion to avoid the singular matrix issue in 3D FE pad model.

Kim et al. [23] also controlled the tilting motion by adding more nodal constraints in 2D FE pad model.

In this research, to produce an accurate pad elastic deformation, nonlinear time transient journal-pad dynamic analysis is performed, where the dynamic equation of motion of journal and elastic pads are solved simultaneously in the same time domain. The nonlinear dynamic equation is solved by adaptive time step Runge-Kutta method using MATLAB ode45 numerical integration scheme. In reality, the pad is free to move around the pivot line (cylindrical pivot) or point (spherical pivot), and the transient dynamic analysis of the pad motion will produce the most realistic pad deformation shape. For the TPJB model to reach the static equilibrium states in the transient dynamic analysis, spinning journal is put inside the TPJB. The spinning journal and pads will reach the steady state with time, where the journal and pad do not move anymore after some time with zero velocities. Detailed algorithm for the static equilibrium analysis will be presented in Part II of this research.

$$\boldsymbol{M}_{\boldsymbol{E.P}}\ddot{\boldsymbol{X}}_{\boldsymbol{E.P}} + \boldsymbol{K}_{\boldsymbol{E.P}}\boldsymbol{X}_{\boldsymbol{E.P}} = \boldsymbol{F}_{\boldsymbol{E.P.FL}} + \boldsymbol{F}_{\boldsymbol{E.P.DRG}} + \boldsymbol{F}_{\boldsymbol{E.P.PVT}} \tag{36}$$

3.2.3 Modal coordinate transformation

Modal coordinate transformation is adopted for the computation time reduction, where the dynamic equation of each mode can be decoupled leading to fast computing. Combination of rigid body mode (pad tilting and pivot translational motions) and other elastic modes can express the flexible pad dynamic behavior. Palazzolo and Kim [23] adopted modal coordinate transformation to reduce the computation time in 2D FE elastic pad model, where low frequency based modes selection was performed to avoid the heavy computation. The FE pad model shown in Fig. 9 (a) has 2805 degrees of freedom. If it is a 5 pads TPJB, the whole degrees of freedom becomes 11220. When the transient pad dynamic equation with the pads full degrees of freedom was tried in this research, solving the equation was impossible due to the heavy computing issue. Selecting number of modes based on low frequency will be discussed in part II of this research. The pad deformation vector $\boldsymbol{X_{E.P}}$ can be expressed in terms of modal displacements $\boldsymbol{Z_{E.P}}$ and mode vectors $\boldsymbol{\Phi_{E.P}}$ as seen in (37). By the relationship between general coordinate and physical coordinate, the equation of motion seen in (36) can be decoupled as depicted in (38) and (39).

$$\boldsymbol{X_{E.P}} = \boldsymbol{\Phi_{E.P} Z_{E.P}} \tag{37}$$

$$\begin{aligned}\boldsymbol{\Phi^T_{E.P} M_P \Phi_{E.P} \ddot{Z}_P} + \boldsymbol{\Phi^T_{E.P} K_P \Phi_{E.P} Z_P} \\ = \boldsymbol{\Phi^T_{E.P} F_{E.P.FLP}} + \boldsymbol{\Phi^T_{E.P} F_{E.P.DRG}} + \boldsymbol{\Phi^T_{E.P} F_{E.P.PVT}}\end{aligned} \tag{38}$$

$$\boldsymbol{m_{E.P} \ddot{Z}_{E.P}} + \boldsymbol{k_{E.P} Z_{E.P}} = \boldsymbol{f_{E.P.FLP}} + \boldsymbol{f_{E.P.DRG}} + \boldsymbol{f_{E.P.PVT}} \tag{39}$$

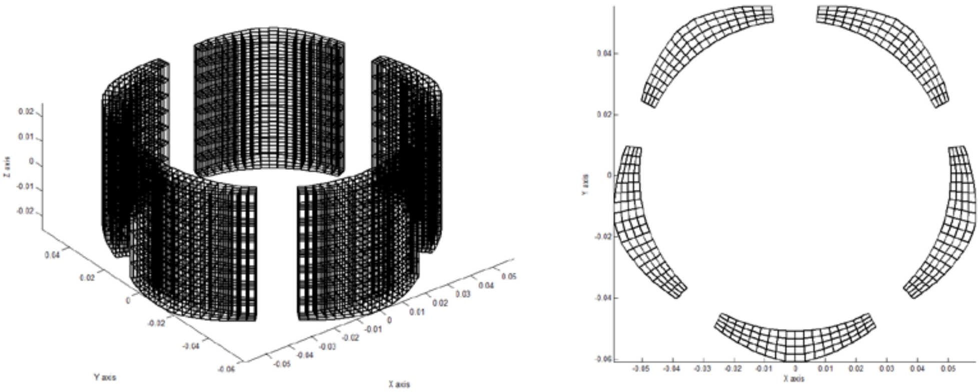

Fig. 9 F.E. model of cylindrical pivot tilting pad

3.3 Nonlinear Pivot Stiffness

Pivot flexibility is known to decrease the rotor critical speeds, and increase the vibration amplitude. Thus it should be taken into account for an accurate prediction of bearing dynamic behavior. The elastic FE pad model discussed in section 3.3 cannot predict the exact local deformation of the pivot area because the real contact length (see $b\ and\ b'$ in Fig. 10) calculated by Hertzian contact theory cannot be considered in the FE pad model. So the analytical method for the pivot stiffness is required for the accurate prediction of pivot stiffness. Kirk [20] and Nicholas [35] developed an analytical pivot stiffness equation of point and line contacts. Hertzian contact theory [34] is adopted for the evaluation of pivot contact area and the resultant stiffness. In this research, the contact area of cylindrical pivot is assumed be an oval shape where both circumferential and transverse radii are taken into account as depicted in Fig. 10. The transverse radii of a bearing housing and pad are big enough for the pad pitch motion to be ignored.

Fig. 10 shows the tilting and pitch motions of bearing pad. On $\eta - \xi$ plane, the bearing pad has a tilting motion around z axis due to the pivot radius R_P as shown in Fig. 10 (a). On $z - \xi$ plane, the bearing pad has a pitch motion around η axis due to the pivot radius R_P' as shown in Fig. 10 (a). In a typical cylindrical pivot, the transverse housing radius R_H' is infinite, and the R_P' is too high to produce a pitch motion. So the pitch motion is ignored, and the R_P' and R_H' are taken into account only for the evaluation of the pivot stiffness.

Fig. 11 shows the schematic diagram for the evaluation of stiffness at the contact of two different radii. The pivot stiffness is calculated by Hertzian contact theory [34] as shown in (40)~(44). C_E is a material property, and K_D, D_C and λ are geometrical parameters. The relationship between D_C and λ is depicted in Table 2. In (43) and (44), the only time varying variable defining pivot stiffness is load on pad F. The load on each pad would be different, and it will be simulated by use of nonlinear time transient analysis in Part II of this research.

This research assumes an oval contact at the cylindrical pivot, negligible resistance to tilting motion, and no pad translation motion in the circumferential direction arising from the rolling on pivot contact. Two types of pivot stiffness can be defined, secant $(k_P)_S$ and tangent $(k_P)_T$ pivot stiffness. The pivot can be assumed to be a typical nonlinear hardening spring as seen in Fig. 12, where pivot displacement (δ) has a fixed value under a given force on the pivot. When it comes to static analysis, pivot displacement is constant under the static load on pad. In this case secant pivot stiffness $(k_P)_S$ should be used since the pivot displacement is a time independent steady value. On the other hand, in time transient analysis, pivot displacement is not a time constant value but varies with time under the time varying fluidic and pivot loads. With the nonlinear time varying pivot deformation, tangent spring rate given by $(k_P)_T$ should be considered based on the relationship between the force and displacement.

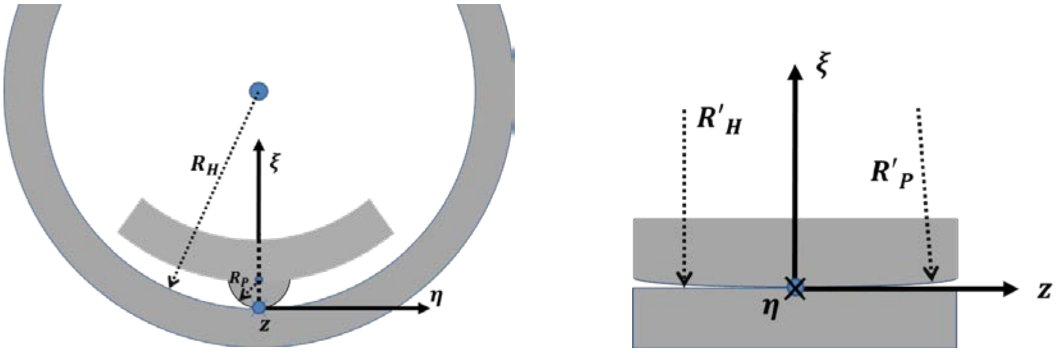

(a) Tilting motion (b) Pitch motion

Fig. 10 Cylindrical pivot

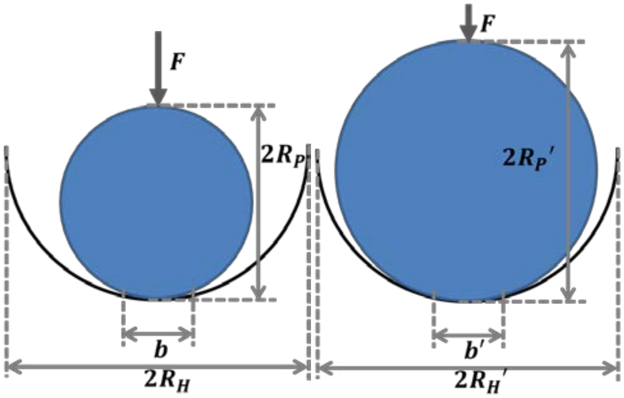

(a) Tilting motion (b) Pitch motion

Fig. 11 Cylindrical pivot model with oval contact

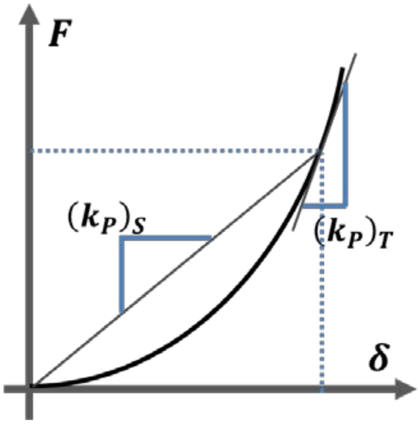

Fig. 12 Secant $(k_P)_S$ and tangent $(k_P)_T$ pivot stiffness

$$C_E = \left(\frac{1-{v_H}^2}{E_H}\right) + \left(\frac{1-{v_P}^2}{E_P}\right) \tag{40}$$

$$K_D = \frac{1.5}{\frac{1}{R_H} + \frac{1}{R_P} + \frac{1}{R_H{}'} + \frac{1}{R_P{}'}} \tag{41}$$

$$D_C = \frac{K_D}{1.5}\sqrt{\left(\frac{1}{R_H} - \frac{1}{R_H{}'}\right)^2 + \left(\frac{1}{R_P} - \frac{1}{R_P{}'}\right)^2 - 2\left(\frac{1}{R_H} - \frac{1}{R_H{}'}\right)\left(\frac{1}{R_P} - \frac{1}{R_P{}'}\right)} \tag{42}$$

$$\delta = \lambda \sqrt[3]{\frac{F^2 C_E^2}{K_D}} \tag{43}$$

$$k_P = \left.\frac{dF}{d\delta}\right|_{F'} \tag{44}$$

Table 2 Relationship between D_C and λ (Roark's formula [34])

D_C	0.00	0.10	0.20	0.30	0.40	0.50	0.60	0.70	0.80	0.90	0.99
λ	0.750	0.748	0.743	0.734	0.721	0.703	0.678	0.644	0.594	0.510	0.288

3.4 Heat Conduction Model

Thermal expansion of shaft and pad affect the film thickness leading to fluidic force change. The thermal expansion is evaluated by use of the thermal gradient evaluated by heat conduction equation .Shaft and pad thermal conductivity is assumed to be constant, and the governing equation of 3D heat flow in the pad and shaft are shown in (45). Temporal derivative of temperature ($\partial T/\partial t$) becomes zero in a steady thermal analysis, and non-zero in a transient analysis. Prescribed temperature of T^* is applied on boundary S_T. On boundary S_h, prescribed convective boundary condition is applied with convection coefficient $\bar{h}$ and ambient temperature T^∞. On boundary S_q, heat flux is prescribed at q^* as seen in (46). If there is not a prescribed thermal boundary condition, the boundary is thermally insulated in that boundary, which means zero heat flux. 3D FE method is adopted to solve the heat conduction equation (45) utilizing eight-nodes iso-parametric elements. 3D FE shaft and pad model is shown in Fig. 14, where axial thermal gradient is taken into account. Fig. 13 shows a schematic diagram for thermal shaft and bearing pad model. Seven times of the entire bearing length is considered as a whole thermal shaft length in the model [28].

Temperature distribution can be solved by (47), where $[\boldsymbol{C_T}][\dot{\boldsymbol{T}}]$ is taken into account in thermal transient analysis. $[\boldsymbol{C_T}]$ and $[\boldsymbol{K_T}]$ are assumed to be time independent, whereas thermal load $[\boldsymbol{F}]$ is time dependent thermal load vector updated each time step depending on the heat flux boundary condition between solid structure and lubricant. When it comes to the spinning shaft, orbit averaged heat flux boundary condition is adopted [6], which was explained in section 2.7.

$$\frac{\partial^2 T}{\partial x^2} + \frac{\partial^2 T}{\partial y^2} + \frac{\partial^2 T}{\partial z^2} = \frac{\rho c}{k}\frac{\partial T}{\partial t} \tag{45}$$

$$\begin{aligned} T &= T^* && on \quad S_T \\ q &= q^* && on \quad S_q \\ q &= \bar{h}(T - T^{\infty}) && on \quad S_h \end{aligned} \tag{46}$$

$$[\boldsymbol{C_T}][\dot{\boldsymbol{T}}] + [\boldsymbol{K_T}][\boldsymbol{T}] = [\boldsymbol{F_T}] \tag{47}$$

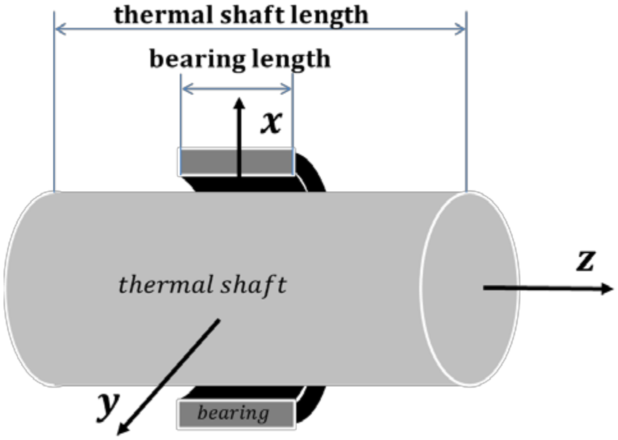

Fig. 13 Heat conduction model of bearing and shaft

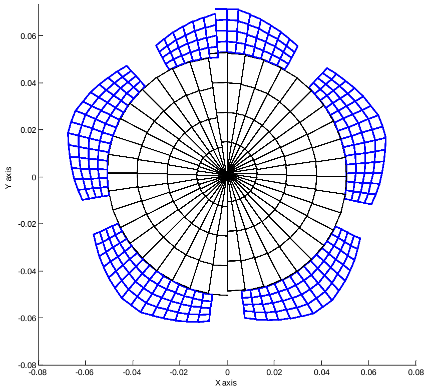

(a) Journal and pads FE model on *x*-*y* plane

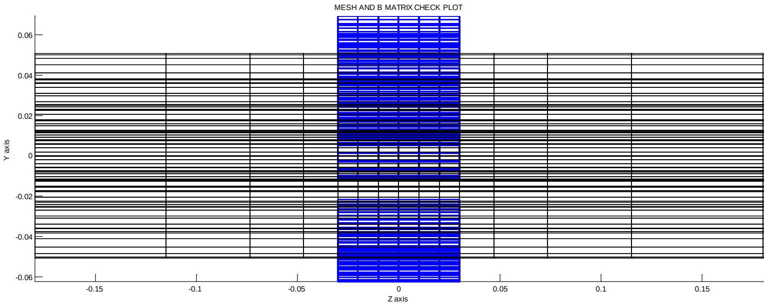

(b) Journal and pads FE model on *x*-*z* plane

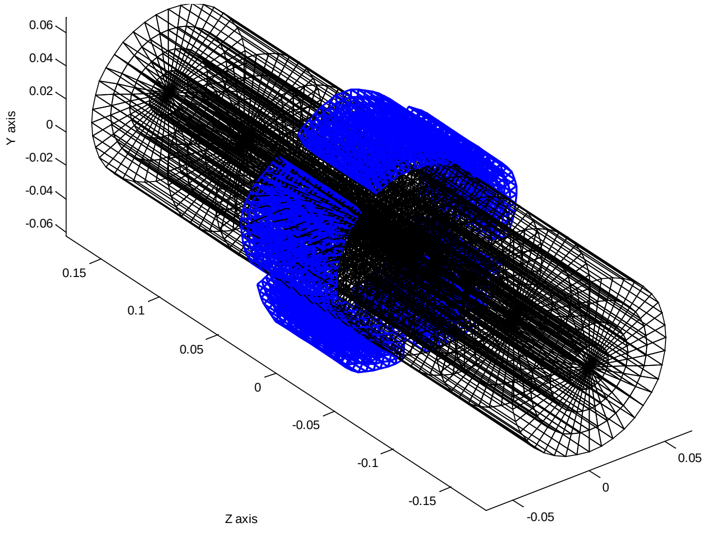

(c) 3D shaft and pads FE model

Fig. 14 3D TPJB system FE model

3.5 Thermal Distortion Model

$$\boldsymbol{K_E X_E} = \boldsymbol{F_{E.T}} \tag{48}$$

The main goal of this section is to analyze the thermal load induced distortion of bearing pad and shaft. In this research, pad dynamic behavior is taken into account in a transient dynamic analysis leading to time varying film thickness change. On the other hand, the thermal deformation of the journal and pad is assumed to be quasi-static during the transient dynamic analysis. So the amount of the thermal deformation is calculated by static equation as seen in (48). It is a good assumption because the pad elastic deformation is fluctuating within a short space of time due to the fast journal orbiting, whereas the thermal deformation is caused by the thermal gradient which varies very slowly relative to the journal orbiting.

3D elastic FE model is adopted to solve the thermal deformation problems leading to the change of film thickness and the resultant fluidic force. The temperature distribution ($\boldsymbol{T}$) calculated in the heat conduction equation shown in section 3.4 is applied to the current elastic pad and shaft FE model so that the associated thermal load ($\boldsymbol{F_{E.T}}$) can be determined yielding a nodal thermal expansion ($\boldsymbol{X_E}$). The heat conduction and the thermal expansion model share the same FE problem domain. The constitutive relation and the equilibrium equation are coupled to describe the thermal distortion, which is composed of mechanical deformation and thermal distortion. Both of them are assumed to be very small compare to the element mesh size so the superposition principle is used. [36]

3.5.1 Pad thermal distortion

For the calculation of the pad thermal deformation, additional constraints should be considered because the pad pivot constraint causes a singular matrix problem in static analysis under a steady thermal expansion force. Wrong constraints may cause a physically wrong thermally deformed pad shape. If the pad outer radial surface nodes are fully clamped, pad thermal bending can be ignored, which means accurate pad thermal distortion shape cannot be predicted producing an unrealistic film thickness change.

Fig. 15 shows three different groups of nodal constraint for the pad thermal deformation analysis. Constraints of group A and B are identical to the flexible pad dynamic F.E. model with rigid pivot as discussed in section 3.2. Gray outlined node C is additionally constrained in x and z direction and free to move in y direction to consider the thermal expansion in the radial direction. The resultant thermal deformation of the pad surface is transformed into the film thickness change ($h_{T.E.P.}$) yielding the changed fluidic force and dynamic behavior of the bearing dynamic system. The film thickness change ($h_{T.E.P.}$) due to the pad thermal distortion is measured in the radial direction. The fluid film thickness evaluation method will be discussed in section 0 more in depth.

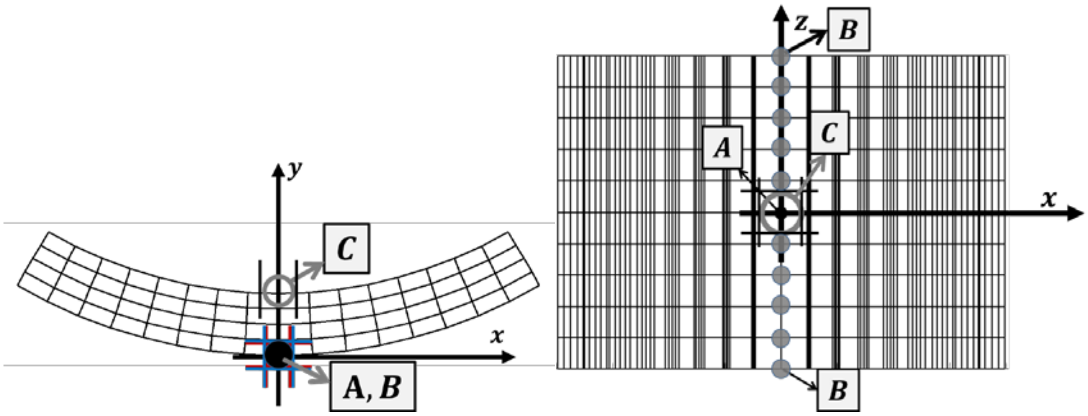

(a) *x*-*y* plane

(b) *x*-*z* plane

Fig. 15 Nodal constraints of pad thermal deformation model

3.5.2 Shaft thermal expansion

The thermal expansion shaft FE model shares the same problem nodal domain with the shaft heat conduction model discussed in section3.4. Fig. 16 shows schematic diagram for shaft thermal expansion model on the *x*-*z* plane, where the *x* is in the radial direction and *z* is in the axial direction. Left end side of the shaft is fully clamped, whereas the right end side is constrained in the *x* and *y* direction. This means that the shaft right end can move in the axial direction freely to avoid the shaft thermal compression in the axial direction leading to the over predicted thermal expansion in the radial direction and reduced film thickness leading to wrong prediction of fluidic force. The amount of the shaft thermal expansion ($h_{T.E.J.}$) is measured from the shaft radial center to the thermally expanded shaft outer radial surface. This 2D profile of journal surface thermal expansion will be added into the film thickness formula, which will be discussed in next section 0.

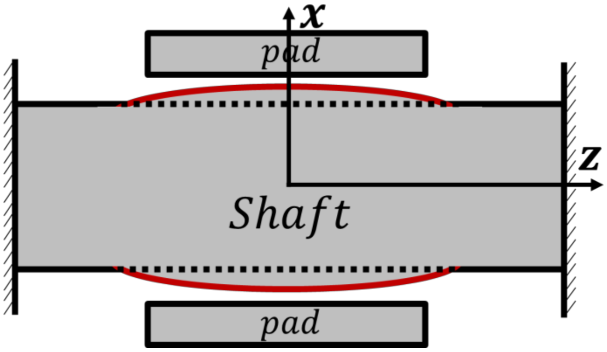

Fig. 16 Constraints for 3D shaft thermal expansion model

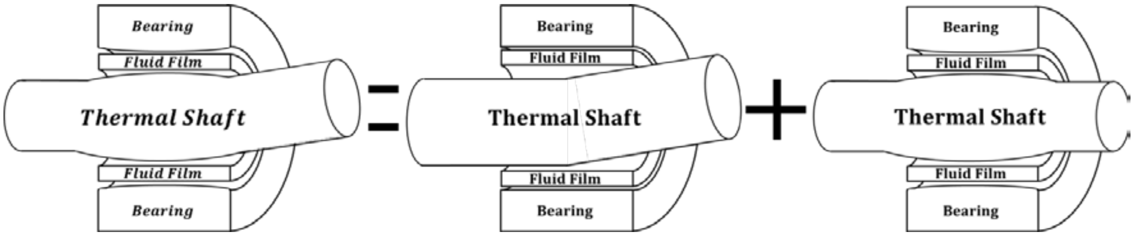

(a) Thermal deformation (b) Thermal bow (c) Thermal expansion

Fig. 17 Thermal deformation of shaft

3.6 Shaft Thermal Bending Induced Imbalance Force

The thermal bending eccentricity and phase caused by the asymmetric journal heating is known to cause a significant change to the rotordynamic behavior. In earlier studies [9, 10, 37, 38], thermal bow angle and phase were evaluated by an analytical method utilizing a journal diametral temperature differential and a hot spot phase, where the phase differential between the hot spot and the thermal bow is assumed to stay constant at 180°, and the thermal gradient between the hot spot and the cold spot is linear. Fig. 18 (c) shows the phase relationship between the hot spot, cold spot, high spot, heavy spot and thermal bow. If the journal surface temperature shows a sinusoidal variation in the circumferential direction, and the phase differential between the hot spot and cold spot stays constant at 180°, then the thermal bow phase will coincide with cold spot phase. This phase relationship has been assumed in earlier studies. This study does not use the assumed phase relationship but use a 3D energy equation and 3D thermal gradient inside the 3D thermo-elastic F.E. shaft model to calculate the thermal induced bending phase ($\emptyset_{T.BOW}$) and the eccentricity (e) which are shown in Fig. 18.

In earlier studies, a simply assumed thermal induced imbalance force acting on a lumped overhung mass has been taken into account. In reality, the thermal induced imbalance force does not act on a single lumped mass but is distributed in the rotor length since the thermal bow effect is continuous in the axial direction. This research presents a new method for the evaluation of the thermal bending eccentricity, phase and the resultant thermal induced imbalance forces distributed on the nodes (n) of F.E. rotordynamic model as shown in (51) and (52).

First, the thermal bow induced eccentricity and the phase should be calculated to produce the thermal induced imbalance force seen in (51) and (52). Shaft thermal distortion is evaluated by use of the 3D elastic F.E. model, and the shaft thermal gradient is calculated by the heat conduction F.E. model. Fig. 18 (a) and (b) show the schematic diagram for the evaluation of the thermal bending induced eccentricity distribution. The symbol ξ denotes the thermal bow axis lying on the *x*-*y* plane. In this study, the simulation model has a single overhung mass located on the right side of the rotor system as seen in Fig. 54. So the thermal induced eccentricity distribution is considered on the right hand side of the NDE bearing location (z_{NDE}), which means that the thermal imbalance force on the left side of the NDE bearing is assumed to be zero. (see the first case of equation (49)) If the axial position of the dynamic rotor node is located inside the thermal shaft ($z_{NDE} < z \leq l_{te}$ in Fig. 18(a)), the nodal eccentricity value (e_n) is evaluated by the eccentricity ($e_{F.E}$) calculated by the thermal deformation of the shaft F.E. model. Since the dynamic rotor node and the thermal shaft nodal position in the axial direction do not coincide, interpolation method is used. (see the second case of equation (49)) If the axial position of the dynamic rotor node is outside the thermal shaft ($z > l_{te}$ in Fig. 18(a)), then the thermal bending angle (β_ξ), the eccentricity (e_e) at the end of the thermal shaft, and the distance (d_n) between the right end of the thermal shaft and the current node's axial position are used for the evaluation of the thermal bow induced eccentricity (e_n). (see the third case of equation (49)) The nodal thermal bow phase distribution at *n*th node ($\emptyset_{T.BOW_n}$) is evaluated by the same method as in the calculation of the thermal eccentricity. (see the equation(50)) The thermal bow induced imbalance force ($F_{x_{T.B}}, F_{y_{T.B}}$) can be expressed by means of nodal values acting on the F.E. rotordynamic model as seen in (51) and (52), where M_n denotes a point mass of *n*th node of the F.E. rotor dynamic model, and NO_{ROTOR} indicates number of nodes of the rotordynamic F.E. model.

$$e_n = \begin{cases} 0, & 0 \leq z < z_{NDE} \\ e_{F.E}, & z_{NDE} \leq z < l_{te} \\ e_e + d_n \cdot \sin(\beta_\xi), & l_{te} \leq z \end{cases} \tag{49}$$

$$\emptyset_{T.BOW_n} = \begin{cases} 0, & 0 \leq z < z_{NDE} \\ \emptyset_{T.BOW_{F.E}}(z), & z_{NDE} \leq z < l_{te} \\ \emptyset_{T.BOW_e} & l_{te} \leq z \end{cases} \tag{50}$$

$$F_{x_{T.B}}(n) = \sum_{n=1}^{NO_{ROTOR}} M_n \cdot e_n \cdot \omega^2 \cdot cos(\omega t + \emptyset_{T.BOW_n}) \tag{51}$$

$$F_{y_{T.B}}(n) = \sum_{n=1}^{NO_{ROTOR}} M_n \cdot e_n \cdot \omega^2 \cdot sin(\omega t + \emptyset_{T.BOW_n}) \tag{52}$$

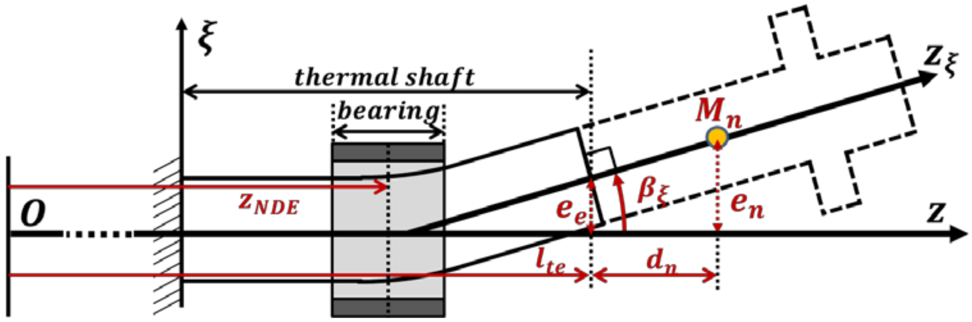

(a) Thermal bending angle

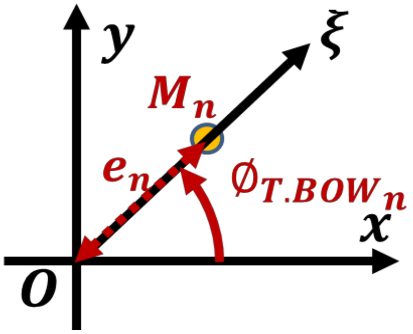

(b) Thermal bow phase

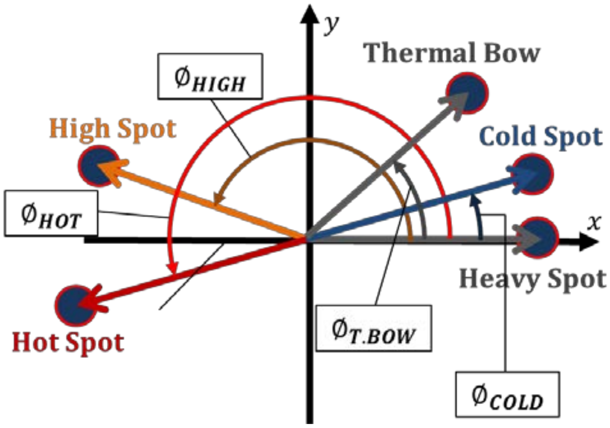

(c) Phase relationship

Fig. 18 Evaluation of thermal bow vector

3.7 Asymmetric Thermal Expansion of Spinning Shaft

Prior studies ignored the effect of asymmetric thermal expansion of the shaft surface caused by the journal surface, diametral temperature differential. Earlier studies had considered uniform thermal expansion of the shaft surface both in the axial and circumferential directions, where the volume averaged temperature and other simplified assumptions were used. In this section, a new shaft thermal expansion model is presented, where the 3D thermal gradient inside the 3D thermo-elastic shaft is considered.

If the journal diametral temperature differential exists, the asymmetric thermal expansion will also exist as well. Fig. 19 (a) shows the spinning ($\omega\ rad/sec$) shaft with the non-uniform thermal expansion in the circumferential direction(θ). Note that $h_{T.E.J}(t,\theta,z)$ is defined as the amount of the thermal expansion of the journal surface in the radial direction(r) due to the asymmetric journal heating, and observed at the fixed frame. So, this is a function of the time(t), circumferential (θ) and axial (z) positions as seen in Fig. 19 (a) and (b).

The amount of the film thickness reduction due to the thermal expansion of the spinning journal is $h_{T.E.J}(t,\theta,z)$ as seen in (53). The shift of the center of mass due to the thermal expansion is assumed to be zero, which means that the shaft spins on the original *z* axis. This asymmetric thermal deformation of the spinning journal makes a change to the temporal derivative of the film thickness reduction ($dh_{T.E.J}/dt$) as well as the film thickness reduction ($h_{T.E.J}$). Fig. 19 (b) shows the schematic diagram for the evaluation of $dh_{T.E.J}/dt$. Point A indicates a specific nodal position on the journal surface before the thermal expansion. The thermal expansion of the journal in the radial direction(r) shifted point A to B. Note that the slope (d_B) at point B is defined as the rate at which the amount of the thermal expansion $(h_{T.E.J})$ changes in the circumferential direction(θ), and measured at a fixed frame as seen in (54).

The slope (d_B) will be zero at the hot spot and the cold spot, and have the maximum value between the two spots if the journal surface temperature changes sinusoidally in the circumferential direction. The linear velocity at point B (v_B) can be defined by (55).

The decreasing rate of the film thickness at point B due to the asymmetric shaft thermal expansion $(dh_{T.E.J}/dt)$ can be evaluated by multiplying the slope (d_B) by the linear velocity (v_B) as seen in (56). And the time derivative of the film thickness (dh/dt) can be evaluated by subtracting the decreasing rate from the original temporal derivative of the film thickness as seen in (57). The slope in the axial direction does not affect the time derivative of the film thickness (dh/dt) because the shaft surface is assumed to move only in the circumferential direction (θ).

Note that the film thickness (h) and the temporal derivative of the film thickness (dh/dt) are evaluated at a fixed frame, and they are updated each time step of the time transient THD analysis for the evaluation of the fluidic force acting on the pad and rotor, and the moment acting on the pivot.

Decrease of the film thickness due to the thermal expansion of the pad $(h_{T.E.P})$ is also taken into account. Both the lubricant and pad are on fixed frame, which means both the two elements are assumed to be fixed in the circumferential direction (θ).

The thermal gradient in the pad and shaft is assumed to quasi-static during the dynamic transient analysis. So the temporal derivative of the film thickness due to the pad thermal distortion ($dh_{T.E.P}/dt$) is assumed to be zero. In reality, it would be negligible.

$$h_{T.E.}(t,\theta,z) = h_{T.E.J}(t,\theta,z) + h_{T.E.P}(\theta,z) \tag{53}$$

$$d_B(t,\theta,z) = \frac{dh_{T.E.J}}{(R + h_{T.E.J}) \cdot d\theta} \tag{54}$$

$$v_B(t,\theta,z) = (R + h_{T.E.J}) \cdot \omega \tag{55}$$

$$\frac{dh_{T.E.}}{dt} = d_B \cdot v_B \tag{56}$$

$$\frac{dh(\theta,\mathrm{z})}{dt} = \frac{dh_o(\theta,\mathrm{z})}{dt} - \frac{dh_{T.E.}(\theta,\mathrm{z})}{dt} \tag{57}$$

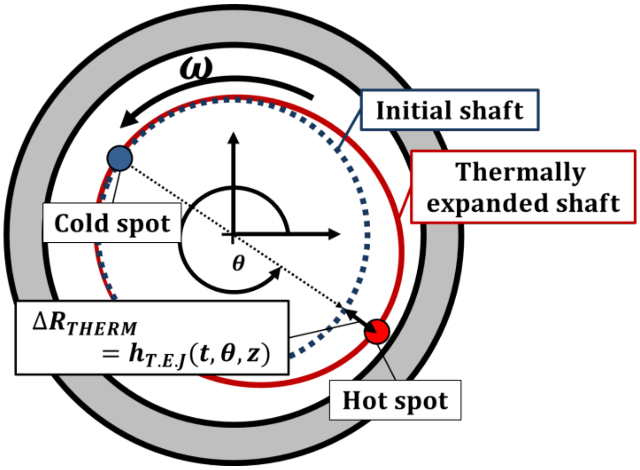

(a) Spinning shaft with asymmetric thermal expansion

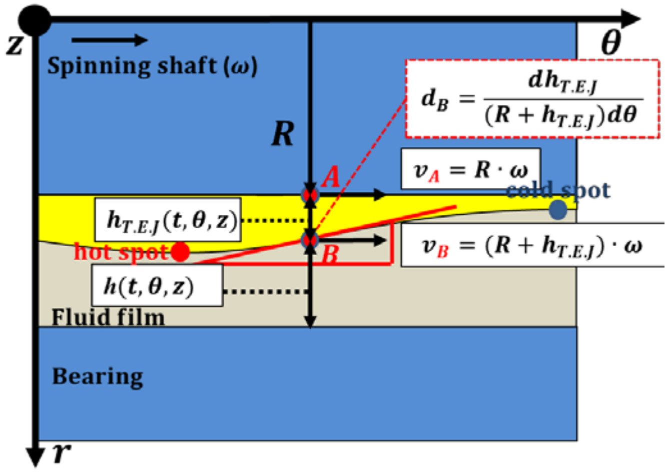

(b) Film thickness with thermal expansion of spinning shaft

Fig. 19 Asymmetric thermal expansion of shaft

3.8 Rotor- Dynamic Model

Lateral vibration is considered for the dynamic analysis of rotor system, and modal coordinate transformation is used for the computation time reduction. Modal analysis is a useful tool for the rotor-bearing system analysis for the reduction of degrees of freedom without a loss of accuracy. The system response can be assumed to be a linear combination of the eigenvectors which are orthogonal. The equation of motion for the rotor-bearing system in physical coordinate can be expressed by

$$\boldsymbol{M_R}\boldsymbol{\ddot{X}_R} + (\boldsymbol{C_{GYRO}} + \boldsymbol{C_{BRG}})\boldsymbol{\dot{X}_R} + (\boldsymbol{K_{STRUC}} + \boldsymbol{K_{BRG}})\boldsymbol{X_R} = \boldsymbol{F_R} \tag{58}$$

The state vector $\boldsymbol{\dot{z}_R} = \left[\boldsymbol{\dot{X}_R}^{\boldsymbol{T}} \quad \boldsymbol{X_R}^{\boldsymbol{T}}\right]^{\boldsymbol{T}}$ allows the second order matrix-vector differential equations to become

$$\begin{bmatrix} \boldsymbol{\ddot{X}_R} \\ \boldsymbol{\dot{X}_R} \end{bmatrix} = \begin{bmatrix} -\boldsymbol{M_R}^{-\boldsymbol{1}}\boldsymbol{C_R} & -\boldsymbol{M_R}^{-\boldsymbol{1}}\boldsymbol{K_R} \\ \boldsymbol{I} & \boldsymbol{0} \end{bmatrix} \begin{bmatrix} \boldsymbol{\dot{X}_R} \\ \boldsymbol{X_R} \end{bmatrix} + \begin{bmatrix} \boldsymbol{M_R}^{-\boldsymbol{1}}\boldsymbol{F_R} \\ \boldsymbol{0} \end{bmatrix} \tag{59}$$

where $\boldsymbol{K_R} = \boldsymbol{K_{STRUC}} + \boldsymbol{K_{BRG}}$ and $\boldsymbol{C_R} = \boldsymbol{C_{GYRO}} + \boldsymbol{C_{BRG}}$. This equation can be shortened as

$$\boldsymbol{\dot{z}_R} = \boldsymbol{D_R}\boldsymbol{z_R} + \boldsymbol{\widetilde{F}_R} \tag{60}$$

If the free vibration problem is considered by setting $\boldsymbol{\widetilde{F}_R} = \boldsymbol{0}$, and $\mathbf{z_R} = \boldsymbol{\psi_{R_i}} e^{\lambda_i t}$ which yields

$$\boldsymbol{\lambda_i}\boldsymbol{\psi_{R_i}} = \boldsymbol{D_R}\boldsymbol{\psi_{R_i}} \tag{61}$$

The eigenvalues of $\boldsymbol{D_R}^{\boldsymbol{T}}$ are the same as the eigenvalues of $\boldsymbol{D_R}$; however, the eigenvectors of $\boldsymbol{D_R}^{\boldsymbol{T}}$ are not identical to the ones of $\boldsymbol{D_R}$. The eigenvectors of $\boldsymbol{D_R}^{\boldsymbol{T}}$ satisfy

$$\boldsymbol{\lambda_i}\boldsymbol{\phi_{R_i}} = \boldsymbol{D_R}^{\boldsymbol{T}}\boldsymbol{\phi_{R_i}} \tag{62}$$

Typically, $\boldsymbol{\psi_R}$ is called a right eigenvector, and $\boldsymbol{\phi_R}$ is referred to as a left eigenvector of $\boldsymbol{D_R}$. If $\boldsymbol{\psi_R}$ is normalized so that $\boldsymbol{\phi_R}^{\boldsymbol{T}}\boldsymbol{\psi_R} = \boldsymbol{I}$, $\boldsymbol{\phi_R}$ and $\boldsymbol{\psi_R}$ satisfy the following conditions [39].

$$\boldsymbol{\phi_R}^{\boldsymbol{T}}{}_{\boldsymbol{m}}\boldsymbol{\psi_{R_n}} = \begin{cases} 0, if\ m \neq n \\ 1, if\ m = n \end{cases} \tag{63}$$

$$\boldsymbol{\phi_R}^{\boldsymbol{T}}{}_{\boldsymbol{m}}\boldsymbol{D_R}\boldsymbol{\psi_{R_n}} = \begin{cases} 0, if\ m \neq n \\ \lambda_n, if\ m = n \end{cases} \tag{64}$$

Hence, the utilization of left and right eigenvectors diagonalizes the first order matrix-vector differential equation. Since only a small number ($\boldsymbol{L}$) of the entire eigenmodes (***N***) are used to evaluate the linear combination of eigenvectors, the approximate expression for $\boldsymbol{z_R}$ can be expressed by:

$$\boldsymbol{z_R}(\boldsymbol{t}) = \sum_{\boldsymbol{l=1}}^{\boldsymbol{2L}} \boldsymbol{\xi_l}\,(\boldsymbol{t}) \cdot \boldsymbol{\psi_{R_l}} \qquad (\boldsymbol{L} \ll \boldsymbol{N}) \tag{65}$$

In this research, the rotor dynamic behavior is assumed to be dominated by lower eigenmodes, and the highest eigenmode is chosen at the five times as high as the rotor spin frequency.

3.9 Rigid Pad Film Thickness Model

3.9.1 Bearing clearance

Fig. 20 shows a schematic diagram of journal and nonzero preload pad. The local coordinate system $\eta - \xi$ is fixed at the geometric center of the bearing O_b. This center coincides with journal center. The bearing radius R_b is distance between A and O_b. The pad radius R_p indicates the distance between B and O_p, where O_p is fixed at the geometric center of the pad. The bearing clearance, C_b, and pad clearance, C_p, are defined by:

$$\begin{gathered} C_p = R_p - R \\ C_b = R_b - R \end{gathered} \tag{66}$$

The preload, m_b, is defined in terms of bearing clearance, C_b, and pad clearance, C_p, as follows:

$$m_b = 1 - \frac{C_b}{C_p} \tag{67}$$

The offset is the ratio of the length between the pad leading edge and pivot to the pad entire arc length. The pad offset seen in Fig. 20 is 0.5 since the pivot is located in the middle of the pad in circumferential direction.

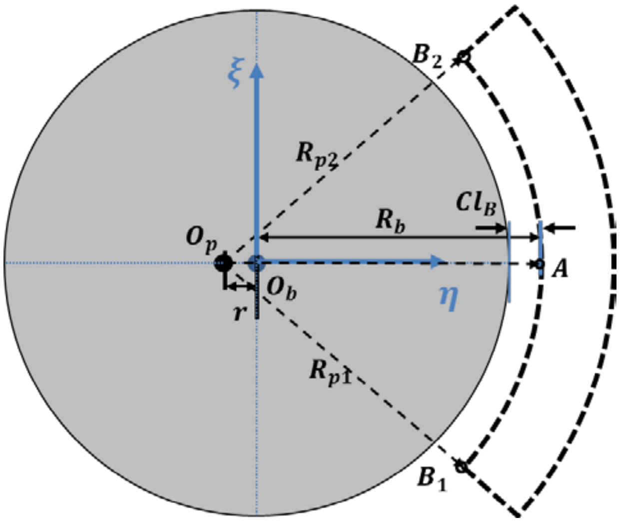

Fig. 20 Schematic diagram of nonzero preload pad

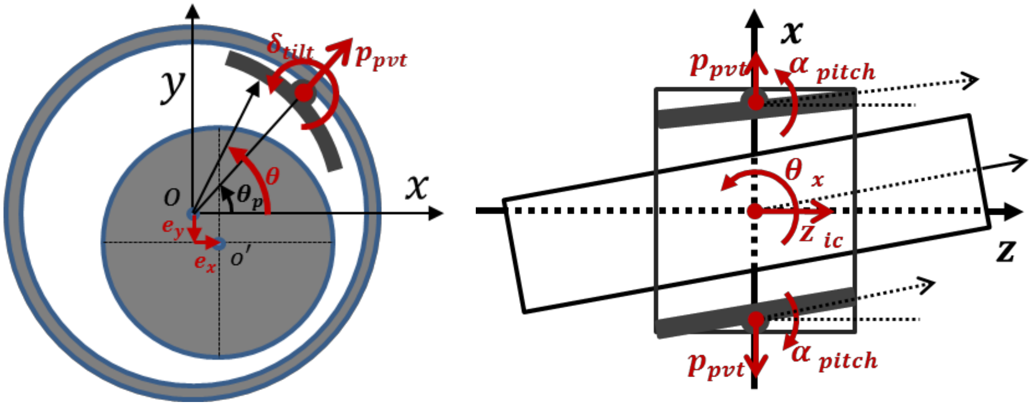

(a) *x*-*y* plane

(b) *x*-*z* plane

Fig. 21 Schematic diagram of shaft and pad 3D motions

3.9.2 Film thickness

In the case of the rigid pad model, many earlier researchers have used similar formula; however, for the newly developed flexible pad model, different approach is required due to the arbitrary elastic deformation of pad. In this section, two different approaches for the evaluation of the film thickness will be discussed.

In this study, pad tilting and pitch, and journal translation, pitch and yaw motions are taken into account to simulate the rotor-bearing 3D motion. Most former researches have considered only journal and pad 2D motion in the *x*-*y* plane as seen in Fig. 21 (a), which means shaft's translation motion and pad tilting and translation motions in the *x*-*y* plane are simulated. 2D motion film thickness formula is modified to consider the shaft pitch (θ_y) and yaw (θ_x) motions, and pad pitch motion (α_{pitch}) as seen in (68). The pad pitch motion is taken into account only in the case of the spherical pivot model as seen in Fig. 21 (b). The temporal derivative of the film thickness formula is given by (69). Thermal expansion of the spinning journal ($h_{T.E.J}(t,\theta,z)$) and pad ($h_{T.E.P}(\theta,z)$) are also taken into account in the film thickness formula, and temporal derivative of the spinning journal thermal expansion observed in the fixed frame ($dh_{T.E.J}(t,\theta,z)/dt$) is taken into account. This effect will be discussed in depth in next section.

$$h(\theta,z) = CL_P - \left(e_x + z\theta_x - p_{pvt}\cos(\theta_p) - z\alpha_{pitch}\cos(\theta_p)\right)\cos(\theta) - \left(e_y + z\theta_y - p_{pvt}\sin(\theta_p) - z\alpha_{pitch}\sin(\theta_p)\right)\sin(\theta) - (CL_P - CL_B)\cos(\theta-\theta_p) - \delta_{tilt}R\sin(\theta-\theta_p) - h_{T.E.J}(t,\theta,z) - h_{T.E.P}(\theta,z) \tag{68}$$

$$\begin{aligned}\frac{dh(\theta,z_{ic})}{dt} = &-\left(\frac{de_x}{dt}+\ z\frac{d\theta_x}{dt}-\frac{dp_{pvt}}{dt}cos(\theta_p)-z\frac{d\alpha_{pitch}}{dt}cos(\theta_p)\right)cos(\theta)\\ &-\Bigg(\frac{de_y}{dt}+\ z\frac{d\theta_y}{dt}-\frac{dp_{pvt}}{dt}sin(\theta_p)\\ &-z\frac{d\alpha_{pitch}}{dt}sin(\theta_p)\Bigg)sin(\theta)-\frac{d\delta_{tilt}}{dt}R\,sin(\theta-\theta_p)\\ &-\frac{dh_{T.E.J}(t,\theta,z)}{dt}\end{aligned} \tag{69}$$

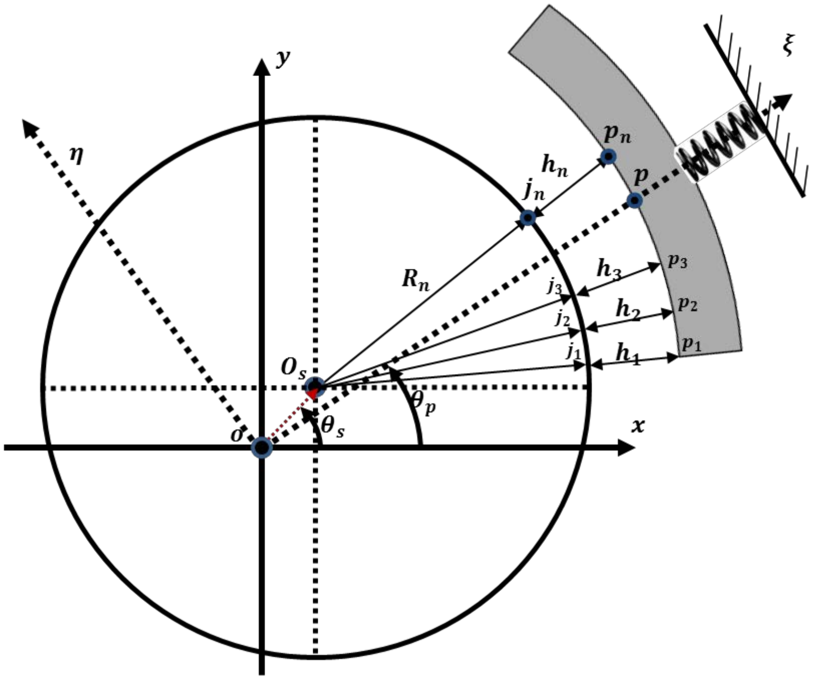

Fig. 22 Nodal film thickness with flexible pad

3.10 Flexible Pad Film Thickness Model

Earlier studies [23, 25] have assumed a quasi-static pad elastic deformation during the transient dynamic analysis. In this research, arbitrary pad deformation under the fluidic pressure and pivot force is considered each time step in the transient dynamic analysis. A schematic diagram for the evaluation of the nodal film thickness and temporal derivative of that is portrayed schematically in Fig. 22. The film thickness (h_n) is calculated at each nodal point of FE pad surface denoted by p_n. Corresponding nodes on the spinning journal are j_n as seen in Fig. 22. Elastic pad nodal position on nth node is defined by (x_n, y_n, z_n), and the nodal position of shaft center is defined by (x_s, y_s, z_s). Since the pad dynamic behavior is determined purely by modal coordinates, pad nodal position (x_n, y_n, z_n) includes tilting, yaw and pitch motions depending on the pivot type.

The nodal film thickness value can be expressed by (70) and the temporal derivative is (71). R_s is the initial journal radius without thermal expansion and $h_{T.E.J}(\theta, z)$ is the thermal expansion of shaft in the radial direction. If the shaft thermal expansion is taken into account, the radius of shaft R_n can be expressed in terms of R_s and $h_{T.E.J}(\theta, z)$. If the thermal expansion of the shaft surface is not constant in the circumferential direction, the time derivative of the thermally expanded journal radius $dh_{T.E.J}(\theta, z)/dt$ [27, 28] should be taken into account in dh_n/dt.

$$h_n = \sqrt{(x_n - x_s - z\theta_x)^2 + \left(y_n - y_s - z\theta_y\right)^2} - R_s - h_{T.E.J}(\theta, z) - h_{T.E.P}(\theta, z) \tag{70}$$

$$\frac{dh_n}{dt} = \frac{1}{\sqrt{(x_n - x_s - z\theta_x)^2 + \left(y_n - y_s - z\theta_y\right)^2}} \cdot \left\{ \begin{array}{c} (x_n - x_s - z\theta_x) \cdot \left(\frac{dx_n}{dt} - \frac{dx_s}{dt} - z\frac{d\theta_x}{dt}\right) \\ + \left(y_n - y_s - z\theta_y\right) \cdot \left(\frac{dy_n}{dt} - \frac{dy_s}{dt} - z\frac{d\theta_y}{dt}\right) \end{array} \right\} \tag{71}$$

4 DYNAMIC COEFFICIENT OF TPJB

4.1 Rigid Pad

Earlier studies have adopted iteration schemes such as Newton-Raphson method for the evaluation of TPJB static equilibrium condition, where every variable reaches steady state by use of separate iteration closed loops as many as the variables. In this research, nonlinear transient dynamic analysis method is adopted to find the static equilibrium conditions of journal, bearing pad and thermal gradient. Full dynamic coefficient matrix of rigid pad TPJB is shown in (72), where pad tilting and pivot motions are taken into account. $\Delta\boldsymbol{\delta}$ denotes a perturbed tilting angle matrix, $\Delta\boldsymbol{p}$ is a perturbed pivot displacement matrix at a static equilibrium condition. $\boldsymbol{\Delta T_{\delta}}$ is an moment acting around the pivot, and $\Delta\boldsymbol{F_p}$ denotes the load on pivot produced by perturbed tilting angle $\Delta\boldsymbol{\delta}$. The rigid pad dynamic model has advantage of fast computation compared to the flexible pad model arising from its small number of degrees of freedom. On the other hand, the modal coordinate transformation in flexible pad model requires heavy computation leading to increase of computation time.

After the static equilibrium condition of the TPJB is achieved as seen in Fig. 23, every variable related to the dynamic behavior is perturbed by Δx, Δy, $\Delta\boldsymbol{\delta}$ and $\Delta\boldsymbol{p}$ as depicted in (72). k_{xx}, k_{yx}, $\boldsymbol{K_{\delta x}}$ and $\boldsymbol{K_{px}}$ are force coefficients produced by perturbing journal position by Δx in the *x* direction. $F_x(+\Delta x)$ and $F_y(+\Delta x)$ are the forces acting on the journal in the *x* and *y* directions respectively as seen in (73) and (74). $\boldsymbol{M_{\delta}}(+\Delta x)$ is a moment vector acting around each pivot, and $\boldsymbol{F_p}(+\Delta x)$ is a load on pivot vector caused by $+\Delta x$ as depicted in (75) and (76). Perturbed tilting angle $\Delta\boldsymbol{\delta}$ around the static equilibrium condition also produces the forces on journal and pad. $F_x(+\Delta\boldsymbol{\delta})$, $M_\delta(+\Delta\boldsymbol{\delta})$ and $F_p(+\Delta\boldsymbol{\delta})$ are force acting on the journal in the *x* direction, moment around the pivot and force in the pivot radial direction caused by tilting angle respectively as shown in (77), (78) and (79). Perturbed pivot displacement also produces forces acting on journal, pivot and pad as seen in (80)~(84). In case of $\boldsymbol{K_{pp}}$, perturbed pivot displacement generates two different types of forces, $F_{p_{fluid}}(+\Delta\boldsymbol{p})$ and $F_{p_{pivot}}(+\Delta\boldsymbol{p})$. $F_{p_{fluid}}(+\Delta\boldsymbol{p})$ is a load on pivot induced by an external fluidic force, and $F_{p_{pivot}}(+\Delta\boldsymbol{p})$ is pivot spring force induced by an pivot stiffness. $\boldsymbol{K_{pp}}$ is a linear combination of $\boldsymbol{K_{p_{fluid}p}}$ and $\boldsymbol{K_{p_{pivot}p}}$ as seen in (82). In case of the damping matrix, the same procedure as in the stiffness coefficients is performed.

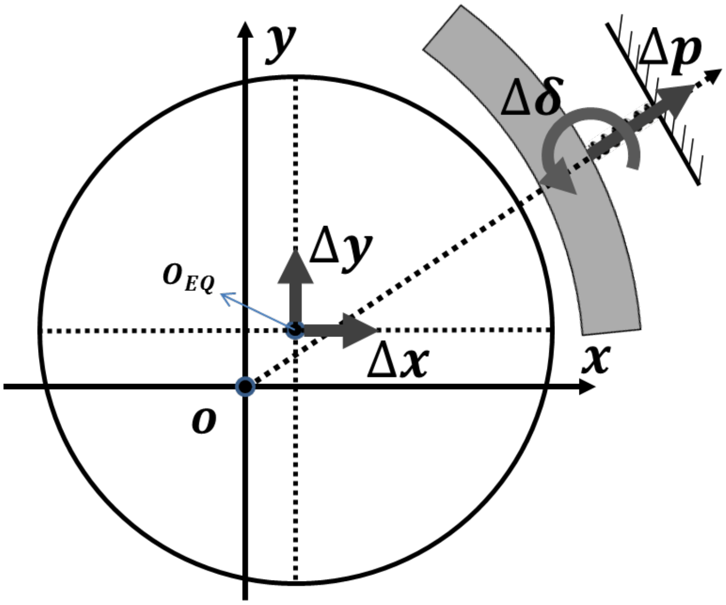

Fig. 23 Static equilibrium condition of variables

$$\begin{bmatrix}\Delta F_x \\ \Delta F_y \\ \Delta \boldsymbol{T}_\delta \\ \Delta \boldsymbol{F_p}\end{bmatrix} = \begin{bmatrix} k_{xx} & k_{xy} & \boldsymbol{K_{x\delta}}^{\boldsymbol{T}} & \boldsymbol{K_{xp}}^{\boldsymbol{T}} \\ k_{yx} & k_{yy} & \boldsymbol{K_{y\delta}}^{\boldsymbol{T}} & \boldsymbol{K_{yp}}^{\boldsymbol{T}} \\ \boldsymbol{K_{\delta x}} & \boldsymbol{K_{\delta y}} & \boldsymbol{K_{\delta\delta}} & \boldsymbol{K_{\delta p}}^{\boldsymbol{T}} \\ \boldsymbol{K_{px}} & \boldsymbol{K_{py}} & \boldsymbol{K_{p\delta}} & \boldsymbol{K_{pp}} \end{bmatrix} \begin{bmatrix}\Delta x \\ \Delta y \\ \Delta \boldsymbol{\delta} \\ \Delta \boldsymbol{p}\end{bmatrix} \tag{72}$$

$$k_{xx} = -\frac{F_x(+\Delta x) - F_x(-\Delta x)}{2\Delta x} \tag{73}$$

$$k_{yx} = -\frac{F_y(+\Delta x) - F_y(-\Delta x)}{2\Delta x} \tag{74}$$

$$\boldsymbol{K_{\delta x}} = -\frac{\boldsymbol{M_\delta}(+\Delta x) - \boldsymbol{M_\delta}(-\Delta x)}{2\Delta x} \tag{75}$$

$$\boldsymbol{K}_{\boldsymbol{px}} = -\frac{\boldsymbol{F}_{\boldsymbol{p}}(+\Delta x) - \boldsymbol{F}_{\boldsymbol{p}}(-\Delta x)}{2\Delta x} \tag{76}$$

$$\boldsymbol{K}_{x\boldsymbol{\delta}} = -\frac{F_x(+\Delta\boldsymbol{\delta}) - F_x(-\Delta\boldsymbol{\delta})}{2\Delta\boldsymbol{\delta}} \tag{77}$$

$$\boldsymbol{K}_{\boldsymbol{\delta\delta}} = -\frac{M_{\boldsymbol{\delta}}(+\Delta\boldsymbol{\delta}) - M_{\boldsymbol{\delta}}(-\Delta\boldsymbol{\delta})}{2\Delta\boldsymbol{\delta}} \tag{78}$$

$$\boldsymbol{K}_{p\boldsymbol{\delta}} = -\frac{F_p(+\Delta\boldsymbol{\delta}) - F_p(-\Delta\boldsymbol{\delta})}{2\Delta\boldsymbol{\delta}} \tag{79}$$

$$\boldsymbol{K}_{x\boldsymbol{p}} = -\frac{F_x(+\Delta\boldsymbol{p}) - F_x(-\Delta\boldsymbol{p})}{2\Delta\boldsymbol{p}} \tag{80}$$

$$\boldsymbol{K}_{\delta\boldsymbol{p}} = -\frac{F_{\boldsymbol{\delta}}(+\Delta\boldsymbol{p}) - F_{\boldsymbol{\delta}}(-\Delta\boldsymbol{p})}{2\Delta\boldsymbol{p}} \tag{81}$$

$$\boldsymbol{K}_{\boldsymbol{pp}} = \boldsymbol{K}_{\boldsymbol{p}_{\boldsymbol{fluid}}\boldsymbol{p}} + \boldsymbol{K}_{\boldsymbol{p}_{\boldsymbol{pivot}}\boldsymbol{p}} \tag{82}$$

$$\boldsymbol{K}_{\boldsymbol{p}_{\boldsymbol{fluid}}\boldsymbol{p}} = -\frac{F_{p_{fluid}}(+\Delta\boldsymbol{p}) - F_{p_{fluid}}(-\Delta\boldsymbol{p})}{2\Delta\boldsymbol{p}} \tag{83}$$

$$\boldsymbol{K}_{\boldsymbol{p}_{\boldsymbol{pivot}}\boldsymbol{p}} = -\frac{F_{p_{pivot}}(+\Delta\boldsymbol{p}) - F_{p_{pivot}}(-\Delta\boldsymbol{p})}{2\Delta\boldsymbol{p}} \tag{84}$$

4.2 Flexible Pad

Detailed algorithm for the evaluation of the static equilibrium condition of spinning journal and flexible pad will be discussed in Part II of this research. After the shaft and pad reach the static equilibrium condition, dynamic coefficient is obtained by perturbing variables related to the pad and journal positions. The exact deformation of structural component requires infinitely many degrees of freedom, and the deformation of the pad F.E. model can be expressed by means of the number of degrees of freedom. Kim [10] and Gadangi [11] used a reduced number of mode shapes to express the pad deformation and evaluate the dynamic coefficient. In the previous section 4.1, pad deformation was expressed by means of the reduced number of degrees of freedom of flexible FE pad model. As in the modal coordinate transformation, the perturbed variables consist of journal position and generalized coordinates of pad. Full dynamic coefficient matrix is depicted in (85), where the pad perturbation in generalized coordinate is expressed by $\Delta\boldsymbol{m}$. The number of degrees of freedom to express the pad dynamic motion will be discussed in Part II of this research. The calculation method of k_{xx}, k_{xy}, k_{yx} and k_{yy} are explained in the previous section 4.1. k_{xx}, k_{yx} and $\boldsymbol{K_{mx}}$ are force coefficients caused by perturbed journal position Δx. Perturbed journal position Δx produces the change of fluidic force. The fluidic force acting on the FE pad is expressed by means of nodal values $\boldsymbol{F_{E.P.Fluid}}$. For the evaluation of $\boldsymbol{K_{mx}}$, fluidic nodal force in terms of physical coordinate should be transformed into the generalized fluidic force by being multiplied by $\boldsymbol{\Phi_{E.P}^{T}}$ as seen in (86). For the evaluation of $\boldsymbol{K_{xm}}$, pad position expressed by means of generalized coordinate should be perturbed by $\Delta\boldsymbol{m}$ as shown in (87). The perturbed pad position $\Delta\boldsymbol{m}$ produces fluidic force $F_x(+\Delta\boldsymbol{m})$ in *x* direction.

$\boldsymbol{K}_{\boldsymbol{mm}}$ consists of three components, $\boldsymbol{K}_{\boldsymbol{mm}}^{\boldsymbol{fluid}}$, $\boldsymbol{K}_{\boldsymbol{mm}}^{\boldsymbol{structural}}$ and $\boldsymbol{K}_{\boldsymbol{mm}}^{\boldsymbol{N.LIN.Pivot}}$ as depicted in (88). Firstly, the perturbed modal displacement $\Delta\boldsymbol{m}$ causes pad deformation accordance with the following mode shape, and this deformed pad makes a change in lubricant clearance. The perturbed film thickness produces change in fluid film pressure leading to change of the fluid force on pad surface. This perturbed force on pad is converted into the change in a modal force, $\Delta\boldsymbol{F}_{\boldsymbol{m}}$ as seen in (89). Secondly, pad structural deformation caused by the perturbed $\Delta\boldsymbol{m}$ causes the pad deformation accordance with the modal vector and generates internal structural force. The structural coefficient coincides with the diagonal modal stiffness matrix $\boldsymbol{k}_{\boldsymbol{E.P}}$ as seen in (90), which was discussed in (39). When it comes to the nonlinear pivot stiffness pad model, modal forces acting on the pivot nodes produced by nonlinear pivot stiffness should be taken into account because the pivot stiffness is not considered in the FE pad structural stiffness matrix $\boldsymbol{K}_{\boldsymbol{E.P}}$ discussed in (35).

$$\begin{bmatrix} \Delta F_x \\ \Delta F_y \\ \Delta\boldsymbol{F}_{\boldsymbol{m}} \end{bmatrix} = \begin{bmatrix} k_{xx} & k_{xy} & \boldsymbol{K}_{\boldsymbol{xm}}{}^{\boldsymbol{T}} \\ k_{yx} & k_{yy} & \boldsymbol{K}_{\boldsymbol{ym}}{}^{\boldsymbol{T}} \\ \boldsymbol{K}_{\boldsymbol{mx}} & \boldsymbol{K}_{\boldsymbol{my}} & \boldsymbol{K}_{\boldsymbol{mm}} \end{bmatrix} \begin{bmatrix} \Delta x \\ \Delta y \\ \Delta\boldsymbol{m} \end{bmatrix} \tag{85}$$

where

$$\boldsymbol{K}_{\boldsymbol{mx}} = -\frac{F_m^{Fluid}(+\Delta x) - F_m^{Fluid}(-\Delta x)}{2\Delta x} \tag{86}$$

$$= -\frac{\boldsymbol{\Phi}_{\boldsymbol{E.P}}^{\boldsymbol{T}}\boldsymbol{F}_{\boldsymbol{E.P.Fluid}}(+\Delta x) - \boldsymbol{\Phi}_{\boldsymbol{E.P}}^{\boldsymbol{T}}\boldsymbol{F}_{\boldsymbol{E.P.Fluid}}(-\Delta x)}{2\Delta x}$$

$$\boldsymbol{K}_{\boldsymbol{xm}} = -\frac{F_x(+\Delta\boldsymbol{m}) - F_x(-\Delta\boldsymbol{m})}{2\Delta\boldsymbol{m}} \tag{87}$$

$$\boldsymbol{K}_{\boldsymbol{mm}} = \boldsymbol{K}_{\boldsymbol{mm}}^{\boldsymbol{fluid}} + \boldsymbol{K}_{\boldsymbol{mm}}^{\boldsymbol{structural}} + \boldsymbol{K}_{\boldsymbol{mm}}^{\boldsymbol{N.LIN.Pivot}} \tag{88}$$

$$\boldsymbol{K}_{\boldsymbol{mm}}^{\boldsymbol{fluid}} = -\frac{F_m(+\Delta\boldsymbol{m}) - F_m(-\Delta\boldsymbol{m})}{2\Delta\boldsymbol{m}} \tag{89}$$

$$= -\frac{\boldsymbol{\Phi}_{\boldsymbol{E.P}}^{\boldsymbol{T}}\boldsymbol{F}_{\boldsymbol{E.P.FLUID}}(+\Delta\boldsymbol{m}) - \boldsymbol{\Phi}_{\boldsymbol{E.P}}^{\boldsymbol{T}}\boldsymbol{F}_{\boldsymbol{E.P.FLUID}}(-\Delta\boldsymbol{m})}{2\Delta\boldsymbol{m}}$$

$$\boldsymbol{K}_{\boldsymbol{mm}}^{\boldsymbol{structural}} = \boldsymbol{k}_{\boldsymbol{E.P}} \tag{90}$$

$$\boldsymbol{K}_{\boldsymbol{mm}}^{\boldsymbol{N.LIN.Pivot}} = -\frac{\boldsymbol{F}_{\boldsymbol{m}}^{\boldsymbol{N.LIN.Pivot}}(+\Delta\boldsymbol{m}) - \boldsymbol{F}_{\boldsymbol{m}}^{\boldsymbol{N.LIN.Pivot}}(-\Delta\boldsymbol{m})}{2\Delta\boldsymbol{m}} \tag{91}$$

$$= -\frac{\boldsymbol{\Phi}_{\boldsymbol{E.P}}^{\boldsymbol{T}}\boldsymbol{F}_{\boldsymbol{E.P.PVT}}(+\Delta\boldsymbol{m}) - \boldsymbol{\Phi}_{\boldsymbol{E.P}}^{\boldsymbol{T}}\boldsymbol{F}_{\boldsymbol{E.P.PVT}}(-\Delta\boldsymbol{m})}{2\Delta\boldsymbol{m}}$$

4.3 Synchronously Reduced Dynamic Coefficient

After full stiffness and damping matrices are obtained, coefficient reduction is necessary in order to be used for rotor system stability analysis. Pads' degree of freedom such as pad rotation and pad modal deformation are eliminated assuming that the pads' oscillating frequencies are the same as the shaft spinning frequency. Unreduced equation of motion for bearing system is expressed by:

$$\begin{bmatrix} \boldsymbol{M_{mm}} & \boldsymbol{M_{ms}} \\ \boldsymbol{M_{sm}} & \boldsymbol{M_{ss}} \end{bmatrix} \begin{bmatrix} \ddot{\boldsymbol{X}}_{\boldsymbol{m}} \\ \ddot{\boldsymbol{X}}_{\boldsymbol{s}} \end{bmatrix} + \begin{bmatrix} \boldsymbol{C_{mm}} & \boldsymbol{C_{ms}} \\ \boldsymbol{C_{sm}} & \boldsymbol{C_{ss}} \end{bmatrix} \begin{bmatrix} \dot{\boldsymbol{X}}_{\boldsymbol{m}} \\ \dot{\boldsymbol{X}}_{\boldsymbol{s}} \end{bmatrix} + \begin{bmatrix} \boldsymbol{K_{mm}} & \boldsymbol{K_{ms}} \\ \boldsymbol{K_{sm}} & \boldsymbol{K_{ss}} \end{bmatrix} \begin{bmatrix} \boldsymbol{X_m} \\ \boldsymbol{X_s} \end{bmatrix} = \begin{bmatrix} \boldsymbol{F_m} \\ \boldsymbol{0} \end{bmatrix} \tag{92}$$

where m denotes the master and s denotes the slave degrees of freedom. Introducing the frequency ω of the pad oscillation,

$$\begin{bmatrix} \Delta x \\ \Delta y \\ \Delta \delta^i \\ \Delta {r^i}_{imode} \\ \Delta F_X \\ \Delta F_Y \end{bmatrix} = \boldsymbol{e^{i\omega t}} \begin{bmatrix} \Delta \hat{X} \\ \Delta \hat{Y} \\ \Delta \widehat{\delta^i} \\ \Delta \widehat{r^i}_{imode} \\ \Delta \widehat{F_X} \\ \Delta \widehat{F_Y} \end{bmatrix} \tag{93}$$

The first two components of this vector in the above equation (5.28) are master degrees of freedom, and the rest of them are slave degrees of freedom. Substituting Equation (5.28) into Equation (5.27)

$$-\boldsymbol{\omega}^2 \begin{bmatrix} \boldsymbol{M_{mm}} & \boldsymbol{0} \\ \boldsymbol{0} & \boldsymbol{M_{ss}} \end{bmatrix} \begin{bmatrix} \widehat{\boldsymbol{X}}_{\boldsymbol{m}} \\ \widehat{\boldsymbol{X}}_{\boldsymbol{S}} \end{bmatrix} + \boldsymbol{i\omega} \begin{bmatrix} \boldsymbol{C_{mm}} & \boldsymbol{C_{ms}} \\ \boldsymbol{C_{sm}} & \boldsymbol{C_{ss}} \end{bmatrix} \begin{bmatrix} \widehat{\boldsymbol{X}}_{\boldsymbol{m}} \\ \widehat{\boldsymbol{X}}_{\boldsymbol{S}} \end{bmatrix} + \begin{bmatrix} \boldsymbol{K_{mm}} & \boldsymbol{K_{ms}} \\ \boldsymbol{K_{sm}} & \boldsymbol{K_{ss}} \end{bmatrix} \begin{bmatrix} \widehat{\boldsymbol{X}}_{\boldsymbol{m}} \\ \widehat{\boldsymbol{X}}_{\boldsymbol{S}} \end{bmatrix} = \begin{bmatrix} \widehat{\boldsymbol{F}}_{\boldsymbol{m}} \\ \boldsymbol{0} \end{bmatrix} \tag{94}$$

Slave mass matrix, is added to stiffness matrix, which becomes the real part of the right hand side of Equation (5.29)

$$-\boldsymbol{\omega}^2 \begin{bmatrix} \boldsymbol{M}_{mm} & \mathbf{0} \\ \mathbf{0} & \mathbf{0} \end{bmatrix} \begin{bmatrix} \widehat{\boldsymbol{X}}_m \\ \widehat{\boldsymbol{X}}_S \end{bmatrix} + \boldsymbol{i\omega} \begin{bmatrix} \boldsymbol{C}_{mm} & \boldsymbol{C}_{ms} \\ \boldsymbol{C}_{sm} & \boldsymbol{C}_{ss} \end{bmatrix} \begin{bmatrix} \widehat{\boldsymbol{X}}_m \\ \widehat{\boldsymbol{X}}_S \end{bmatrix} + \begin{bmatrix} \boldsymbol{K}_{mm} & \boldsymbol{K}_{ms} \\ \boldsymbol{K}_{sm} & \boldsymbol{K}_{ss} - \boldsymbol{\omega}^2 \boldsymbol{M}_{ss} \end{bmatrix} \begin{bmatrix} \widehat{\boldsymbol{X}}_m \\ \widehat{\boldsymbol{X}}_S \end{bmatrix} = \begin{bmatrix} \widehat{\boldsymbol{F}}_m \\ \mathbf{0} \end{bmatrix} \tag{95}$$

Rearranging the Equation

$$\begin{bmatrix} \boldsymbol{Z}_{mm} & \boldsymbol{Z}_{ms} \\ \boldsymbol{Z}_{sm} & \boldsymbol{Z}_{ss} \end{bmatrix} \begin{bmatrix} \widehat{\boldsymbol{X}}_m \\ \widehat{\boldsymbol{X}}_S \end{bmatrix} = \boldsymbol{\omega}^2 \begin{bmatrix} \boldsymbol{M}_{mm} & \mathbf{0} \\ \mathbf{0} & \mathbf{0} \end{bmatrix} \begin{bmatrix} \widehat{\boldsymbol{X}}_m \\ \widehat{\boldsymbol{X}}_S \end{bmatrix} + \begin{bmatrix} \widehat{\boldsymbol{F}}_m \\ \mathbf{0} \end{bmatrix} \tag{96}$$

Guyan reduction is employed to reduce Equation, and it is given by:

$$\boldsymbol{Z'}_{mm} \widehat{\boldsymbol{X}}_m = \boldsymbol{\omega}^2 \boldsymbol{M}_{mm} + \widehat{\boldsymbol{F}}_m \tag{97}$$

$$\boldsymbol{Z'}_{mm} = \boldsymbol{Z}_{mm} - \boldsymbol{Z}_{ms} \boldsymbol{Z}_{ss}{}^{-1} \boldsymbol{Z}_{sm}$$

Reduced dynamic coefficients are calculated from complex coefficients of Equation

$$\begin{bmatrix} \boldsymbol{C}_{XX}{}^{*} & \boldsymbol{C}_{XY}{}^{*} \\ \boldsymbol{C}_{YX}{}^{*} & \boldsymbol{C}_{YY}{}^{*} \end{bmatrix} = \frac{1}{\omega} Im(\boldsymbol{Z'}_{mm}), \qquad \begin{bmatrix} \boldsymbol{K}_{XX}{}^{*} & \boldsymbol{K}_{XY}{}^{*} \\ \boldsymbol{K}_{YX}{}^{*} & \boldsymbol{K}_{YY}{}^{*} \end{bmatrix} = Re(\boldsymbol{Z'}_{mm}) \tag{98}$$

5 ALGORITHM*

The Morton simulation algorithm discussed in this section came from published journals by Suh and Palazzolo [27, 28].

There are two sub-sections explaining about the numerical algorithm for the static equilibrium analysis of flexible pad TPJB system. The first section 5.1.1 is about the global system where the dynamic and thermal systems reach the steady state simultaneously in an iteration scheme. In the next section 5.1.2, static equilibrium condition of dynamic system is achieved by use of the nonlinear transient journal bearing dynamic analysis, where the journal and bearing systems converge into a static equilibrium states with time. It is the same situation as an experimentalist puts a spinning journal inside the TPJB system, and waits for the bearing system to reach the steady state after some time. In the bearing dynamic system, thermal condition remains constant except for the lubricant temperature. After the steady state is achieved in the dynamic analysis loop, newly updated lubricant thermal gradient is used to perform the static thermal analysis of bearing pad and journal in section 5.1.1. After the global system's steady states are achieved, dynamic coefficients are evaluated.

---

* Reprinted with permission from "Three-Dimensional THD Morton Effect Simulation Part I: Theoretical Model" by Suh, J., and Palazzolo, A, 2014. Journal of Tribology, 136(3), 031707, Copyright 2014 by ASME.

5.1 Algorithm for Dynamic Coefficient of TPJB

5.1.1 Algorithm for static equilibrium analysis of shaft-bearing system

This section provides an algorithm for the static equilibrium analysis of spinning journal and flexible pads. Earlier studies [22, 23, 24, 40] have adopted iteration algorithms such as Newton-Raphson method for the static equilibrium analysis of TPJB regardless of pad flexibility. The elastic pad model has been constrained not only at the pivot nodes but also at additional nodal positions to control the tilting angle and avoid the singular matrix problem at a static elastic pad analysis under external fluidic force. This method produces unrealistic pad elastic deformation due to the additional constraints and sometimes causes divergence problem at a heavy load case. The only way to resolve the issue is to conduct a transient dynamic analysis, where the elastic pad dynamic motion converges into a steady state under a time varying fluidic pressure. In this research, the journal and pads converge into a steady state together in the same numerical integration solver. This is equivalent to where the spinning journal with zero imbalance force is put inside the TPJB, where the pads and spinning journal positions reach static equilibrium condition with zero velocity. This is the most realistic elastic pad dynamic model and requires a new novel algorithm. Fig. 24 shows the algorithm to produce the static equilibrium condition of shaft-bearing system. Shaft and pads dynamic behavior, and thermal gradient are converging in the algorithm. The following explains the algorithm.

1) Temperature distribution in the shaft ($\mathrm{Temp}_{\mathrm{Shaft}}$), pads ($\mathrm{Temp}_{\mathrm{Pads}}$) and lubricant ($\mathrm{Temp}_{\mathrm{Film}}$), fluid viscosity ($\mu_0$), and journal-bearing states ($\mathrm{Y}_{\mathrm{o}_{\mathrm{DYN}}}$) become the initial conditions.

2) Mass ($\mathrm{M}_{\mathrm{Pads}}$) and stiffness ($\mathrm{K}_{\mathrm{Pads}}$) FE matrices of elastic pad model is generated based on the bearing pad inputs. Accurate geometry should be produced where the bearing clearance and preload are taken into account together for an exact film thickness evaluation.

3) Prior to the modal coordinate transformation, eigenvector (Φ_{Pad}) of elastic FE pad is created. Diagonalized modal mass ($\mathrm{M}_{\mathrm{Pads}_{\mathrm{modal}}}$) and modal stiffness ($\mathrm{K}_{\mathrm{Pads}_{\mathrm{modal}}}$) matrices are generated by use of the eigenvector (Φ_{Pad}).

4) At given thermal and dynamic states, nonlinear transient dynamic analysis is conducted from $t_{o_{DYN}}$ to $t_{E_{DYN}}$. Typically the time span between $t_{o_{DYN}}$ and $t_{E_{DYN}}$ is five times period of journal spinning. For the static equilibrium analysis, a spinning journal with zero imbalance is simulated with pad dynamic motion. The algorithm of this procedure will be discussed in next section 5.1.2 more in detail.

5) After the zero size journal orbit is achieved, thermal analysis of pads and shaft will be performed in next step. If not, the transient dynamic analysis should be re-performed to produce the static equilibrium conditions of journal and pad at a given thermal boundary condition.

6) Given the lubricant temperature and pad temperature solved in previous step, new heat flux boundary condition ($\mathrm{Flux}_{\mathrm{Pads}}$) in the interface between lubricant and pad is produced.

7) Based on the heat flux boundary condition and user defined thermal boundary condition around the pad, static solution of thermal gradient ($\mathrm{Temp}_{\mathrm{Pads}}$) is evaluated.

8) Thermal expansion of the pad surface ($h_{T.E.P}$) is calculated by pre-calculated thermal gradient ($\mathrm{Temp}_{\mathrm{Pads}}$). This value is taken into account for the film thickness (h). The pad deformation and the resultant film thickness may vary in a short space of time due to the fluctuating load condition; however, the thermal gradient can be assumed to be a quasi-static value during the transient dynamic analysis which will be discussed in next section 5.1.2. So the change of the film thickness due to the thermal expansion of pad and shaft is also assumed to be quasi-static during the dynamic transient analysis.

9) The iteration loop between 6) and 9) is repeated until the convergence of pad temperature ($\mathrm{Temp}_{\mathrm{Pads}}$) is achieved.

10) At a given lubricant temperature ($\mathrm{Temp}_{\mathrm{Film}}$) and shaft thermal gradient ($\mathrm{Temp}_{\mathrm{Shaft}}$) produced in the previous step, new heat flux ($\mathrm{Flux}_{\mathrm{Shaft}}$) and temperature boundary condition ($\mathrm{Temp}_{\mathrm{B.C.}_{\mathrm{Shaft}}}$) at the interface between lubricant and spinning journal is calculated adopting the orbit averaging flux boundary condition [6] as discussed in Part I of this research.

11) By use of the heat flux boundary condition ($\mathrm{Flux}_{\mathrm{Shaft}}$) and user-defined thermal boundary condition around the shaft ($\mathrm{Temp}_{\mathrm{B.C.}_{\mathrm{Shaft}}}$), thermal gradient ($\mathrm{Temp}_{\mathrm{Shaft}}$) in the shaft is calculated.

12) Thermal expansion of shaft ($h_{T.E.J}$) is calculated by use of the elastic FE shaft model at a given thermal load, and this value will change the film thickness in next step of nonlinear transient dynamic solver.

13) The iteration loop from 10) to 13) is repeated until the convergence of the shaft temperature ($\mathrm{Temp}_{\mathrm{Shaft}}$) is achieved.

14) The iteration loop from 4) to 14) is repeated until the convergences of the journal position, pad position, pad temperature and shaft temperature are achieved.

15) By use of the static equilibrium condition of journal, bearing pad and lubricant temperature, frequency reduced dynamic coefficients are calculated.

5.1.2 Algorithm for nonlinear transient bearing dynamic analysis

Use of the full degrees of freedom of elastic FE pad causes heavy computing problem. In this research, low frequency based mode selection is performed, which will be discussed in section 6.3. Pads elastic deformation arising from the external fluidic load and nonlinear pivot force is analyzed in nonlinear transient dynamic solver as the fluidic pressure acting on the pad surface is fluctuating in a brief space of time. The thermal distortion caused by thermal load ($\boldsymbol{F_{E.T}}$) can be assumed to be quasi-static during the five times period of rotor spin speed. Therefore, the pad thermal expansion effect is added on the film thickness (h) as a time independent value while the pad elastic deformation due to the external fluidic load is changing.

One of the unique contributions of this research is the use of the nonlinear transient dynamic solver to find the static equilibrium condition of the flexible pad TPJB and spinning journal. This nonlinear transient dynamic method is also be applicable to the transient rotordynamic analysis where the change of the pad deformation within a very short time during a single orbiting should be taken into account. On the other hand, earlier studies have assumed that the pad deformation is constant at a single orbiting or a very long simulation time. Fig. 25 shows the algorithm for the transient bearing dynamic analysis, and the following explains it.

4) TRANSIENT.THERMO.DYNAMIC.SOLVER is an adaptive time step numerical integration solver. The dynamic equation is integrated from $t_{0_{DYN}}$ to $t_{E_{DYN}}$ with the initial conditions, $\mathrm{Y}_{0_{\mathrm{DYN}}}$ and $\mathrm{Temp}_{\mathrm{Film}}$.

4-1) Initial state $\mathrm{Y}_{0_{\mathrm{DYN}}}$ of dynamic system consists of journal states in physical coordinate and pad states in a modal coordinate. So it should be divided into each variable to be used in the following sub-functions.

4-2) Prior to the calculation of fluidic force, the pad nodal position and velocity expressed by means of modal coordinate should be transformed into the physical coordinate.

4-3) Newly developed film thickness formula explained in Part I of this research produces the film thickness (h) and time derivative of this ($\dot{h}$) by use of the journal ($\mathrm{X}_{\mathrm{shaft}}, \dot{\mathrm{X}}_{\mathrm{shaft}}$), and pad states ($\mathrm{Y}_{\mathrm{pad}}, \dot{\mathrm{Y}}_{\mathrm{pad}}$).

4-4) Fluidic pressure ($\mathrm{Pressure}_{\mathrm{Film}}$) and velocity ($\mathrm{Vel}_{\mathrm{Film}}$) are calculated by generalized Reynolds equation FE program using the pre-calculated lubricant thickness and viscosity.

4-5) Inlet temperature ($\mathrm{Temp}_{\mathrm{inlet}}$) is calculated by use of the supply lubricant temperature, fluidic velocity and film thickness,

4-6) Based on the pre-calculated values ($h, \dot{h}$: film thickness, μ: viscosity, $\mathrm{Pressure}_{\mathrm{Film}}$: fluidic pressure, $\mathrm{Vel}_{\mathrm{Film}}$: fluid velocity, $\mathrm{Temp}_{\mathrm{inlet}}$: inlet temperature), 3D energy equation is solved considering axial conduction and convection. 3D viscosity profile (μ) is updated in the energy equation as a function of lubricant temperature ($\mathrm{Temp}_{\mathrm{Film}}$).

4-7) Forces acting on the pad ($\mathrm{Pressure}_{\mathrm{Film}}$) should be transformed into modal forces ($F_{pad_{modal}}$) prior to the pad dynamic analysis in the modal coordinate.

4-8) Pad and journal dynamic analysis are performed in the same time step under a zero imbalance force. $\boldsymbol{Force_{Rotor}}$ acting on the spinning journal includes a gravity force, fluidic force acting on the journal and other user defined forces. $\boldsymbol{Force_{Pad_{modal}}}$ acting on the pad surface includes a fluidic force on the pad surface and nonlinear pivot force in terms of modal coordinate.

4-9) The whole process from 4-2) to 4-9) is conducted until $\boldsymbol{t \geq t_{E_{DYN}}}$.

4-10) Adaptive time step (Δt) numerical integration solver is adopted, and the numerical integration is performed from next time step ($t = t + \Delta t$).

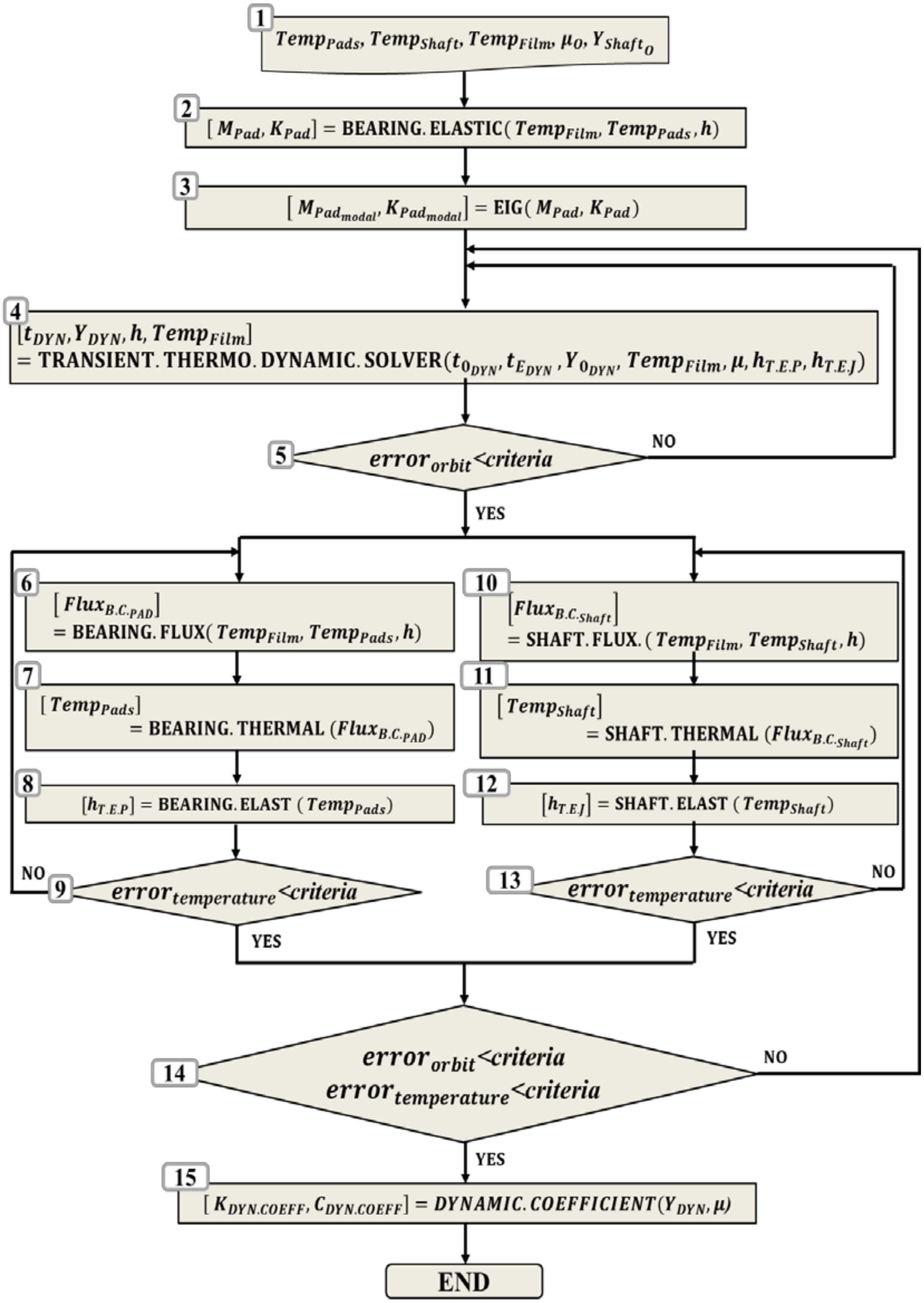

Fig. 24 Algorithm for static equilibrium analysis of shaft-bearing system

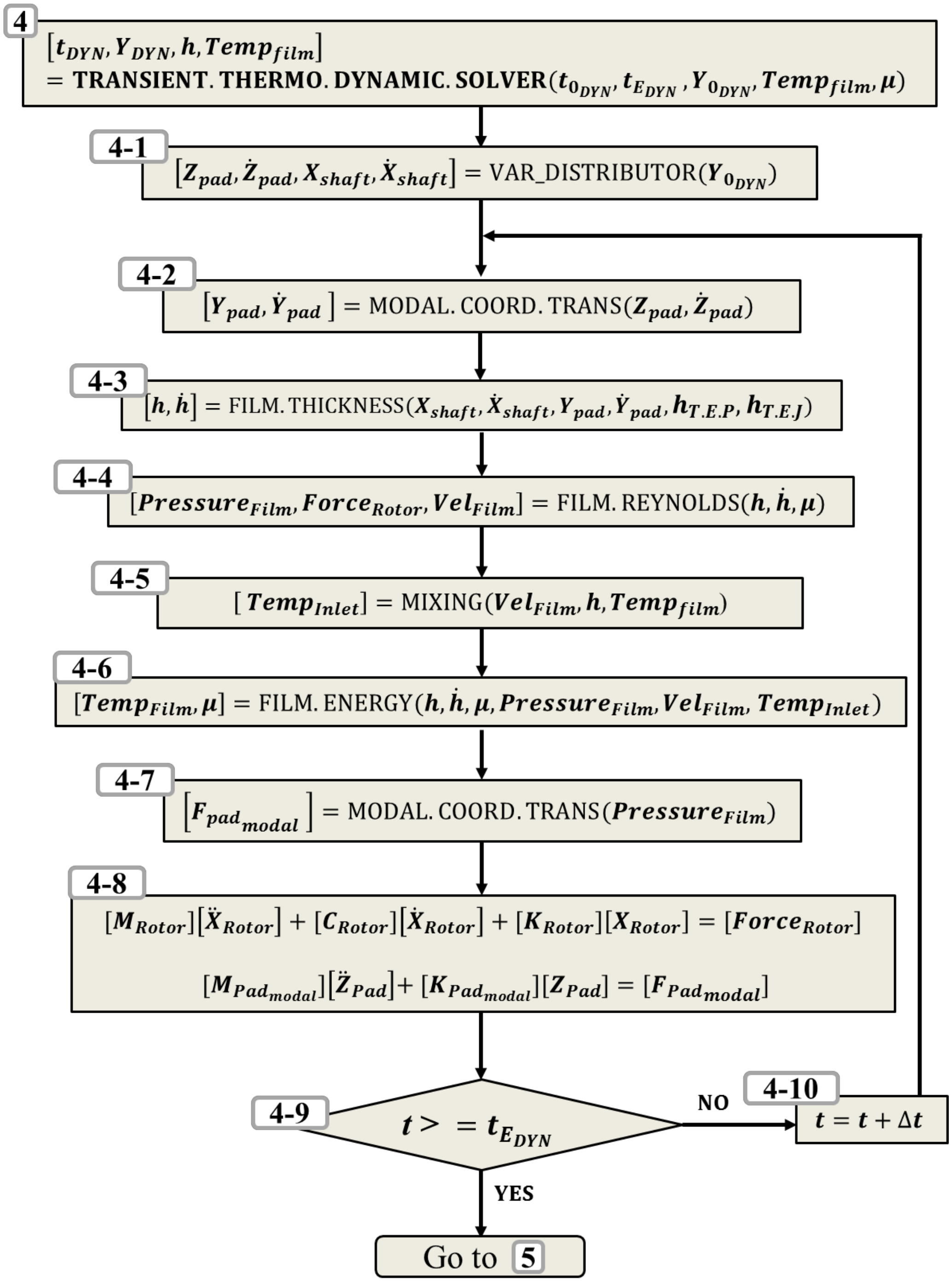

Fig. 25 Algorithm for thermo-dynamic rotor-bearing transient analysis

5.2 Nonlinear Transient Morton Analysis

The Morton effect can be analyzed by solving a complex time varying relationship between thermal and THD equations. In this regard, thermal refers to the transient heat conduction problems being solved in the journal and bearing, and THD includes both the solutions for temperatures in the lubricant film and the solution for shaft vibrations. Typically, the thermal growth in the Morton effect problem takes several minutes to several hours, and the general numerical integration scheme for the transient analysis demands a lot of computation. So a staggered integration scheme is adopted for the efficient computing without a loss of accuracy, where two types of solutions are integrated separately and interact with each other. The algorithm is motivated by Lee and Palazzolo's study [13] .The staggered integration scheme consists of thermal and THD equations, where the thermal solutions of bearing and shaft are integrated with a constant heat source evaluated by heat flux boundary conditions between lubricant, bearing and shaft. The integration time of the thermal system is relatively longer than the THD system due to the bigger thermal time constant. The THD solution is integrated by a flexible rotor and tilting-pad bearing dynamic equations combined with the Reynolds equation and energy equation, which are updated at each numerical integration time step. Both the physical coordinates of the thermal and the dynamic systems are converted into the modal coordinate for the computational efficiency. The staggered integration scheme assumes that once the steady state of the THD system with a smaller thermal time constant is achieved, there will be no significant change in the system without changing the thermal boundary conditions surrounded by the bearing and the spinning shaft.

After the THD system reaches the steady state, a new heat flux boundary condition is re-evaluated, and it is applied into the initial condition of the thermal-only system. After a relatively longer simulation time of the thermal-only system, the final temperature distribution of the bearing and rotor is used for the new thermal boundary conditions of the THD system. This alternate process is extended to get the transient analysis results. The time span of the thermal system's integration is decided by a trial and error. The algorithm for the Morton effect simulation is shown in Fig. 27, and the following explains it.

1) Temperature distribution in the shaft ($\mathrm{Y}_{0_{\mathrm{THERM}_{\mathrm{SHAFT}}}}$) and pads ($\mathrm{Y}_{0_{\mathrm{THERM}_{\mathrm{PAD}}}}$), and displacement and velocity of the flexible rotor and rigid pads ($\mathrm{Y}_{0_{\mathrm{DYN}}}$) become the initial conditions of the Morton effect analysis.

2) 'sub_DYN_Transient' is for a variable time step numerical integration of THD analysis. The dynamic equation is integrated from t_0 to $\mathrm{t}_{\mathrm{E}_{\mathrm{DYN}}}$ with the initial state, $\mathrm{Y}_{0_{\mathrm{DYN}}}$. There are two types of imbalance forces. The first one is the initial mechanical imbalance force, and the second one is the thermal bow induced imbalance force. The initial mechanical eccentricity stays constant with time, and the thermal induced imbalance is recalculated at each staggered integration time step based on the thermal gradient and the resultant thermal distortion of the shaft. During the dynamic transient analysis, six sub-procedures are conducted as follows:

2-1) ‘sub_Filmthickness’ evaluates the film thickness (h) and time derivatives of the film thickness (dh/dt) given the rotor and pads states ($\mathrm{Y_{DYN}}$). Thermal expansion of shaft ($h_{T.E.J}$) and pad ($h_{T.E.P}$) are taken into account in the calculation of h and dh/dt.

2-2) Based on h and dh/dt, fluidic force and velocity profiles are calculated by ‘sub_REYNOLDS’, and the velocity profile ($\mathrm{V_{Fluid}}$) is used for the evaluation of the lubricant temperature ($\mathrm{Temp_{Film}}$) and viscosity (μ), which makes a significant effect on the fluidic force ($\mathrm{F_{Fluid}}$).

2-3) Fluidic force ($\mathrm{F_{Fluid}}$), gravity force ($\mathrm{F_{Gravity}}$), initial mechanical imbalance force ($\mathrm{F_{M.E.}}$) and thermal induced imbalance force ($\mathrm{F_{T.B.}}$) are imposed to the dynamic transient analysis of the rotor-bearing system. The net imbalance is calculated as a vector sum of initial imbalance and the thermal induced imbalance.

2-4) ‘sub_Mixing’ evaluates the lubricant temperature distribution flowing into the leading edge of each pad, using the one-dimensional mixing temperature theory.

2-5) 3D energy equation is adopted for the evaluation of the temperature distribution ($\mathrm{Temp_{Film}}$) in the fluid film considering axial convection and conduction. Viscosity distribution (μ), which is a function of the lubricant temperature ($\mathrm{Temp_{Film}}$), is updated in the energy equation. Inlet temperature ($\mathrm{Temp_{Inlet}}$), shaft temperature($\mathrm{Temp_{SHAFT}}$), and pad temperature ($\mathrm{Temp_{PAD}}$) become the thermal boundary conditions of the energy equation.

2-6) Steady state of the synchronous orbit is determined by means of the Poincare plot. In this research, rotordynamic behavior is limited to a synchronous (1X) vibration, and fast Fourier transform (FFT) is performed at each journal orbiting to check the synchronous behavior. Fig. 26 shows a schematic diagram to show the synchronous orbit over a period. If the start point and the end point meet within a pre-defined circle-shaped area which is very small compared with the journal orbit size, it can be considered as a steady state; however, even if the two points meet within the pre-defined error criterion area, the velocity vectors defined by $\overrightarrow{v_s}$ and $\overrightarrow{v_e}$ shown in Fig. 26 may not meet within the prescribed area. This cannot be considered a steady state so both the position and velocity vectors should be taken into account when defining the steady state of the synchronous journal orbit. This process is repeated until the converged orbit is produced. After the steady state of the rotor dynamic system is achieved, thermal transient analysis of bearing and shaft is conducted.

3-1) Heat flux boundary condition between the pad and lubricant is calculated based on (1) the temperature distribution in the pad ($\mathrm{Temp_{PAD}}$), (2) orbit time averaged film thickness, and (3) the orbit time averaged temperature of the lubricant. (see section 2.7)

3-2) The newly updated heat flux boundary condition works as the thermal boundary condition of the pads thermal transient analysis. The numerical integration of the thermal system is conducted from $\mathrm{t_0}$ to $\mathrm{t_{E_{THERM}}}$. The final value of the thermal transient analysis, pad thermal gradient at time $\mathrm{t_{E_{THERM}}}$, works as (1) the thermal induced film thickness change, and (2) thermal boundary condition of the 3D energy equation.

3-3) Final value of the thermal transient analysis is used for the calculation of the pad thermal deformation. Thermally deformed pad causes change of the film thickness ($h_{T.E.P}$), and the effect of the film thickness change is considered in the calculation of the fluidic force.

4-1) Asymmetric heat flux into the synchronously whirling rotor is solved by the orbit time averaged heat flux [6] flowing from fluid film to the spinning shaft surface. The information of the fluid film temperature ($\mathrm{Temp}_{\mathrm{Film}}$,), and the film thickness (h) were saved during the THD transient analysis. (see section 2.7)

4-2) Based on the newly updated heat flux boundary condition, thermal load $[\boldsymbol{F}]$ acting on the shaft thermal transient analysis is updated, and the thermal solution is gained by the numerical integration from t_0 to $\mathrm{t}_{\mathrm{E}_{\mathrm{THERM}}}$. The final value of the thermal transient analysis, shaft thermal gradient at $\mathrm{t}_{\mathrm{E}_{\mathrm{THERM}}}$, works as (1) the thermal expansion force applied to the elastic shaft model, and (2) thermal boundary condition of the 3D energy equation.

4-3) The final value of the shaft's thermal transient analysis is transformed into the thermal expansion force, which works in the 3D elastic shaft's F.E. model. Thermal expansion of the shaft calculated by temperature distribution causes rotor thermal bending and shaft thermal expansion at the bearing location. The shaft thermal bow creates a new thermal bending induced imbalance force ($\mathrm{F}_{\mathrm{T.B.}}$)

working in the THD analysis, and thermal expansion causes a decrease in film thickness ($h_{T.E.J}$).

5) The whole process above is conducted until $\mathrm{t}_{GLOBAL} \geq \mathrm{t}_{E}$.

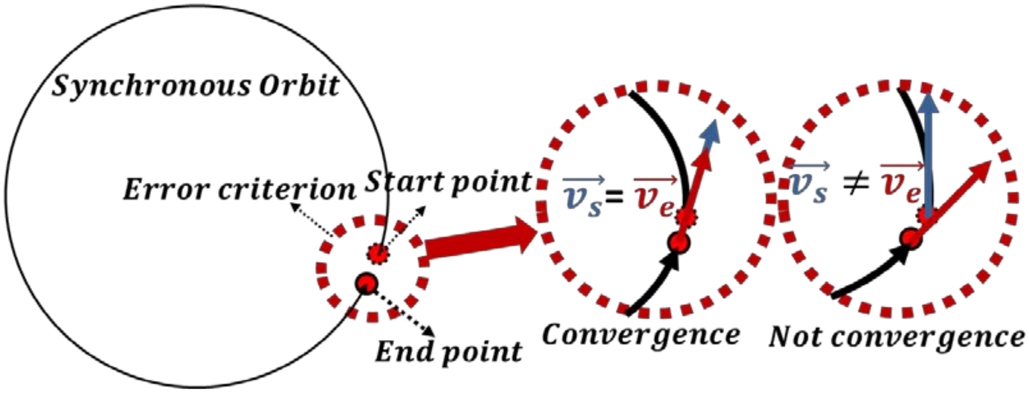

Fig. 26 Steady state error criterion area

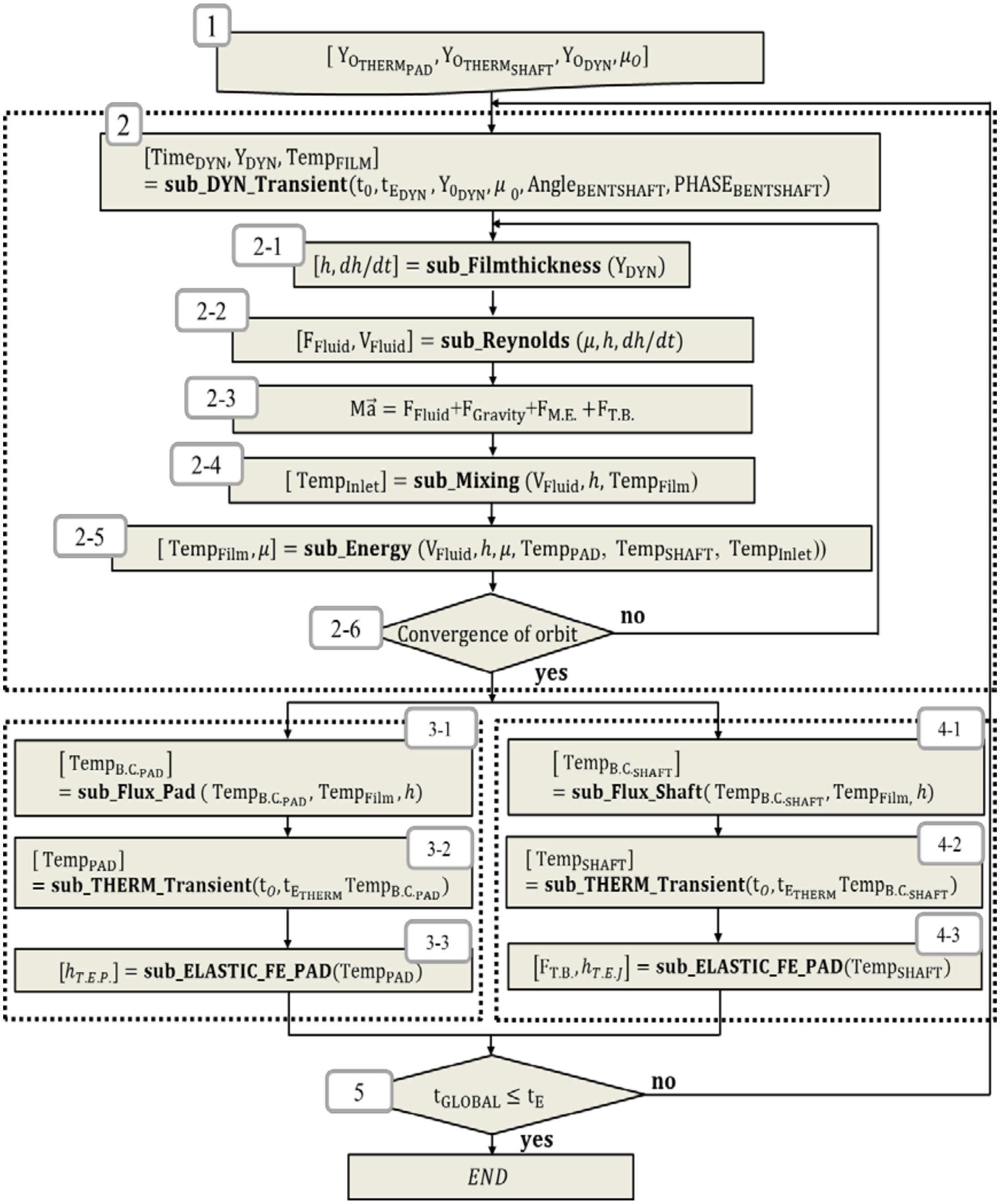

Fig. 27 Algorithm for transient Morton effect analysis

]

5.3 Synchronous Response Amplitude

The nonlinear transient analysis produces time varying thermal and dynamic responses, where the numerical integration of thermal and dynamic systems are performed simultaneously with different integration time. The transient analysis gives a time varying system responses at a constant rotor spin speed such as time varying phases and vibration amplitudes, the most easily recognized dynamic behavior. However, the Morton effect problem occurs very slowly and very heavy computation is required. If a designer or troubleshooter of rotating machinery wants to avoid the Morton effect problem, many different cases with different rotor spin speed should be simulated. It requires a considerable amount of time to simulate many cases and there should be an alternative which is fast and efficient.

Childs and Saha [16] suggested a iteration approach for the Morton effect analysis adopting 2D energy equation and linear dynamic model. Their result is similar to the bode plot with synchronous response amplitude and phase. In this section, newly developed iteration algorithm is suggested, where both nonlinear transient rotor-bearing dynamic and nonlinear thermal analysis are combined to achieve the steady synchronous response amplitude. This iteration procedure is performed at user defined spin speeds.

Detailed numerical procedure for calculating steady Morton effect will be discussed. There are five sub-routines in the main algorithm. The first routine is for the initial conditions for the analysis and includes a closed loop for changing rotor spin speed. At each rotor spin speed defined by the user, synchronous rotor vibration amplitude and phases are calculated, which looks like a bode plot. Another words, the output of this algorithm is bode plot where the thermal bow effect is taken into account and nonlinear transient rotor dynamic analysis is conducted. The second routine is for nonlinear transient rotordynamic analysis, where both numerical integration of rotor-bearing dynamic and thermal system are performed. Rotor-bearing and fluid dynamic problems are solved together interacting on each other. The fluidic force acting on the bearing pad and rotor producing dynamic behavior is evaluated by generalized Reynolds equation being connected to 3D energy equation. The third and fourth loop is for the convergence of thermal gradient in the bearing pad and shaft. In this procedure, the convergence is achieved using flux boundary condition, heat conduction equation and iteration scheme. The last routine is for the convergence of the system variables of whole system which include dynamic and thermal states. The algorithm for the analysis of thermal induced synchronous response amplitude and phase is shown in Fig. 27 The following explains the detailed numerical procedure.

(1) Thermal gradient in the shaft ($\mathrm{Y0}_{\mathrm{THERM}_{\mathrm{SHAFT}}}$) and pads ($\mathrm{Y0}_{\mathrm{THERM}_{\mathrm{PAD}}}$), and dynamic conditions of rotor and pads ($\mathrm{Y0}_{\mathrm{DYN}}$) become the initial states of the Morton effect simulation. RPM_SPAN indicates the rotor spin speed pre-defined by user. At each spin speed, steady dynamic and thermal behaviors due to the thermal bow effect are calculated adopting both transient and steady analysis.

(2) ‘sub_DYN_Transient’ is a sub-function for an adaptive time step numerical integration of thermo-dynamic rotor-bearing system. The thermo-dynamic system is integrated from t_0 to $\mathrm{t}_{\mathrm{E}_{\mathrm{DYN}}}$ with the initial state ($\mathrm{Y}_{0_{\mathrm{DYN}}}$ and μ_0). Two different imbalance forces are acting on the spinning rotor, which are initial

mechanical imbalance defined by user and thermal bow imbalance force induced by an asymmetric journal heating. The initial imbalance is constant with time, and the thermal imbalance varies with time due to the time varying thermal gradient inside the shaft. (2-1) 'sub_Filmthickness' calculates the film thickness (h) and the temporal derivative of the film thickness (dh/dt) at a given rotor and pads states ($\mathrm{Y_{DYN}}$). Thermal expansion of shaft ($h_{T.E.J}$) and pad ($h_{T.E.P}$) are considered for the evaluation of h and dh/dt. (2-2) Fluidic force ($\mathrm{F_{Fluid}}$) and the resultant velocity profile ($\mathrm{V_{Fluid}}$) are evaluated based on h and dh/dt by 'sub_REYNOLDS'. (2-3) Numerical integration for transient rotordynamic analysis is conducted with the imposed physical force acting on the spinning rotor, Fluidic force ($\mathrm{F_{Fluid}}$), gravity force ($\mathrm{F_{Gravity}}$), initial mechanical imbalance force ($\mathrm{F_{M.E.}}$) and thermal induced imbalance force ($\mathrm{F_{T.B.}}$). (2-4) 'sub_Mixing' calculates the inlet temperature flowing into the pad adopting modified mixing temperature theory discussed in this research. (2-5) Lubricant temperature ($\mathrm{Temp_{Film}}$) is calculated by the 3D energy equation. The thermal boundary conditions are lubricant inlet temperature ($\mathrm{Temp_{Inlet}}$), shaft temperature ($\mathrm{Temp_{SHAFT}}$), and pad temperature ($\mathrm{Temp_{PAD}}$). Film viscosity (μ) is updated based on the newly updated lubricant temperature. (2-6) Convergent journal orbit is determined by means of Poincare plot which uses both displacement and velocity. The journal is assumed to show a synchronous orbit. The detailed procedure to determine the convergent orbit is described in the previous section.

(3-1) Heat flux and temperature boundary conditions between the pad and fluid film are calculated using thermal gradient in the pad ($\mathrm{Temp}_{\mathrm{PAD}}$), orbit time averaged film thickness and lubricant temperature. (3-2) Newly updated flux boundary condition produces the pad temperature. To produce the convergent thermo-dynamic states of the rotor-bearing system, steady and transient pad thermal analysis are combined. (3-3) Thermal gradient of the pad produces the thermal expansion of the pad ($h_{T.E.P}$) which is used for the evaluation of the film thickness. (3-4) The iteration loop runs until the pad thermal gradient reaches the steady condition.

(4-1) Flux and temperature boundary condition on the surface of the spinning journal is calculated adopting orbit time average method suggested by Gomiciaga and Keogh [6]. (4-2) Updated flux boundary condition produces the thermal gradient in the shaft. Steady and transient thermal analysis are combined. (4-3) Journal temperature produces the asymmetric thermal expansion leading to the film thickness change ($h_{T.E.J}$). (4-4) The iteration scheme is performed until the temperature distribution reaches the steady state.

(5) The whole procedures are performed until the thermo-dynamic system is convergent.

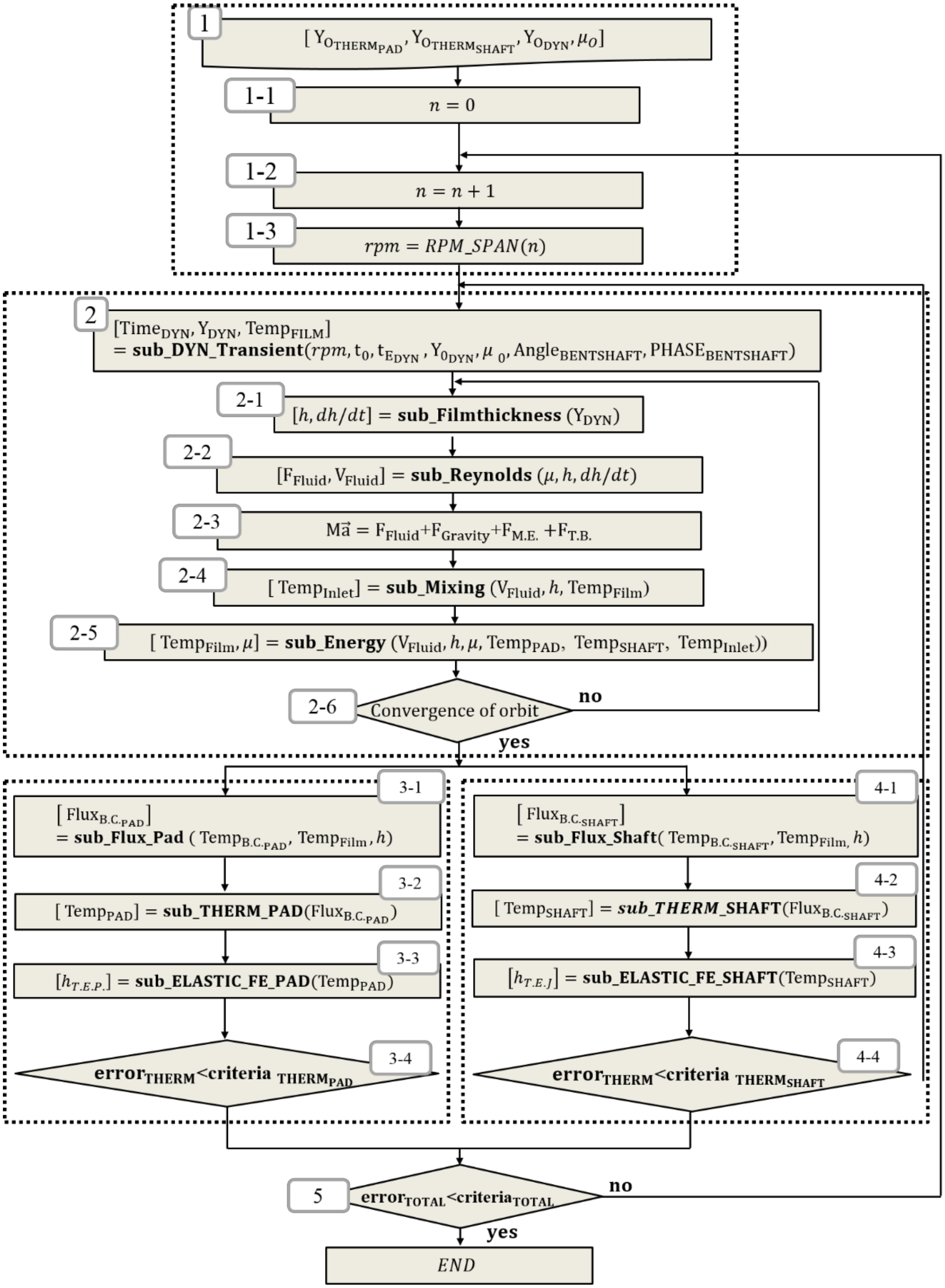

Fig. 28 Steady Morton effect analysis

6 SIMULATION FOR TPJB MODEL

6.1 Someya Table

For the verification of flexible pad TPJB model presented in this research, three different results are compared, where thermal effects are excluded. The first one is Someya's results [41] where the Finite Difference Method (FDM) is adopted. The calculation number is 31 in the Someya's journal-bearing databook, and the bearing input parameters are shown in Table 3. The sommefeld number [41] is expressed by (99), and non-dimensionalized force coefficients can be expressed by (100) and (101). The second result is a rigid-pad TPJB performed in this research. The last model is a flexible pad TPJB model where only 1st rigid body mode is taken into account. Theoretically, the force coefficient of flexible pad model with only rigid body mode should produce the identical results to other two rigid pad models. Direct terms of dynamic coefficients are depicted in Fig. 29, and three models produce identical results.

It can be seen that the newly developed flexible pad TPJB model with transient dynamic analysis works well, which means that the complicated coordinate transformations performed each numerical integration time step, and newly developed nodal based film thickness formula are verified.

$$\text{S: Sommerfeld number} = \frac{\mu N L_{Brg} D_s}{W_{Brg}}\left(\frac{R_s}{C_p}\right) \tag{99}$$

$$K_{ij}\text{: Nondimensional stiffness coefficient} = \frac{C_p k_{ij}}{W_{Brg}}\ (i,j = x,y) \tag{100}$$

$$C_{ij}\text{: Nondimensional damping coefficient} = \frac{C_p \omega c_{ij}}{W_{Brg}} \ (i, j = x, y) \tag{101}$$

Table 3 Bearing configuration

No. Pads	L:D ratio	Preload	Pad arc length	Pivot offset
4	1.0	3/4	80	0.5

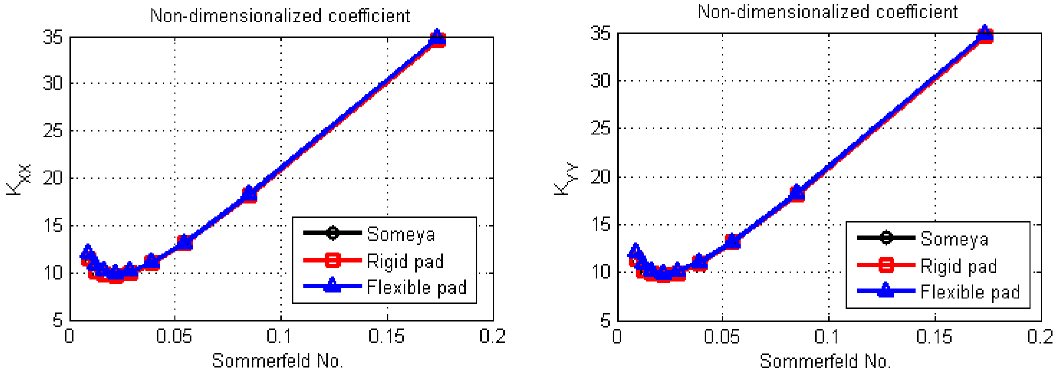

(a) K_{xx} (b) K_{yy}

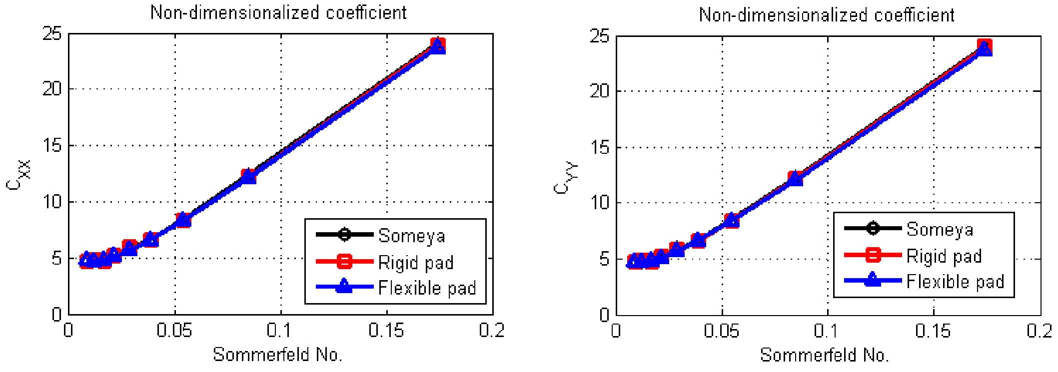

(c) C_{xx} (d) C_{yy}

Fig. 29 Comparison of dynamic coefficient

6.2 Comparison to Experimental Results

The newly developed TPJB model is compared with the experimental work performed by Kulhanek [42]. The bearing input parameters are shown in Table 4. Three different unit load cases (0, 1035, 2413 KPa) are simulated from 7000rpm to 1600rpm. 20 modes of flexible FE pad are selected based on the lower eigenvalue. Pivot configuration is assumed to be identical to parameters provided by Wilke's [43] dissertation shown in Table 5 since the pivot input parameter was not provided by Kulhanek's [42] research paper. Wilke's [43] experimental set up used the same test rig and had the similar bearing configuration with the same journal radius and the same type of pivot.

Fig. 31 (a) and (b) show the direct stiffness and damping coefficients respectively. At zero load condition, theoretical results of k_{xx} and k_{yy} should provide identical results, and the current approach produced the same values as expected. c_{xx} and c_{yy} are also identical. Experimental results does not show the same values in the x and y directions, and it may be due to bearing housing elastic deformation, asymmetric film clearance or measurement error. Current research predicted very similar stiffness coefficient within 20% error and damping coefficient within 30% error as depicted in Fig. 31 (a) and (b).

Fig. 31 (c) and (d) show 1035KPa unit load case. As the rotor spin speed increases, stiffness coefficients increase and damping coefficients decrease. At a low spin speed of 7000rpm, every predicted force coefficient shows similar results to the experimental work within 13% error. As the rotor spin speed increases the differential between numerical and experimental results increases. The differential of damping coefficients increases more than that of stiffness coefficients with the increased rotor spin speed as shown in Fig. 31 (c) and (d). Temperature distribution in the spinning journal, fluid film and bearing pads are described in Fig. 32.

In case of the 2413KPa unit load, the coefficients differential increases with the rotor spin speed as shown in 1035KPa unit load case. Current numerical model predicted higher stiffness coefficients and lower damping values than the experimental results. In a very heavy unit load case, elastic deformation of bearing housing and test rig may cause unpredicted effects.

Fig. 32 shows the pivot stiffness with varying rotor spin speed calculated by Hertzian contact theory [34]. Two bottom pads (pad No: 1 and 5) produce the highest pivot stiffness. At the lowest rotor spin speed of 7000 rpm, bottom pads pivot stiffness (pad No: 1 and 5) are 5 times bigger than the top pad (pad No: 3). At the highest rotor spin speed of 1600rpm, bottom pads have 2.25 times higher pivot stiffness than the top pad (pad No: 3). Lubricant temperature increases with the increased spin speed and the resultant viscous shearing leads to increased thermal expansion of the shaft and bearing pads. This thermal expansion and the resultant decreased film thickness cause the increased fluidic pressure leading to higher pivot stiffness.

Table 4 Bearing parameters

Bearing configurations

Number of pads	5
Load configuration	LBP
Pivot configuration	Cylindrical pivot
Unit load (*KPa*)	2413
Rotor spin speed (rpm)	13000
Pad arc length	57.87
Journal diameter (*mm*)	101.587
Bearing length (*mm*)	60.325
Pad clearance (*mm*)	0.112
Preload	0.5
Lubricant type	ISO VG32
Supply lubricant temperature (℃)	43.3
Mixing factor (β)	0.9
Thermal boundary condition around shaft	Convective, 25(℃)
Thermal boundary condition around bearing pad	Convective, 50(℃)
Convection coefficient (W/m^2)	50

Pad input parameters

Pad thickness (pivot, center) (*mm*)	18.5
Pad thickness (edge, end) (*mm*)	11.5
Young’s modulus (*Pa*)	2.12×10^{11}
Density (kg/m^3)	7850
Heat Capacity (*J/kg℃*)	453
Heat Conductivity (*W/(mK)*)	50
Poison's Ratio	0.29
Thermal Expansion Coefficients (*1/℃*)	1.00×10^{-5}
Reference Temperature (℃)	35

Shaft input parameters

Young's Modulus (*Pa*)	2.10×10^{11}
Density (kg/m^3)	7850
Heat Capacity (*J/kg℃*)	453.6
Heat Conductivity (*W/(mK)*)	50
Poison's Ratio	0.3
Thermal Expansion Coefficients (*1/℃*)	1.00×10^{-5}
Reference Temperature (℃)	35

Table 5 Pivot configuration

	Pivot	Housing
Circumferential radius	62.13mm	-69.85mm
Axial radius	1270 mm	∞
Elastic modulus	212 GPa	206 GPa
Poisson's ratio	0.29	0.288

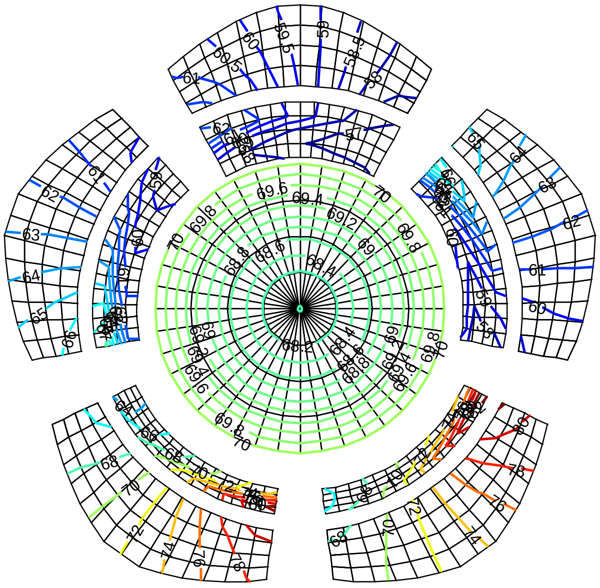

Fig. 30 Temperature distribution on shaft, fluid film and bearing pads

(1035 *KPa*, 7000 *rpm*)

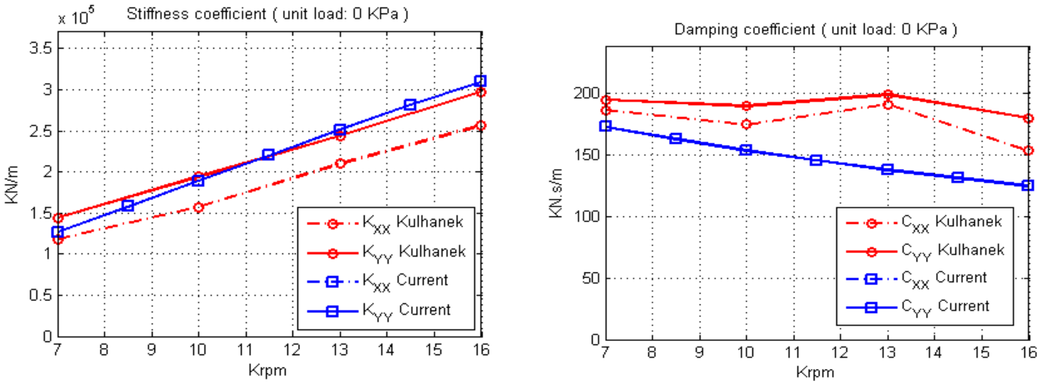

(a) Stiffness coefficient at 0KPa

(b) Damping coefficient at 0KPa

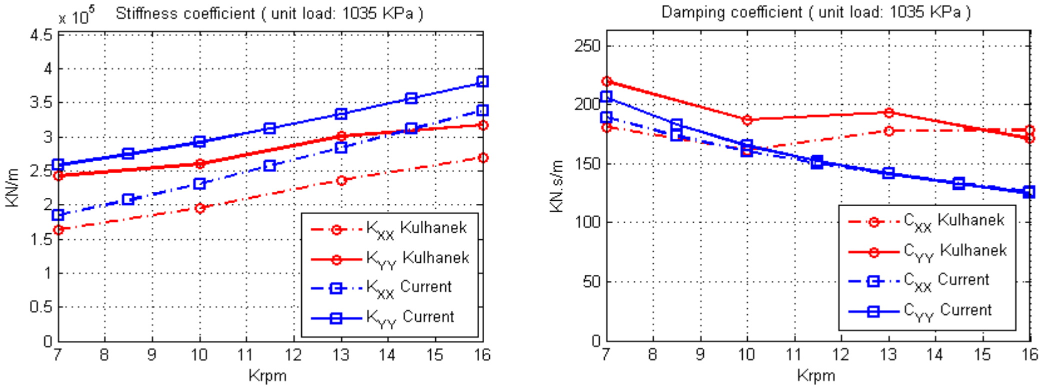

(c) Stiffness coefficient at 1035KPa

(d) Damping coefficient at 1035KPa

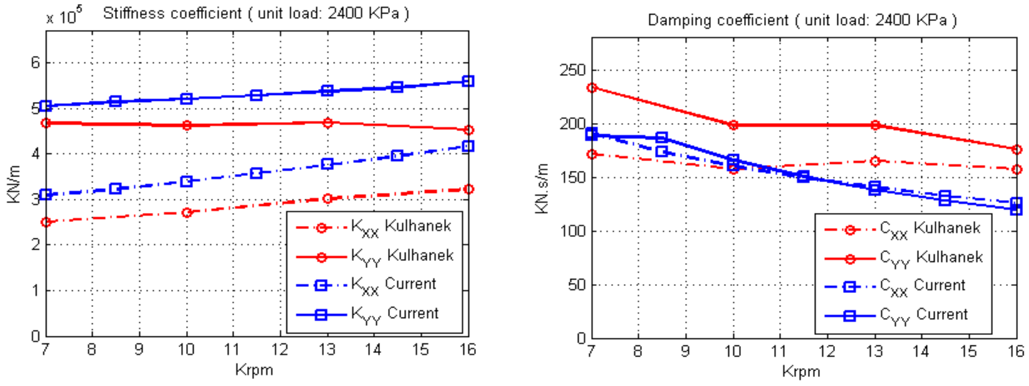

(e) Stiffness coefficient at 2413KPa

(f) Damping coefficient at 2413KPa

Fig. 31 Comparison of dynamic coefficients between Kulhanek [42] and current research.

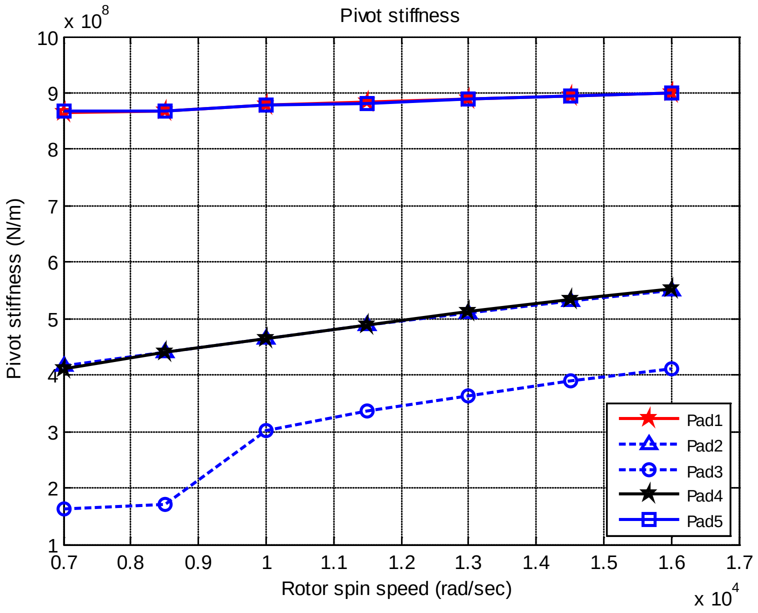

Fig. 32 Nonlinear pivot stiffness with varying rotor spin speed at 2413*KPa*

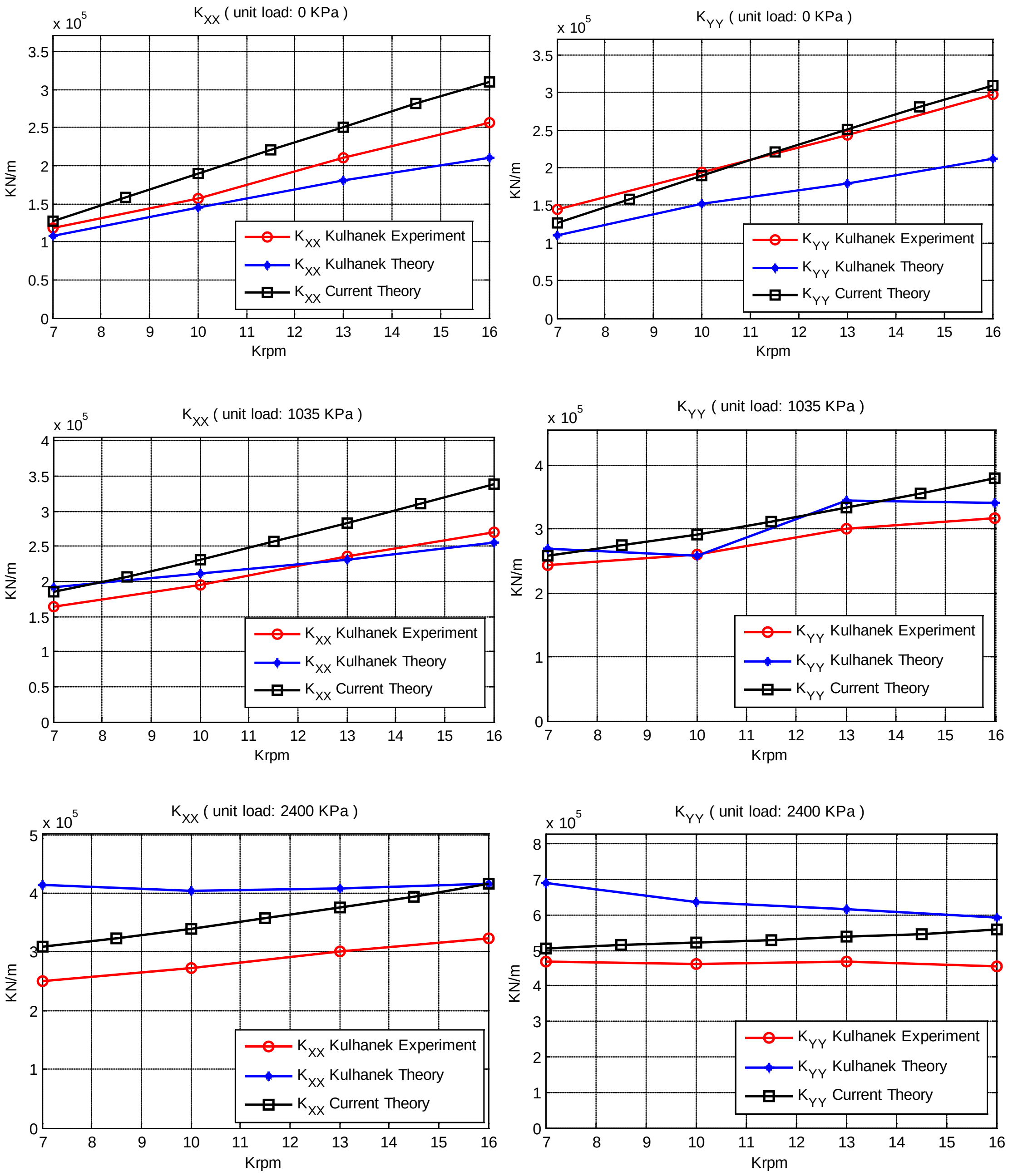

Fig. 33 Comparison between experimental and theoretical results

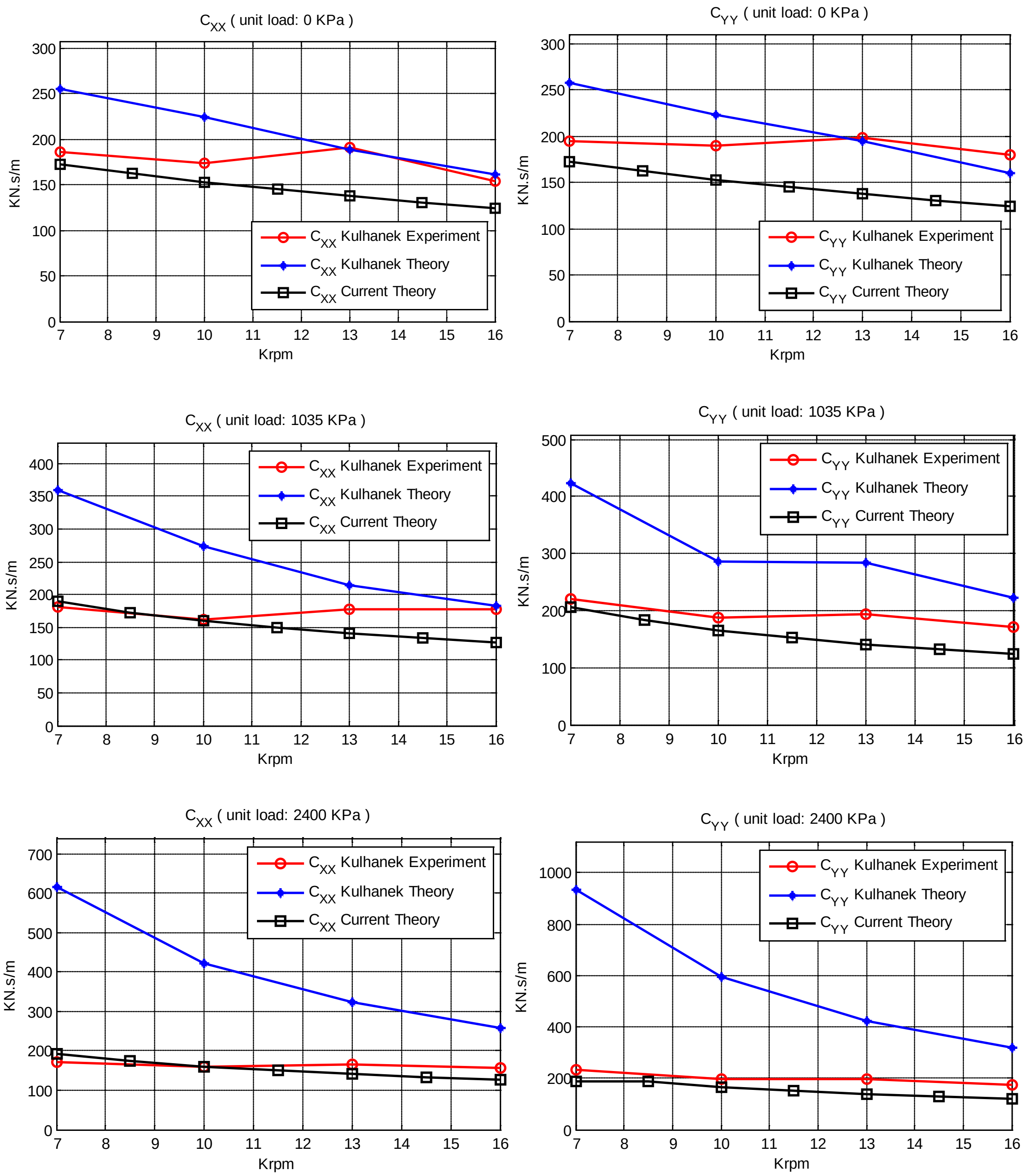

Fig. 34 Comparison between experimental and theoretical results

6.3 Number of Pad's Modes

In this section, static equilibrium condition and dynamic coefficients will be simulated with increasing number of modes of the flexible pad FE model. Bearing configuration is identical to the TPJB simulated in the previous section 6.2. The unit load is constant at 2413 KPa equivalent to 14.787 *KN*. Rotor spin speed is constant at 16 *Krpm*. The 3D FE bearing pad model is shown in Fig. 35, where the pad thickness varies in the circumferential direction. The pad thickness at the pivot location is 12.21mm and the thickness at the circumferential end is 7.59mm. The thickness is increasing linearly in circumferential direction as seen in Fig. 35. Rigid pivot is adopted to see the pad flexibility effect on the bearing static behavior.

Two different models are simulated and compared each other. The first model is elasto-hydro-dynamic (EHD) TPJB model, where thermal effects are not taken into account but only pad flexibility effect is considered. The second model is TEHD TPJB model with the consideration of varying viscosity, thermal expansion and pad flexibility.

Simulation method is to increase the number of modes from 1 to 30. The first mode is rigid body mode equivalent to pad tilting motion shown in Fig. 43 (a). Direct stiffness terms are shown in Fig. 36. Noticeable change of the stiffness occurs at 4th and 10th modes as shown in Fig. 43 (b) and (c) respectively. Pad bending in x-y plane occurs at 4th mode as described in Fig. 43 (b), and bending both in x-y and x-z plane occurs at 10th mode as shown in Fig. 43 (c). TEHD model predicted higher stiffness coefficients due to the thermal expansion of the shaft and pads. Variation of damping coefficients is described in Fig. 37. With the consideration of bending mode (4th model), c_{xx} and c_{yy} of

TEHD model is decreased by 20% and 30% respectively compared to the rigid pad bearing model with the consideration of only 1st mode. Reduction ratio of stiffness coefficients of TEHD TPJB model is around 10%, and the reduction rate of damping coefficients were more than 20%. After 10th mode, noticeable change of the coefficient is not observed as seen in Fig. 36 and Fig. 37. Pad flexibility affected damping coefficient more than stiffness coefficient.

Journal static eccentricity ratio and attitude angle are depicted in Fig. 39. As in the dynamic coefficients, the eccentricity ratio was influenced by 4th and 10th modes. On the other hand, the attitude angle of TEHD model is gradually influenced with the increasing number of modes. 20th mode produced abrupt change as seen in Fig. 39. In case of EHD model where non-thermal effects are taken into account, attitude angle stays at zero. It can be seen that the non-zero attitude angle is produced by the pad thermal expansion.

Average film thickness on pad No.1, 2 and 3 with varying number of modes is described in Fig. 39. Three plots have the same scale in y axis. Even though the journal eccentricity ratio of TEHD model is smaller than EHD model, average film thickness of TEHD model is smaller than EHD model. This means that the thermal expansions of pad and journal tighten the lubricant leading to lower journal eccentricity. Only 4th mode produces a noticeable change in the film thickness. Film thickness on the pad No. 1 (bottom pad) is less than 50% of pad No. 3 (top pad). This is due to the journal weight in $-y$ direction.

Average thermal expansion of journal and pads simulated by TEHD TPJB model is shown in Fig. 40. For the journal thermal expansion, distance between journal radial center and each node on journal outer radial surface is measured. Pad thermal expansion is measured only in the radial direction to see the thermal expansion effects on the film thickness as described in Part I of this research. Even though the average temperature of pad is higher than the shaft (see Fig. 41), shaft thermal expansion is more than twice bigger than the pads.

Average temperature of the shaft, lubricant and pads are shown in Fig. 41. Even though the only heat source of this bearing system is the viscous shearing in the lubricant, the average temperature of the pad is higher than lubricant. This is due to the lubricant thermal gradient in radial direction. Peak temperature is described in Fig. 42. The lubricant which is the only heat source in the problem domain has the highest temperature. It can be seen that the reason of the bearing pads' highest average temperature is the lubricant thermal gradient in radial direction. Only the 4th mode has the noticeable influence on the temperature as seen in Fig. 41 and Fig. 42.

Even after the decrease of the lubricant viscosity caused by increased lubricant temperature, stiffness coefficient of TEHD model produced higher value than EHD model. The thermal expansion of shaft and pad is thought to tighten the fluid film leading to stiffened system.

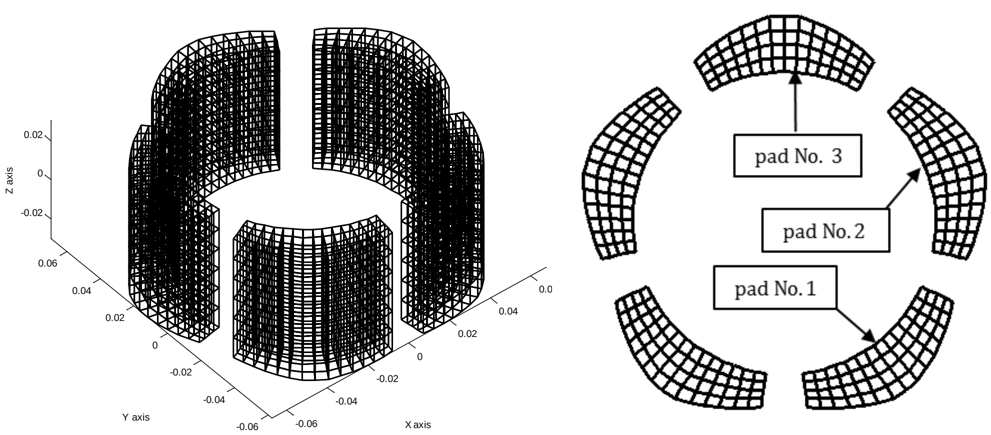

Fig. 35 Bearing pad F.E. model

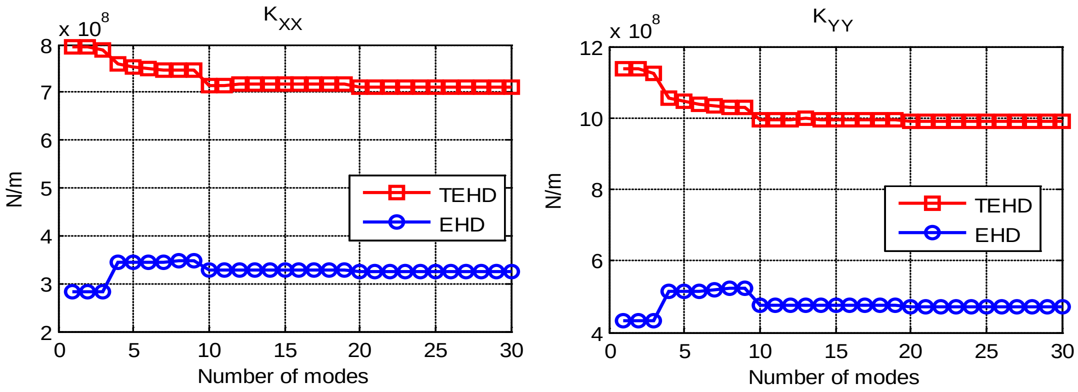

Fig. 36 Stiffness coefficients with varying number of modes

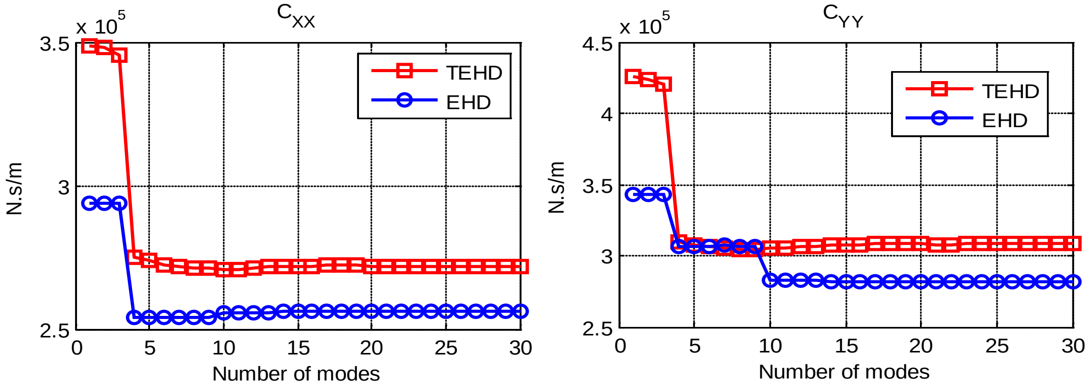

Fig. 37 Damping coefficients with varying number of modes

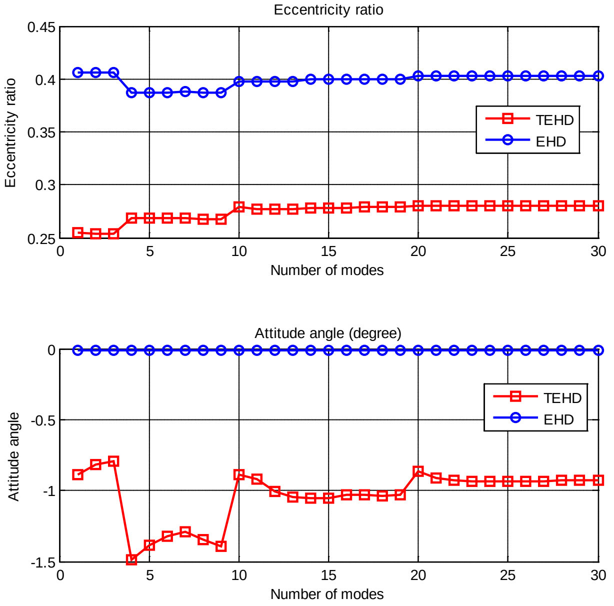

Fig. 38 Static equilibrium conditions with varying number of modes

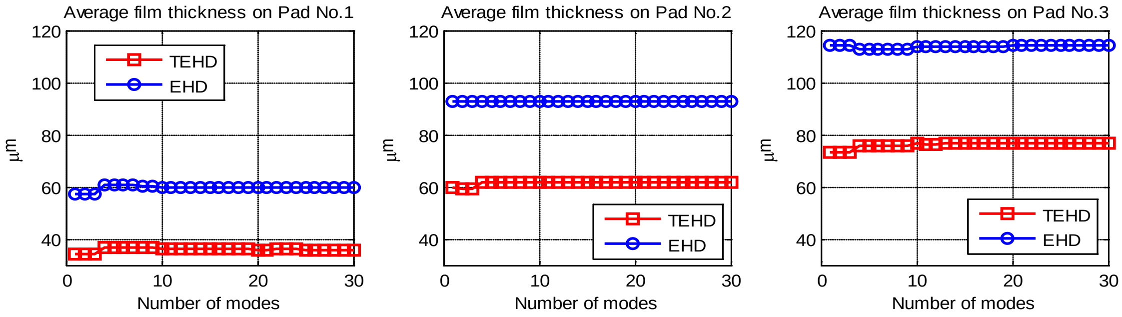

Fig. 39 Average film thickness with varying number of modes

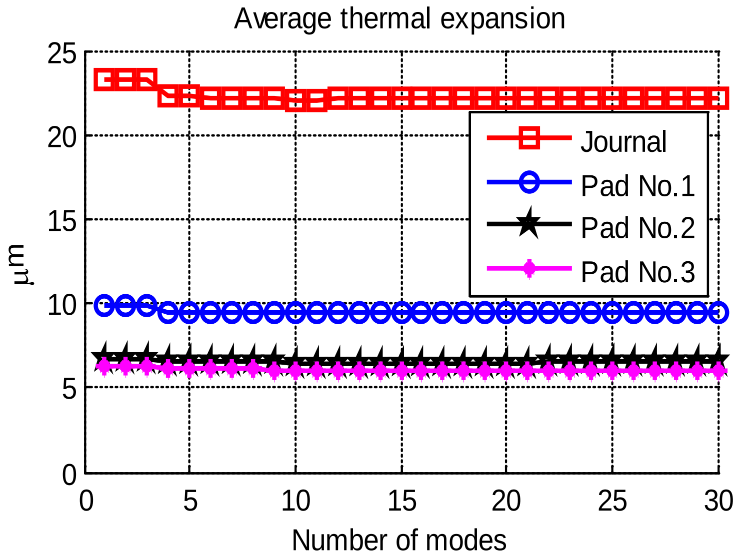

Fig. 40 Average thermal expansion of journal and pads (TEHD model)

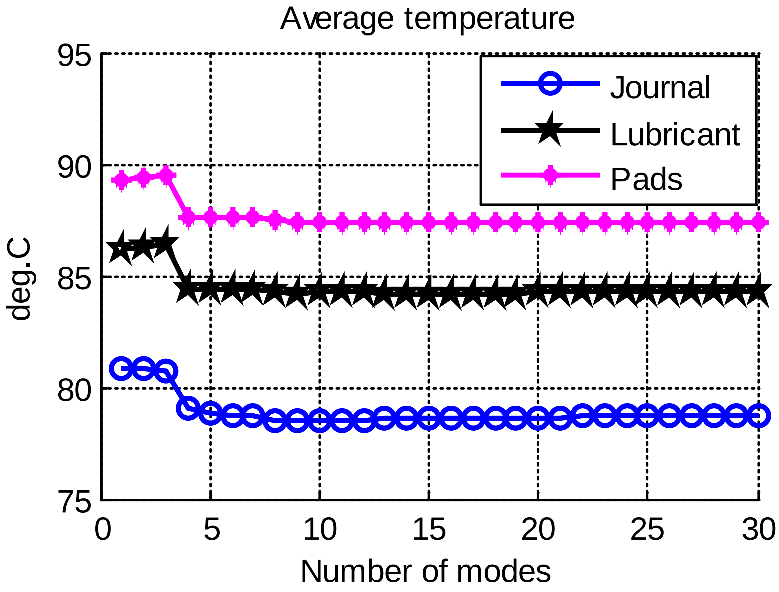

Fig. 41 Average temperature

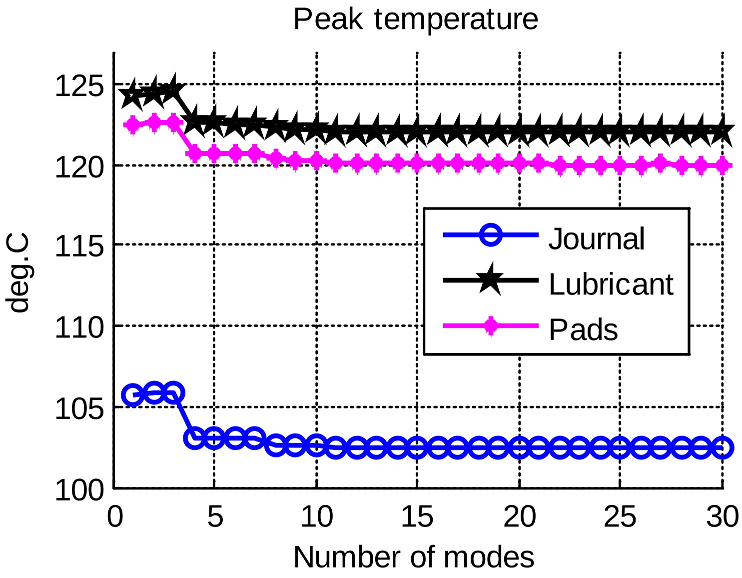

Fig. 42 Peak temperature in shaft, lubricant and pads

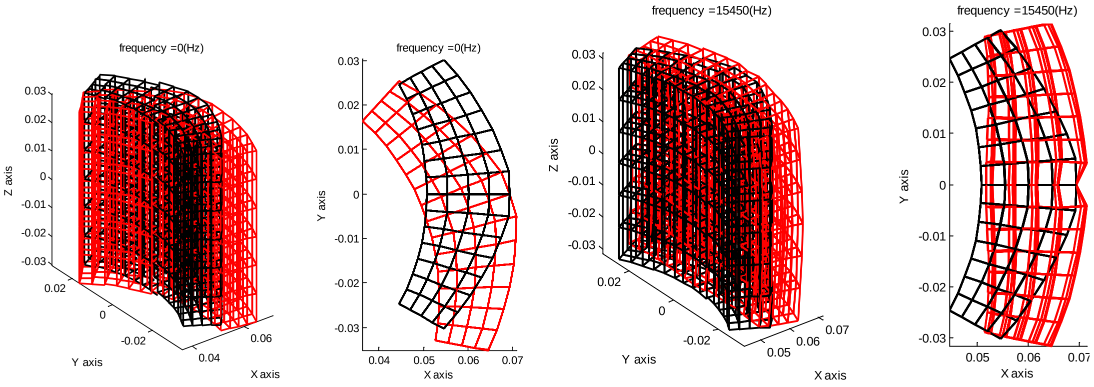

(a) 1st mode (0 *Hz*, rigid body mode) (b) 4th mode (15450 *Hz*)

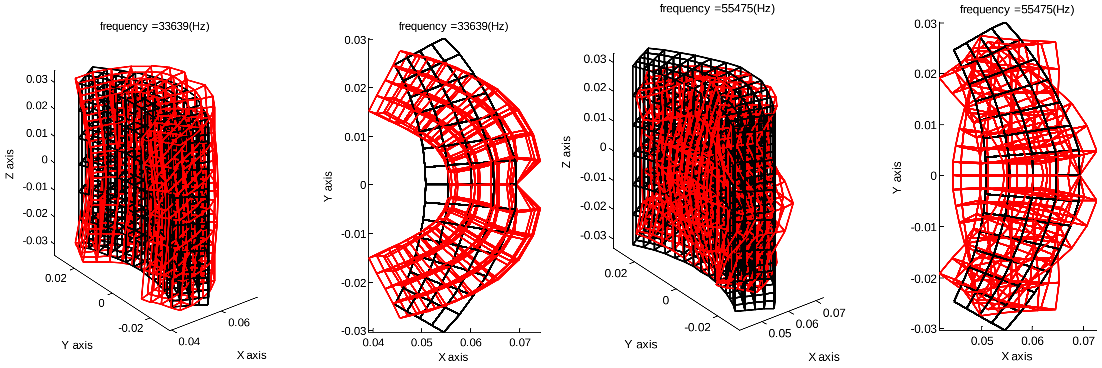

(c) 10th model (33639 *Hz*) (d) 20th mode (55475 *Hz*)

Fig. 43 Mode shapes of flexible pad with rocker-pivot

6.4 Pad Thickness Effect

In this section, three TEHD TPJB models with different pad thickness are simulated with the rotor spin speed ranging from 7,000 rpm to 16,000 rpm. Bearing unit load is constant at 1034 *KPa*, and nonlinear pivot (see

Table 5) is considered, whereas rigid pivot model is simulated in the previous section to examine the pad flexibility effect. The three different pad FE models with different thickness are shown in Fig. 44. Bearing No. 1 has the same configuration as studied in the previous section 6.3 as shown in Fig. 44 (a), and two others have 70% and 40% of its initial pad thickness as shown in Fig. 44 (a) and (b) respectively. 30 modes are selected based on the lower eigenvalue.

Direct stiffness and damping terms are drawn in Fig. 45 (a) and (b) with varying rotor spin speed respectively. As the spin speed increases, stiffness coefficient differential increases. On the other hand, damping coefficient differential stays constant as seen in Fig. 45 (b). Thinner pad produced increased journal eccentricity ratio caused by the pad elastic deformation under the journal weight as seen in Fig. 45 (c). Thinner pad moved the journal position clock-wise (CW).

Fig. 46 compares the temperature differential between different pad models. Thicker pad produced higher peak and average temperature all over the shaft, lubricant and bearing pad. From the viewpoint of the pad flexibility, thicker pad is stiffer than thin pad leading to decreased elastic deformation, decreased film thickness and increased viscous shearing. From the viewpoint of the pad thermal expansion, at the same temperature distribution, thicker pad would produce bigger thermal expansion in the radial direction due to its thickness. And, thicker pad's higher average temperature will cause bigger thermal expansion than in the same temperature condition.

Fig. 47 compares nonlinear pivot stiffness at each pad with varying rotor spin speed. As in the previous sections, bottom pad produces the highest pivot stiffness due to the journal weight direction. The thinnest pad shows the lowest pivot stiffness. Minimum film thickness on each pad is shown in Fig. 48. The minimum film thickness was increased by the thinner pad due to the increased pad elastic deformation and less pad thermal expansion. The thermal and elastic deformation may cause the pad preload change, which will be investigated more in detail in next section.

In this section, many numerical results were analyzed and compared. To recognize the pad thickness effect at a glance, quantitative analysis is performed.

Table 6 shows the drop ratios of variables due to the decreased pad thickness. The drop ratio was calculated at each spin speed and averaged over the speed. By reducing the pad thickness by 30% of its initial thickness, the maximum drop ratio happens at damping coefficients which are 9% and 10%. When the pad thickness was reduced by 60% which is twice as big as the 30% reduction, damping coefficient drop ratios are 30% of c_{xx} and 33% of c_{yy} which are almost three times that of 30% reduction model. On the other hand, stiffness coefficients are decreased by 10% of k_{xx} and 14% of k_{yy}. It can be seen that the damping coefficient is more influenced by the pad flexibility than the stiffness coefficient is.

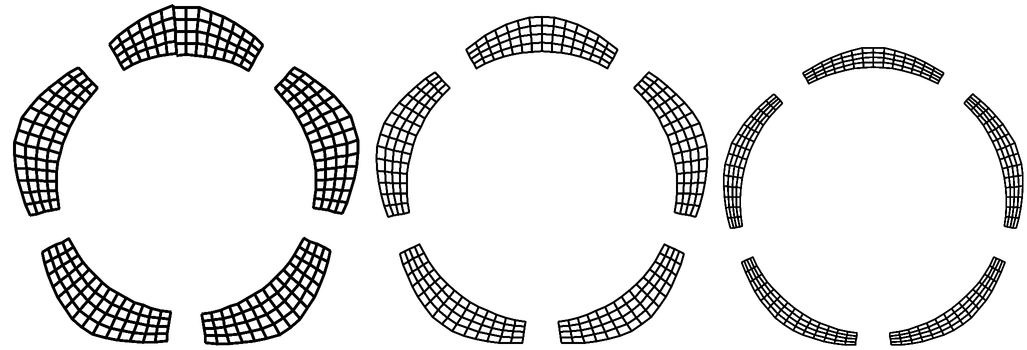

(a) Initial pad thickness (model No.1)

(b) 70% thickness (model No.2)

(c) 40% thickness (model No.3)

Fig. 44 Three different pad thickness

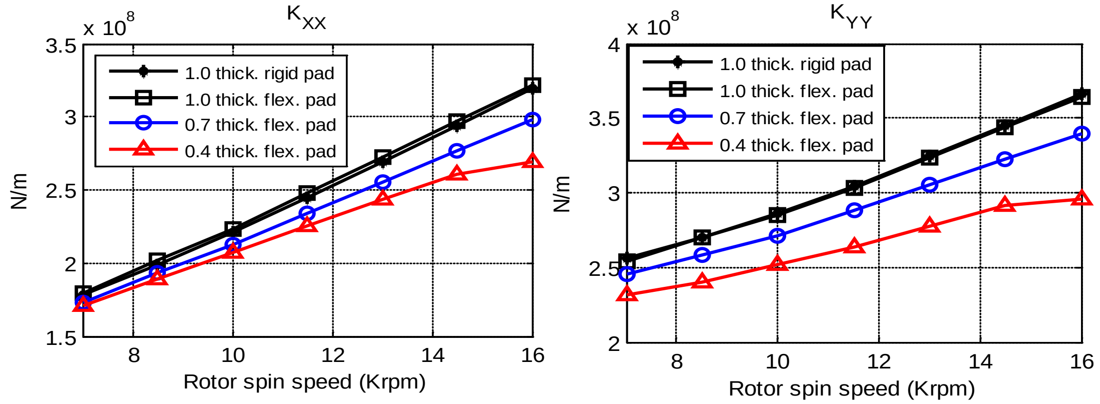

(a) Stiffness coefficient

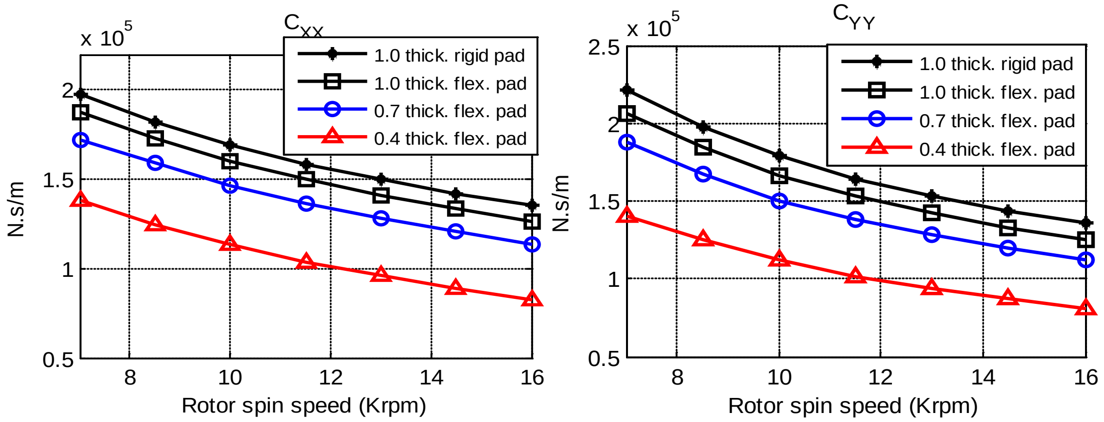

(b) Damping coefficient

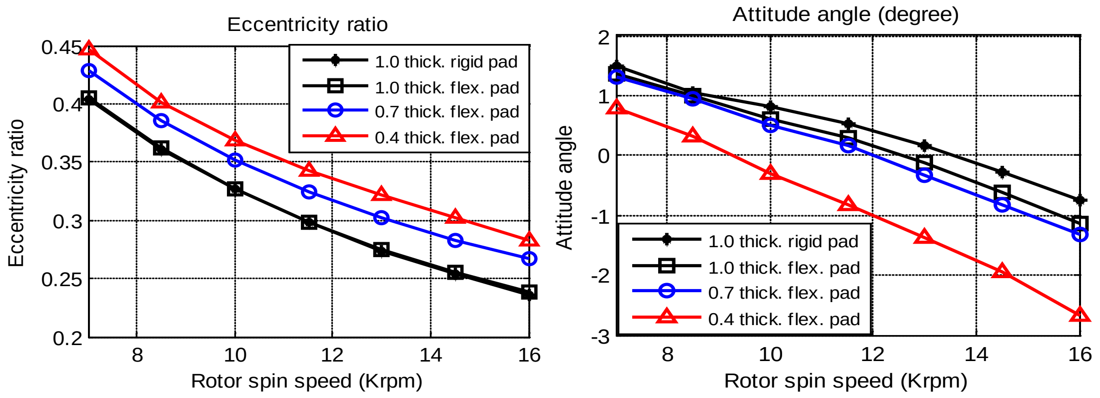

(c) Static equilibrium condition

Fig. 45 Pad thickness effects on stiffness coefficient

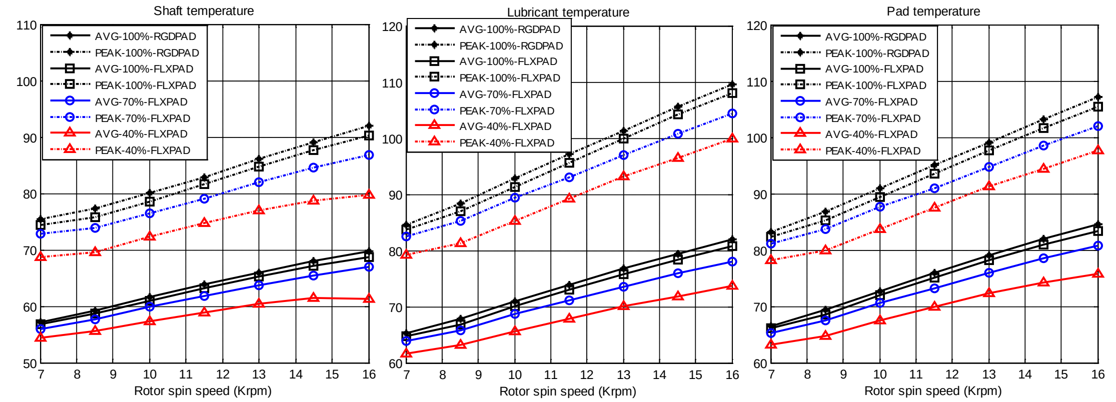

Fig. 46 Average and peak temperature in shaft, lubricant and pad

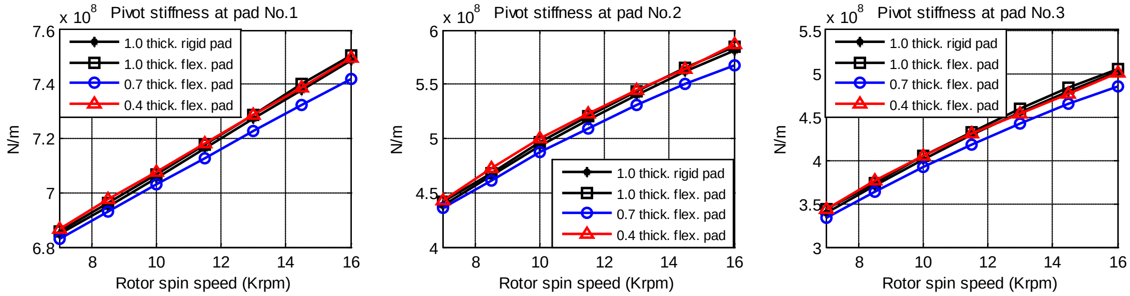

Fig. 47 Pivot stiffness with different pad thickness

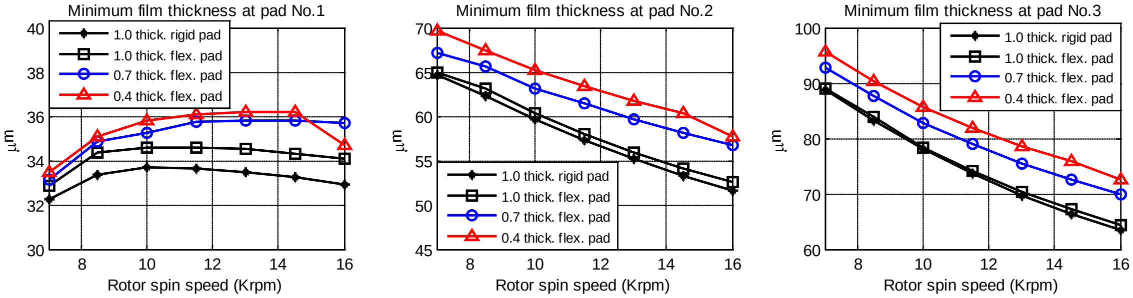

Fig. 48 Minimum film thickness with different pad thickness

Table 6 Parameter drop ratio caused by reduced pad thickness

(* averaged over the rotor spin speed)

	0.7thick (30% drop)	0.4thick (60% drop)
k_{xx}	6 %	10 %
k_{yy}	5 %	14 %
c_{xx}	9 %	30 %
c_{yy}	10 %	33 %
Average shaft temperature	2 %	7 %
Average lubricant temperature	2 %	7 %
Average pad temperature	2 %	7 %
Peak shaft temperature	3 %	9 %
Peak lubricant temperature	3 %	7 %
Peak pad temperature	3 %	6 %
Minimum film thickness at pad No. 1	3%	3%

6.5 Preload Change due to Thermal and Elastic Pad Deformation

In the previous section 6.4, three bearing models with different pad thickness were simulated. Bearing pad preload is one of the critical design factors for TPJB. Even though the TPJB is machined in accordance with the design parameters, the pad will produce preload change under the thermal and elastic loads. It is challenging to measure the two deformations separately in a test rig since they physically coexist. One of the strengths of this numerical approach is that the separate measurement of elastic and thermal deformations is available. The TPJB model introduced in this research is capable of both 3D thermal deformation under the thermal load, and elastic deformation under the fluidic and pivot loads. A schematic diagram for the evaluation of the preload change is shown in Fig. 49. The initial pad shape without the deformation is plotted in a dotted line, and the deformed shape under the thermal or external load is plotted in a bold line. After the elastic or thermal deformation, the initial bearing clearance (Cl_b) will be changed due to the pad deformation at the pivot location (see Fig. 49 (a)). In this research, the preload change is measured after the pad deformation at the pivot location is offset as seen in Fig. 49 (b).

The pad elastic deformation under the fluidic and pivot load is measured only by means of the modal displacement at the static equilibrium condition excluding rigid body modes equivalent to tilting and pivot translational motions. Thermal deformation of the pad is measured based on the film thickness change explained in section 3.5. For the evaluation of the Cl_b' arising from thermal or elastic deformation, shaft thermal expansion is not considered.

The pad is assumed to maintain a circular shape under the thermal or elastic deformation. So the preload change is measured by three points on $x - y$ plane. A', B_1' and B_2' are located on the deformed pad shape, and A, B_1 and B_2 are on the initial shape. If the deformed bearing clearance is offset so that the Cl_b' equals to Cl_b, A' and A coincide each other. The bearing pad preload without deformation can be defined by (102). According to the definition of the bearing pad preload, distance between A and O_P and the distance between O_P and B_n are coincident. B_1 is located under the *x* axis, and B_2 is located above the *x* axis as shown in Fig. 49. Based on the definition of the preload, the equation is derived as shown in (103). The only unknown is $x_{o_p'}$, and the solution of the equation (103) is (104). The preload induced by elastic or thermal deformation can be defined by (105) and (106).

Fig. 50 shows the decreased film thickness arising from the pad thermal deformation. They are measured at pad No. 1, 16 *Krpm* and different pad thickness. The thickest pad produced the biggest thermal expansion, and it is thought that the thicker pad produced more thermal expansion. Thermal expansion at the pivot location is bigger than at both circumferential ends of the pad, which means the pad is unfolded by the thermal deformation leading to an increased preload.

Fig. 51 shows the decreased film thickness due to the pad elastic deformation under the fluidic and pivot load. They are measured at the same conditions as in the Fig. 50 (b). The thinnest pad shows the biggest elastic deformation in the radial direction. The thinner pad may produce more elastic deflection due to the decreased pad structural stiffness. The deflection shape varies both in the axial and circumferential directions. As in the thermal deformation, pad is unfolded by the external load leading to the increased preload.

Fig. 52 shows the preload change rate at three different pad thickness models as shown in (107). 100% change rate means the doubled preload. Each axial position may produce different preload, and they are averaged over the axial position. In case of original pad model shown in Fig. 52 (a), pad No.1 shows the biggest change rate of the preload. Thermal load induced preload change rate dominates the total preload change. The biggest thermal load induced preload change rate of pad No.1 is arising from the higher viscous shearing caused by higher load on pad. Other pads show lower preload change rates due to the lower viscous shearing. At the pad No.1 of the thinnest pad model (40%), preload change rate due to the elastic deformation accounts for more than 70% of the whole preload change. With the decreased pad thickness, the preload change rate induced by the elastic deformation increases as shown in Fig. 52. The thermal load induced preload change rate stays constant regardless of pad thickness.

At a thick pad, preload change is mainly due to the thermal deformation. On the other hand, elastic deformation is the main source of the increased preload in a thin pad. Both thermal and elastic deformations made the pad unfold.

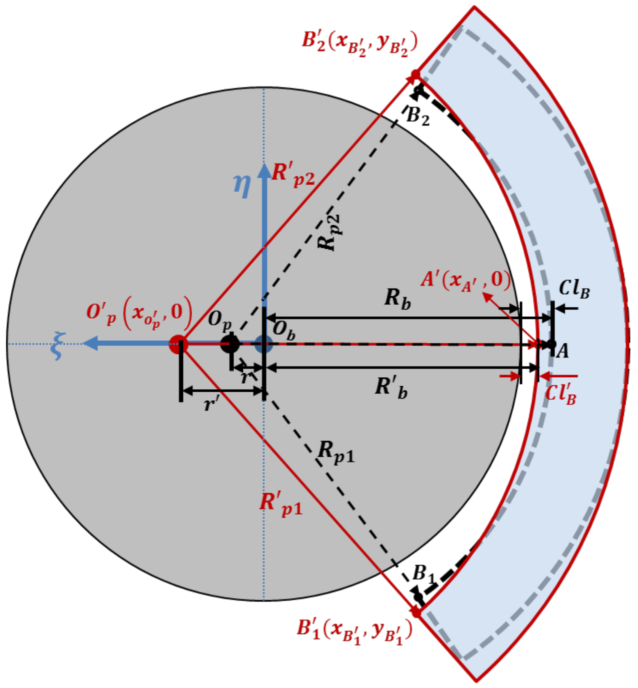

(a) Non-offset model

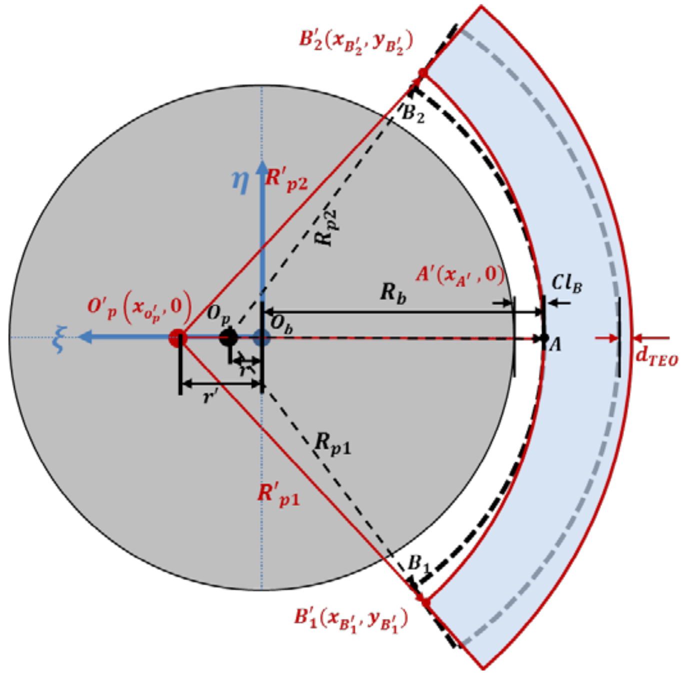

(b) Offset model

Fig. 49 Measurement of preload change

$$M_p = 1 - \frac{Cl_b}{Cl_p} = \frac{r}{r + Cl_b} \tag{102}$$

$$\left(x_{o'_p} - x_{B'_1}\right)^2 + {y_{B'_1}}^2 = \left(x_{o'_p} - x_{A'}\right)^2 \tag{103}$$

$$x_{o'_p} = \frac{{x_{A'}}^2 - {x_{B'_1}}^2 - {y_{B'_1}}^2}{2(x_{A'} - x_{B'_1})} \tag{104}$$

$$r' = Cl'_p - Cl'_b \tag{105}$$

$$M'_p = 1 - \frac{Cl'_b}{Cl'_p} = \frac{r'}{r' + Cl'_b} = \frac{x_{o'_p}}{x_{o'_p} + Cl'_b} \tag{106}$$

$$M'_p = \frac{M'_p - M_P}{M_P} \times 100\ (\%) \tag{107}$$

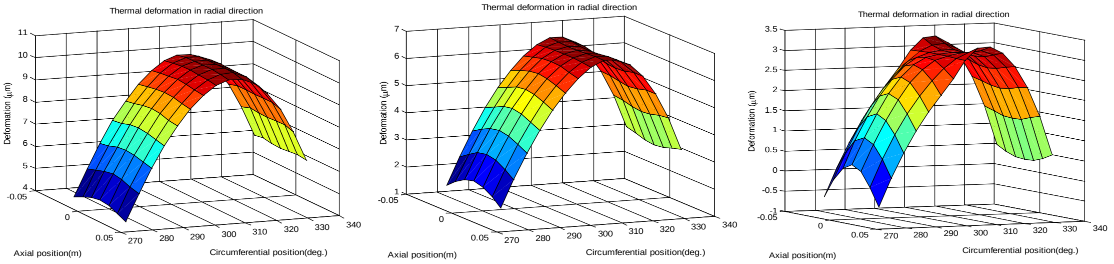

(a) 100% pad thickness (b) 70% pad thickness (c) 40% pad thickness

Fig. 50 Thermal deformation of pad No.1 at 16*Krpm*

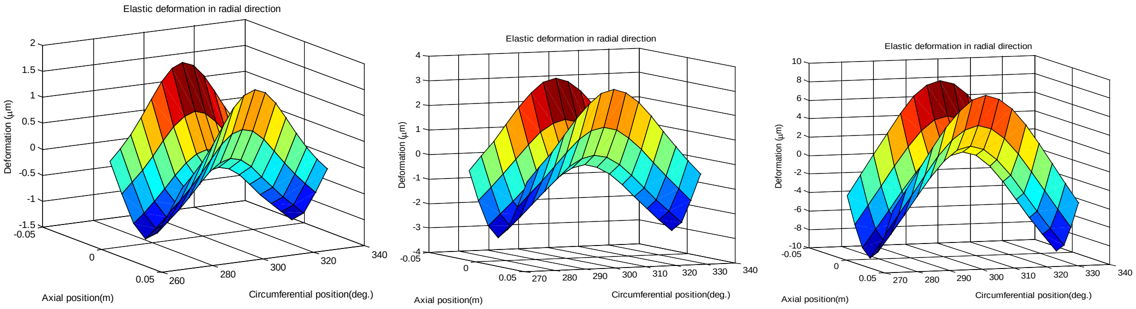

(a) 100% pad thickness (b) 70% pad thickness (c) 40% pad thickness

Fig. 51 Elastic deformation of pad No.1 at 16*Krpm*

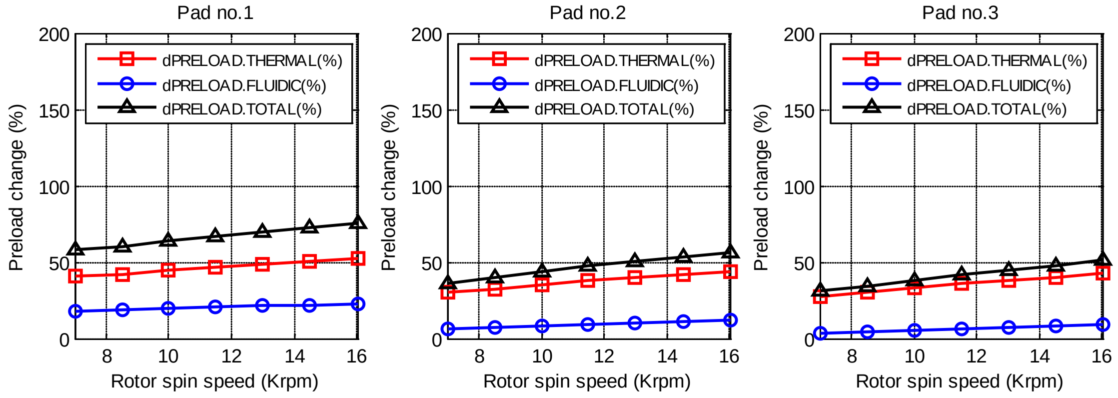

(a) 100% pad thickness

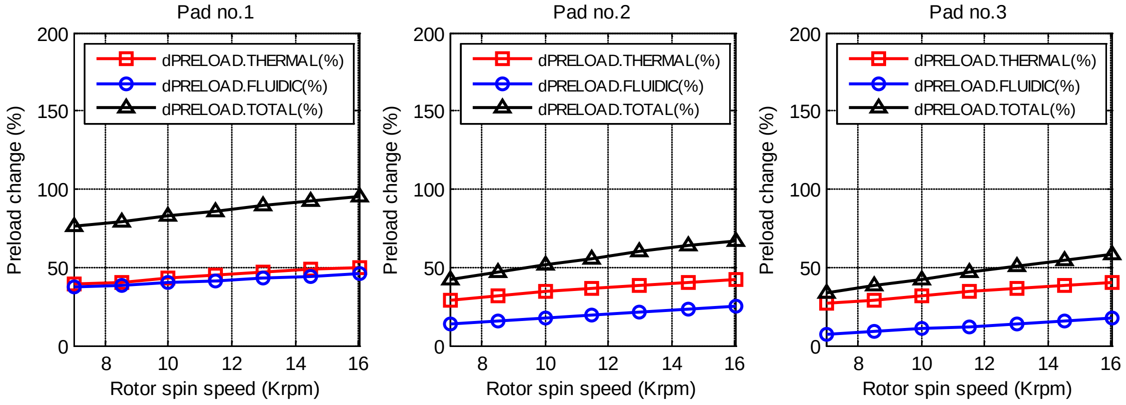

(b) 70% pad thickness

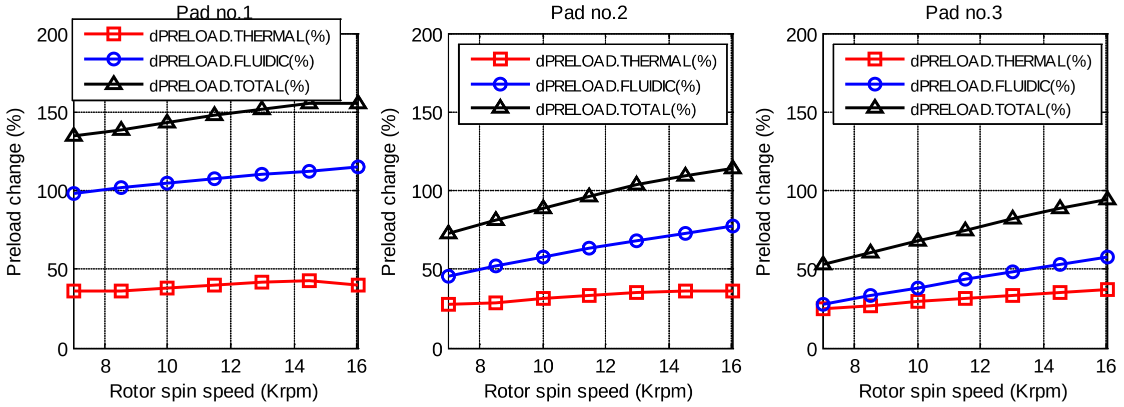

(c) 40% pad thickness

Fig. 52 Preload change due to the thermal and fluidic load

6.6 Pad Flexibility and Pivot Stiffness without Thermal Effect

This section examines the pad flexibility effect and pivot stiffness effect. Table 7 shows eight different simulation models in accordance with the thermal effects and flexibility effects. The input parameters are identical to Kulhanek's [42] research.

Fig. 53 shows dynamic coefficients of four different models. Varying viscosity Reynolds equation is solved, and heat conduction and thermal expansion of bearing pads and journal are taken into account. THD-R produces the highest stiffness and damping coefficients. With the consideration of pad flexibility (TEHD-R), both stiffness and damping coefficients decreased. If the pivot stiffness is considered (THD-F), drop rates of dynamic coefficients are much larger than that of flexible pad model (TEHD-R).

Table 8 shows the dynamic coefficient drop ratios with respect to the rigid pad and rigid pivot model. Both pad flexibility and pivot flexibility decreased dynamic coefficients. In case of the 'Flexible Pad-Rigid Pivot' model, drop ratio of damping coefficient is more than twice that of stiffness coefficient. In the case of the 'Rigid Pad-Flexible Pivot,' the whole drop ratio is much larger than 'Flexible Pad-Rigid Pivot.' The 'Flexible Pad- Flexible Pivot' produces the lowest dynamic coefficients. Pivot flexibility is thought to govern the decrease of the dynamic coefficients as seen in Table 8.

Table 7 Bearing models for comparison

Bearing model	Pad elasticity	Pivot Stiffness
Rigid Pad- Rigid Pivot (THD-R)	No	Rigid
Rigid Pad-Flexible Pivot (THD-F)	No	Flexible
Flexible Pad-Rigid Pivot (TEHD-R)	Yes	Rigid
Flexible Pad- Flexible Pivot (TEHD-F)	Yes	Flexible

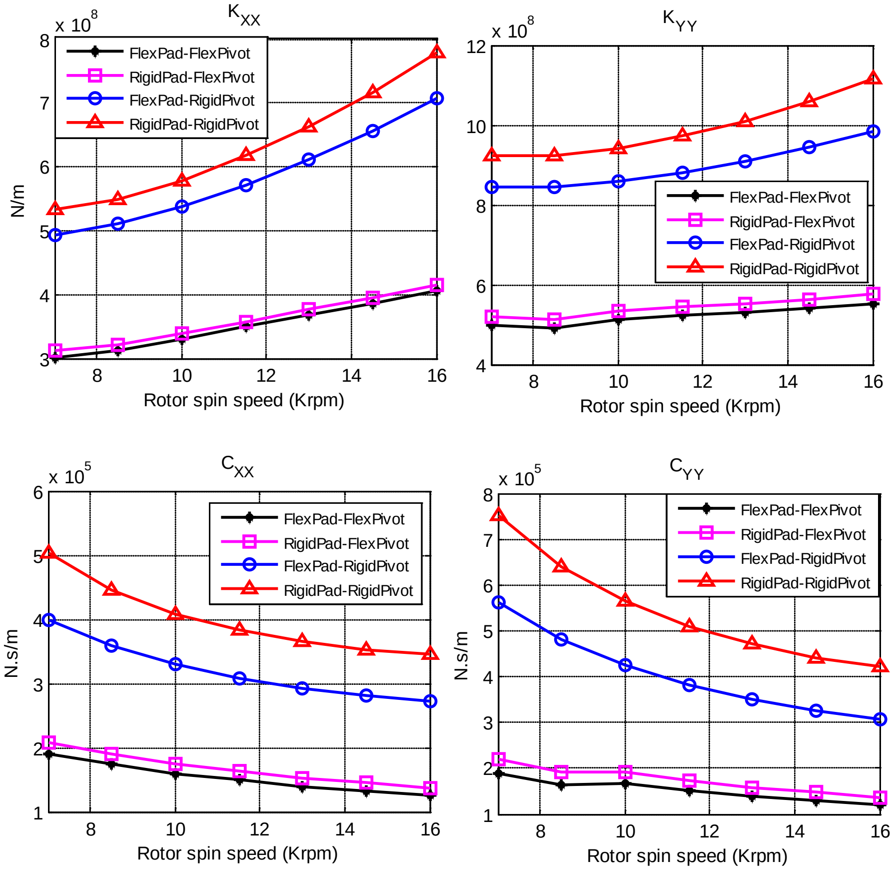

Fig. 53 Dynamic coefficient of thermal model

Table 8 Dynamic coefficient decrease ratio with respect to THD-R model (%)

	K_{xx}	K_{yy}	C_{xx}	C_{yy}
Flexible Pad-Rigid Pivot	-8%	-10%	-20%	-25%
Rigid Pad-Flexible Pivot	-43%	-45%	-58%	-68%
Flexible Pad- Flexible Pivot	-45%	-47%	-62%	-72%

7 SIMULATION FOR MORTON EFFECT*

Some of the Morton simulation results shown in this section came from published journals by Suh and Palazzolo [27, 28] and are updated for the dissertation.

7.1 Morton Effect Simulation Model

Morton effect predictions are presented for one rotor-bearing system presented by de Jongh and van der Hoeven's published literature [15], and the input parameters are provided by Balbahadur and Kirk's [9] research. Fig. 54 shows the rotor dynamic model (total mass:265 kg, total length: 1.195m), where the linear bearing is located at node number 4 (black colored), and the non-linear bearing is at 12 (red colored).

Lubricant properties and shaft geometries are shown in Table 9, and bearing configurations are depicted in Table 10. The linear bearing dynamic coefficients are assumed to be constant at $K_{xx} = K_{yy} = 1.70 \times 10^8\ (N/m)$, and $C_{xx} = C_{yy} = 1.00 \times 10^5 (Ns/m)$, and cross coupled terms are assumed to be zero as seen in Table 11.

Fig. 55 shows the thermal shaft and bearing model, where seven thermal boundary surfaces are defined by red arrows. All surfaces have convective boundary conditions with ambient temperature of 60°C as shown in Table 12 and Table 13. The total length of thermal shaft is seven times of bearing length as described in section 0. The non-driven end (NDE) bearing input parameter is given in Table 8. The thermal bow

---

* Reprinted with permission from "Three-Dimensional THD Morton Effect Analysis Part II: Parametric Studies," Journal of Tribology" by Suh, J., and Palazzolo, A., 2014. 136(3), 031706, Copyright 2014 by ASME.

model is considered only at the NDE bearing location. In de Jongh and van der Hoeven's [15] test bed, the film clearance was reduced to 84.21% of its initial value to reproduce the unstable rotor behavior at the site. In this research, the initial imbalance distribution is located on the right hand side of the NDE bearing, and three cases of nodal imbalance values are considered as shown in Table 4. The Morton effect problems in the test bed described in de Jongh and van der Hoeven's research [15] are as below:

a) Above 8000 rpm, the rotor started to show unstable behavior at any spin speed.

b) Within one or two minutes, it reached vibration trip level.

c) Cyclic oscillations in the phase of amplitude could be seen.

d) Hysteresis could be seen in the vibration amplitudes differential between run-up and coast-down.

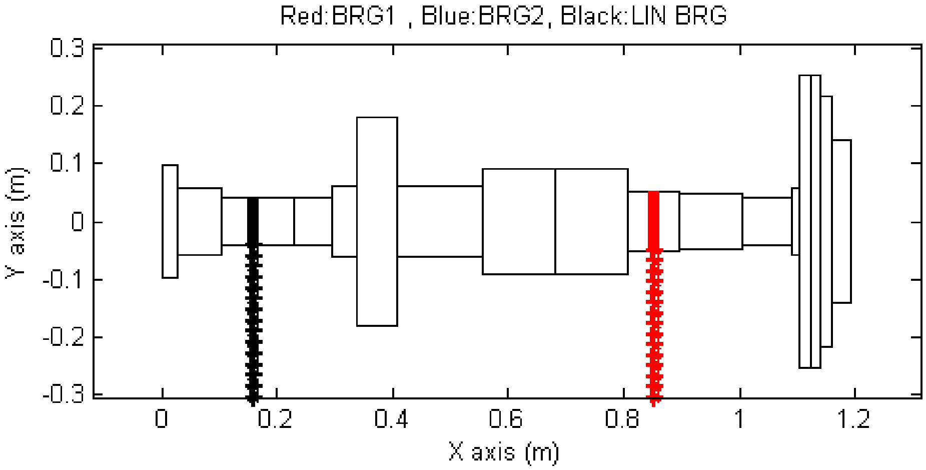

Fig. 54 Longitudinal section of rotor model

Table 9 Lubricant and shaft input parameters

Lubricant parameters	
Viscosity at 50℃ (Ns/m²)	0.0203
Viscosity coefficient(1/℃)	0.031
Supply temperature (℃)	50
Inlet pressure (Pa)	1.32E+05
Reference temperature (℃)	50
Mixing coefficient (β)	0.8
Density (kg/m³)	860
Heat capacity (J/kg℃)	2000
Heat conductivity (W/(mK))	0.13
Shaft/Rotor parameters	
Young's modulus (Pa)	2.10E+11
Density (kg/m³)	7850
Heat capacity (J/kg℃)	453.6
Heat conductivity (W/(mK))	50
Poison's ratio	0.3
Thermal expansion coefficients (1/℃)	1.30E-05
Reference temperature (℃)	25
Thermal shaft length (m)	0.3556

Table 10 Bearing pad input parameters

Bearing/Pad parameters	
Pad type	Load on pad
Number of pads	5
Pad arc length (degree)	56
Offset	0.5
Radius of shaft (m)	0.0508
Bearing clearance (m)	7.49E-05
Preload	0.5
Pad thickness (m)	0.0127
Bearing length (m)	0.0508
Young's modulus (Pa)	2.1E+11
Poison's ratio	0.3
Thermal expansion coefficients (1/℃)	1.30E-05
Density (kg/m³)	7850
Heat capacity (J/kg℃)	453.6
Heat conductivity (W/(mK))	50
Reference temperature (℃)	25

Table 11 Linear bearing location and dynamic coefficients

Linear bearing (node No: 4)	
Kxx, Kyy (N/m)	1.70E+08
Cxx, Cyy (Ns/m)	1.00E+05

Table 12 Shaft's thermal boundary condition

	Ambient temperature (℃)	Convection coefficient $W/(m^2K)$
①Left end	60	50
②Left side	60	50
③Right side	60	50
④Right end	60	50

Table 13 Pads' thermal boundary condition

	Ambient temperature (℃)	Convection coefficient W/(m²K)
⑤Bearing radial out	60	50
⑥Axial left end	60	50
⑦Axial right end	60	50

Table 14 Initial imbalance distribution

	Node No.	Imbalance $(kg \cdot m)$
Case 1	18	2.7×10^{-4}
Case 2	18	2.7×10^{-5}
Case 3	18	2.7×10^{-6}

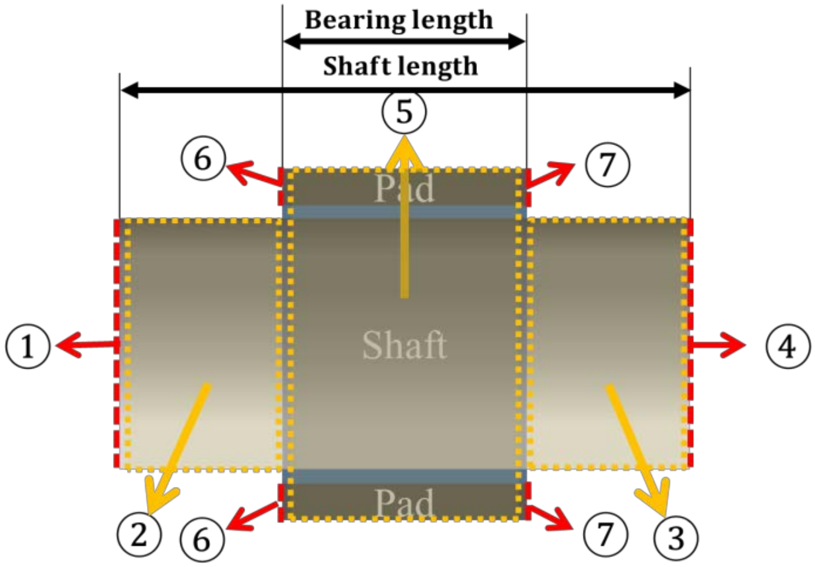

Fig. 55 Seven surface with prescribed convection or fixed temperature conditions

7.2 2D Energy Equation vs 3D Energy Equation

Gomiciaga and Keogh [6] adopted three-dimensional energy equation approach to predict the thermal gradient inside the synchronously orbiting shaft. Their research was limited to prescribed journal orbit without a dynamic model. Childs and Saha [16] and Lee and Palazzolo [13]'s studies considered 2D energy equation to predict the thermal bow induced rotor instability problem. In this section, both static equilibrium analysis with zero size orbit and transient Morton effect simulation with large size orbit will be performed using both 2D and 3D energy equations, and the results will be examined.

7.2.1 Static equilibrium analysis

The static equilibrium analysis of the rotor-bearing system with the input parameters shown in Table 1 and Table 2 was conducted using both 2D and 3D energy equations. Fig. 56 compares the dynamic coefficients, journal static condition and temperatures calculated both by the 2D and 3D energy equations over the spin speed ranging from 4500 rpm to 15500 rpm. Both heat conduction and thermal deformation are taken into account in the shaft and bearing model using the 3D F.E. model.

In the case of the dynamic coefficients, static eccentricity and average fluid film temperature, both 2D and 3D energy equations produce very similar results, and the differences are negligible as can be in Fig. 56 (a)~(f). The journal attitude angle differential between the 2D and 3D energy equations increases with the spin speed yielding 2° at 15500 rpm as seen in Fig. 56 (e). The peak and average lubricant temperatures are compared in Fig. 56 (c) and (f) that produce a linear trend between the rotor spin speed and temperature. The peak temperature differential is 5°C at the highest spin speed as seen in Fig. 56 (c). The root cause of the higher temperature of the 3D energy equation is thought to be the viscous shearing arising from the axial fluid flow considered only in the 3D energy equation. In practice, the 2D energy equation is solved more than 50 times faster than the 3D energy equation due to its smaller F.E. matrix size. Hence, the 2D energy equation is a good assumption and suitable for the static equilibrium analysis for its fast calculation ability.

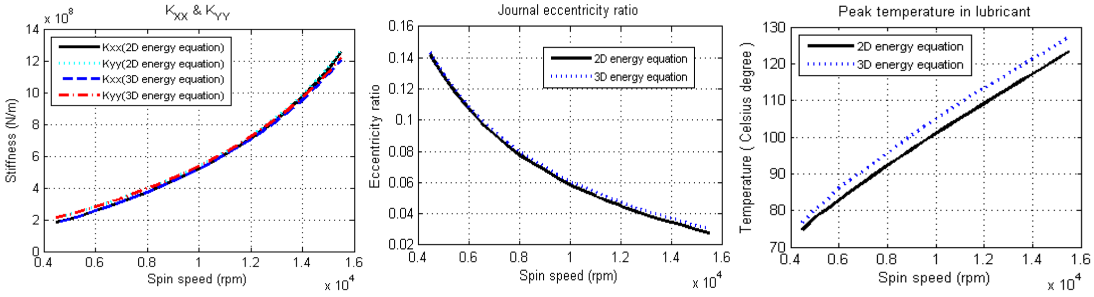

(a) K_{xx} and K_{yy}

(b) Static eccentricity

(c) Peak temperature in lubricant

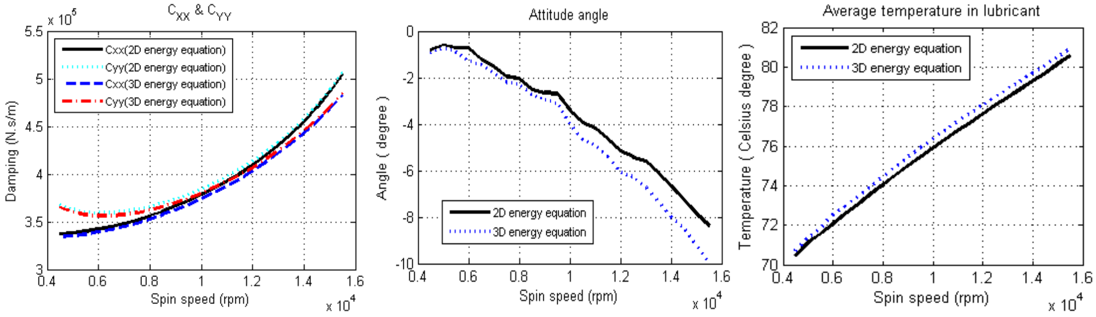

(d) C_{xx} and C_{yy}

(e) Attitude angle

(f) Average temperature in lubricant

Fig. 56 Steady state analysis of rotor-bearing system with 2D and 3D energy equations

7.2.2 Transient Morton effect analysis

In the previous section 7.2.1, the 2D energy equation was proved to be a good assumption for the static equilibrium analysis, when the orbit size is zero. This section examines the transient rotordynamic analysis with a large orbit size using both 2D and 3D energy equations, where the journal differential heating and the resultant thermal imbalance force are taken into account. The rotor-bearing input parameters are identical to those in the previous section. In the case of the initial imbalance, case 1 in Table 14 is selected to produce a orbit and a resultant higher viscous shearing. Rotor spin speed remains constant at 7200 rpm.

Journal temperature differential is described in Fig. 57 (a). The vibration amplitudes at the NDE bearing and that at the end of the overhung disk are shown in Fig. 57 (b) and (c) respectively. 2D energy equation model failed after t=1.1 (*minute*) due to rubbing problem as the minimum film thickness decays into zero as seen in Fig. 57 (h).

Fig. 57 (d)~(f) show the time scaled plot to compare two models easily. Thermal bow induced eccentricity at the end of the rotor is depicted in Fig. 57 (g). Fig. 58 shows the variation of journal surface temperature differential with the axial position at t=1.1 (*minute*) of 2D energy equation model and at t=20 (*minute*) of 3D energy equation model. L indicates the bearing length, and z is the axial position so $|z/L|$=0.5 on the x-axis indicates the both ends of the bearing. The journal temperature differential of the 2D energy equation shows ten times as big as the result of the 3D energy equation, and the vibration amplitude at the NDE bearing location of the 2D energy equation is 6.87 times higher than the 3D energy equation. It can be seen that the 2D energy equation over-predicts the temperature differential all over the thermal shaft length.

In section 3.5, seven times the bearing length was considered as the thermal shaft length, and the journal temperature differential at the end of the shaft decays to zero as can be seen in Fig. 59 and Fig. 60. The thermal shaft length should be long enough for the surface temperature differential to converge to zero at the both ends of the thermal shaft for the exact thermal bow calculation. If the temperature differential is not zero at the both ends, the length should be increased since the short thermal shaft length may produce under estimated thermal bending angle leading to under-estimated Morton effect simulation result.

The bigger thermal induced imbalance is found to be the root cause of the higher vibration amplitude in this section. This processes decrease the minimum film thickness, and finally causes bearing failure due to the rubbing problem as can be seen in Fig. 57 (h), where the temperature differential becomes divergent by approaching the bearing clearance.

It is evident that the 2D energy equation is neither reliable nor suitable for the Morton effect simulation with large orbit due to its (1) over-predicted vibration amplitude and (2) over-predicted journal surface temperature differential.

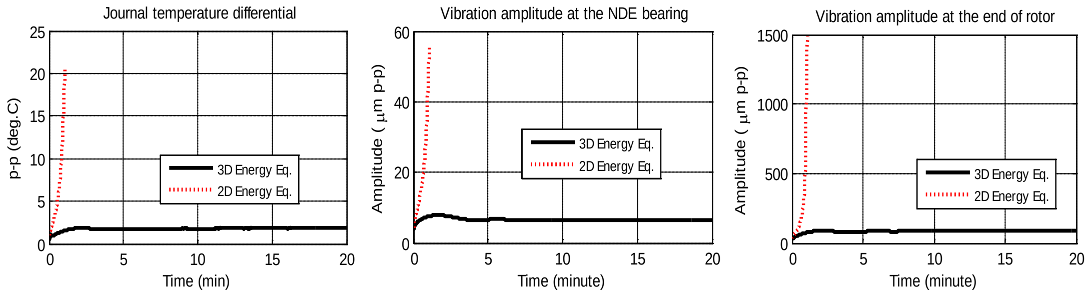

(a) Journal temperature differential

(b) Vibration amplitude at NDE bearing

(c) Vibration amplitude at the end of the rotor

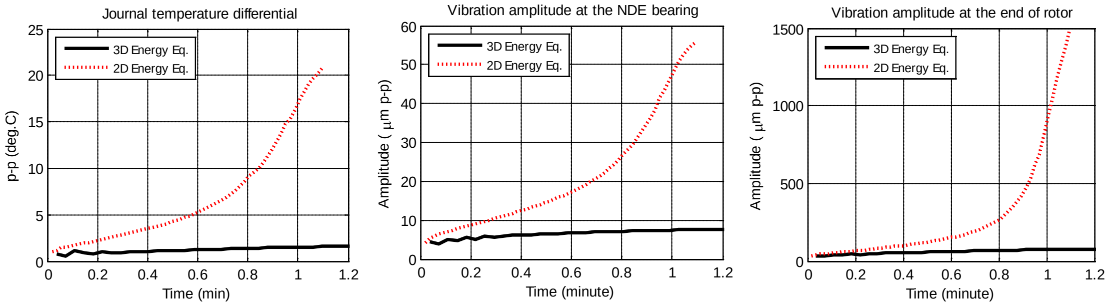

(d) Journal temperature differential (reduced time scale)

(e) Vibration amplitude at NDE bearing (reduced time scale)

(f) Vibration amplitude at the end of the rotor (reduced time scale)

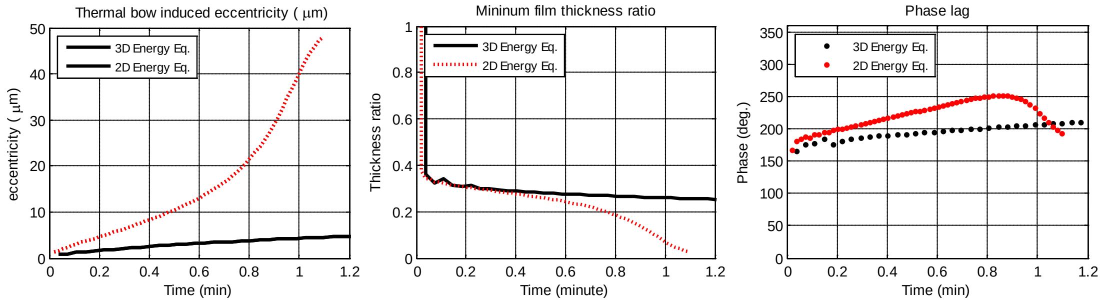

(g) Thermal bow induced eccentricity at the end of rotor (reduced time scale)

(h) Minimum film thickness ratio (reduced time scale)

(i) Lagging phase with respect to the imbalance (reduced time scale)

Fig. 57 Comparison of 2D and 3D energy equations for transient Morton effect analysis

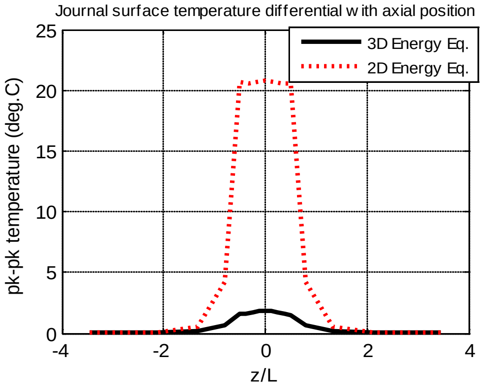

Fig. 58 Journal temperature differential with axial position

(2D Energy Eq. t=1.1min, 3D Energy Eq. t=20min)

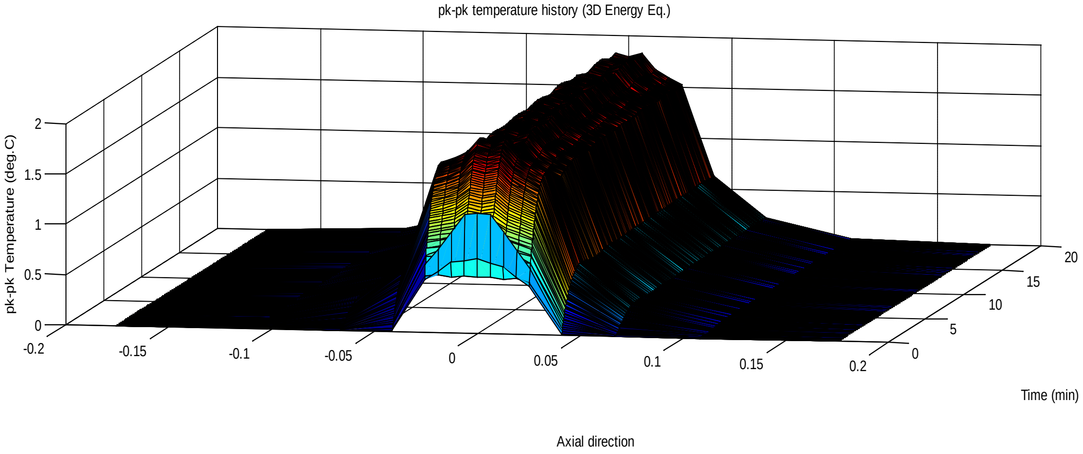

Fig. 59 Journal temperature differential with axial position and time

(3D energy equation)

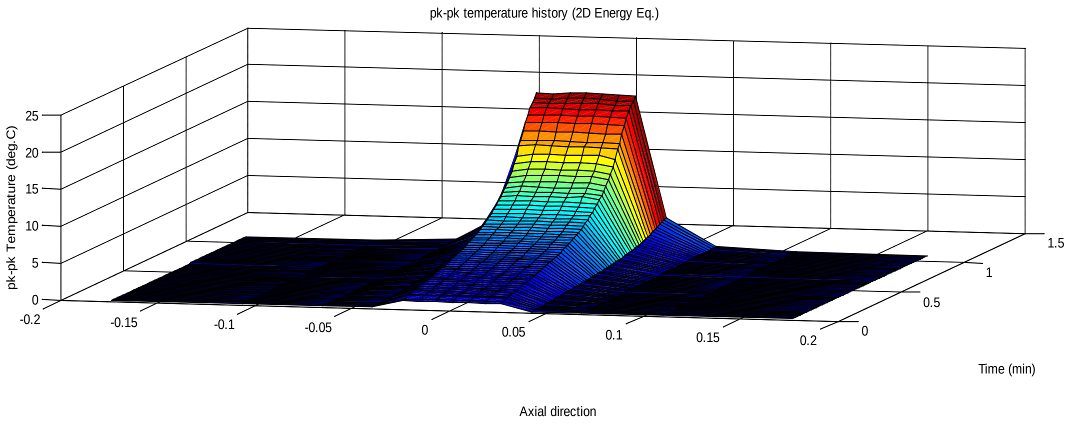

Fig. 60 Journal temperature differential with axial position and time

(2D energy equation)

7.3 Rotor Spin Speed

It is known that if the hot spot is gradually moving around the journal circumference, it gives rise to the spiral vibration [6]. Murphy and Lorenz [11] introduced a first order differential equation with time independent coefficients, where 'thermal velocity' is calculated for the evaluation of the transient movement of the hot spot around the spinning shaft surface. They assumed linear vector relationships between the high spot, hot spot and thermal bow phases.

In this research, the thermal bending amplitude and phase angle are calculated by the 3D F.E. shaft model, where the 3D thermal gradient is considered. In this section, the influence of the thermal imbalance vector on the Morton effect problem is examined. Input parameters are identical to the rotor-bearing model described in Table 9, Table 11, Table 12 and Table 13. The initial imbalance is case 1 in Table 14.

According to de Jongh and van der Hoeven's experiment [15], the Morton effect problems started to show the synchronous thermal instability problem at any spin speed above 8000 rpm. The transient Morton effect simulation is performed at two different rotor spin speeds, 7200 rpm and 8200 rpm. The vibration amplitudes at the NDE bearing and at the end of the overhung rotor are compared in Fig. 65 (a) and (b). Fig. 64 shows the frequency response of the rotor-bearing system shown in Fig. 54. The phase lag indicates the lagging phase with respect to the initial imbalance vector, and amplitude shows the vibration amplitude at the NDE bearing under the mechanical imbalance distribution of case 1 in Table 14. According to the bode plot shown in Fig. 64, 7200 rpm is closer to the third critical speed 7291rpm whose mode shape is shown in Fig. 62, and the linear analysis predicted 36% higher vibration level at 7500 rpm than 8500 rpm. However, the transient Morton effect analysis predicted that the vibration level at 7500 rpm is less than 15% of the amplitude of 8500 rpm at $t=10$ (*minutes*), which is identical to de Jongh and van der Hoeven's research [15]. The linear system analysis result shown in Fig. 64 could not predict the Morton effect problem.

Fig. 65 (e) describes the initial mechanical imbalance vector, time varying thermal imbalance vector and the vector sum of other two vectors at 7500 rpm. The thermal bow vector moves around the journal circumference counter clockwise, the rotor spinning direction, converging into $0.1 \times 10^{-3} m{\cdot}kg\angle 165°$. At the beginning, the phase differential between the initial imbalance and the thermal bow vector is 15° which is less than 90°. At $t=2$ (*minutes*), the phase differential between the two imbalance vectors converges into 165°, which means that the two vectors are in the opposite direction, leading to the decrease of the imbalance vector sum amplitude. The vibration amplitude with the thermal bending is found to be lower than the amplitude without the Morton effect as seen in Fig. 65 (e). In this case, the vibration amplitude is decreased by the Morton effect.

As the spin speed is increased to 8500 rpm, the thermal vector moves around the journal circumference counter clockwise in the rotor spin direction. Both the amplitude and the phase of the thermal bow vector increase with time without convergence. Even if the phase differential between the thermal bow and initial imbalance vectors is 180° at $t=4.5$ (*minutes*), the vibration amplitude is larger than that of 7500 rpm since the amplitude of the thermal induced imbalance is at least 3 times higher than the amplitude of the initial imbalance vector. The shape of the nodal vibration amplitude at the end of the rotor at 8500 rpm is similar to the journal temperature differential as seen in Fig. 65 (b) and (c), which means that the dynamic behavior of the rotor-bearing system experiencing Morton effect is governed by the journal temperature differential and the corresponding thermal bow vector. The dynamic behavior is found to be governed by the thermal bow vector as can be seen in Fig. 65 (d). The 1X filtered polar plot produces a spiral vibration with the circular shape known as a unique characteristic of the Morton effect problem, whereas the long oval shape can be observed in the journal-bearing rubbing problem. [44] According to the bode plot, the p-p vibration amplitude at the bearing location is 4.05μm at 7200 rpm, and 4.36μm at 8200 rpm.

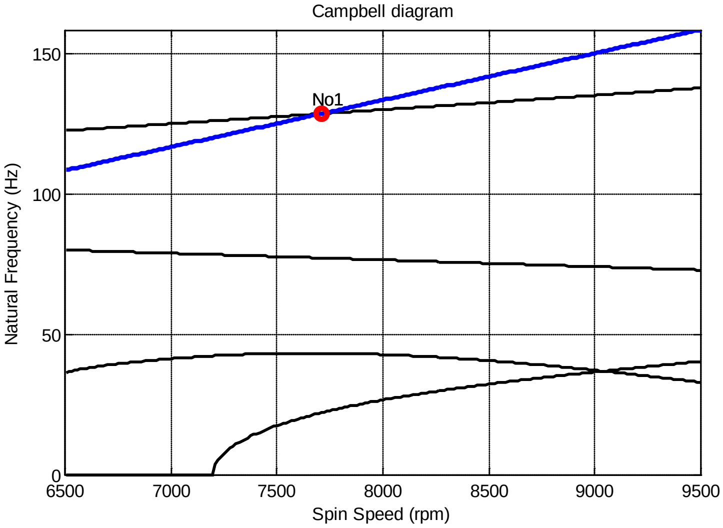

Fig. 61 Campbell diagram

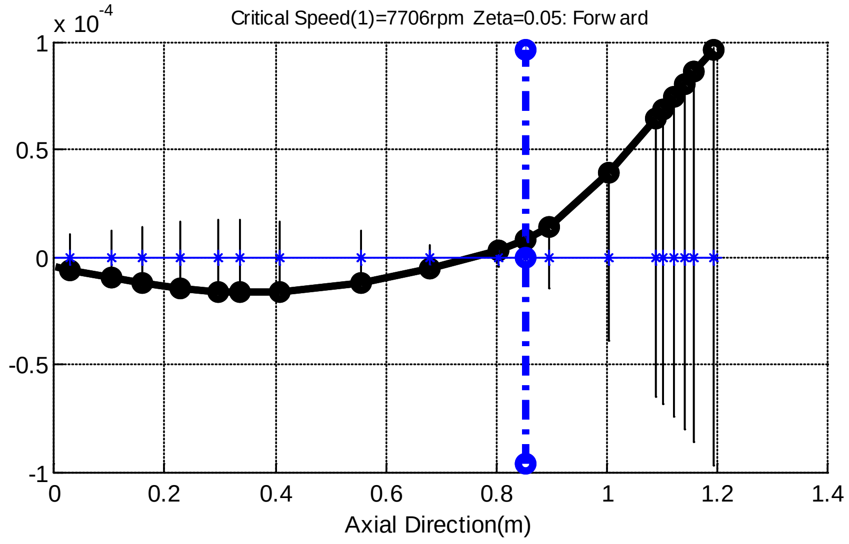

Fig. 62 Mode shape at 7706 rpm (zeta = 0.05)

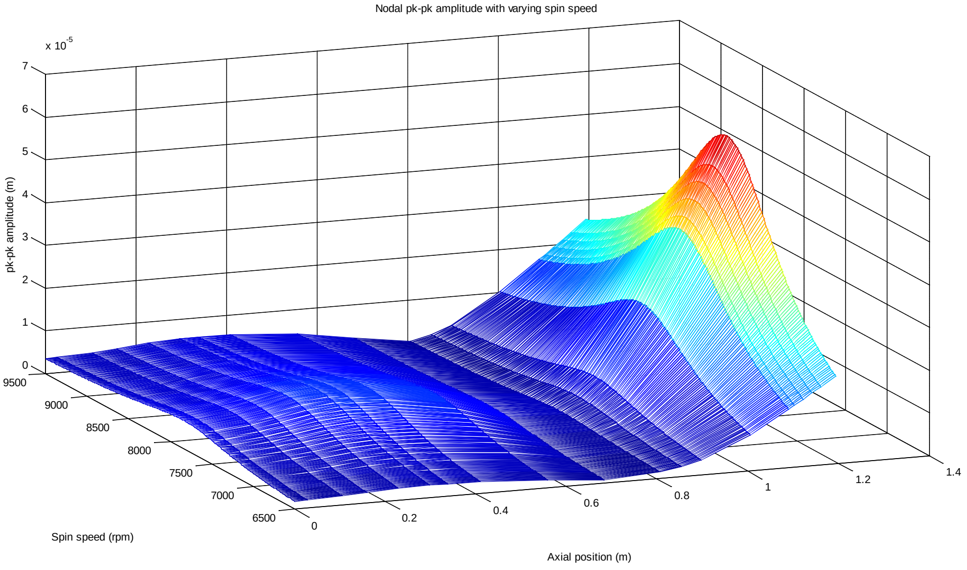

Fig. 63 Nodal amplitude of rotor under the given imbalance force

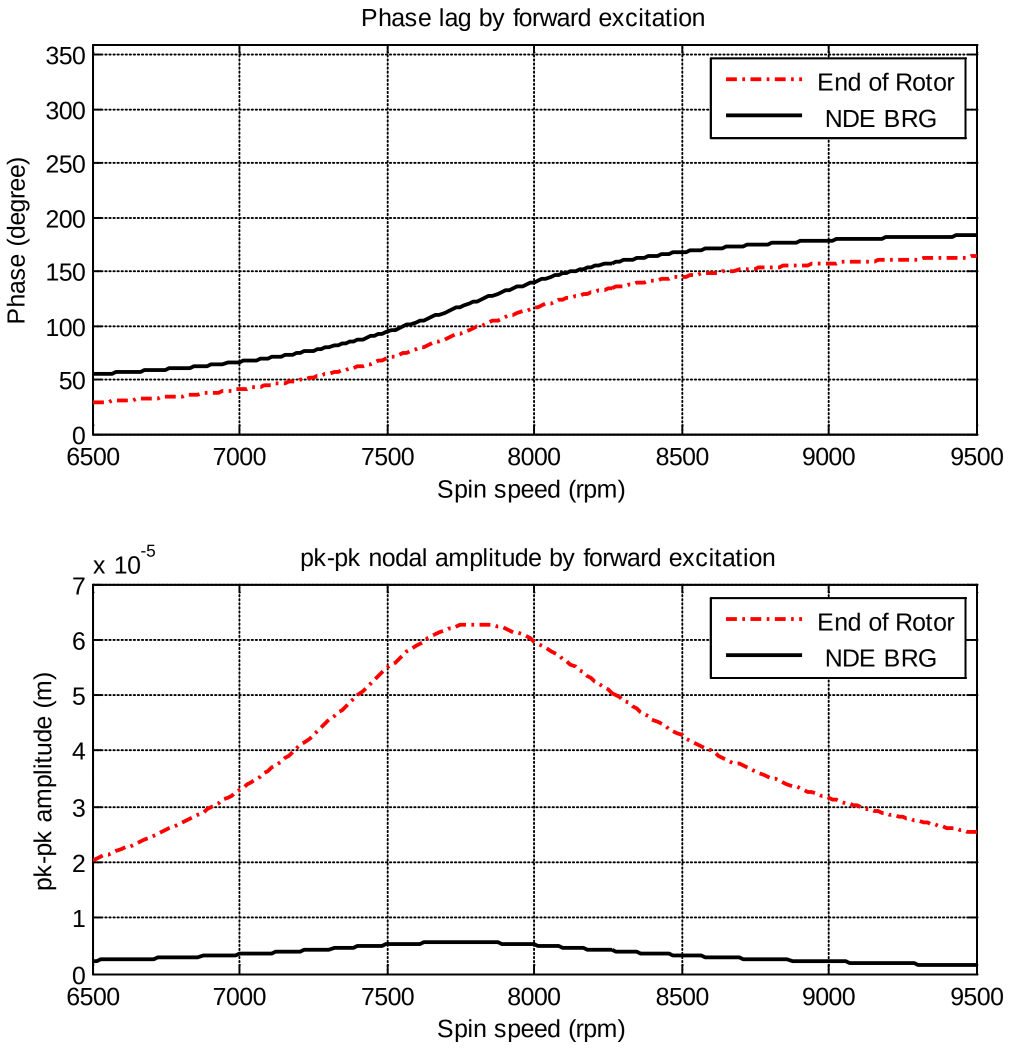

Fig. 64 Bode plot

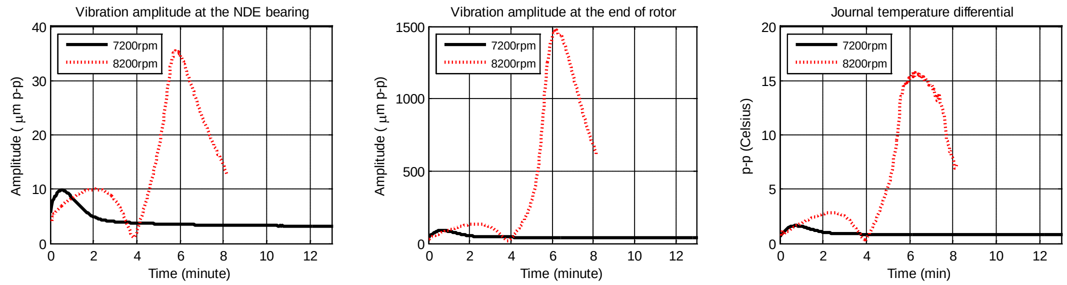

(a) Vibration amplitude at the NDE bearing

(b) Vibration amplitude at the end of the rotor

(c) Journal surface temperature differential

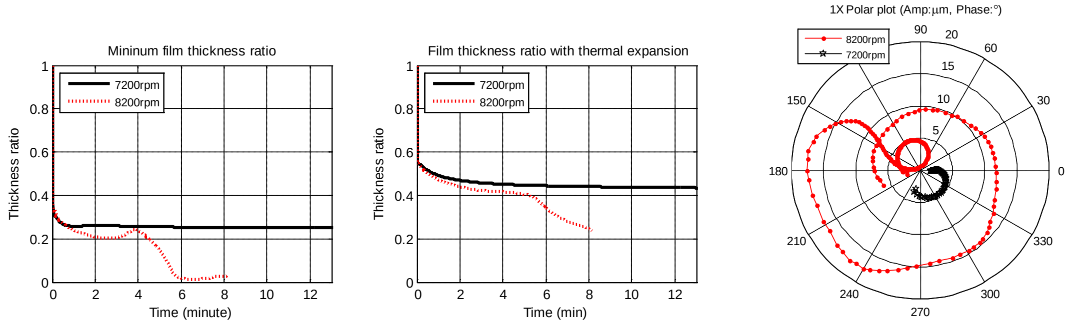

(d) Minimum film thickness ratio

(e) Thermally reduced minimum film thickness ratio

(f) 1X filtered polar plot (Amplitude:μm,Phase:deg.)

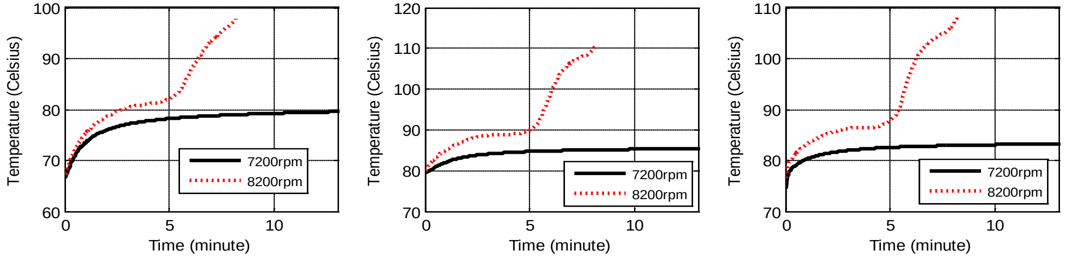

(g) Average temperature of shaft

(h) Average temperature of bearing pad

(i) Average temperature of lubricant

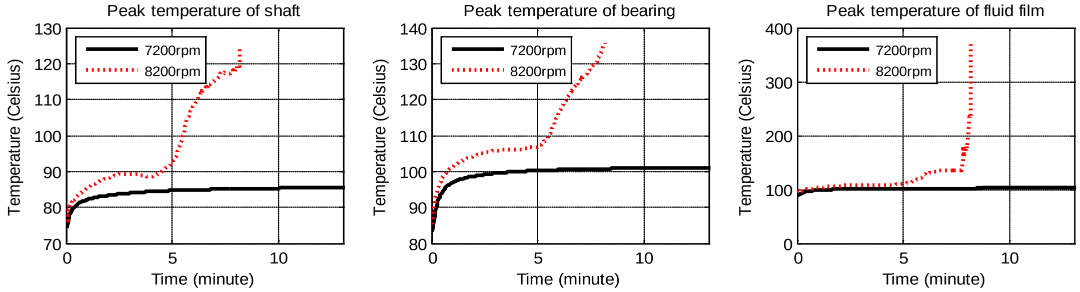

(j) Peak temperature of shaft

(k) Peak temperature of bearing pad

(l) Peak temperature of lubricant

Fig. 65 Transient Morton effect simulation result (7200 rpm VS 8200 rpm)

7.4 Phase Relationship

Fig. 66 shows a schematic diagram explaining the phase relationship. Related literature assumed that the phase of the cold spot ($\emptyset_{COLD}$) coincides with the thermal bow phase ($\emptyset_{THERM.BOW}$), which means the phase differential between the cold spot ($\emptyset_{COLD}$) and the hot spot ($\emptyset_{HOT}$) remains constant at 180°. In addition, the phase differential between the high spot ($\emptyset_{HIGH}$) and the hot spot ($\emptyset_{HOT}$) has been assumed to remain constant during the journal orbiting.

De Jongh and Morton's experiment [14] observed that the hot spot lags the high spot by 20°. Larsson's research [7, 8] assumed that the hot spot ($\emptyset_{HOT}$) coincides with the high spot ($\emptyset_{HIGH}$), and the cold spot ($\emptyset_{COLD}$) will be formed on the shaft surface experiencing maximum film thickness ($\emptyset_{HIGH} + 180°$). In other words, the phase differential between hot spot ($\emptyset_{HOT}$) and cold spot ($\emptyset_{COLD}$) remains constant at 180°, and the thermal bow phase ($\emptyset_{THERM.BOW}$) and the cold spot ($\emptyset_{COLD}$) coincide with each other. Gomiciaga and Keogh's simulation [6] showed that there exists a phase lag between the high spot ($\emptyset_{HIGH}$) and hot spot ($\emptyset_{HOT}$) ranging from 0° to 60°.

In this section, the phase relationship was examined by comparing two simulation cases, whose rotor spin speeds are constant at 7200rpm and 8200 rpm. The rotor-bearing system is identical to the earlier-described model shown in Table 1~3, and the initial imbalance is case 1 shown in Table 4. The simulation results of 7200 rpm model are described in Fig. 67, where the system is supposed to be stable, and Fig. 68 shows the 8200 rpm model which is supposed to be unstable with oscillation of journal temperature differential.

When the rotor spin speed is 7200 rpm, the temperature differential reaches the steady state after $t=3$ ($minutes$) as shown in Fig. 67. The phase differential between the high spot ($\emptyset_{HIGH}$) leads the hot spot ($\emptyset_{HOT}$) by 52° as shown in the second plot of Fig. 67. The 3rd plot shows thermal bow phase ($\emptyset_{THERM.BOW}$) and cold spot phase ($\emptyset_{COLD}$), and they show almost the same value. The fourth plot shows the phase differential between the hot spot ($\emptyset_{HOT}$) and the thermal bow ($\emptyset_{THERM.BOW}$), which is around 190°. This is similar to the assumption of the earlier method that employed a linear approach. The last plot, shows the phase differential between the hot spot ($\emptyset_{HOT}$) and the cold spot ($\emptyset_{COLD}$), and it stays constant at around 190°.

When the rotor spin speed is increased to 8200 rpm, the temperature differential oscillates without convergence over the period of $t=4$ ($minutes$) as seen in Fig. 68. After the journal temperature differential becomes over 10 ℃, the phase differential between the hot spot ($\emptyset_{HOT}$) and the high spot ($\emptyset_{HIGH}$) stays constant at almost 15°. The phase differential between hot spot ($\emptyset_{HOT}$) and cold spot ($\emptyset_{COLD}$) shown in the last plot of Fig. 68 becomes over 200° after the journal temperature differential reach 10 ℃. The fourth plot draws the phase differential between hot spot ($\emptyset_{HOT}$) and thermal bow ($\emptyset_{THERM.BOW}$), which is oscillating between 190° and 250°. This has been assumed to be constant at 180° in earlier approaches. The time varying phase differential between hot spot ($\emptyset_{\mathrm{HOT}}$) and thermal bow ($\emptyset_{\mathrm{THERM.BOW}}$) can make a significant difference from the earlier studies, since the phase of the thermal bow ($\emptyset_{\mathrm{THERM.BOW}}$) induced imbalance vector is the main source of the synchronous thermal instability problem. Incorrect prediction of the thermal bow phase ($\emptyset_{THERM.BOW}$) may lead to an inaccurate Morton effect simulation result. In this section, the amount of the thermal induced imbalance and the phase were evaluated based on 3D F.E. heat conduction and thermal expansion model. It is evident that the 3D F.E. model for the thermal bending evaluation gives more sophisticated and accurate prediction than the analytical method of earlier studies.

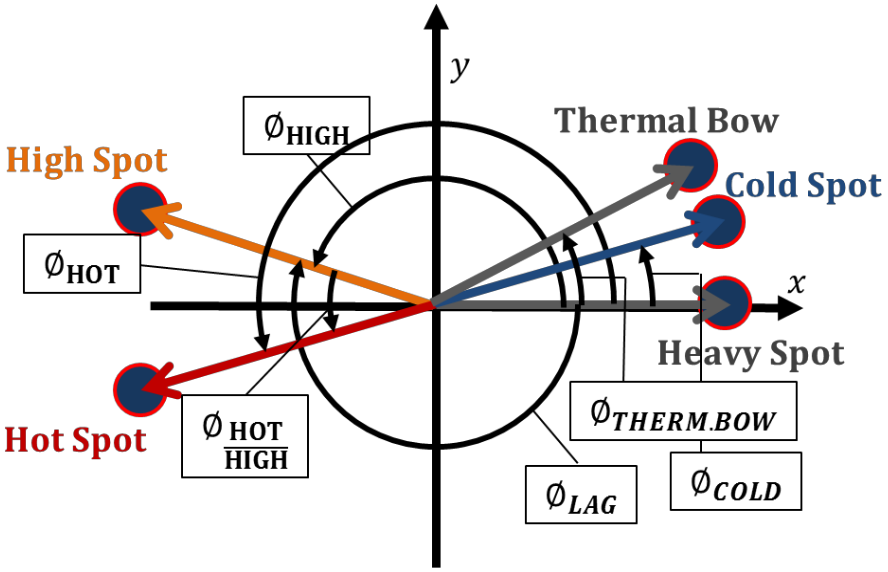

Fig. 66 Phase relationship

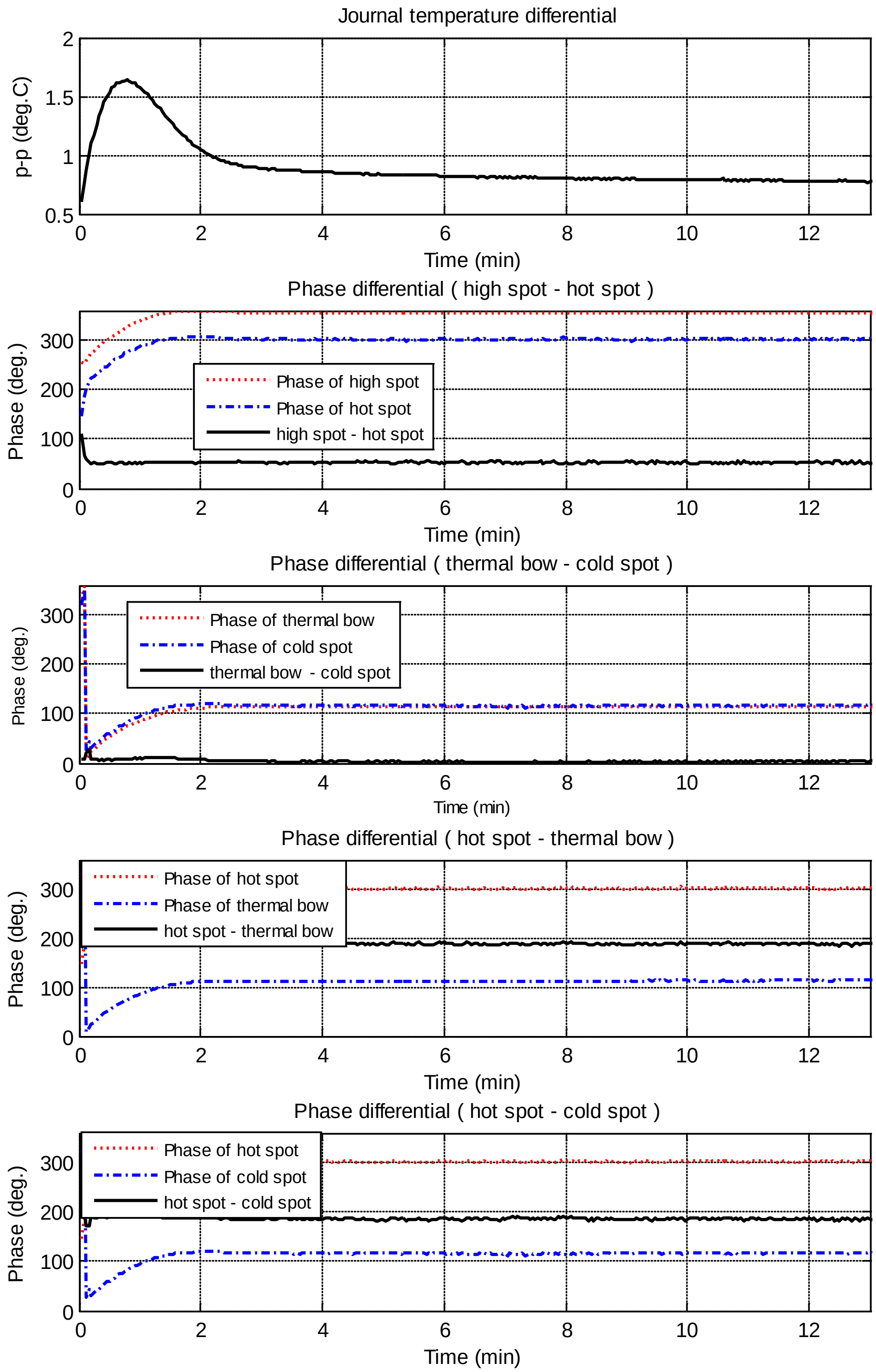

Fig. 67 Temperature differential and phase information (Case1: 7200 rpm)

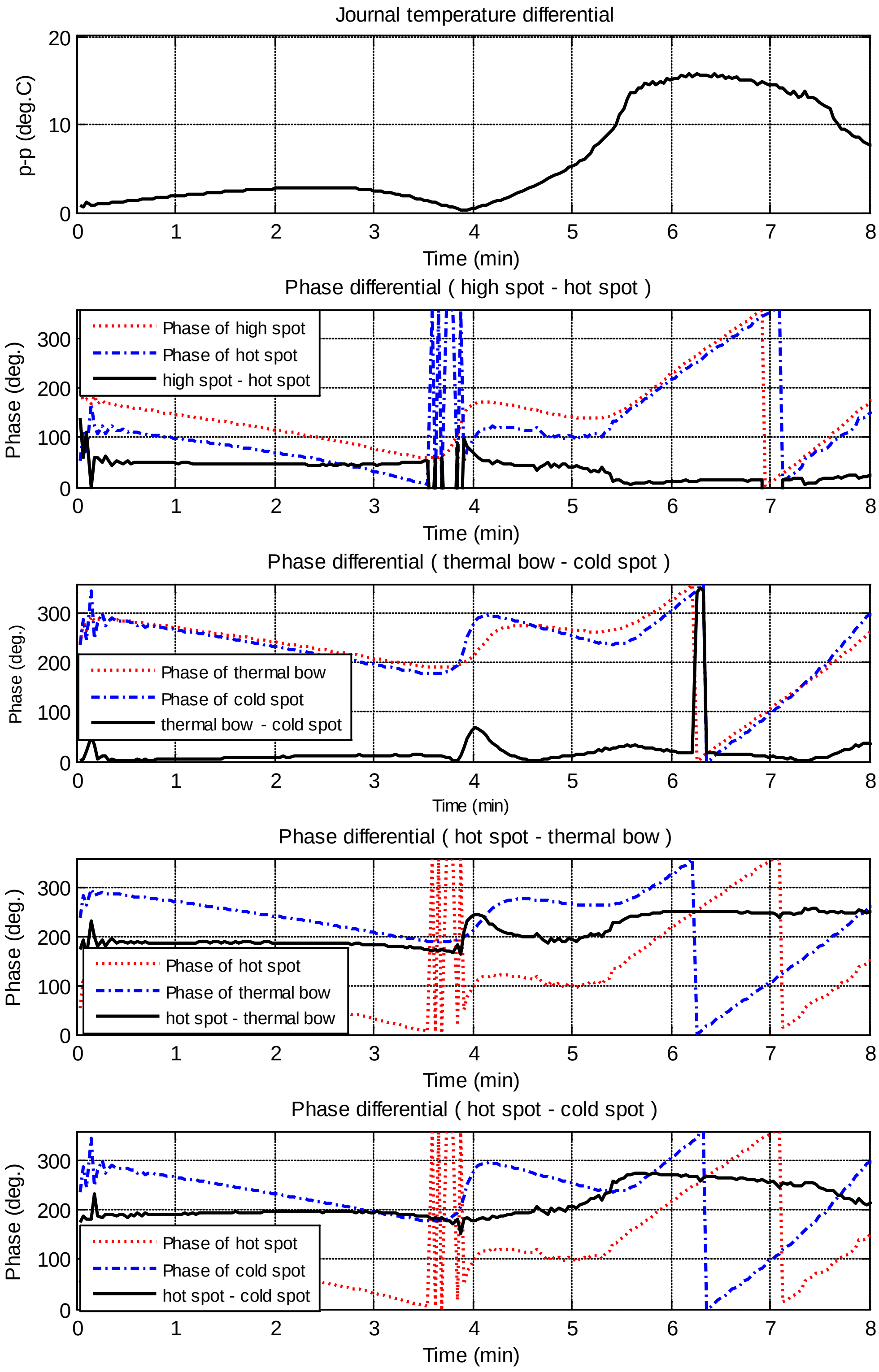

Fig. 68 Temperature differential and phase information (Case 2: 8200 rpm)

7.5 Thermal Bow Effect

7.5.1 Nonlinear transient analysis

The asymmetric temperature across the journal diameter caused the rotor to bow at the NDE bearing location, inducing an imbalance of overhung mass, changing the vibration amplitude and phase of synchronous vibrations, and the journal's asymmetric temperature. In this section, the thermal bow induced synchronous whirl phenomenon is studied by comparing non-thermal bow and thermal bow models at 8200 rpm constant spin speed. The rotor-bearing system and the thermal boundary conditions are identical to the earlier-described rotor-bearing model shown in section 7.1, and the initial imbalance distribution is case 1. The rotor-bearing configuration of the non-thermal bow model is identical to the thermal bow model except for the thermal bow induced imbalance distribution, in other words the only imbalance force acting on the non-thermal bow model is the initial mechanical imbalance.

Fig. 69 (a) shows the journal surface temperature differential at the bearing center in the axial direction. The journal temperature differential of the thermal bow model oscillates and increases after t=4(*minute*). The bearing shows rubbing failure at t=8(*minute*) as the minimum film clearance decays to zero as shown in Fig. 69 (e). However, the temperature differential of the non-thermal bow model does not oscillate but converges to 1.2°*C* of *p-p* temperature. Fig. 69 (b) shows the vibration amplitude at the NDE bearing. The vibration level in common with the *p-p* temperature oscillates over the period of 4 minutes. On the other hand, the non-thermal bow model does not show any oscillation or an increase of vibration level. In Fig. 69 (d), the thermal bow model shows moving phase lag relative to the initial imbalance vector, while the non-thermal bow model shows steady converging phase lag. Fig. 69 (f) shows the 1X filtered polar plot where the vibration amplitude and lagging phase are drawn. It is evident that the thermal bow effect makes a significant change in the rotordynamic behavior.

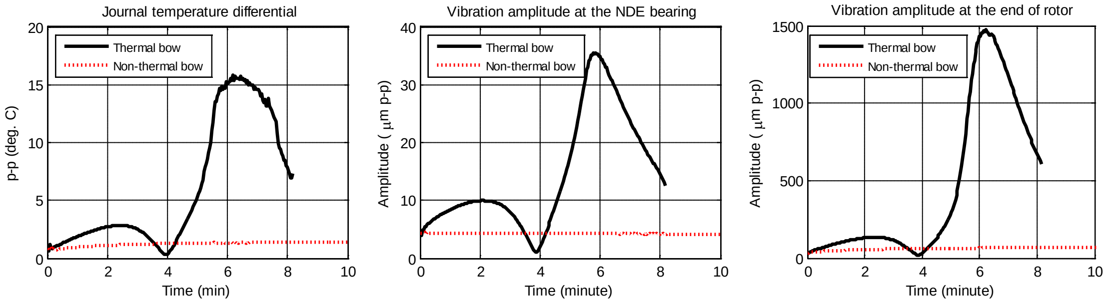

(a) Journal surface temperature differential

(b) Vibration amplitude at the NDE bearing

(c) Phase lag relative to imbalance force vector

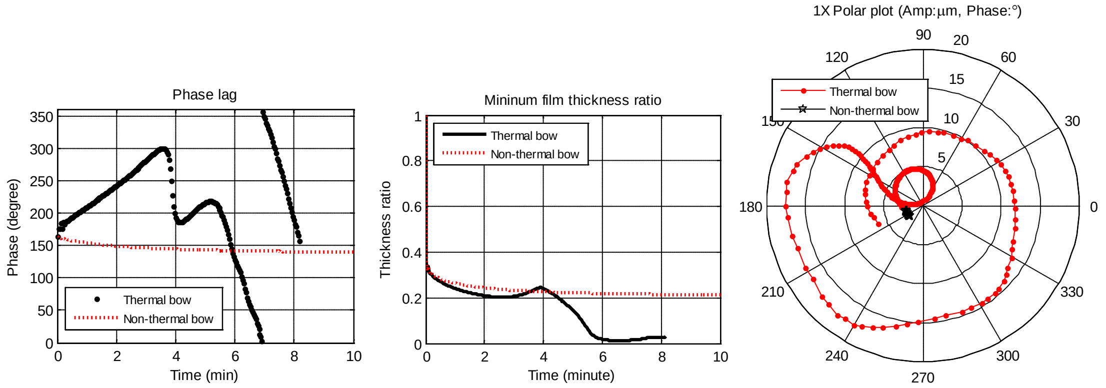

(d) Phase lag relative to imbalance force vector

(e) Minimum film thickness ratio

(f) 1X filtered polar plot

Fig. 69 Thermal bow VS non-thermal bow model

7.5.2 Synchronous response amplitude

Another useful approach for the evaluation of the thermal bow induced rotordynamic instability problem is steady Morton analysis. The algorithm for this method is introduced in section 5.3. The steady Morton analysis is performed from 6500 *rpm* to 8500 *rpm*. Fig. 70 (a) and (b) show the vibration amplitude at the NDE bearing location and at the right end of the rotor respectively. As explained in section 5.3, if the minimum film thickness reaches 7% of the initial bearing clearance, the algorithm stops and move to next rotor spin speed to prevent the program error caused by rubbing problem. Black square dots depict the non-thermal bow model and red circles are the thermal bow model. Over 7700rpm, thermal bow produces evident increased vibration amplitude. Fig. 70 (c) shows the journal temperature differential and (d) is the minimum film thickness journal experiences each orbiting. The Morton problem happens abruptly from 7800 rpm as shown in Fig. 70. Between 6500 rpm and 7500 rpm the vibration amplitude and journal temperature differential agrees very well between non-thermal bow model and thermal bow model.

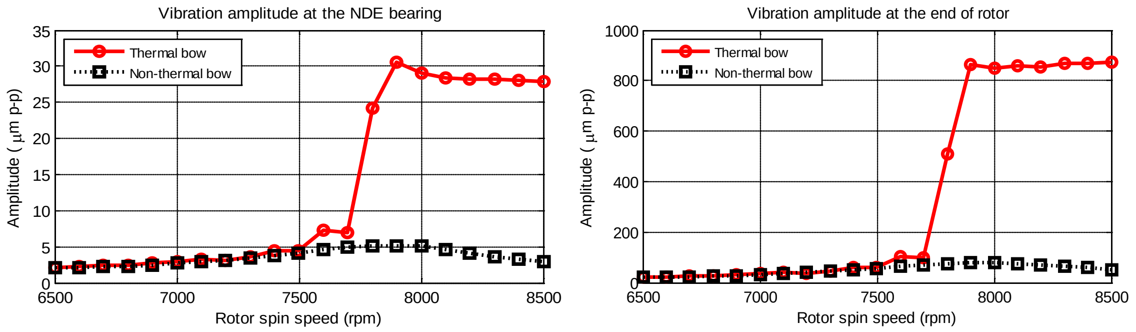

(a) Vibration amplitude at the NDE bearing

(b) Vibration amplitude at the end of rotor

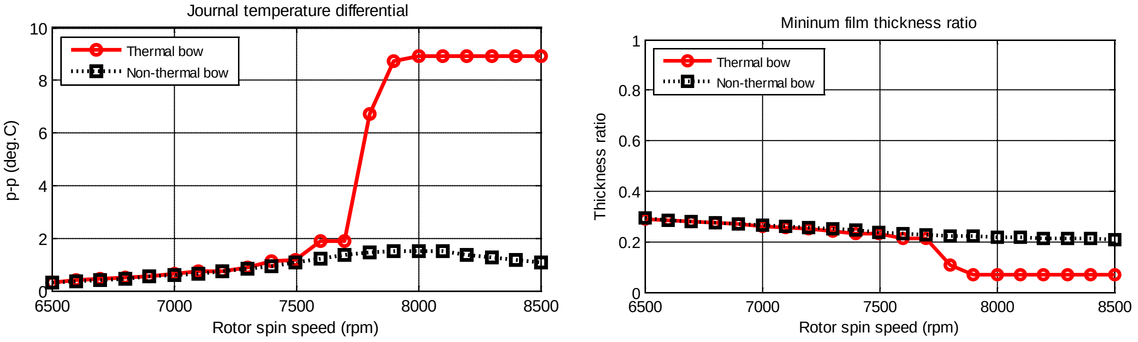

(c) Journal temperature differential

(d) Minimum film thickness ratio

Fig. 70 Comparison of thermal bow and non-thermal bow models

7.6 Hysteresis Vibration Amplitude Curve with Varying Spin Speed

De Jongh and Morton[14] and De Jongh and van der Hoeven[15]'s literatures showed the hysteresis vibration with time varying spin speed by experimental studies. The hysteresis vibration amplitude is one of the easily recognized phenomena of the Morton effect problem. In this section, the hysteresis phenomenon is simulated with time varying spin speed as shown in Fig. 71 (a), where both non-thermal bow and thermal bow models are described together. At first, rotor spin speed is gradually increasing from 6700 *rpm* to 7100 *rpm* with a growth rate of 400 (*rpm/min*) as can be seen in Table 15 and Fig. 71 (a). At 7100 *rpm*, the vibration level with and without thermal bow are around 60 μm.

After the rotor spin speed reaches 8000 *rpm* with the growth rate of 2700 *rpm/min,* it is gradually increasing up to 8200 *rpm* for 90*sec*. The vibration amplitude is increased up to 1300 μm which is 2100% higher than at 7100 *rpm*. Without thermal bow, the increase rate is just 177%.

From 170 (*sec*), the rotor spin speed is decreasing to 7300*rpm* with the rate of 2700 *rpm/min,* which is the same as the increasing rate from 60*sec* to 80*sec* as seen in Table 15 and Fig. 71 (a).

Fig. 71 (c) shows the lagging phase with respect to the imbalance force vector at the NDE bearing location. In case of the non-thermal bow model, lagging phase shape changes with the similar shape to the rotor spin speed, while the thermal bow model does show strange shape.

Fig. 72 shows a bode-plot, where the hysteresis vibration amplitude with the time varying spin speed can be observed. Non-thermal bow model shows very weak hysteresis vibration amplitude and lagging phase. This is due to the growing temperature as shown in Fig. 71 (d). The thermal bow model produces an evident hysteresis vibration amplitude and phase angle.

Fig. 73 describes the thermal bow vector vs. initial imbalance vector. Since the hot spot tends to move around the journal surface counter clockwise which is same as the shaft spinning direction, the thermal induced imbalance vector cannot go back the way it came when the spin speed is reduced. The residual thermal bow and the moving thermal bow are the main causes of the hysteresis vibration. Fig. 74 shows the 1X filtered polar plot. As in the thermal bow vector, it moves counter clockwise which is same as the shaft spinning direction and does not go back the way it came when the spin speed is reduced.

Table 15 Time varying rotor spin speed

Time (sec)	RPM (rev/min)
0	6700
60	7100
80	8000
170	8200
200	7300
240	7250

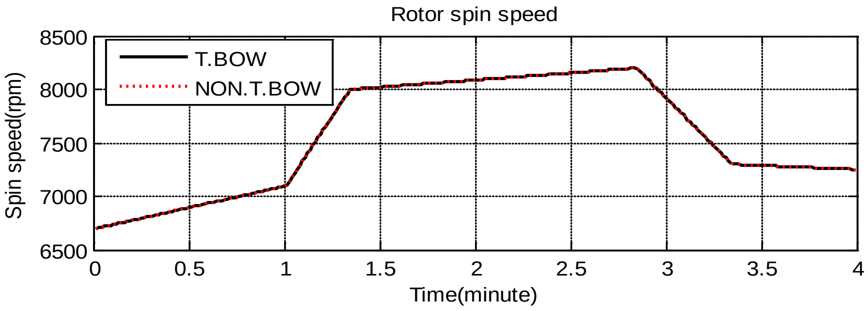

(a) Rotor spin speed

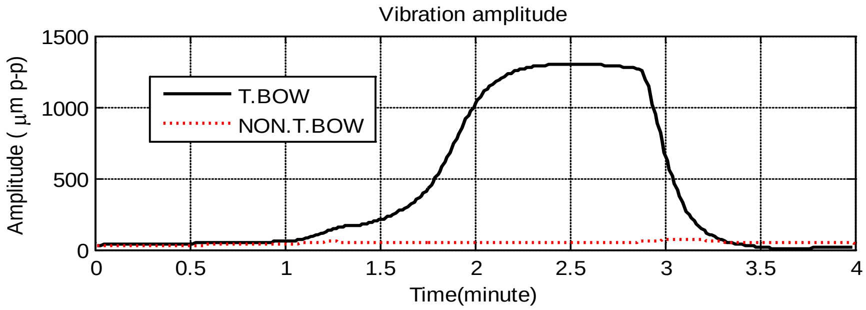

(b) Vibration amplitude at the end of rotor

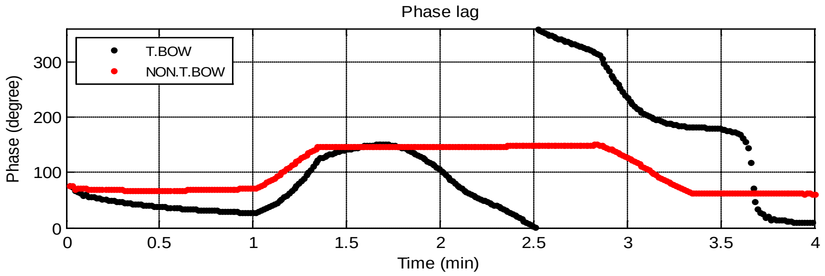

(c) Lagging phase with respect to the imbalance vector

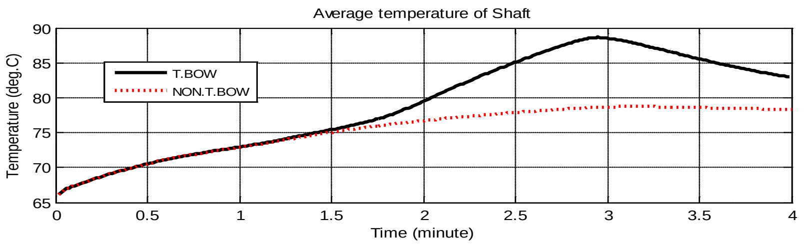

(d) Average temperature of shaft

Fig. 71 Time varying rotor spin speed and vibration amplitude at the end of rotor

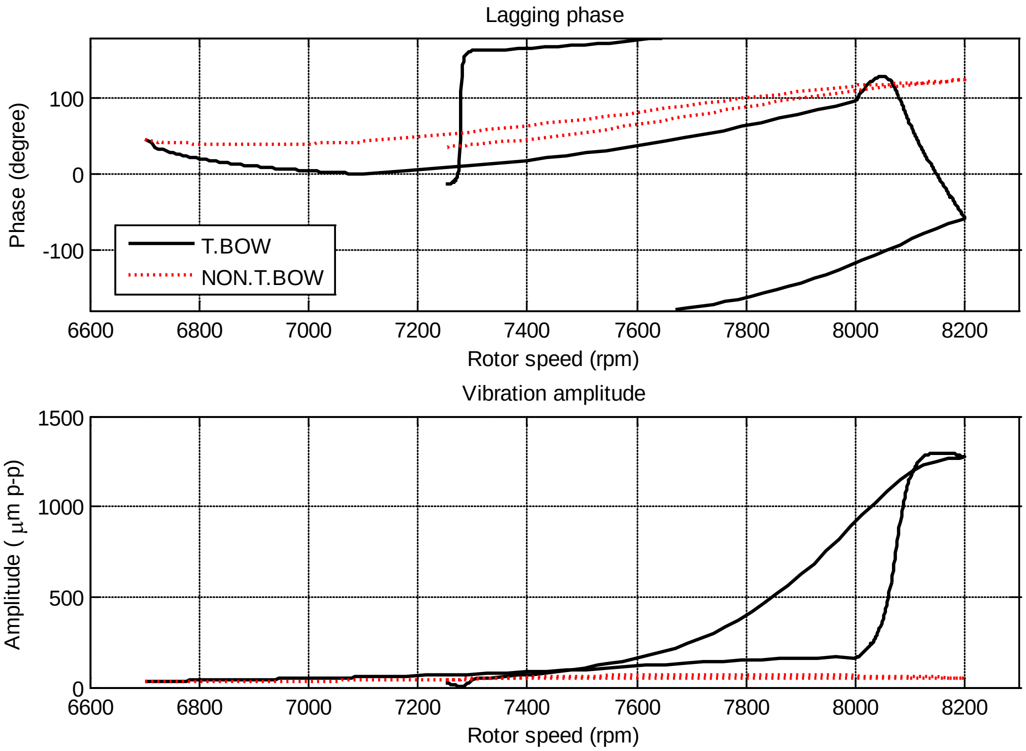

Fig. 72 Hysteresis vibration amplitude at the end of rotor

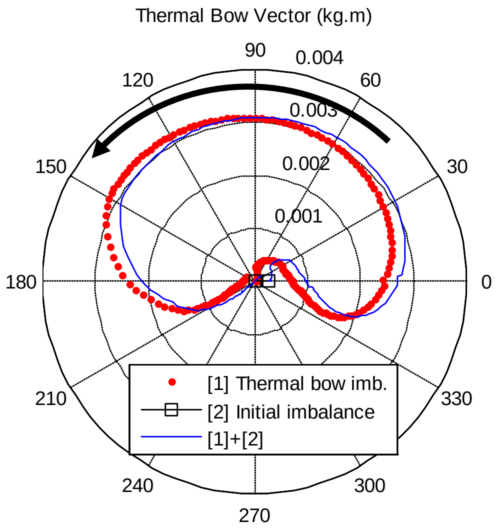

Fig. 73 Thermal bow vector

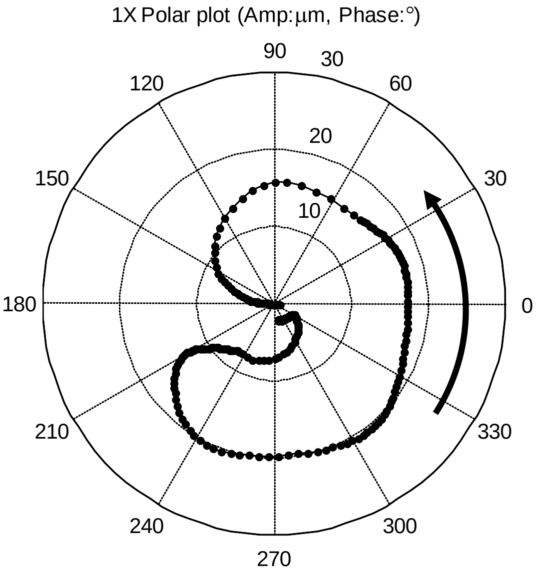

Fig. 74 1X filtered polar plot of thermal bow model

7.7 Asymmetric Thermal Expansion

Asymmetric thermal expansion of the spinning journal in the circumferential direction has not been considered in earlier studies, and the related theoretical model is introduced in section 3.7. In this section, the effect of shaft asymmetric thermal expansion will be examined by comparing asymmetric thermal expansion model to the symmetric expansion model whose uniform thermal deformation is evaluated by the shaft volume averaged temperature. The input parameters are identical to the rotor-bearing model introduced in previous section. The initial imbalance distribution is case 1 in Table 4, and the rotor spin speed remains constant at 8200 rpm. Fig. 75 (a) and (b) show the vibration amplitude at the NDE bearing location and at the end of the rotor. With the consideration of the asymmetric thermal expansion, the bearing failure happened after 8*min*, and the symmetric thermal expansion model produced bearing failure after 10*min* due to the rubbing problem as seen inFig. 75 (e). This means that the asymmetric thermal expansion model produces stronger Morton effect problem leading to fast development of thermal bow. The change rate of lagging phase of asymmetric thermal expansion model is faster than symmetric thermal expansion model as seen in Fig. 75 (f). Fig. 75 (c) compares the journal temperature differential, where the asymmetric thermal expansion model gives rise to the increased journal temperature differential after $t=4$ (*minutes*). The thermally expanded shaft area around the hot spot will reduce the film thickness yielding increased viscous shearing. It will cause higher temporal derivative of the film thickness (dh/dt) leading to an increased fluidic force and viscous shearing. The overall vibration amplitude with the asymmetric thermal expansion was increased being compared to the symmetric model as seen in Fig. 75 (a) and (b). The time period for 360° phase angle change of the hot spot and the lagging phase is around 4.5 (*minutes*) with the uniform thermal expansion model, and 3.8 (*minutes*) with the asymmetric thermal expansion model. It means that the increased viscous shearing causes the decreased time period for 360° phase angle change of hot spot and phase lag.Fig. 75 (d) shows journal surface thermal expansion ratio at *t= 5.5* (*minutes*), where the journal temperature differential is 7.9°C. The thermal expansion ratio is calculated by dividing the amount of the journal surface thermal expansion ($h_{T.E.J}$) by the bearing clearance (Cl_B). The film clearance is reduced by about 50% due to the thermal expansion of the shaft. The maximum expansion ratio is 0.517 at hot spot, and the minimum ratio is 0.49 at cold spot as seen in Fig. 75 (d). The expansion ratio differential between the hot spot and the cold spot is 2.7% which is a very small value compared with the bearing clearance (Cl_B). The maximum slope (d_B) is 2.18×10^{-5}, and the linear velocity on the spinning shaft surface (v_B) is 45.22 *m/sec*. The time derivative of the film thickness ($dh_{T.E.J}/dt$) becomes 9.85×10^{-4} *m/sec* by multiplying v_B and d_B. If the journal synchronous orbit is assumed to be a circular shape with the peak-peak amplitude 30 μm as shown in Fig. 75 (a) at *t=5.5* (*minutes*), and the pad tilting angular velocity is ignored, the maximum temporal derivative of the film thickness ($dh_{T.E.J}/dt$) due to the synchronous orbiting is 0.0058 *m/s*. The ratio of $dh_{T.E.J}/dt$ to dh/dt is 17%. The 2.7% of film clearance differential causes the same change of film thickness; however, it caused 17% change of the temporal derivative of the film thickness (dh/dt). The temporal derivative of the film thickness (dh/dt) is closely related to the damping coefficients, and this change cannot be employed in the linear model since the asymmetric thermal expansion cannot be calculated with zero orbit size with non-asymmetric heating.

The asymmetric shaft thermal expansion effect has not been taken into account in any earlier studies, and it is evident that the shaft asymmetric thermal expansion produces a change to the dynamic behavior of the rotor-bearing system accompanied by Morton effect. Further study is needed to evaluate if the increased vibration is due to the increased thermal bow or due to the decreased damping coefficient arising from the asymmetric thermal expansion. The non-uniform thermal expansion is a more realistic model, and uniform shaft thermal expansion model will produce an under-estimated viscous shearing leading to a change of simulation result.

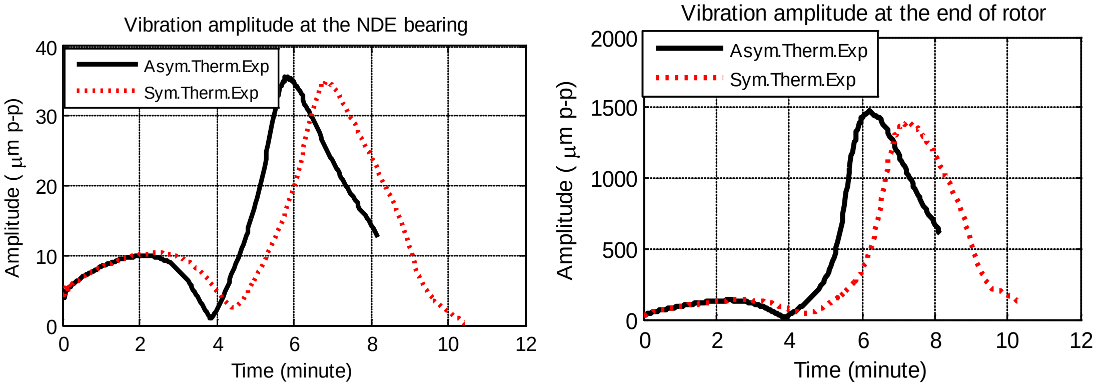

(a) Vibration amplitude at the NDE bearing

(b) Vibration amplitude at the end of the rotor

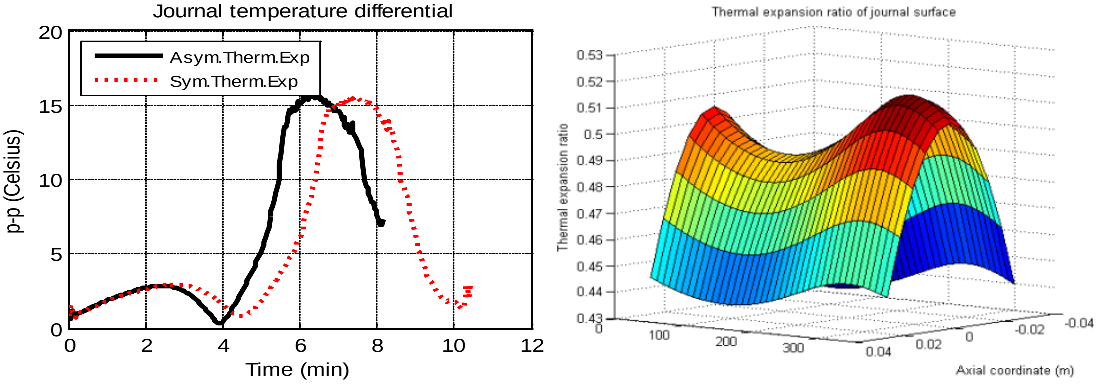

(c) Journal temperature differential with time

(d) Thermal expansion ratio of journal surface (delta T = 7.9°C)

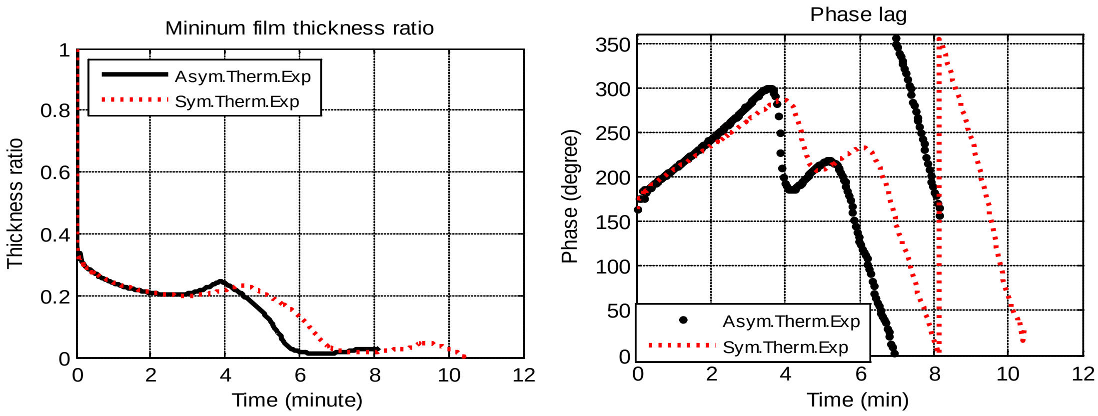

(e) Hot spot phase

(f) Phase lag

Fig. 75 Asymmetric shaft thermal expansion

7.8 Drag Moment Effect

This section examines the drag torque effect on Morton effect problem. The drag moment model was introduced in section 2.6. The first model does not consider the drag moment and the second model considers drag moment. The input parameters are identical to the ones explained in section 7.1. Fig. 76 (a) and (b) show the vibration amplitude at the NDE bearing and at the end of the rotor. By five minutes of simulation time, two models show almost the same results, and after five minutes, drag moment model produces more rapid development of Morton effect problem. Finally, the drag moment bearing model fails 1 minutes earlier than the non-drag moment model. The bearing failure is due to the rubbing problem between the spinning journal and bearing pad as seen in Fig. 76 (d).

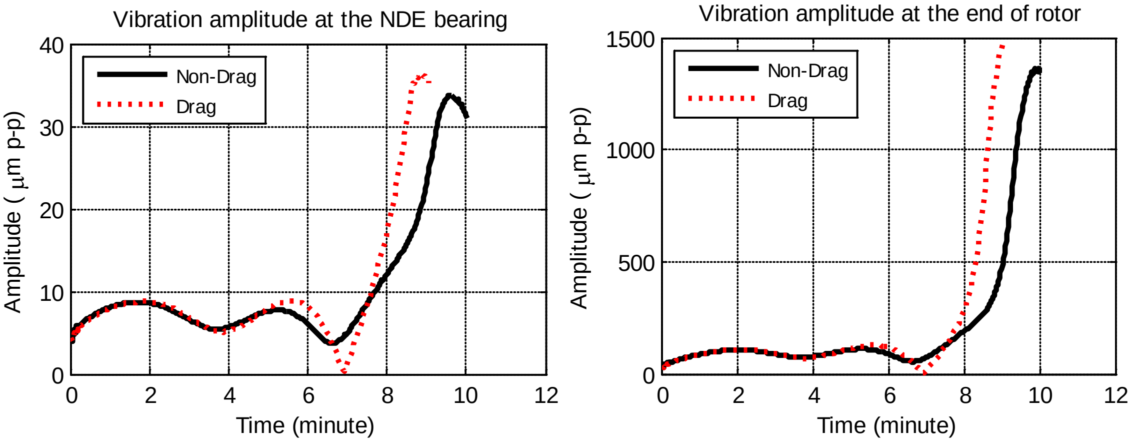

(a) Vibration amplitude at the NDE bearing

(b) Vibration amplitude at the end of the rotor

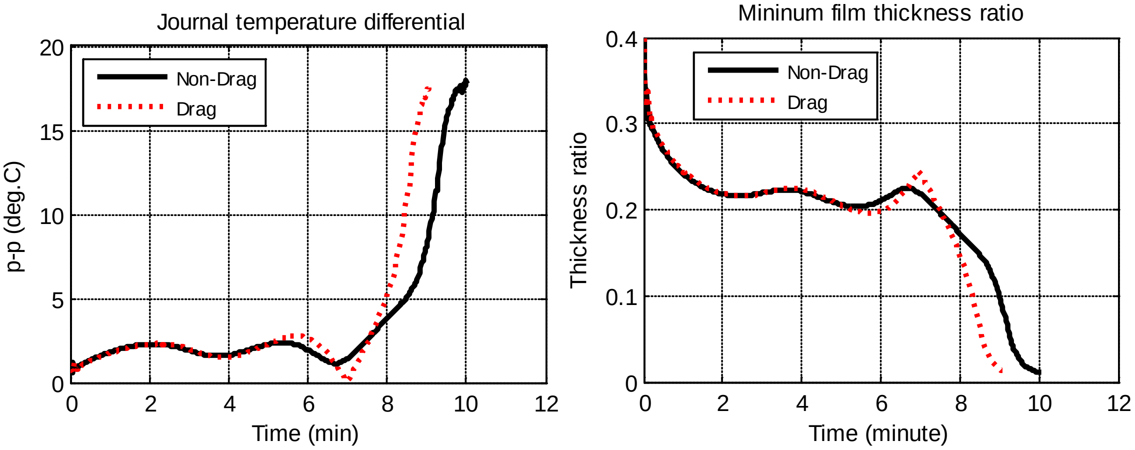

(c) Journal temperature differential

(d) Minimum film thickness ratio

Fig. 76 Comparison between non-drag moment and drag moment model

8 PARAMETRIC STUDIES*

Some of the parametric studies studied in this section came from published journals written by Suh and Palazzolo [27,28] and modified.

8.1 Thermal Boundary Condition

The thermal boundary condition effect on the Morton effect problem is studied by comparing three different simulation models of (1) convective boundary condition with an ambient temperature of $25°C$, (2) convective boundary condition with the ambient temperature of 60°C and (3) insulated boundary condition around the pad and shaft. The second model has convective boundary condition around the bearing and shaft's surfaces as described in Table 12 and Table 13 with ambient temperature of $60°C$. The third model is thermally insulated on all around the surfaces on the pad and shaft. The input parameters are identical to the rotor-bearing model shown in section 7.1 and the initial imbalance is case 1. The rotor spin speed stays at 8200 rpm. Fig. 77 (a) and (b) show the vibration amplitude at the NDE bearing and at the end of the rotor respectively. The convective boundary condition with $60°C$ ambient temperature lowered the mean vibration amplitude at the end of the rotor by 10%, which is the same amount as the drop of journal temperature differential as shown in (c). The average temperatures in the shaft, pads and lubricant are shown in Fig. 77 (d), (e), and (f)

---

*Reprinted with permission from "Three-Dimensional THD Morton Effect Analysis Part II: Parametric Studies," Journal of Tribology" by Suh, J., and Palazzolo, A., 2014. 136(3), 031706, Copyright 2014 by ASME.

respectively. With the cooler thermal boundary condition, the average temperature is reduced. It is clear that the convective boundary condition with cooler ambient temperature mitigated the vibration amplitude caused by the Morton effect problem. Fig. 77 (g), (h) and (i) show the peak temperature which show the similar trend as in the average temperature.

To study about the relationship between Morton effect problem and linear system response, dynamic coefficients are calculated with different thermal boundary conditions as seen in Fig. 78. With the reduced ambient temperature, both stiffness coefficient and damping coefficient are reduced. This is due to the decreased thermal expansion arising from the decreased temperature distribution in the shaft and pads as seen in Fig. 79 and Fig. 80. The increased film thickness lowered the stiffness and damping coefficients.

The linear system response at the NDE bearing location is shown in Fig. 81. The vibration amplitudes at 8200*rpm* of three different thermal boundary conditions show the same value. In case of the lagging phase with respect to the imbalance force vector, the first system shows the highest value.

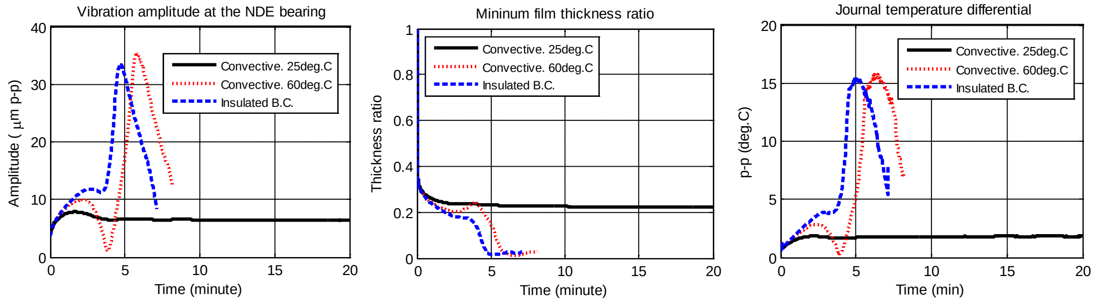

(a) Vibration amplitude at the NDE bearing

(b) Minimum film thickness ratio

(c) Journal temperature differential

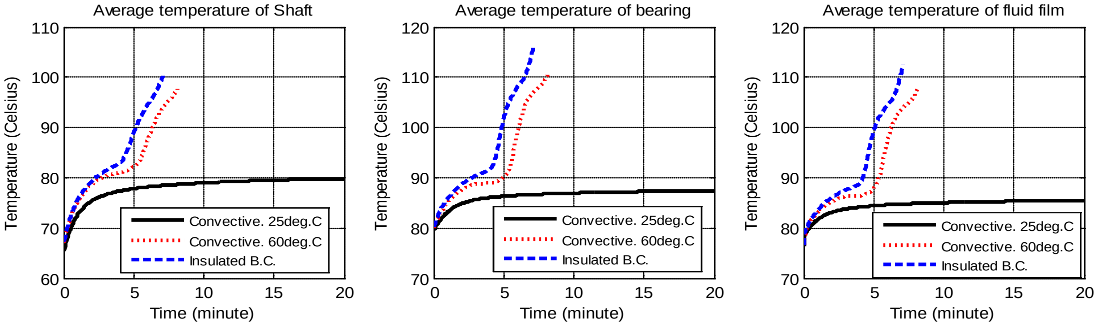

(d) Average temperature of shaft

(e) Average temperature of bearing pads

(f) Average temperature of lubricant

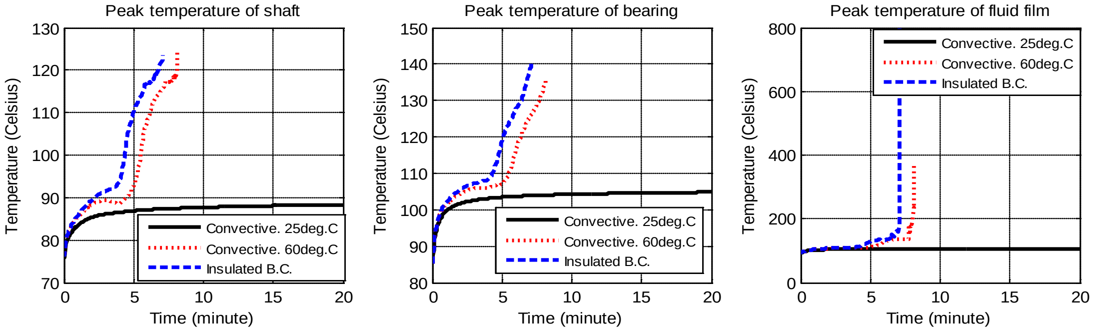

(g) Peak temperature of shaft

(h) Peak temperature of bearing pads

(i) Peak temperature of lubricant

Fig. 77 The effect of thermal boundary condition

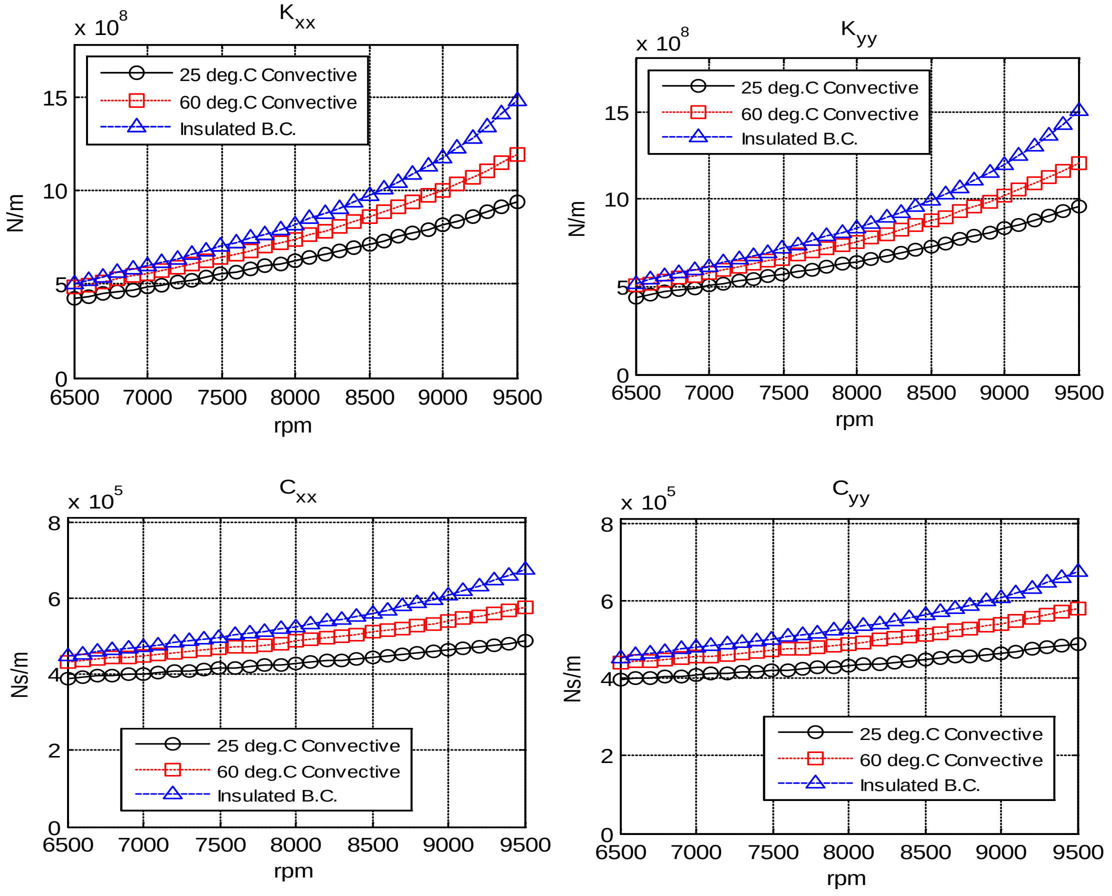

Fig. 78 Dynamic coefficients with different thermal boundary conditions

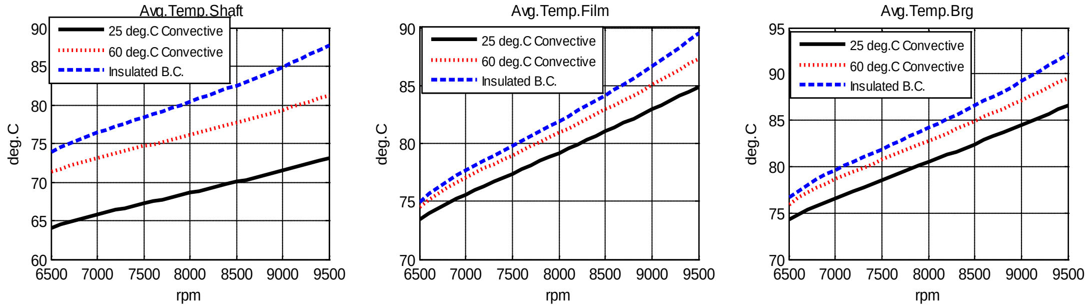
Avg.Temp.Shaft

Avg.Temp.Film

Avg.Temp.Brg

Fig. 79 Average temperature with different thermal boundary conditions

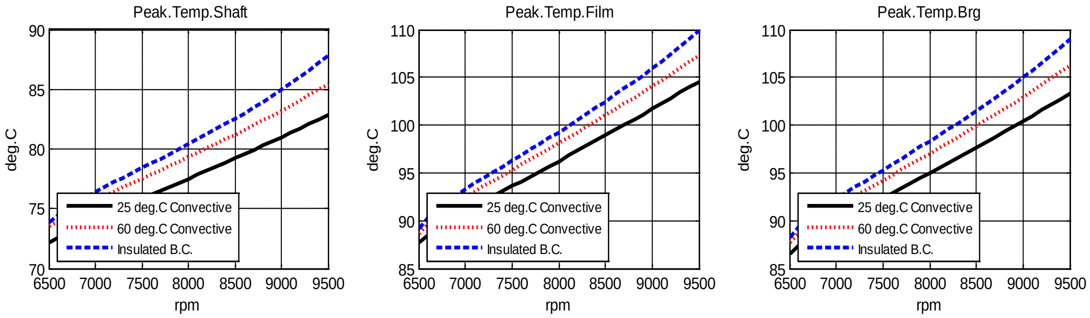
Peak.Temp.Shaft

Peak.Temp.Film

Peak.Temp.Brg

Fig. 80 Peak temperature with different thermal boundary conditions

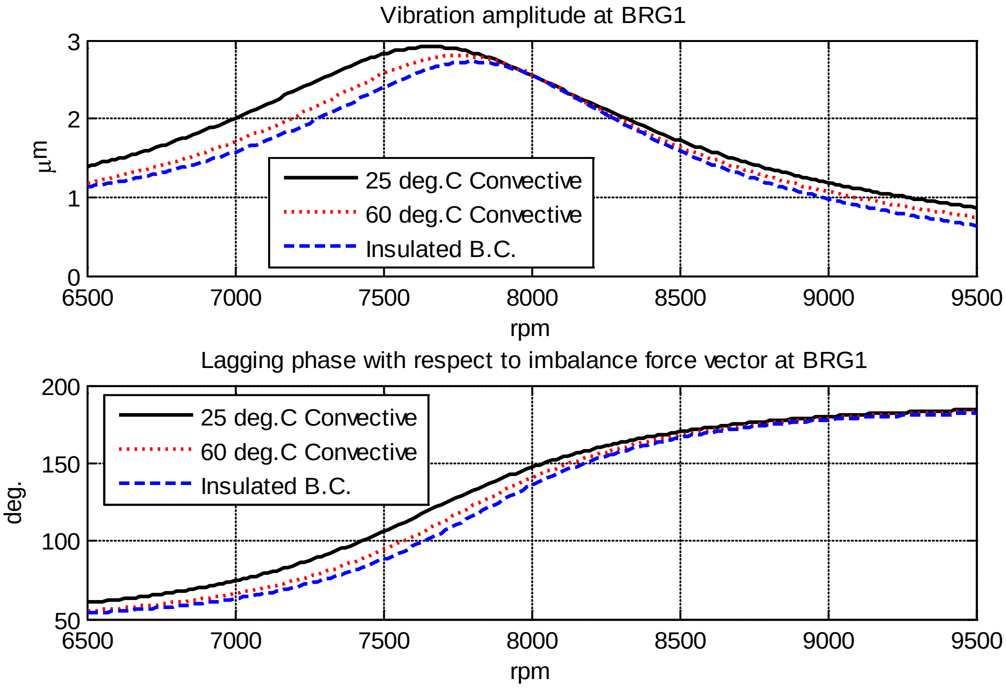

Fig. 81 Vibration amplitude and lagging phase at NDE bearing with different thermal boundary conditions

8.2 Supply Temperature

If a serious Morton effect problem happens, lowering the supply lubricant temperature can be one of the quick remedies. The supply temperature effect on the Morton effect problem is studied in this section. Simulation results of three different lubricant supply temperature, 30°*C*, 50°*C* and 70°*C*, will be compared. Other input parameters are identical to the rotor-bearing system described in Table 12 and Table 13. The initial imbalance is Case 1, and the rotor spin speed is constant at 8200 rpm.

Fig. 82 (a) and (b) show the vibration amplitudes at the NDE bearing location and at the end of the rotor respectively. The highest supply temperature model (70°*C*) produces quick bearing failure at *t*=2 (*minute*), and the 50°*C* supply temperature model produces bearing failure at *t*=8 (*minute*). After 6 minute, the vibration amplitude is decreasing, and this is just due to the thermal expansion of the shaft and pad.
Fig. 82 (d~f) show the average temperature in the shaft, lubricant and bearing pad. With the decreasing vibration amplitude, the temperature is still increasing. This means that the thermally expanded shaft and pad keeps the spinning journal leading to decreased vibration amplitude and rubbing failure as described in
Fig. 82 (c).

The lowest supply temperature model produces the mitigated thermal bow induced instability problem, where no thermal bow growth is observed. This is a significant drop of the journal temperature differential and the resultant vibration level at the end of the rotor as can be seen in
Fig. 82 (b) and (c).

The vibration amplitude at the bearing location has a significant relevance to the bearing safety problem because the extremely high vibration level will cause the bearing failure. Reduced supply temperature lowered the peak vibration level at the NDE bearing as seen in Fig. 82 (a). Average temperature in the shaft, pads and lubricant are shown in Fig. 82 (d~f) respectively.

The minimum film thickness ratio is illustrated in Fig. 82 (c), where the decreased inlet temperature increases the minimum film thickness. It can be seen that the decreased supply temperature mitigated the thermal bending angle yielding the decreased vibration amplitude. The cooling effect will limit the amount of thermal expansion of the shaft and pad resulting in the increased film thickness. The reduced lubricant temperature increased the lubricant viscosity producing the increased bearing stiffness coefficients. Cooling the inlet lubricant temperature is found to be a good remedy for the Morton effect problem.

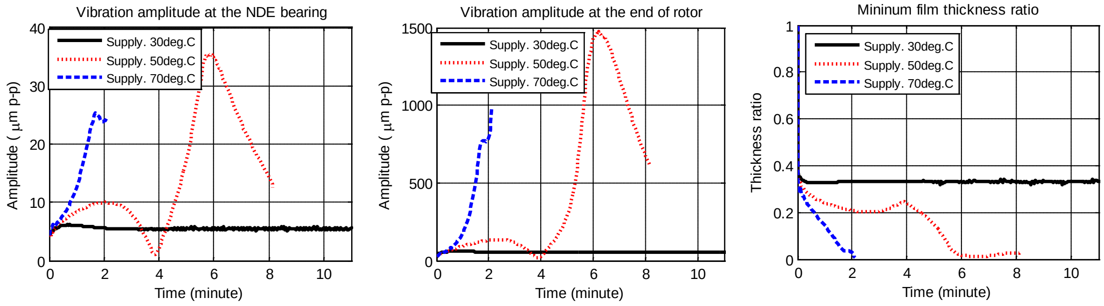

(a) Vibration amplitude at the NDE bearing

(b) Vibration amplitude at the end of the rotor

(c) Minimum film thickness ratio

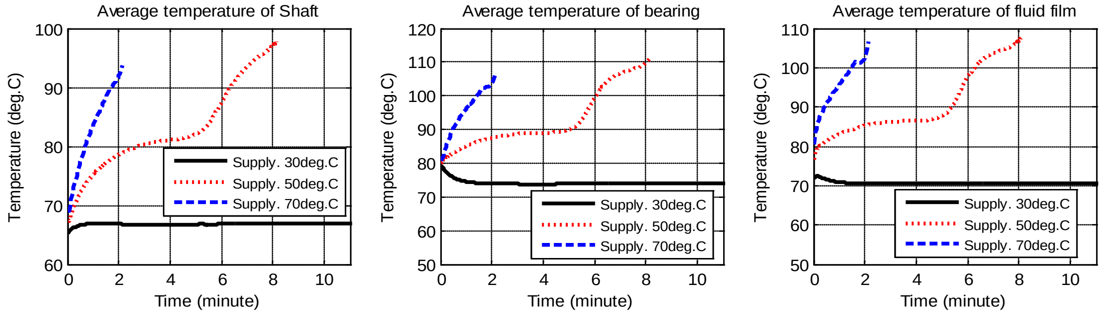

(d) Average temperature of shaft

(e) Average temperature of bearing pads

(f) Average temperature of lubricant

Fig. 82 Inlet temperature effect on the synchronous thermal instability problem

8.3 Pivot Type Effect

This section examines the pivot type effect on the Morton effect problem. Typically cylindrical pivot produces only tilting motion, whereas the spherical pivot produces tilting, yawing and pitching motion due to its pivot properties. When the thermal bow happens, cylindrical pivot will produce decreased minimum film thickness since the pivot cannot compensate the thermal bow motion as can be seen in Fig. 83 (a).

In case of the spherical pivot, pitching and yawing motions are able to increase minimum film thickness arising from the thermal bow as can be seen in Fig. 83 (b). Two simulation models have the same input parameters as seen in section 7.1 except for the pivot type. Fig. 84 (a)~(c) show the journal temperature differential, vibration amplitude at the NDE bearing and minimum film thickness ratio respectively. As expected, cylindrical pivot model produces more rapid increase of vibration amplitude and journal temperature differential. After 8 *minutes*, spherical pivot model also shows bearing failure due to the rubbing between spinning journal and bearing pad. The minimum film thickness with time shown in Fig. 84 (c) shows the evidence of the bearing rubbing failure.

Fig. 85 shows the journal temperature differential with thermal shaft axial position and time. The spherical pivot shown in Fig. 85 (a) produces axially symmetric value, whereas the cylindrical pivot model shown in Fig. 85 (b) shows axially asymmetric value. The temperature differential on the right side produces higher temperature differential.

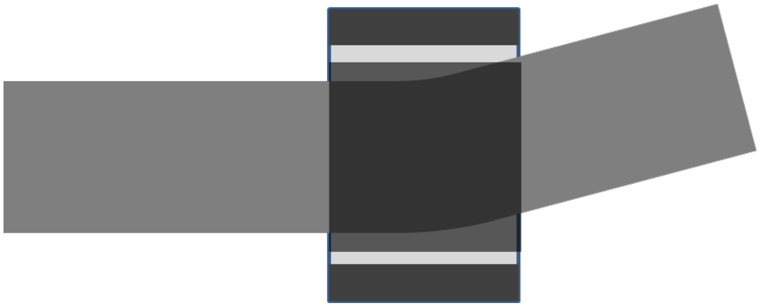

(a) Spherical pivot

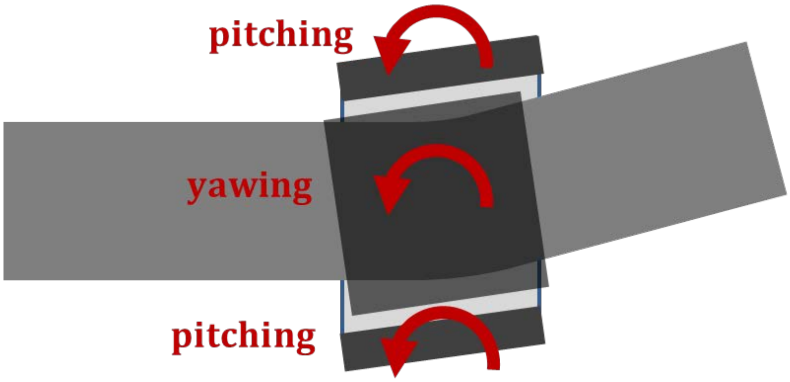

(b) Cylindrical pivot

Fig. 83 Spherical pivot motion

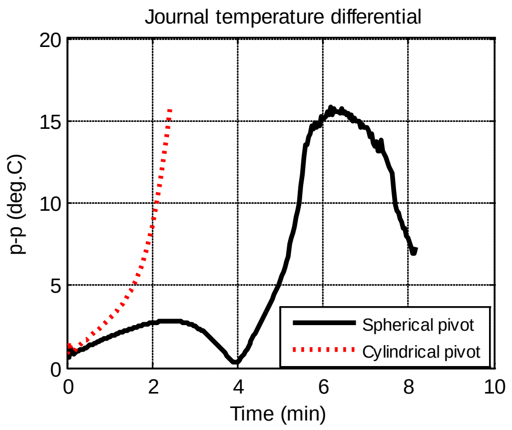

(a) Journal temperature differential

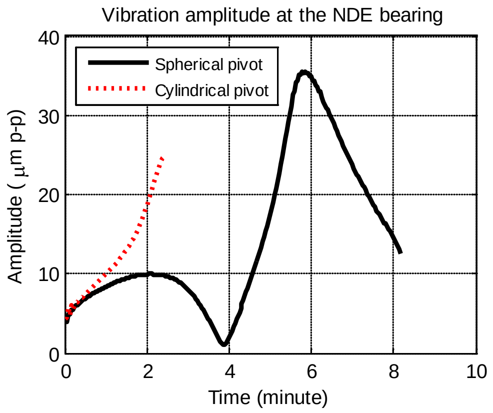

(b) Vibration amplitude at the NDE bearing

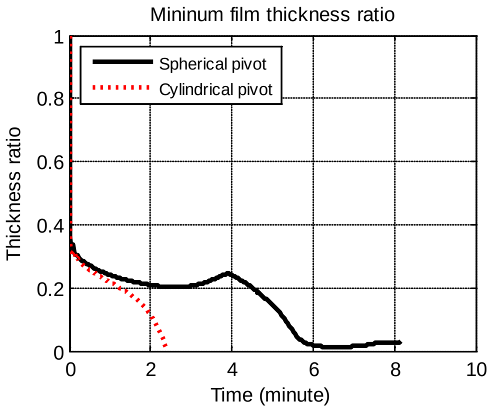

(c) Minimum film thickness ratio

Fig. 84 Effect of pivot type on Morton effect problem

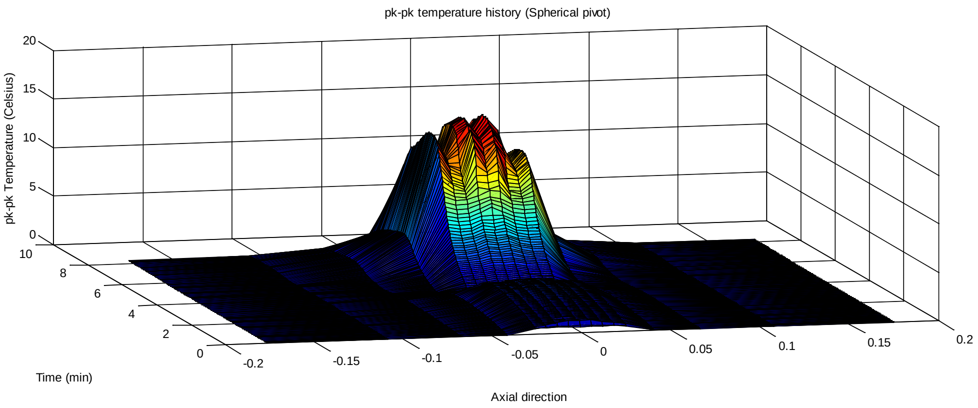

(a) Spherical pivot

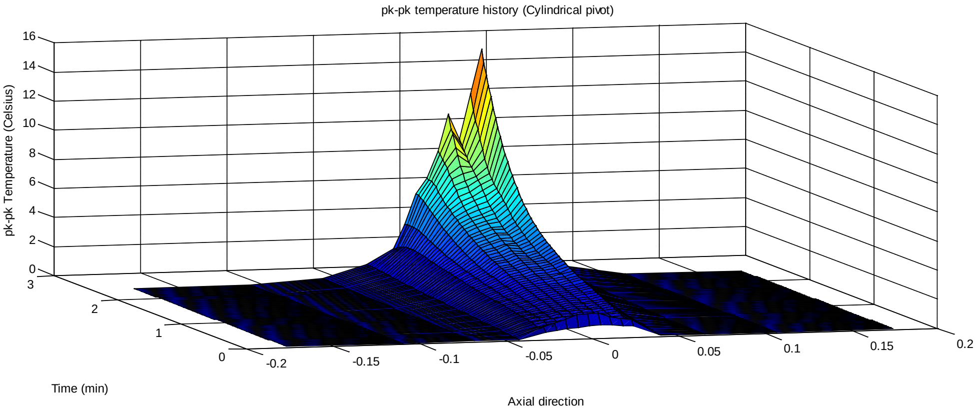

(b) Cylindrical pivot

Fig. 85 Journal temperature differential

8.4 Pivot Effect at 25°C Boundary Temperature

This section examines the same simulation model as in the previous section 8.3 with decreased temperature convective boundary condition around the bearing pad and shaft. The ambient air temperature is changed from 60℃ to 25℃ to produce more evident effect of the pivot type. Fig. 86 (a)~(c) show the journal temperature differential, vibration amplitude at the NDE bearing and vibration amplitude at the end of rotor respectively. With the decreased ambient temperature, cylindrical pivot shows bearing failure at 6.5 *minutes*, whereas the 60℃ ambient temperature model produced bearing failure at 2.5 *minutes*.With the decreased ambient temperature of 25℃, the spherical pivot model which showed bearing failure with 60℃ ambient temperature produces no Morton as can be seen in Fig. 86. The minimum film thickness stays at constant. Cylindrical pivot still shows moving lagging phase as see in Fig. 86 (d) and (f), whereas the spherical pivot model produces converging phase. The minimum film thickness ratio of cylindrical pivot decays to zero rapidly as seen in Fig. 86 (e). Peak temperature in the shaft, lubricant and bearing pad are shown in Fig. 86 (g)~(i). Cylindrical pivot shows very rapid increase of the peak temperature, and this is due to the rapidly decreased film thickness as shown in Fig. 86 (e). Journal temperature differential with axial position and time is shown in Fig. 87. As simulated in the previous section 8.3, the main reason why the cylindrical pivot produces more severe Morton effect problem is that the smaller film thickness the journal is experiencing causes more severe hot spot.

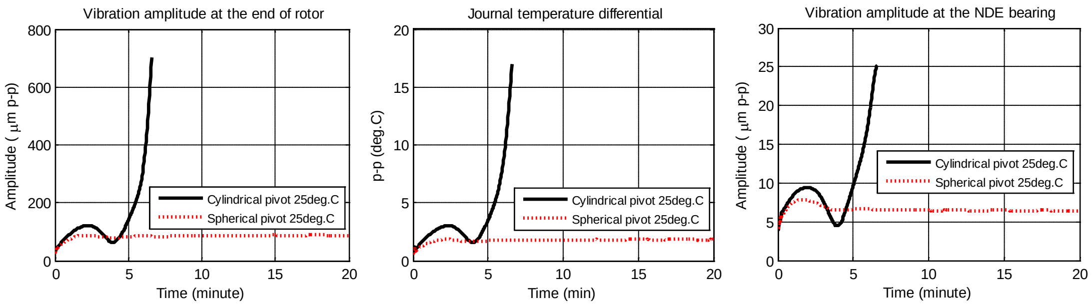

(a) Journal temperature differential

(b) Vibration amplitude at the NDE bearing

(c) Vibration amplitude at the end of rotor

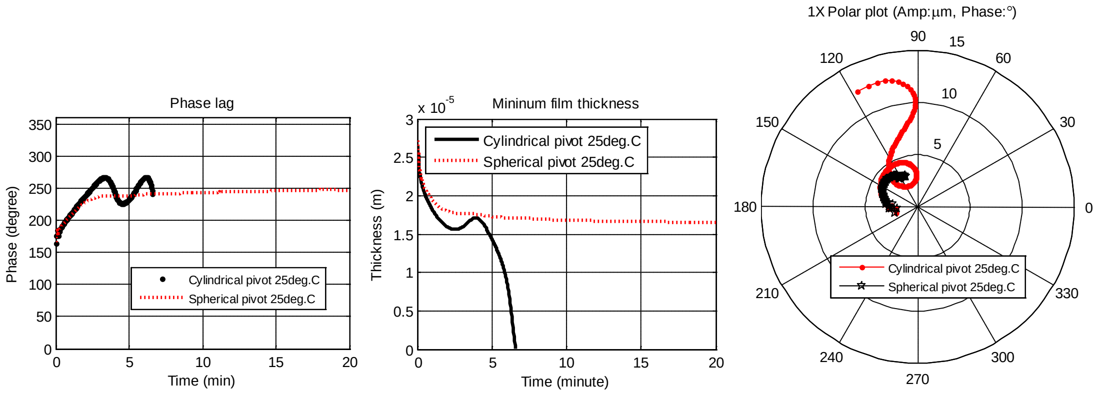

(d) Lagging phase with respect to imbalance vector

(e) Minimum film thickness

(f) 1X filtered polar plot

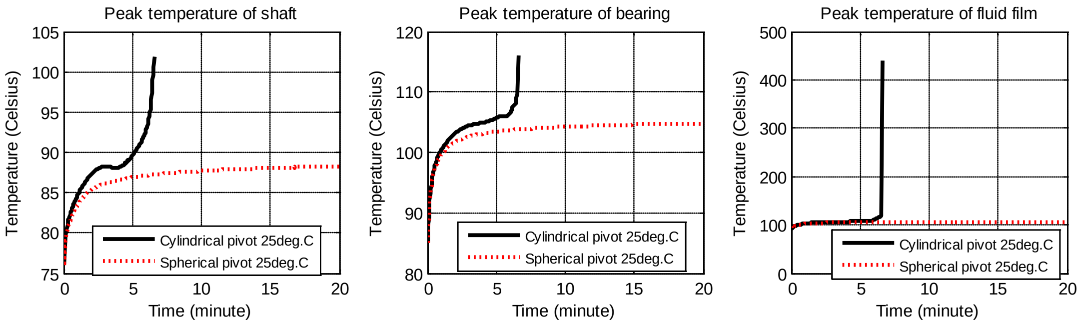

(g) Peak temperature of shaft

(h) Peak temperature of bearing pads

(i) Peak temperature of lubricant

Fig. 86 Effects of pivot type on Morton effect problem

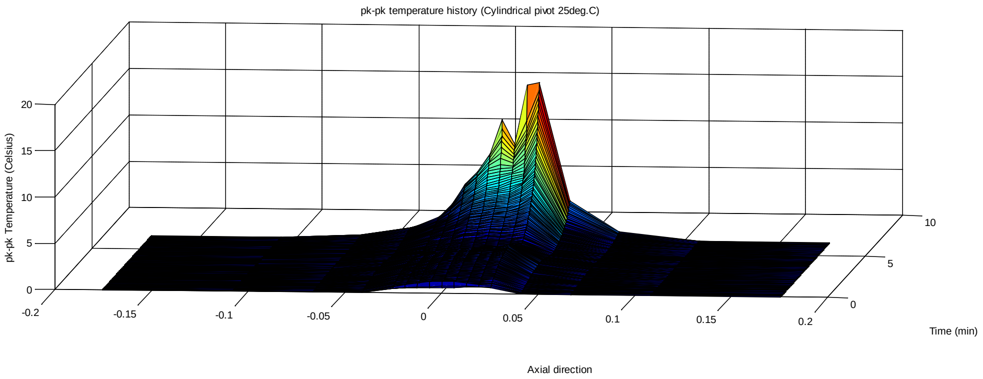

(a) Cylindrical pivot

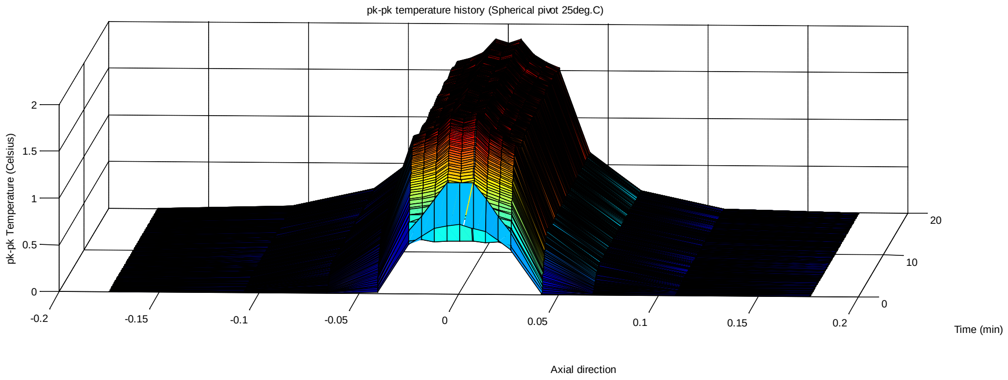

(b) Spherical pivot

Fig. 87 Journal temperature differential

8.5 Initial Imbalance

De Jongh and van der Hoeven [15] described that the rotor-bearing system in the test bed was very sensitive to the initial imbalance. In this section, three different imbalance values are simulated and compared, whose imbalances are shown in Table 14. The ratio of three initial imbalances is 100:10:1 and other input parameters are identical each other as in the previous section.

The vibration amplitudes at the NDE bearing and at the end of the rotor are shown in Fig. 88 (a) and (b) respectively. The bearing failure of 100%, 10% and 1% imbalance models occur at 8$minute$, 13$minute$ and 14$minute$ respectively. The vibration amplitude decreases after they reach the maximum value. The decreasing vibration amplitude does not mean that the Morton effect problem is mitigated. As seen in Fig. 88 (g)~(i), average temperature in shaft, lubricant and bearing pad are still increasing even after the vibration amplitude starts decreasing, which means the film clearance is decreasing with the increasing temperature of bearing pad and shaft.

Fig. 88 (d) shows the thermally reduced bearing clearance ratio which is calculated by (108). The radius of shaft (R_{shaft}) is assumed to thermally expanded based on the volume averaged shaft temperature ($T_{avg_{shaft}}$), and the pad is also assumed to be thermally expanded with the volume averaged temperature ($T_{avg_{pad}}$). They are assumed to be evenly expanded with the increased volume averaged temperature.

Fig. 88 (e) shows the minimum film thickness ratio journal experiences each orbiting. Even after the vibration amplitude is decreasing after the maximum value, the thermally reduced bearing clearance ratio is decreasing, and the minimum film thickness ratio rarely increases.

Reduced initial imbalance is thought to slow down the start point where the Morton effect problem is observed by the vibration amplitude as seen in Fig. 88 (a)~(c). Even if the initial imbalance force is very small, the thermal bow induced imbalance force will be accumulated with time. This thermal imbalance force will act like a mechanical imbalance force leading to Morton effect problem. According to the simulation results performed in this section, Morton effect is thought to happen regardless of the amount of the initial imbalance force.

$$Cl_{ratio_{therm}} = \frac{Cl_B - R_{shaft} \cdot \alpha_{shaft}\left(T_{avg_{shaft}} - T_{ref_{shaft}}\right) - t_{pad} \cdot \alpha_{pad}\left(T_{avg_{pad}} - T_{ref_{pad}}\right)}{Cl_B} \tag{108}$$

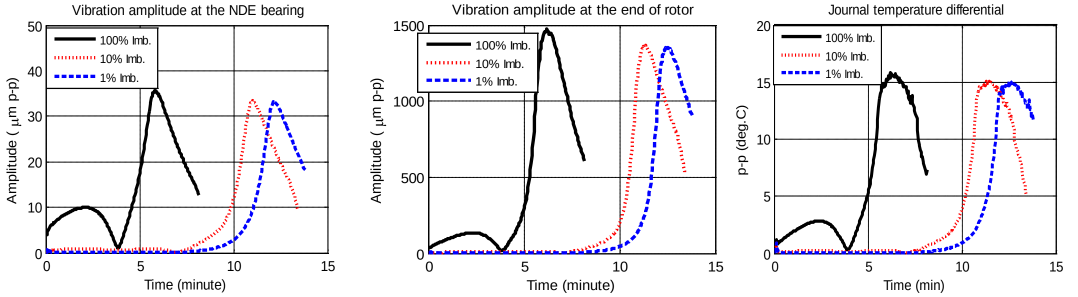

(a) Vibration amplitude at the NDE bearing

(b) Journal temperature differential with time

(c) Journal temperature differential

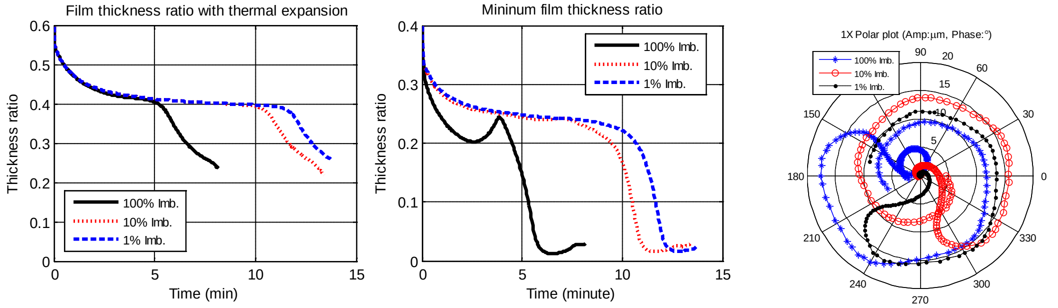

(d) Thermally reduced film thickness ratio

(e) Minimum film thickness ratio

(f) 1X filtered polar plot

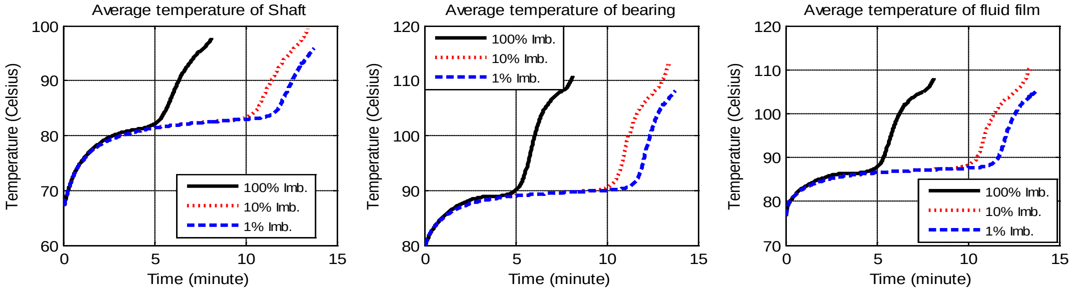

(g) Average temperature of shaft

(h) Average temperature of bearing pads

(i) Average temperature of lubricant

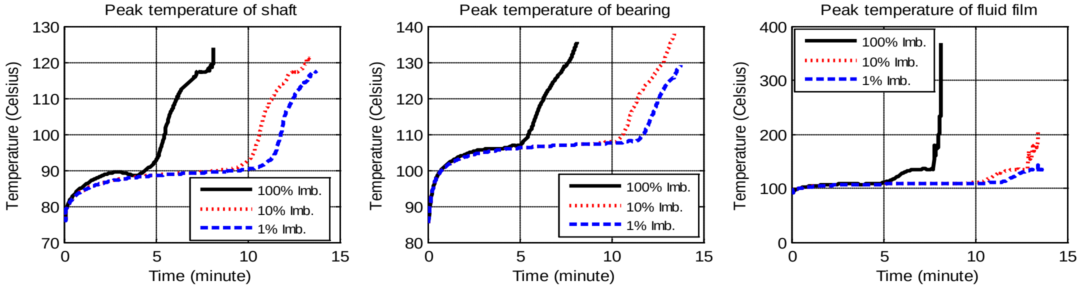

(j) Peak temperature of shaft

(k) Peak temperature of bearing pads

(l) Peak temperature of lubricant

Fig. 88 Comparison of different initial imbalance

8.6 Bearing Clearance

This section examines the film clearance effects on the thermal bow induced synchronous rotor instability problem. Except for the bearing clearance, the input parameters are identical to the rotor-bearing configurations including preload as shown in section 7.1. Three different bearing clearance values, $0.97 \times Cl_B$, $1.0 \times Cl_B$ and $1.03 \times Cl_B$, are examined. Rotor spin speed is constant at 8200 rpm.

Fig. 89 (a)~(c) show the vibration amplitude at the NDE bearing, vibration amplitude at the end of the rotor and journal temperature differential. Decreased bearing clearance increased the development rate of the Morton effect problem. The increased bearing clearance mitigated Morton effect with constant vibration amplitude and journal temperature differential. The higher increase rate of the vibration amplitude is thought to be worsened Morton problem. Even though the nonlinear transient Morton effect analysis requires a heavy computation, it is capable of more sensitive simulation. In the case of the steady Morton analysis, both $0.97 \times Cl_B$ and $1.0 \times Cl_B$ will produce the same Morton instability problem; however, in transient analysis, the different increase rates of the vibration amplitude give more sensitive parametric study.

Thermally reduced film thickness ratio ($Cl_{ratio_{therm}}$) shown in Fig. 89 (d) indicates the ratio of the bearing clearance reduced by shaft and pad thermal expansion to the initial bearing clearance (Cl_B) as seen in (108). The volume averaged thermal expansion of the shaft in the radial direction ($R_{shaft} \cdot \alpha_{shaft} \cdot (T_{avg_{shaft}} - T_{ref_{shaft}})$) and pad ($t_{pad} \cdot \alpha_{pad} \cdot (T_{avg_{pad}} - T_{ref_{pad}})$) are considered. t_{pad} indicates the pad thickness, α_{shaft} is thermal expansion coefficient of the shaft, and $T_{ref_{shaft}}$ indicates a reference temperature for the evaluation of the shaft thermal expansion. This value ($Cl_{ratio_{therm}}$) does not reflect the actual thermal expansion considering 3D thermal gradient in the pad and shaft but considers the volume and temperature averaged thermal expansion. For the evaluation of the shaft average temperature ($T_{avg_{shaft}}$), journal temperature distribution inside the bearing length is averaged, which means the shaft thermal gradient outside the bearing location is not taken into account. Five pads' temperature distributions are averaged to evaluate the pads average temperature ($T_{avg_{pad}}$).

Minimum film thickness ratio shown in Fig. 89 (e) is the ratio of the minimum film thickness journal experiences at a single orbiting to the bearing clearance (Cl_B). Even though the vibration amplitude decreases after the maximum value, the minimum film thickness ratio does not change much. The average temperature in the shaft, lubricant and bearing pad are still increasing, which means the decreased vibration amplitude does not mean the mitigated Morton problem but a thermally tightened bearing clearance leading to bearing rubbing failure.

When the bearing clearance is reduced to $0.97 \times Cl_B$, the vibration amplitudes and the journal temperature differential show the highest increase rates at the beginning as seen in Fig. 89 (a)~(c). However, after *t*=2 (*minutes*), the vibration amplitude at the NDE bearing drops rapidly with oscillation decaying to almost zero minimum film clearance at *t=2.5* (*minutes*) as shown in Fig. 89 (e). At the same moment, the energy equation encountered on a numerical problem caused by the extremely high lubricant peak temperature (see Fig. 89 (l)) and reduced minimum film clearance decaying to zero

(Fig. 89 (e)). The vibration amplitude is thought to be limited due to (1) the thermal expansions of the shaft and pads and (2) the corresponding decreased film thickness. At $t=2.5$ (*minutes*), the thermally reduced bearing clearance is decreased to 32% of its initial value due to the excessive thermal expansion as seen in Fig. 89 (d). Reduced film thickness produces higher viscous shearing leading to a higher temperature and the increased heat flux flowing into the pads and shaft. The increased temperatures of the shaft and pad give rises to the increased thermal expansion yielding the decreased film thickness, and vice versa. This process will be repeated until a converged temperature is produced as in $1.03 \times Cl_B$ model or will be repeated until the temperature becomes divergent leading to rubbing problem between the shaft and bearing as in other cases ($0.79 \times Cl_B$, $1.00 \times Cl_B$). In these cases, the average temperatures become divergent by getting close to the clearance as can be seen in Fig. 89 (g), (h), and (i). The moving phase lags are shown in Fig. 89 (f). According to the simulation results in the previous sections, the increased viscous shearing caused the increased change rate of the lagging phase and the hot spot phase. In this section, the reduced film clearance equivalent to the increased viscous shearing leads to the stiff slope meaning the higher change rate of the moving phase lag.

If the bearing clearance is increased to $1.03 \times Cl_B$, the mean vibration amplitude over the 12 (*minutes*) at the NDE bearing location does not show any oscillation as can be seen in Fig. 89 (a). The increased film clearance reduces the viscous shearing leading to a mitigated journal asymmetric heating. The average temperatures of the shaft, lubricant and pads are much lower than other two models as seen in Fig. 89 (g)~(i).

To investigate the relationship between Morton effect problem and linear system properties, bearing dynamic coefficients are calculated with different bearing clearances as see in Fig. 90. The bearing dynamic coefficients are calculated from 6500*rpm* to 9200*rpm*. With the decreased bearing clearance, both stiffness and damping coefficients are increased. At the higher rotor spin speed, the coefficient differential is bigger.

Linear system response at the NDE bearing location is calculated as seen in Fig. 91. With the decreased bearing clearance, peak vibration amplitude is decreased, whereas the vibration value is increased with the increased bearing clearance. The peak frequency is increased by decreased bearing clearance. Is it thought that the tightened bearing produces stiffer system properties leading to increased natural frequency. Stiffened system shows quicker phase change around the peak vibration value.

Even though the linear analysis predicted lower vibration amplitude with reduced bearing clearance at 8200 rpm, the Morton effect did not happen at the increased bearing clearance model where the linear system predicted bigger vibration value. Only with the 3% increase of the bearing clearance, the Morton effect problem is mitigated.

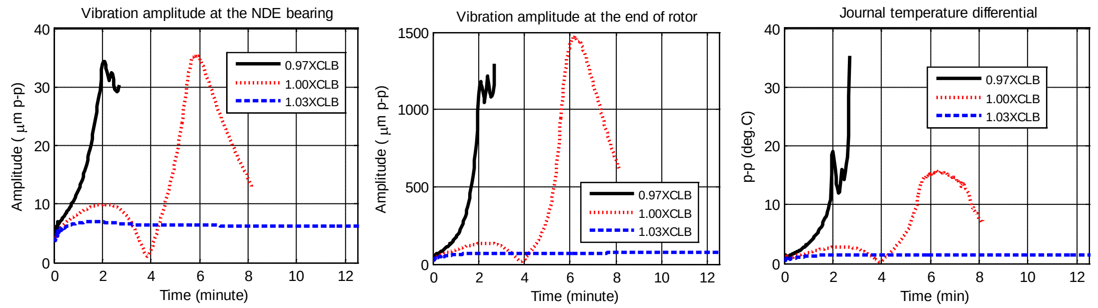

(a) Vibration amplitude at the NDE bearing

(b) Vibration amplitude at the end of the rotor

(c) Journal temperature differential

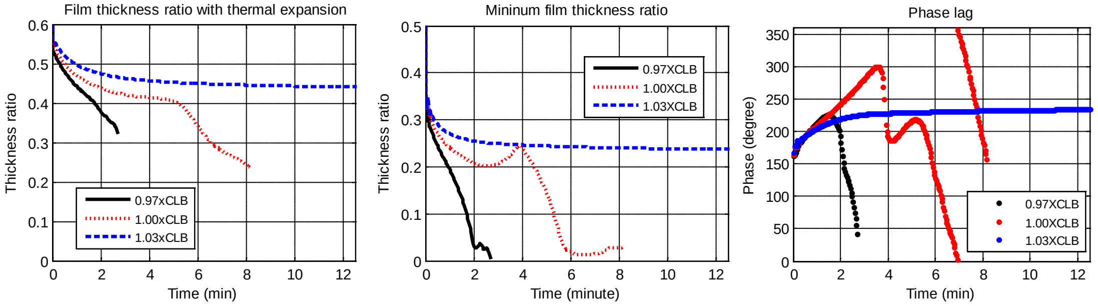

(d) Thermally reduced film thickness ratio

(e) Minimum film thickness ratio

(f) Lagging phase with respect to imbalance force

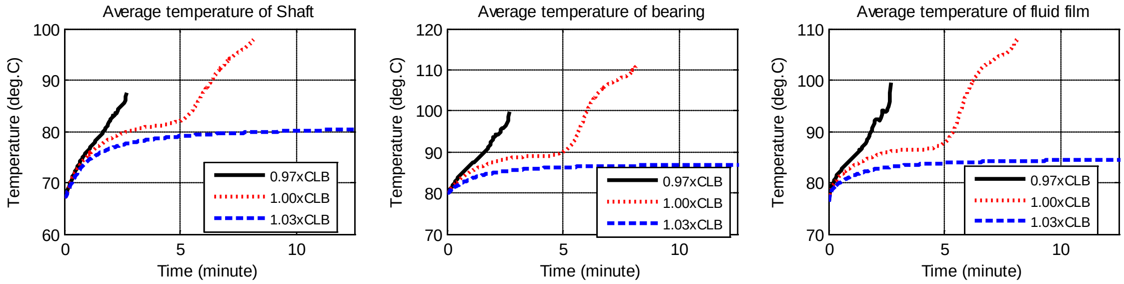

(g) Average temperature of shaft

(h) Average temperature of bearing pads

(i) Average temperature of lubricant

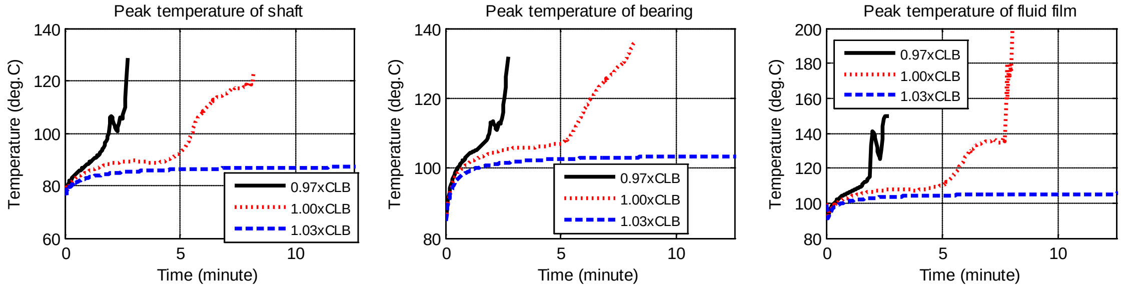

(j) Peak temperature of shaft

(k) Peak temperature of bearing pads

(l) Peak temperature of lubricant

Fig. 89 Film clearance effect on the Morton effect problem

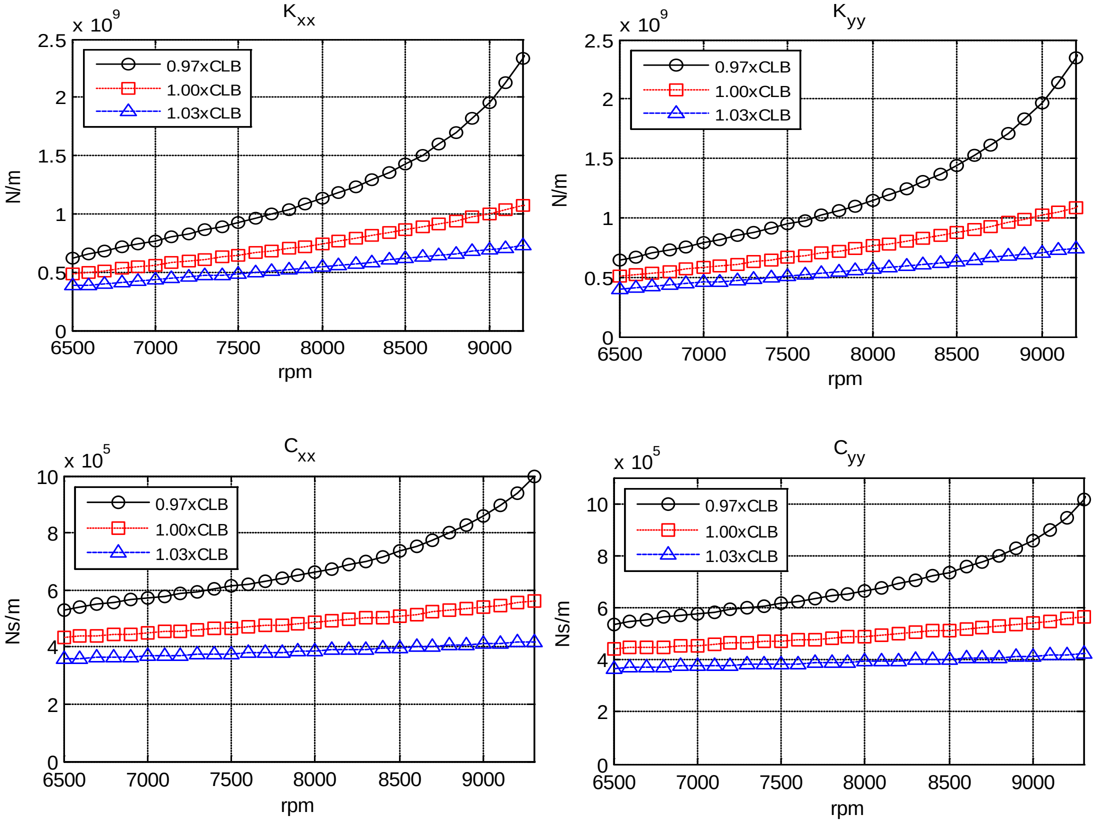

Fig. 90 Dynamic coefficients with different bearing clearance

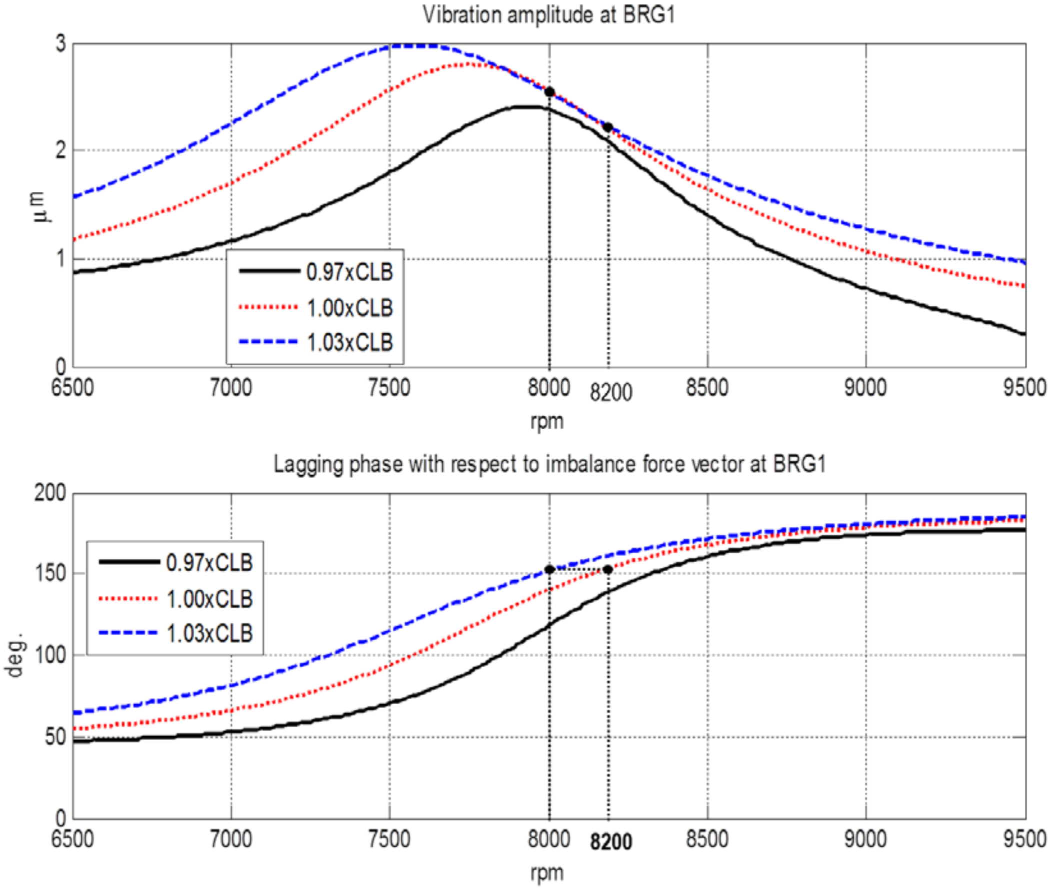

Fig. 91 Linear system response at the NDE bearing location

8.7 Pad Flexibility

In section 3.2, flexible pad dynamic model was introduced, and the new film thickness formula was explained in section 3.10. In this section, nonlinear transient Morton effect simulation is performed considering the flexible pad dynamic model. Three different models are simulated, which are rigid pad model, flexible pad model with the original thickness and flexible pad model with 85% of its initial thickness.

The minimum film thickness ratio is depicted in Fig. 92 (c). The rigid pad model fails at 2.5 minutes due to the rubbing problem, and the flexible pad with 100% thickness fails after 5 minutes of simulation time. On the other hand, the 70% pad thickness model shows stable dynamic behavior. The thin pad may produce less amount of thermal expansion due to the less thickness leading to less decrease of film thickness and the resultant reduced Morton effect. Fig. 92 (a) and (b) show the vibration amplitude at the NDE bearing and at the end of the rotor respectively. At the beginning, rigid pad's increase rate of the vibration amplitude shows the highest value.

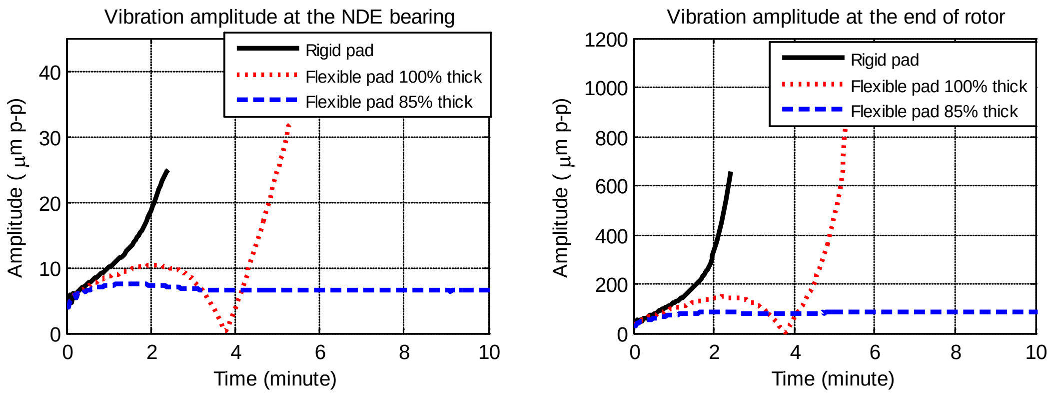

(a) Vibration amplitude at the NDE bearing

(b) Vibration amplitude at the end of the rotor

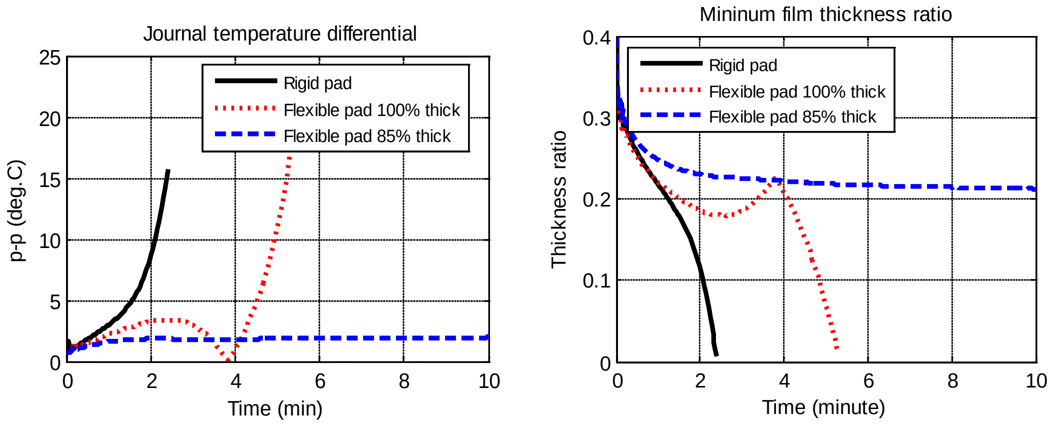

(c) Journal temperature differential

(d) Minimum film thickness ratio

Fig. 92 Pad flexibility effect on Morton effect problem.

9 CONCLUSIONS

(a) The earlier studies have adopted analytical methods for the evaluation of the thermal bow angle and phase, assuming that the thermal bow phase coincides with the cold spot. On the other hand, the present work presented a new approach for the thermal bow eccentricity and phase, where the thermal gradient and the heat conduction inside the 3D thermo-elastic FE shaft model are employed.

(b) 3D film thickness formula is employed to simulate the 3D rotor-bearing dynamic motion.

(c) Asymmetric shaft thermal expansion model is developed, where the temporal derivative of the film thickness due to the spinning shaft is taken into account.

(d) Modified mixing temperature theory is presented, where the recirculated flow from the upstream pad to the downstream pad is limited by adopting the mixing coefficient factor. For the 3D bearing model, the axial inlet temperature variation is considered.

(e) The 2D energy equation is found to be a good assumption, and suitable for the static equilibrium analysis, where the journal differential heating can be ignored and the orbit size is zero. However, the Morton effect simulation with large orbit motion showed different results. The vibration amplitude at the NDE bearing location of the 2D energy equation was 687% higher than the 3D energy equation, and the journal surface temperature differential of the 2D energy equation was 1000% higher than the 3D energy equation. The 3D energy equation is found to be suitable for the Morton effect simulation.

(f) The thermal bow effect makes a significant change to the dynamic behavior of the rotor-bearing system. Hysteresis vibration amplitude with the time varying rotor spin speed was observed, which is the noticeable characteristic of the synchronous thermal instability problem.

This study presents a new novel method to calculate the cyclic amplitude and synchronous vibrations resulting from the journal surface temperature differential in a tilting-pad journal bearing. This new modeling method is improved from the previous study [13] as follows:

(a) The 3D FE shaft and pad models consider more sophisticated thermal boundary conditions that make changes to the thermo-hydro-dynamic behavior.

(b) Asymmetric shaft thermal expansion model can consider more realistic film thickness profile leading to a reliable prediction of the Morton effect problem.

(c) Pad thermal deformation is modeled using the thermo-elastic 3D finite element model, and the pad material property effect could be examined.

(d) Pivot stiffness and pad flexibility effect was included.

(e) Thermal bow angle and phase were evaluated by the 3D finite element model considering the shaft's internal temperature distribution.

(f) The phase relationships among the hot spot, cold spot, high spot, thermal bow and heavy spot are studied by nonlinear transient rotordynamic analysis. Inaccurate prediction of the thermal bending and phase may give rise to a wrong Morton effect simulation result.

(g) The thermal induced imbalance vector is known to increase the vibration level, which is the synchronous rotor instability problem known as the Morton effect; however, it is shown that the thermal induced imbalance can lower the vibration amplitude when the two phases of the initial imbalance and the thermal bending vector are in the opposite direction, and the amplitudes of the two imbalance vectors are similar.

(h) The journal synchronous orbiting in a fluid film bearing inherently generates the asymmetric heating in the circumferential direction. Earlier studies neglected the asymmetric radial thermal expansion of the shaft arising from the asymmetric heating, but this is now shown to make a change to the rotor-bearing system dynamic behavior. In this study, 2.7% of the film clearance differential in the circumferential direction arising from the asymmetric journal thermal expansion caused a 5% change in the mean vibration level at the NDE bearing location, and a 17% change in the mean journal surface temperature differential.

(i) Increased convection and reduced supply lubricant temperature mitigated the Morton effect problem.

(j) Excessive reduction of film clearance resulted in a divergent temperature causing a rubbing problem between the stationary part and the rotating shaft.

(k) Thermal deformation of the pad and shaft made notable changes to the Morton effect response.

Table 16 provides a condensed summary based on the above observations. One should interpret these results with the awareness that although the Morton effect may be decreased with a certain parameter change other undesired consequences may occur, such as a shift in critical speed, etc.

Table 16 Parameter changes required to reduce Morton effect

Parameter	Changes required for M.E. reduction	Physical explanation
Thermal boundary conditions	Increase convection by lowering ambient temperature or increase convection coefficient	Decreased thermal expansion of the shaft and pad limits the viscous shearing
Supply lubricant temperature	Reduce inlet lubricant temperature	Decreased thermal expansion of the shaft and pad
Film clearance	Increase the bearing clearance	Increasing film thickness decreases viscous shearing associated with the Morton problem
Pivot type	Use of spherical pivot	Spherical pivot will produce more symmetric journal temperature differential than cylindrical pivot leading to mitigated Morton problem
Pad thickness	Use of thin pad	Thin pad produces increased minimum film thickness as in the linear static equilibrium analysis limiting the heat generated by the viscous shearing

This study presented a new sophisticated modeling method and algorithm for the evaluation of the static equilibrium condition of the flexible pad and pivot TPJB, adopting nonlinear transient dynamic analysis. It includes flexible pad and the nonlinear pivot stiffness effects which is function of pad-pivot material properties, load on pad and pivot shape. This study can be summarized as follows:

(a) Dynamic equation of motion for flexible FE pad model was produced, where the pad dynamic behavior was presented by means of modal coordinate. To avoid a singular matrix problem and produce more realistic pad elastic deformation, nonlinear transient pad dynamic analysis is adopted. On the other hand, earlier studies have adopted additional constraints leading to unrealistic pad deformation, where static analysis of pad elastic deformation is performed.

(b) Each time step of the transient dynamic analysis, coordinate transformation is performed to produce the film thickness in the physical coordinate and the pad elastic deformation in the modal coordinate.

(c) For the computational efficiency, modal coordinate transformation is adopted in flexible pad dynamic analysis. Pad tilting motion, pivot translation motion and elastic deformation can be expressed by means of modal displacement.

(d) Nonlinear pivot stiffness model considering Hertzian contact theory is adopted for more accurate prediction of TPJB dynamic behavior.

(e) Heat conduction equation of journal and bearing pad was presented by use of 3D FE model.

(f) Thermal distortions of 3D shaft and pad were evaluated adopting FE analysis, and the 2D thermal expansion profile was used in film thickness evaluation.

(g) Due to the arbitrary pad elastic deformation, conventional film thickness formula cannot be used. So a new formula is developed to calculate the nodal film thickness profile of the flexible pad TPJB model.

(h) Full dynamic coefficients were presented by means of journal translational motion and modal displacement of flexible FE pad, and synchronously reduced dynamic coefficient was presented.

(i) For the verification of the new TPJB model, flexible pad model only with the consideration of the rigid body mode was simulated and compared with the rigid pad TPJB model. Each TPJB model showed identical result.

(j) The simulation results were compared with the experimental work of Kulhanek's [42] research, and they agreed well with 20% maximum error of stiffness coefficients and 30% maximum error of damping coefficient. Current numerical model predicted higher stiffness coefficients and lower damping values than the experimental work.

(k) Static equilibrium condition and dynamic coefficients are simulated with varying number of modes of the FE pad. The 1st bending mode was found to have the biggest influence on the TPJB dynamic behavior.

(l) Three pad models with different thickness are simulated and compared each other. The drop rate of the damping coefficient due to the reduced pad thickness was bigger than that of the stiffness coefficient.

(m) The preload change due to the thermal and elastic deformation was simulated. At the thinnest pad, preload change induced by elastic deformation was bigger than that induced by the thermal deformation. [13]

(n) Both elastic and thermal deformation was found to increase the bearing pad preload.

Present study can be extended to a nonlinear time transient rotordynamic analysis with a large imbalance motion. [24]

REFERENCES

[1] Tieu, A., 1973, "Oil-Film Temperature Distribution in an Infinitely Wide Slider Bearing: An Application of the Finite-Element Method," Journal of Mechanical Engineering Science, 15(4), pp. 311-320.

[2] Khonsari, M., and Beaman, J., 1986, "Thermohydrodynamic Analysis of Laminar Incompressible Journal Bearings," ASLE transactions, 29(2), pp. 141-150.

[3] Knight, J., and Barrett, L., 1988, "Analysis of Tilting Pad Journal Bearings with Heat Transfer Effects," Journal of tribology, 110(1), pp. 128-133.

[4] Earles, L., Armentrout, R., and Palazzolo, A., 1990, "A Finite Element Approach to Pad Flexibility Effects in Tilt Pad Journal Bearings: Part II—Assembled Bearing and System Analysis," Journal of Tribology, 112(2), pp. 178-182.

[5] Keogh, P., and Morton, P., 1993, "Journal Bearing Differential Heating Evaluation with Influence on Rotor Dynamic Behaviour," Proceedings of the Royal Society of London. Series A: Mathematical and Physical Sciences, 441(1913), pp. 527-548.

[6] Gomiciaga, R., and Keogh, P., 1999, "Orbit Induced Journal Temperature Variation in Hydrodynamic Bearings," Journal of tribology, 121(1), pp. 77-84.

[7] Larsson, B., 1999, "Journal Asymmetric Heating. Part I: Nonstationary Bow," Journal of tribology, 121(1), pp. 157-163.

[8] Larsson, B., 1999, "Journal Asymmetric Heating. Part II: Alteration of Rotor Dynamic Properties," Journal of tribology, 121(1), pp. 164-168.

[9] Balbahadur, A., and Kirk, R., 2004, "Part II—Case Studies for a Synchronous Thermal Instability Operating in Overhung Rotors," International Journal of Rotating Machinery, 10(6), pp. 477-487.

[10] Balbahadur, A. C., and Kirk, R., 2004, "Part I—Theoretical Model for a Synchronous Thermal Instability Operating in Overhung Rotors," International Journal of Rotating Machinery, 10(6), pp. 469-475.

[11] Murphy, B. T., and Lorenz, J. A., 2010, "Simplified Morton Effect Analysis for Synchronous Spiral Instability," Journal of Vibration and Acoustics, 132(5), pp. 051008.

[12] Childs, D. W., and Saha, R., 2012, "A New, Iterative, Synchronous-Response Algorithm for Analyzing the Morton Effect," Journal of Engineering for Gas Turbines and Power, 134(7), pp. 072501.

[13] Lee, J. G., and Palazzolo, A., 2013, "Morton Effect Cyclic Vibration Amplitude Determination for Tilt Pad Bearing Supported Machinery," Journal of Tribology-Transactions of the ASME, 135(1), pp. 011701.

[14] De Jongh, F., Morton, P., and Holmes, R., 1996, "The Synchronous Instability of a Compressor Rotor Due to Bearing Journal Differential Heating," Journal of engineering for gas turbines and power, 118(4), pp. 816-824.

[15] De Jongh, F. M., and Van Der Hoeven, P., 1998, "Application of a Heat Barrier Sleeve to Prevent Synchronous Rotor Instability," Proceedings of the 27th Turbomachinery Symposium, pp. 17-26.

[16] Childs, D. W., and Saha, R., 2012, "A New, Iterative, Synchronous-Response Algorithm for Analyzing the Morton Effect," Journal of Engineering for Gas Turbines and Power-Transactions of the ASME, 134(7), pp. 072501.

[17] Lund, J., 1964, "Spring and Damping Coefficients for the Tilting-Pad Journal Bearing," ASLE transactions, 7(4), pp. 342-352.

[18] Nilsson, L., 1978, "The Influence of Bearing Flexibility on the Dynamic Performance of Radial Oil Film Bearings," Symposium, Elastohydrodynamic and related Topics, Paper IX, pp. 331.

[19] Lund, J. W., and Pedersen, L. B., 1987, "The Influence of Pad Flexibility on the Dynamic Coefficients of a Tilting Pad Journal Bearing," Journal of tribology, 109(1), pp. 65-70.

[20] Kirk, R., and Reedy, S., 1988, "Evaluation of Pivot Stiffness for Typical Tilting-Pad Journal Bearing Designs," Journal of Vibration, Acoustics Stress and Reliability in Design, 110(2), pp. 165-171.

[21] Earles, L., Armentrout, R., and Palazzolo, A., 1990, "A Finite Element Approach to Pad Flexibility Effects in Tilt Pad Journal Bearings: Part I—Single Pad Analysis," Journal of Tribology, 112(2), pp. 169-176.

[22] Kim, J., Palazzolo, A. B., and Gadangi, R. K., 1994, "Tehd Analysis for Tilting-Pad Journal Bearings Using Upwind Finite Element Method," Tribology transactions, 37(4), pp. 771-783.

[23] Kim, J., Palazzolo, A., and Gadangi, R., 1995, "Dynamic Characteristics of Tehd Tilt Pad Journal Bearing Simulation Including Multiple Mode Pad Flexibility Model," Journal of vibration and acoustics, 117(1), pp. 123-135.

[24] Gadangi, R., and Palazzolo, A., 1995, "Transient Analysis of Tilt Pad Journal Bearings Including Effects of Pad Flexibility and Fluid Film Temperature," Journal of tribology, 117(2), pp. 302-307.

[25] Desbordes, H., Wai, C. C. H., Fillon, M., and FrêNe, J., 1995, "The Effects of Three-Dimensional Pad Deformations on Tilting-Pad Journal Bearings under Dynamic Loading," Journal of tribology, 117(3), pp. 379-384.

[26] Wilkes, J. C., and Childs, D. W., 2013, "Improving Tilting Pad Journal Bearing Predictions—Part I: Model Development and Impact of Rotor Excited Versus Bearing Excited Impedance Coefficients," Journal of Engineering for Gas Turbines and Power, 135(1), pp. 012502.

[27] Suh, J., and Palazzolo, A., 2014, "Three-Dimensional THD Morton Effect Analysis Part II: Parametric Studies," Journal of Tribology, 136(3), pp. 031706

[28] Suh, J., and Palazzolo, A., 2014, "Three-Dimensional THD Morton Effect Simulation Part I: Theoretical Model," Journal of Tribology, 136(3), pp. 031707

[29] Lund, J., and Thomsen, K., 1978, "A Calculation Method and Data for the Dynamic Coefficients of Oil-Lubricated Journal Bearings," Topics in fluid film bearing and rotor bearing system design and optimization, pp. 1000118.

[30] Hamrock, B. J., Schmid, S. R., and Jacobson, B. O., 2004, Fundamentals of Fluid Film Lubrication, Taylor & Francis, New York.

[31] Wong, P., Wang, R., and Lingard, S., 1996, "Pressure and Temperature Dependence of the Density of Liquid Lubricants," Wear, 201(1), pp. 58-63.

[32] Heinrich, J., Huyakorn, P., Zienkiewicz, O., and Mitchell, A., 1977, "An ‘Upwind’ Finite Element Scheme for Two-Dimensional Convective Transport Equation," International Journal for Numerical Methods in Engineering, 11(1), pp. 131-143.

[33] Inman, D. J., 2010, Engineering Vibrations, Prentice-Hall, New York.

[34] Young, W. C., and Budynas, R. G., 2002, Roark's Formulas for Stress and Strain, McGraw-Hill, New York,

[35] Nicholas, J. C., and Wygant, K., 2005, "Tilting Pad Journal Bearing Pivot Design for High Load Applications," Proceedings of the 24th Turbomachinery Symposium, pp. 179-193.

[36] Cook, R. D., 1994, Finite Element Modeling for Stress Analysis, John Wiley & Sons, Inc., Hoboken, New Jersey.

[37] Childs, D. W., and Saha, R., 2012, "A New, Iterative, Synchronous-Response Algorithm for Analyzing the Morton Effect," Journal of Engineering for Gas Turbines and Power-Transactions of the ASME, 134(7), pp. 179-193.

[38] Lee, J. G., and Palazzolo, A., 2013, "Morton Effect Cyclic Vibration Amplitude Determination for Tilt Pad Bearing Supported Machinery," Journal of Tribology-Transactions of the ASME, 135(1), pp. 179-193.

[39] Meirovitch, L., and Parker, R., 2001, Fundamentals of Vibrations, Waveland Press Inc., Long Grove, Illinois.

[40] Desbordes, H., Fillon, M., Frene, J., and Chan Hew Wai, C., 1995, "The Effects of Three-Dimensional Pad Deformations on Tilting-Pad Journal Bearings under Dynamic Loading," Journal of tribology, 117(3), pp. 379-384.

[41] Someya, T., 1989, Journal-Bearing Databook, Springer-Verlag, Berlin, Germany.

[42] Kulhanek, C., and Childs, D., 2012, "Measured Static and Rotordynamic Coefficient Results for a Rocker-Pivot, Tilting-Pad Bearing with 50 and 60% Offsets," Journal of engineering for gas turbines and power, 134(5), pp. 052505.

[43] Wilkes, J. C., 2011, "Measured and Predicted Rotor-Pad Transfer Functions for a Rocker-Pivot Tilting-Pad Journal Bearing," Ph.D. Dissertation, Texas A&M University, College Station, Texas.

[44] P.G.Morton, 2007, "The Morton Effect and Light Rubs in Rotating Machinery," Orbit, 27(1), pp. 44-51.

APPENDIX A

VARIABLE VISCOSITY REYNODLS EQUATION FOR INCOMPRESSIBLE LUBRICANTS

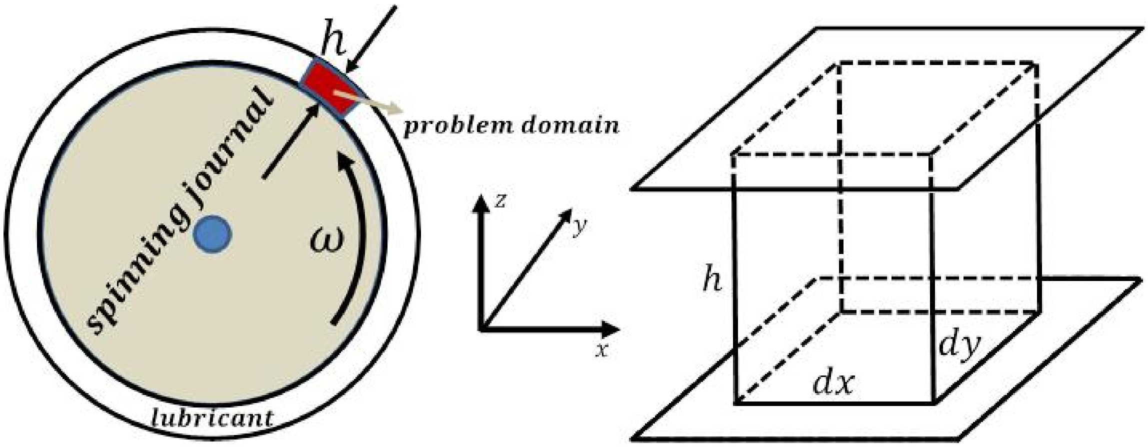

Figure A. 1 Problem domain

Figure A. 1 shows a problem domain of Reynolds equation which extends across the fluid film thickness in a bearing. h denotes film thickness at the current problem domain, and dx and dy are width and length respectively. Q_x and Q_y shown in Figure A. **2** are flow rates per unit width in the x and **y** direction respectively. $v_z(0)$ and $v_z(h)$ are surface velocities of the plane in the z direction. The two surfaces bound the fluid film in the z direction. Continuity equation can be derived by mass conservation law.

$$\frac{\partial}{\partial t}(\rho h) = -\frac{\partial}{\partial x}(\rho Q_x) - \frac{\partial}{\partial y}(\rho Q_y) \tag{A. 1}$$

Figure A. 3 shows the schematic diagram for momentum equation of the fluid film domain. The quantity p is fluid pressure and τ is shear stress acting on the differential lubricant volume. Newtonian fluid has the following properties:

$$\tau = \mu \frac{du}{dz} \tag{A. 2}$$

where u denotes the fluid velocity in the x direction and μ is an absolute viscosity.

When Newton's 2nd law is applied and initial forces are ignored, the following equations are obtained.

$$x \text{ momentum equation: } \frac{\partial p}{\partial x} = \frac{\partial}{\partial z}\left(\mu \frac{du}{dz}\right) \tag{A. 3}$$

$$y \text{ momentum equation: } \frac{\partial p}{\partial y} = \frac{\partial}{\partial z}\left(\mu \frac{dv}{dz}\right) \tag{A. 4}$$

$$z \text{ momentum equation: } \frac{\partial p}{\partial y} = 0 \tag{A. 5}$$

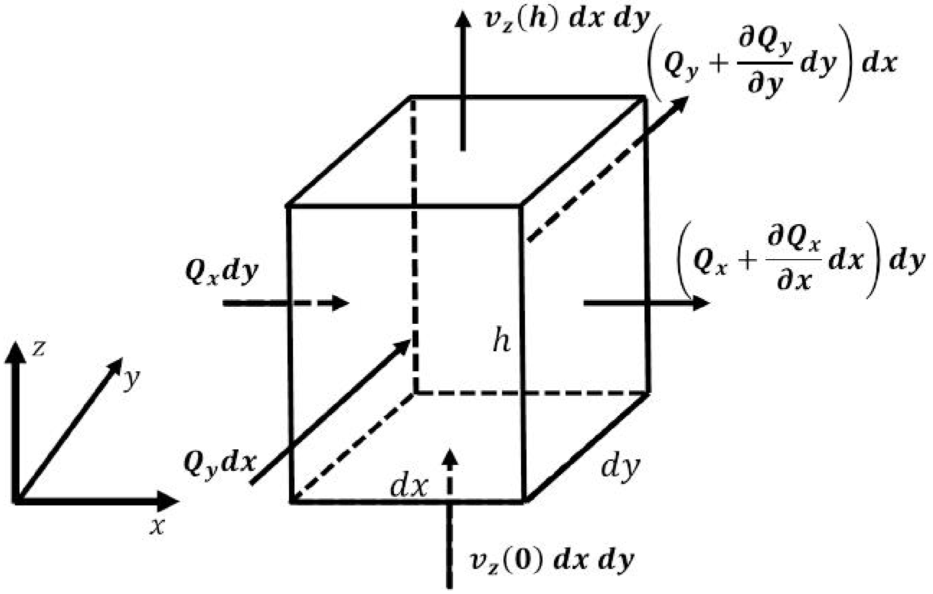

Figure A. 2 Schematic diagram for continuity equation

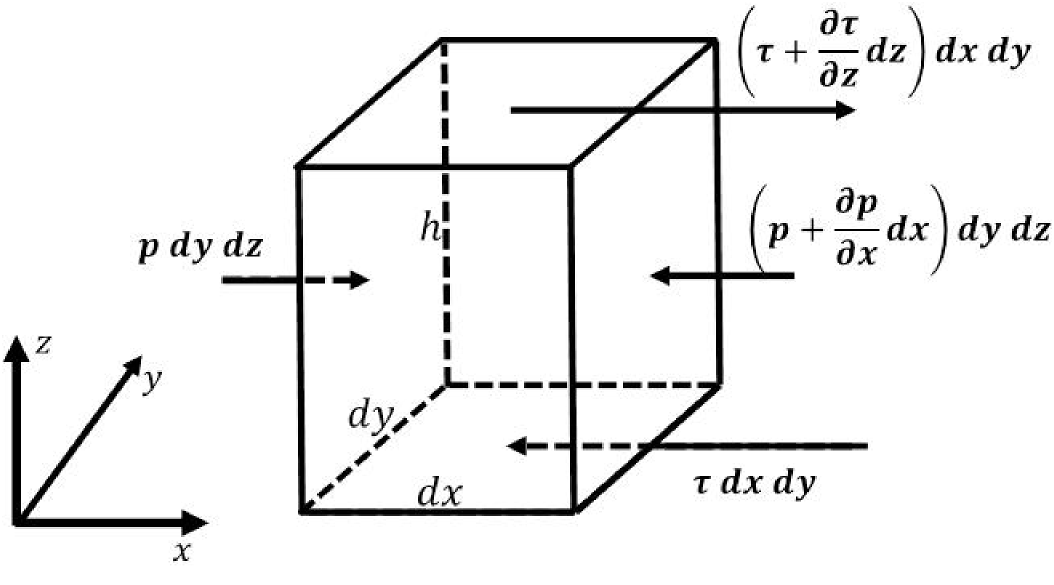

Figure A. 3 Schematic diagram for momentum equation

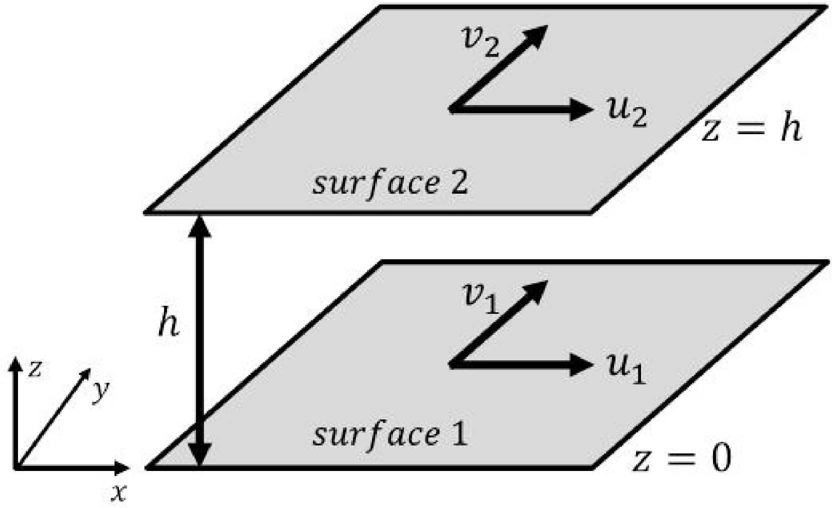

Figure A. 4 Surface velocities where the fluid film is bounded

The lubricant is bounded in the *z* direction by the spinning journal and bearing pad surfaces as depicted in Figure A. 4. From momentum equation in the *x* direction (A. 3),

$$\frac{\partial u}{\partial z} = \frac{1}{\mu}\frac{\partial p}{\partial x}z + \frac{1}{\mu}C_1 \tag{A. 6}$$

$$u = \frac{\partial p}{\partial x}\int_0^z \frac{\xi}{\mu}d\xi + \int_0^z \frac{1}{\mu}d\xi \cdot C_1 + C_2 \tag{A. 7}$$

The fluid velocities at the surface 1 and surface 2 are as follows:

$$u(0) = u_2 = C_2 \tag{A. 8}$$

$$u(h) = \frac{\partial p}{\partial x}\int_0^h \frac{\xi}{\mu} d\xi + \int_0^h \frac{1}{\mu} d\xi \cdot C_1 + C_2 = u_1 \tag{A. 9}$$

These boundary conditions lead to:

$$C_2 = u_2 \tag{A. 10}$$

$$C_1 = \frac{u_1 - u_2 - \frac{\partial p}{\partial x}\int_0^h \frac{\xi}{\mu} d\xi}{\int_0^h \frac{1}{\mu} d\xi} \tag{A. 11}$$

$$\boldsymbol{u}(z) = \nabla p \int_0^z \frac{\xi}{\mu} d\xi + \int_0^z \frac{1}{\mu} d\xi \cdot \frac{u_1 - u_2 - \nabla p \int_0^h \frac{\xi}{\mu} d\xi}{\int_0^h \frac{1}{\mu} d\xi} + u_2 \tag{A. 12}$$

$$\boldsymbol{u}(z) = \nabla p \left(\int_0^z \frac{\xi}{\mu} d\xi - \frac{\int_0^h \frac{\xi}{\mu} d\xi}{\int_0^h \frac{1}{\mu} d\xi} \int_0^z \frac{1}{\mu} d\xi \right) + \frac{\int_0^z \frac{1}{\mu} d\xi}{\int_0^h \frac{1}{\mu} d\xi} (\boldsymbol{u_1} - \boldsymbol{u_2}) + \boldsymbol{u_2} \tag{A. 13}$$

Vector $\boldsymbol{u}$ becomes the function of z, film thickness direction. The flow rate vector $\boldsymbol{Q}$ denotes the direction and amount of flowing lubricant in the problem domain per second as below:

$$\boldsymbol{Q} = \int_0^h \boldsymbol{u}(z)\, dz \tag{A. 14}$$

Integration of (A. 13) in the z direction as shown in (A. 14) leads to the following equation.

$$\boldsymbol{Q} = \nabla p \int_0^h \left(\int_0^z \frac{\xi}{\mu} d\xi - \frac{\int_0^h \frac{\xi}{\mu} d\xi}{\int_0^h \frac{1}{\mu} d\xi} \int_0^z \frac{1}{\mu} d\xi \right) dz + (\boldsymbol{u_1} - \boldsymbol{u_2}) \int_0^h \frac{\int_0^z \frac{1}{\mu} d\xi}{\int_0^h \frac{1}{\mu} d\xi}\, dz + \int_0^h \boldsymbol{u_2}\, dz \tag{A. 15}$$

$$\boldsymbol{Q} = D_1 \nabla p + D_2 (\boldsymbol{u_1} - \boldsymbol{u_2}) + h\boldsymbol{u_2} \tag{A. 16}$$

Substitution of (A. 16) into the continuity equation (A. 1), assuming constant density ρ and considering $\boldsymbol{u_1}$ only in the *x* direction, yields the generalized Reynolds equation below, where R denotes the radius of spinning journal with angular velocity ω.

$$\nabla(D_1 \nabla p) + (\nabla D_2) R\omega + \frac{dh}{dt} = 0. \tag{A. 17}$$

APPENDIX B

FINITE ELEMENT FORMULATION OF REYNOLDS EQUATION

The generalized Reynolds equation has been derived in APPENDIX A. This section deals with the derivation of finite element solution of that. The function for the generalized Reynolds equation with the boundary condition discussed above can be obtained by use of variation al principles and is given by:

$$\nabla(D_1\nabla p) + (\nabla D_2)U + \frac{dh}{dt} = 0 \; in \; \Omega \qquad \text{(B. 1)}$$

subject to the boundary conditions;

$$\begin{aligned} p &= P^* \qquad on\; S_p \\ q &= q^* \qquad on\; S_q \end{aligned} \qquad \text{(B. 2)}$$

The problem domain is described in Figure B. 1 where discretization is performed. The boundary is composed of two areas, prescribed pressure on S_p and prescribed lubricant flow on S_q, where they cannot overlap. The functional for generalized Reynolds equation with the prescribed boundary conditions can be produced by use of variational principles and shown in (). The finite element method produces pressure distribution by making the functional. This is performed by dividing the problem domain Ω into finite number of elements as shown in Figure B. 1

$$_p = \int_{\Omega} \left(-\frac{1}{2}C_1\nabla P \cdot \nabla P + C_2 U \cdot \nabla P + P\frac{\partial h}{\partial t}\right) d\Omega + \int_{S_q} pq \cdot ndS \qquad \text{(B. 3)}$$

To discretize the problem domain, function p minimizing the functional should be calculated. The first derivative of the functional with respect to the function p vanishes at the minimum as shown below:

$$\frac{\partial J_p}{\partial p} = 0 \qquad \text{(B. 4)}$$

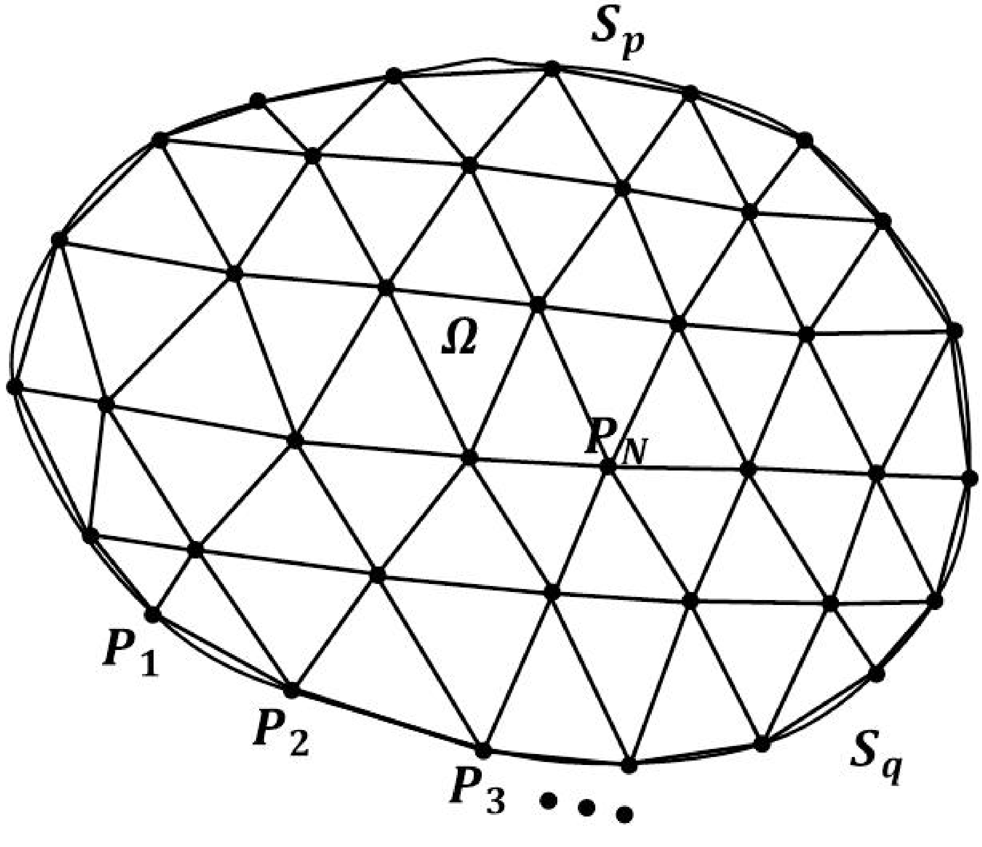

Figure B. 1 Discretized problem domain for Reynolds equation

The finite element formula is produced by use of Galerkin method, where an approximation function can be written in terms of the shape function and nodal values as seen in (B. 5). ***N*** is the shape function and ***P*** is the nodal pressure vector. Three node, triangular simplex element has been found to perform well for interpolation of two-dimensional pressure domain $\boldsymbol{p}$ in the element area $\Omega_{\boldsymbol{e}}$. Finite element formula is derived by incorporating the formula (B. 5). The global finite element matrices is expressed as seen in (B. 6).

$$\boldsymbol{P_{approx}} = \boldsymbol{N^T} \cdot \boldsymbol{P_e} \tag{B. 5}$$

where

$\boldsymbol{N^T} = [N_1 \; N_2 \; N_3]$

$\boldsymbol{P_e^T} = [P_{1e} \; P_{2e} \; P_{3e}]$

$$\boldsymbol{K_f P} = \boldsymbol{F_f} \tag{B. 6}$$

where

$$\boldsymbol{K_f} = -\int_{\Omega} C_1 \left(\frac{\partial N_i}{\partial x} \frac{\partial N_j}{\partial x} + \frac{\partial N_i}{\partial y} \frac{\partial N_j}{\partial y} \right) d\Omega$$

$$\boldsymbol{F_f} = \boldsymbol{B_f} + \boldsymbol{S_f} + \boldsymbol{L_f}$$

$$\boldsymbol{B_f} = \int_{\Omega} C_2 U_x \frac{\partial N_i}{\partial x} d\Omega + \int_{\Omega} C_2 U_y \frac{\partial N_i}{\partial y} d\Omega \quad (\boldsymbol{wedge\ effet})$$

$$\boldsymbol{S_f} = -\frac{\partial h}{\partial t} \int_{\Omega} N_i \, d\Omega \quad (\boldsymbol{squeeze\ effect})$$

$$\boldsymbol{L_f} = -\int_{S_q} q N_i \, dS \quad (\boldsymbol{imposed\ boundary\ flow\ effect})$$

The physical causes of the pressure force terms are

$\boldsymbol{B_f}$: drag of lubricant into converging or diverging wedges

$\boldsymbol{S_f}$: squeeze (damping)

$\boldsymbol{L_f}$: Imposed flow on boundary

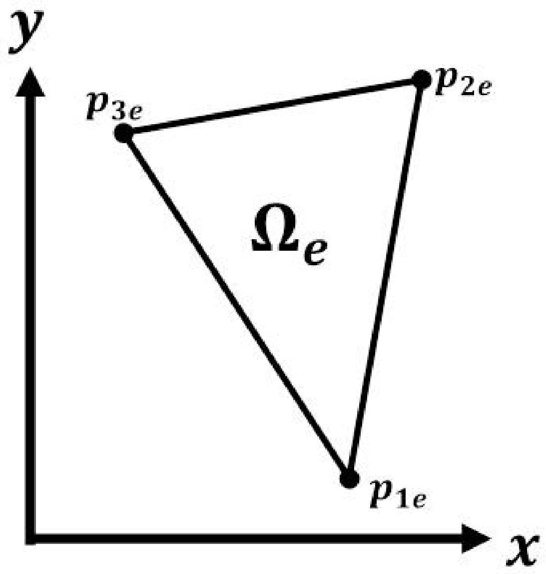

Figure B. 2 Triangular simplex element for fluid pressure interpolation

The linear interpolation of pressure in the three-node, simplex element is described in Figure B. 2. The shape functions are

$$N_n = \frac{1}{2\Omega_e}(a_n + b_n + c_n), \qquad n = 1,2,3 \tag{B. 7}$$

The element area Ω_e is given by:

$$\Omega_e = \frac{1}{2}|(x_2y_3 - x_3y_2) - (x_1y_3 - y_1x_3) + (x_1y_2 - x_2y_1)| \tag{B. 8}$$

The coefficients are obtained by:

$$\begin{bmatrix} a_1 & a_2 & a_3 \\ b_1 & b_2 & b_3 \\ c_1 & c_2 & c_3 \end{bmatrix} = \begin{bmatrix} x_2y_3 - x_3y_2 & x_3y_1 - x_1y_3 & x_1y_2 - x_2y_1 \\ y_2 - y_3 & y_3 - y_1 & y_1 - y_2 \\ x_3 - x_2 & x_1 - x_3 & x_2 - x_1 \end{bmatrix} \tag{B. 9}$$

The final elemental matrices and vectors are given by:

$$\boldsymbol{K_f^e} = -(b_ib_j + c_ic_j)\frac{\overline{C_1}}{4\Omega_e} \tag{B. 10}$$

$$\boldsymbol{B_f^e} = (Ub_i)\frac{\overline{C_2}}{2} \quad (wedge\ effet) \tag{B. 11}$$

$$\boldsymbol{S_f^e} = -\frac{\rho\Omega_e}{3}\frac{\partial h}{\partial t} \quad (squeeze\ effct) \tag{B. 12}$$

$$\boldsymbol{L_f^e} = -q\frac{L_{i-j}}{2} \quad (imposed\ boundary\ flow\ effect) \tag{B. 13}$$

$$\overline{C_\iota} = \frac{1}{\Omega_e} \int_{\Omega} C_i d\Omega \quad (i = 1,2) \tag{B. 14}$$

The global stiffness matrix and force vectors are assembled by the nodal connectivity matrix. The global matrix gives a symmetric banded one. The solution produces a solution vector containing the nodal pressure values.

APPENDIX C

FINITE ELEMENT FORMULATION OF ENERGY EQUATION

In previous section, generalized Reynolds equation produced fluidic pressure distribution in the thin film. For the evaluation of the temperature distribution in the lubricant by energy equation, fluid velocity profile should be provided. The velocity can be calculated by the relationship between fluidic pressure and flow rate as discussed in the derivation of Reynolds equation of APPENDIX A. The governing energy equation is given by

$$\rho C_p \left(\frac{\partial T}{\partial t} + \boldsymbol{u} \cdot \nabla T \right) = k(\nabla \cdot \nabla T) + \Phi \qquad \text{in } \Omega \tag{C. 1}$$

subject to the boundary conditions;

$$\begin{aligned} T &= T^* && on\ S_T \\ q &= q^* && on\ S_q \\ q &= -h(T - T_\infty) && on\ S_h \end{aligned} \tag{C. 2}$$

For the weighted residual equation, Galerkin method is adopted. The resultant equation becomes (C. 3) with the weight function (W).

$$\int_\Omega W \left(\rho C_p \left(\frac{\partial T}{\partial t} + \boldsymbol{u} \cdot \nabla T \right) - \nabla \cdot (k \nabla T) - \Phi \right) d\Omega \tag{C. 3}$$

Applying Gauss theorem and boundary conditions shown in (C. 2) produces:

$$\int_{\Omega} \rho C_p \frac{\partial T}{\partial t} W \, d\Omega + \int_{\Omega} \rho C_p \, \boldsymbol{u} \cdot \nabla T \, W \, d\Omega - \int_{\Omega} \Phi W \, d\Omega$$

$$- \int_{\Omega} k\nabla T \cdot \nabla W \, d\Omega - \int_{\mathrm{S_T}} (kTW) \cdot \boldsymbol{n} \, dS_{\mathrm{T}} + \int_{\mathrm{S_q}} q^{*} W \, dS_{\mathrm{q}} \qquad \text{(C. 4)}$$

$$- \int_{\mathrm{S_h}} h(T - T_{\infty}) W \, dS_{\mathrm{h}} = 0$$

The approximate solution of the above equation is interpolated throughout the element by use of the shape functions as below:

$$T = N \cdot T$$

$$\boldsymbol{T_{approx}} = \boldsymbol{N^{T}} \cdot \boldsymbol{T_e} = N_j T_j$$

where (C. 5)

$$\boldsymbol{N^{T}} = [\boldsymbol{N_1} \, \boldsymbol{N_2} \, \boldsymbol{N_3} \, \boldsymbol{N_4} \, \boldsymbol{N_5} \, \boldsymbol{N_6} \boldsymbol{N_7} \, \boldsymbol{N_8}]$$

$$\boldsymbol{T_e^{T}} = [\boldsymbol{T_{1e}} \, \boldsymbol{T_{2e}} \, \boldsymbol{T_{3e}} \, \boldsymbol{T_{4e}} \, \boldsymbol{T_{5e}} \, \boldsymbol{T_{6e}} \, \boldsymbol{T_{7e}} \, \boldsymbol{T_{8e}}]$$

The shape function vector $\boldsymbol{N}$ has the shape functions and $\boldsymbol{T_e}$ contains the nodal temperature values on the particular element. Substituting the approximate temperature ($\boldsymbol{T_{approx}}$) into (C. 4) produces the following equation.

$$\left[\int_{\Omega} \rho C_p W N_j \, d\Omega\right] \dot{T}_j + \left[\int_{\Omega} \left(\rho C_p \, W\boldsymbol{u} \cdot \nabla N_j + k\nabla W \cdot \nabla N_j\right) d\Omega + \int_{\mathrm{S_h}} hWN_j \, dS_{\mathrm{h}}\right] T_j$$

$$= \int_{\Omega} \Phi W \, d\Omega + \int_{\mathrm{S_q}} q^{*} W \, dS_{\mathrm{q}} + \int_{\mathrm{S_T}} (k\nabla TW) \cdot \boldsymbol{n} \, dS_{\mathrm{T}} + \int_{\mathrm{S_h}} hT_{\infty} W \, dS_{\mathrm{h}}$$

(C. 6)

The weight function vanishes on the boundary S, so the following integration becomes zero.

$$\int_{\mathrm{S_T}} (k\nabla TW) \cdot \, d\mathrm{S_T} = 0 \tag{C. 7}$$

If the equation (C. 6) is written in matrix and vector form,

$$\boldsymbol{K_E T} = \boldsymbol{F_E} \tag{C. 8}$$

where

$$\begin{aligned}
\boldsymbol{C_M} &= \int_{\Omega} \rho C_p W_r N_s \, d\Omega \\
\boldsymbol{K_v} &= \int_{\Omega} \rho C_p \, W_r \boldsymbol{u} \cdot \nabla N_s \, d\Omega \\
\boldsymbol{K_c} &= \int_{\Omega} k\nabla W_r \cdot \nabla N_s \, d\Omega \\
\boldsymbol{K_h} &= \int_{\mathrm{S_h}} hW_r N_s \, d\Omega \\
\boldsymbol{F_q} &= \int_{\Omega} \Phi W_r \, d\Omega \\
\boldsymbol{F_h} &= \int_{\mathrm{S_h}} hT_\infty W_r \, d\mathrm{S_h} \\
\boldsymbol{F_f} &= \int_{\mathrm{S_q}} q^* W_r \, d\mathrm{S_q}
\end{aligned} \tag{C. 9}$$

For integration on the isoparametric elements, the physical coordinate should be transformed into the natural coordinate. The 1D two-node isoparametric shape function for each natural coordinate is shown in (C. 10), and the 3D eight-node isoparametric shape functions are shown in (C. 11).

$$
\begin{aligned}
&\psi_1(\xi) = \frac{1}{2}(1-\xi) \qquad &&\psi_1(\eta) = \frac{1}{2}(1-\eta) \qquad &&\psi_1(\tau) = \frac{1}{2}(1-\tau)\\
&\psi_2(\xi) = \frac{1}{2}(1+\xi) \qquad &&\psi_2(\eta) = \frac{1}{2}(1-\eta) \qquad &&\psi_2(\tau) = \frac{1}{2}(1-\tau)\\
&\psi_3(\xi) = \frac{1}{2}(1-\xi) \qquad &&\psi_3(\eta) = \frac{1}{2}(1+\eta) \qquad &&\psi_3(\tau) = \frac{1}{2}(1-\tau)\\
&\psi_4(\xi) = \frac{1}{2}(1+\xi) \qquad &&\psi_4(\eta) = \frac{1}{2}(1+\eta) \qquad &&\psi_4(\tau) = \frac{1}{2}(1-\tau)\\
&\psi_5(\xi) = \frac{1}{2}(1-\xi) \qquad &&\psi_5(\eta) = \frac{1}{2}(1-\eta) \qquad &&\psi_5(\tau) = \frac{1}{2}(1+\tau)\\
&\psi_6(\xi) = \frac{1}{2}(1+\xi) \qquad &&\psi_6(\eta) = \frac{1}{2}(1-\eta) \qquad &&\psi_6(\tau) = \frac{1}{2}(1+\tau)\\
&\psi_7(\xi) = \frac{1}{2}(1-\xi) \qquad &&\psi_7(\eta) = \frac{1}{2}(1+\eta) \qquad &&\psi_7(\tau) = \frac{1}{2}(1+\tau)\\
&\psi_8(\xi) = \frac{1}{2}(1+\xi) \qquad &&\psi_8(\eta) = \frac{1}{2}(1+\eta) \qquad &&\psi_8(\tau) = \frac{1}{2}(1+\tau)
\end{aligned}
\tag{C. 10}
$$

$$
\begin{aligned}
N_1 &= \frac{1}{8}(1-\xi)\,(1-\eta)(1-\tau)\\
N_2 &= \frac{1}{8}(1+\xi)(1-\eta)(1-\tau)\\
N_3 &= \frac{1}{8}(1-\xi)(1+\eta)(1-\tau)\\
N_4 &= \frac{1}{8}(1+\xi)(1+\eta)(1-\tau)
\end{aligned}
\tag{C. 11}
$$

$$N_5 = \frac{1}{8}(1-\xi)(1-\eta)(1+\tau)$$

$$N_6 = \frac{1}{8}(1+\xi)\,(1-\eta)(1+\tau)$$

$$N_7 = \frac{1}{8}(1-\xi)(1+\eta)(1+\tau)$$

$$N_8 = \frac{1}{8}(1+\xi)(1+\eta)(1+\tau)$$

The first derivative matrix of the shape function in the eight-node isoparametric element is called a B matrix given by:

$$\frac{\partial N_i}{\partial \xi_j} = \begin{bmatrix} -\frac{1}{8}(1-\eta)(1-\tau) & -\frac{1}{8}(1-\xi)\,(1-\tau) & -\frac{1}{8}(1-\xi)\,(1-\eta) \\ \frac{1}{8}(1-\eta)(1-\tau) & -\frac{1}{8}(1+\xi)(1-\tau) & -\frac{1}{8}(1+\xi)(1-\eta) \\ -\frac{1}{8}(1+\eta)(1-\tau) & \frac{1}{8}(1-\xi)(1-\tau) & -\frac{1}{8}(1-\xi)(1+\eta) \\ \frac{1}{8}(1+\eta)(1-\tau) & \frac{1}{8}(1+\xi)(1-\tau) & -\frac{1}{8}(1+\xi)(1+\eta) \\ -\frac{1}{8}(1-\eta)(1+\tau) & -\frac{1}{8}(1-\xi)(1+\tau) & \frac{1}{8}(1-\xi)(1-\eta) \\ \frac{1}{8}\,(1-\eta)(1+\tau) & -\frac{1}{8}(1+\xi)\,(1+\tau) & \frac{1}{8}(1+\xi)\,(1-\eta) \\ -\frac{1}{8}(1+\eta)(1+\tau) & \frac{1}{8}(1-\xi)(1+\tau) & \frac{1}{8}(1-\xi)(1+\eta) \\ \frac{1}{8}(1+\eta)(1+\tau) & \frac{1}{8}(1+\xi)(1+\tau) & \frac{1}{8}(1+\xi)(1+\eta) \end{bmatrix} \qquad \text{(C. 12)}$$

After the transformation, integration should be performed in the natural coordinate. The integration is perfomred by the transformation below, where *J* is the determinant of the Jacobian matrix.

$$\boldsymbol{C_m}{}_{rs}^{e} = \sum_{\boldsymbol{\tau=1}}^{N_{gauss}} \sum_{\boldsymbol{\xi=1}}^{N_{gauss}} \sum_{\boldsymbol{\varepsilon=1}}^{N_{gauss}} \rho C_p {W_r}^e {N_s}^e J \omega_\varepsilon \omega_\xi \omega_\tau$$

$$\boldsymbol{K_v}{}_{rs}^{e} = \sum_{\boldsymbol{\tau=1}}^{N_{gauss}} \sum_{\boldsymbol{\xi=1}}^{N_{gauss}} \sum_{\boldsymbol{\varepsilon=1}}^{N_{gauss}} \rho C_p \, {W_r}^e \boldsymbol{u} \cdot \nabla {N_s}^e J \omega_\varepsilon \omega_\xi \omega_\tau$$

$$\boldsymbol{K_c}{}_{rs}^{e} = \sum_{\boldsymbol{\tau=1}}^{N_{gauss}} \sum_{\boldsymbol{\xi=1}}^{N_{gauss}} \sum_{\boldsymbol{\varepsilon=1}}^{N_{gauss}} k \nabla {W_r}^e \cdot \nabla {N_s}^e \; J \omega_\varepsilon \omega_\xi \omega_\tau$$

$$\boldsymbol{K_h}{}_{rs}^{e} = \sum_{\boldsymbol{\tau=1}}^{N_{gauss}} \sum_{\boldsymbol{\xi=1}}^{N_{gauss}} \sum_{\boldsymbol{\varepsilon=1}}^{N_{gauss}} h {W_r}^e {N_s}^e J \omega_\varepsilon \omega_\xi \omega_\tau \tag{C. 13}$$

$$\boldsymbol{F_q}{}_{r}^{e} = \sum_{\boldsymbol{\tau=1}}^{N_{gauss}} \sum_{\boldsymbol{\xi=1}}^{N_{gauss}} \sum_{\boldsymbol{\varepsilon=1}}^{N_{gauss}} \Phi {W_r}^e J \omega_\varepsilon \omega_\xi \omega_\tau$$

$$\boldsymbol{F_h}{}_{r}^{e} = \sum_{\boldsymbol{\tau=1}}^{N_{gauss}} \sum_{\boldsymbol{\xi=1}}^{N_{gauss}} \sum_{\boldsymbol{\varepsilon=1}}^{N_{gauss}} h T_\infty {W_r}^e J \, \omega_\varepsilon \omega_\xi \omega_\tau$$

$$\boldsymbol{F_f}{}_{r}^{e} = \sum_{\boldsymbol{\tau=1}}^{N_{gauss}} \sum_{\boldsymbol{\xi=1}}^{N_{gauss}} \sum_{\boldsymbol{\varepsilon=1}}^{N_{gauss}} q^* {W_r}^e J \, \omega_\varepsilon \omega_\xi \omega_\tau$$

The shape and weight functions are calculated at each gauss point. The element matrix and vectors are assembled into a global matrix based on the nodal connectivity matrix. The equation of the global form is

$$[\boldsymbol{C_m}]\dot{\boldsymbol{T}} + [\boldsymbol{K_v} + \boldsymbol{K_c} + \boldsymbol{K} \quad]\boldsymbol{T} = [\boldsymbol{F_q} + \boldsymbol{F_h} + \boldsymbol{F_f}] \tag{C. 14}$$